Section 4

ELECTROMAGNETIC METHODS

Chapter 10
Electromagnetic methods: introduction and principles

10.1 INTRODUCTION

10.1.1 Background

Among all the geophysical methods, the electromagnetic techniques must have the broadest range of different instrumental systems of any, matched by the remarkable range of applications to which these methods are being applied. These methods also show the greatest geographical diversity as some are used extensively and preferentially in the areas in which they were developed. For example, SIROTEM (see Section 11.3) is used predominantly in Australia where it was developed (named after the Australian Commonwealth Scientific Industrial Research Organisation, CSIRO), and Turam systems in

Sweden. The range of EM instruments manufactured by Geonics Ltd, Canada, has been used predominantly in North America, particularly eastern Canada, and now increasingly in Europe. There have been some major developments in the portability and ease of use of some instruments and their ensuing popularity has resulted in the techniques being used more widely. The interpretation methods available are largely dependent upon the instrumentation used for each survey and the information about the plethora of equipment available is widely scattered throughout the literature. However, the diversity of equipment provides a wide range of instruments to choose between in order to select the most appropriate tool for the task in hand. This, rather than being a disadvantage, is a major strength. Modern EM systems provide a very powerful suite of sophisticated instruments. Coupled with major advances in computer interpretation techniques, EM methods are set to become much more heavily used, especially for engineering and environmental applications.

Probably the first electromagnetic method to be used for mineral ore exploration was developed by Karl Sundberg in Sweden over two decades following the First World War (Sundberg 1931). What is now known as the Sundberg method was developed in 1925 and was also used in structural mapping in hydrocarbon exploration (Sundberg and Hedström 1934). Other pioneering work was done in the early 1930s by a Russian geophysicist V.R. Bursian, whose work is little known in the West. Other electromagnetic methods have been available commercially only since the Second World War and particularly since the mid-1960s. EM methods are especially important, not only in mineral and hydrocarbon exploration, but increasingly in environmental geophysics applications.

The different electromagnetic systems available are described briefly in Section 10.1.3 and in more detail in the next chapter. Chapter 12 is devoted to a discussion of 'ground penetrating radar' (GPR). A much more comprehensive and detailed discussion of the various electromagnetic methods, with the exception of ground penetrating radar, has been produced by Misac Nabighian (1987, 1991) and coauthors. Further discussions and descriptions of the various methods have been given in the three-volume treatise *Geotechnical and Environmental Geophysics* edited by Stan Ward (1990).

10.1.2 Applications

The range of applications of EM methods is large. It is dependent upon the type of equipment being used but can be broadly categorised as listed in Table 10.1. Not all EM methods are equally appropriate to the applications listed. For example, ground penetrating radar has very limited use in the direct investigation of landfills by virtue of the high ambient conductivity and the corresponding high attenuation of radiowaves with depth. Conversely, ground conductivity mapping

Table 10.1 The range of applications for EM surveying*

Mineral exploration
Mineral resource evaluation
Groundwater surveys
Mapping contaminant plumes
Geothermal resource investigations
Contaminated land mapping
Landfill surveys
Detection of natural and artificial cavities
Location of geological faults, etc.
Geological mapping
Permafrost mapping, etc.

* Independent of instrument type

does not have the required resolution in comparison with GPR in some archaeological investigations. Furthermore, GPR can be used with care inside buildings, while ground conductivity methods cannot by virtue of interference from ambient electrical noise from mains power lines, etc.

One of the main advantages of the EM methods is that the process of induction does not require direct contact with the ground, as in the case of electrical methods where electrodes have to be planted into the ground surface (see Chapter 7). Consequently, the speed with which EM surveys can be made is much greater than an equivalent survey using contacting electrical resistivity. Furthermore, the induction process also allows the method to be used from aircraft and ships, as well as down boreholes. Similar to electrical resistivity methods, scale model experiments can be undertaken to illustrate particular structures (e.g. Frischknecht 1987). However, numerical models may be used preferentially (Hohmann 1987) but still require large amounts of computing time, and are limited by the computational difficulties in defining especially two- and three-dimensional models. Aspects of the limitations of computer analysis are discussed in more detail in the next chapter.

10.1.3 Types of EM systems

Electromagnetic methods can be classified as either time-domain (TEM) or frequency-domain (FEM) systems. Frequency-domain instruments use either one or more frequencies whereas time-domain equipment makes measurements as a function of time. EM methods can be either passive, utilising natural ground signals (e.g. magnetotellurics) or active, where an artificial transmitter is used either in the near-field (as in ground conductivity meters) or in the far-field (using remote high-powered military transmitters as in the case of VLF mapping).

Table 10.2 A classification of electrical and electromagnetic systems

Transmitter type	Receiver type			
	Ground wire	Both wire and small coil	Small coil (ground)	Small coil (air)
Grounded wire				
Galvanic	Resistivity IP		Magnetometric resistivity (MMR) Magnetic IP (MIP)	
Inductive		CSAMT	Some TEM systems	
Small loop			Slingram Horizontal-loop EM Vertical-loop EM Tilt-angle method Ground conductivity meters (GCM) Some TEM systems Coincident loop Borehole systems	Airborne EM Time-domain towed-bird Helicopter rigid-boom
Large loop (long wire)			Large-loop systems Sundberg method Turam Many TEM systems Borehole systems	
Plane wave				
Vertical antenna		VLF-resistivity	VLF	VLF
Natural geomagnetic field	Telluric currents			

Grounded wires measure potential difference per length, thus electric field. Coils (or fluxgate magnetometers or SQUIDS) measure magnetic field, or its time derivative. A small loop is a 3-D source (magnetic dipole). A long wire (or the long edge of a large loop) is a 2-D source. Natural EM sources are assumed to be 1-D sources. Receivers can be frequency-domain, time-domain (TEM), or both, CSAMT = controlled-oource audio magneto-telluric. This classification, which excludes the high-frequency techniques (radar, etc.), is based on Swift (1988, Table 1, p. 6)

A basic classification of EM systems is given in Table 10.2, which is based on Swift (1988). Each system is described briefly in this section; VLF, ground-conductivity, time-domain EM, telluric and magnetotelluric systems are described in more detail in Chapter 11. Ground penetrating radar is discussed comprehensively in Chapter 12.

Case histories are given where appropriate to illustrate the use of each of the main techniques. In most cases, the concept of each method is described rather than specific equipment systems which may change through continuing development work.

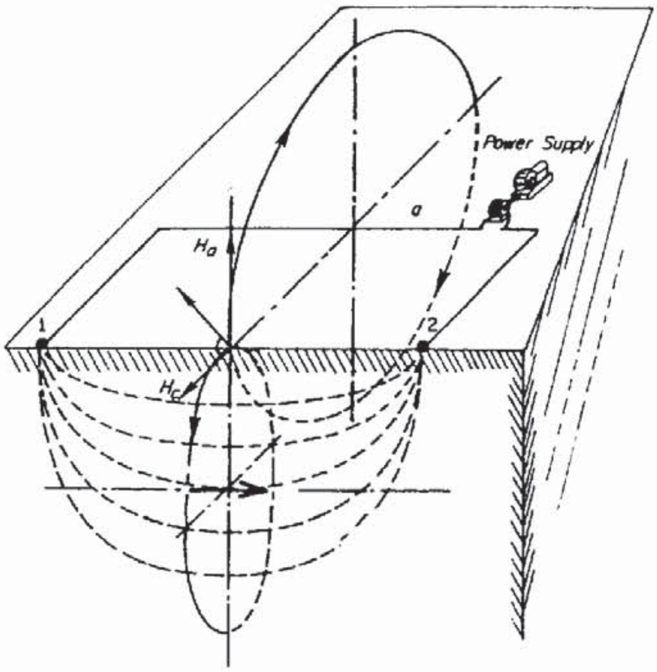

Figure 10.1 Basic concept of a magnetometric resistivity (MMR) field survey layout. Electrodes (1 and 2) are used to inject direct current into the ground. The secondary magnetic field arising from the current flow in the ground is measured at the mid-point by an extremely sensitive magnetometer. Reproduced with permission from Edwards and Nabighian (1991).

The term 'galvanic' used in Table 10.2 describes the injection of electrical current directly into the ground via electrodes; these methods are discussed in detail in Chapters 7 and 9.

10.1.3.1 Magnetometric resistivity (MMR)

Commutated direct current is injected into the ground through two widely separated electrodes. The anomalous conductivity contribution is determined at the midpoint by measuring the secondary magnetic field arising from the flow of current using an extremely sensitive low-noise magnetometer aligned perpendicular to the line between the electrodes (Figure 10.1). For further details, see Chapter 7 and, in particular, the review by Edwards and Nabighian (1991).

10.1.3.2 Small-loop systems

A frequency-domain EM system in which two small coils, one a transmitter and the other a receiver, separated by a constant distance of between 4 m and 100 m, are moved along a survey transect. The primary field is nulled so that the in-phase and quadrature components of the secondary field can be measured. The various combinations of coil orientation are shown in Figure 10.2. Slingram is synonymous with the *horizontal-loop method* (HLEM), Boliden, EM Gun, MaxMin and with Ronka EM methods. *Ground conductivity meters* (GCM) can be classified as being of this type of method. In this case, the quadrature component is normally taken to be a linear measure of the apparent conductivity of the ground; the coplanar

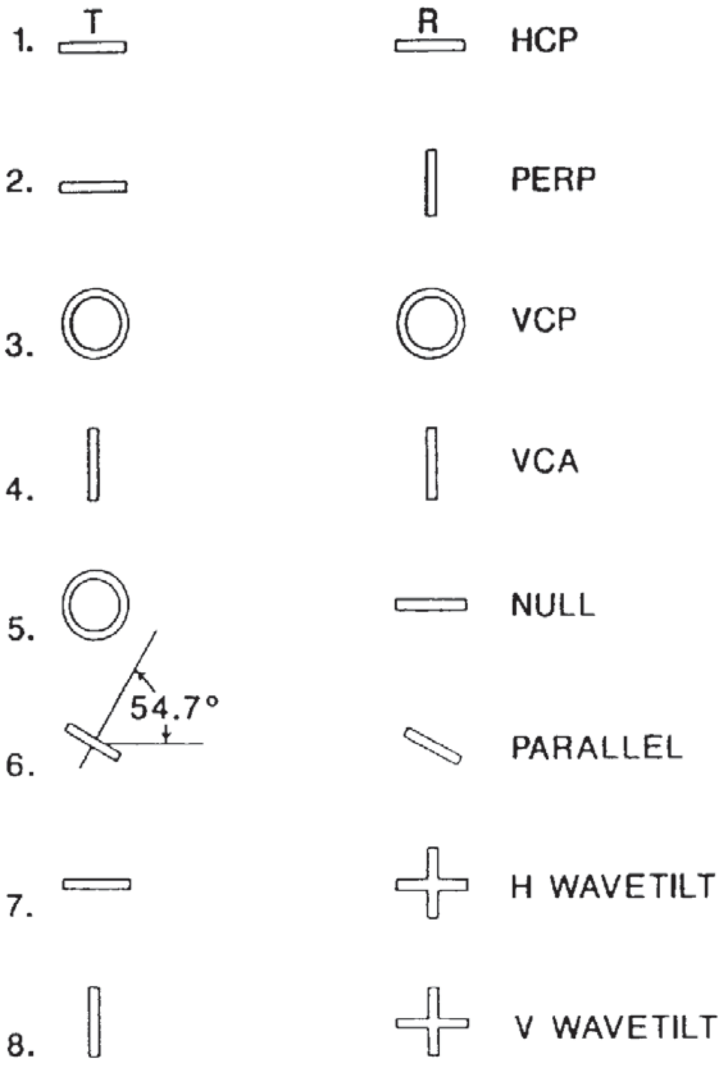

Figure 10.2 Eight common dipolar loop configurations (Tx = transmitter; Rx = receiver). Each rectangle represents the edge-on view of a coil; e.g. to move from configuration 1 to 3, both coils are rotated about a horizontal axis; to move from 3 to 4, each coil is rotated about a vertical axis. HCP = horizontal coplanar; VCP = vertical coplanar; VCA = vertical coaxial; PERP = perpendicular. Reproduced with permission from Frischnecht *et al.* (1991).

coils are deployed both horizontally and vertically; Chapter 11 has more details. For a detailed discussion of small-loop systems, see the review by Frischknecht *et al.* (1991).

10.1.3.3 Large-loop systems

There are two basic configurations in this classification, namely, the original method known as Sundberg's method, and the other, Turam.

Sundberg's method uses a long, grounded, insulated wire a few hundred metres to several kilometres long, or a rectangular loop with the long-side laid in the direction of geological strike (Figure 10.3A and B). Typical loop dimensions are 1200 m by 400 m. Measurements are made along profiles at right-angles to the cable or long side of the loop. Phase reference is taken by using a feeding coil located close to the source loop/cable using the compensator system shown in Figure 10.3C. Normally, only the vertical magnetic field is observed using the receiver coil. If the coil is deployed in three mutually perpendicular planes, then the EM field can be determined completely.

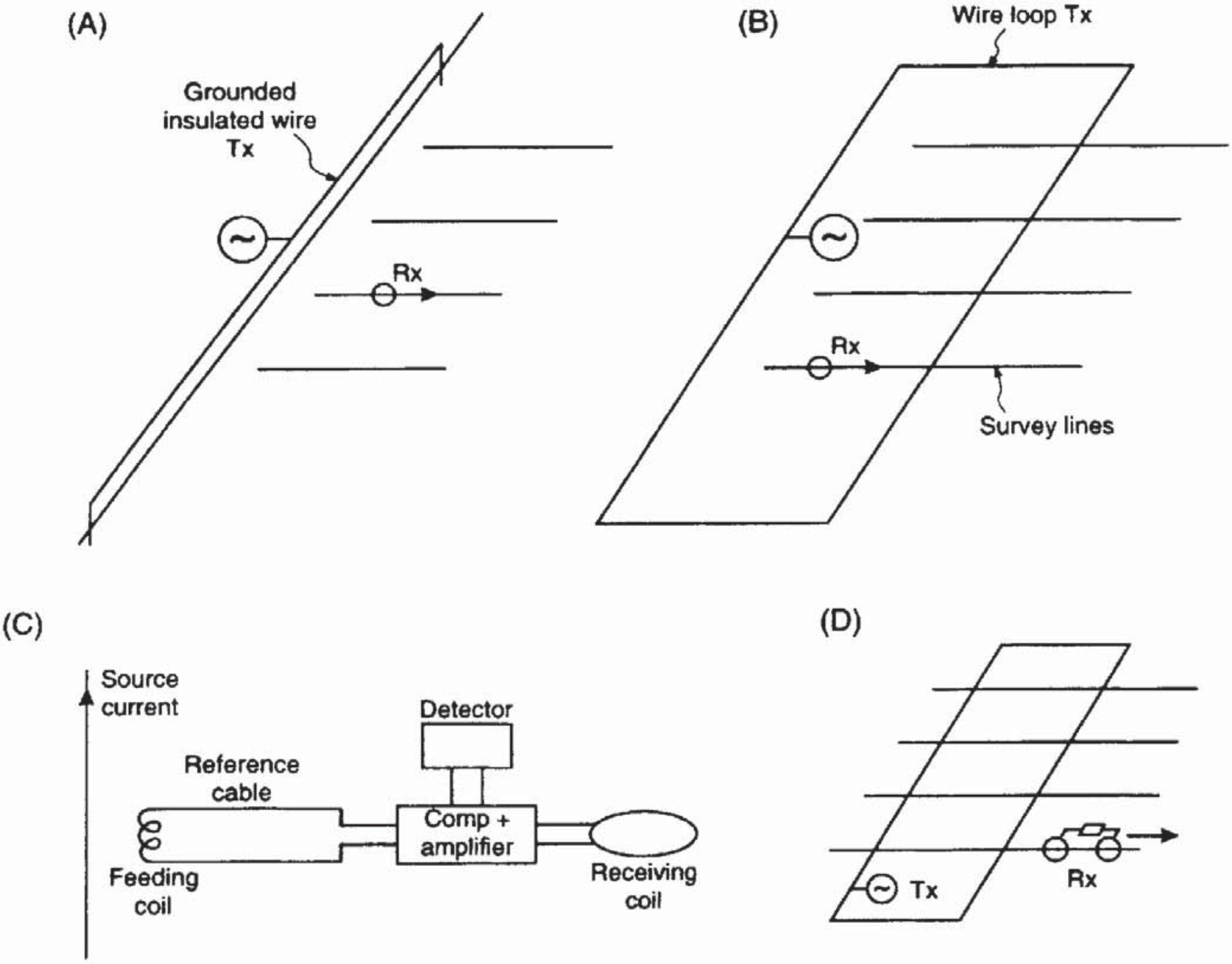

Figure 10.3 (A) Survey layout for the Sundberg method with a long grounded wire, or (B) a grounded wire loop with survey profile lines indicated. Phase reference is determined using a compensator (C) close to the source wire. In the Turam method (D), two separate receiver coils are deployed with a constant separation

The Turam technique overcomes a significant operational difficulty with the Sundberg method, i.e. the necessity to have a feeding coil close to the source cable/loop. In the Turam method, two separate receiver coils are used which are maintained at a constant separation, typically 10–20 m (Figure 10.3D). After each measurement, the coils are moved so that the rear coil then takes the position formerly occupied by the forward one, and so on along the transect. The two coils provide a means whereby a measurement is made of the ratio of the resultant vertical-field amplitudes and phase difference of the vertical fields at two neighbouring points. In effect, by having a constant coil separation and measuring parameters at each of the two locations, the horizontal gradient of phase of the resultant vertical field is determined. A more complete discussion of these two methods has been given by Parasnis (1991).

10.1.3.4 Time-domain systems

If a continuous EM field is produced by a transmitter, the secondary field is either determined by nulling the primary field so as to be able to detect the secondary field, or by measuring the resultant of both primary and secondary fields, and hence computing the secondary field parameters; those of the primary field are known by design. In time-domain or transient EM, the primary field is applied in pulses, typically 20–40 ms long, with the secondary field being measured once the primary field has been switched off over the following 100 ms, for example. One advantage of this is that the transmitter coil can also be used as the receiver. The basic field layouts are shown in Figure 10.4.

Typically a large ungrounded coil, through which a strong direct current is passed, is laid on the ground with the long axis parallel to

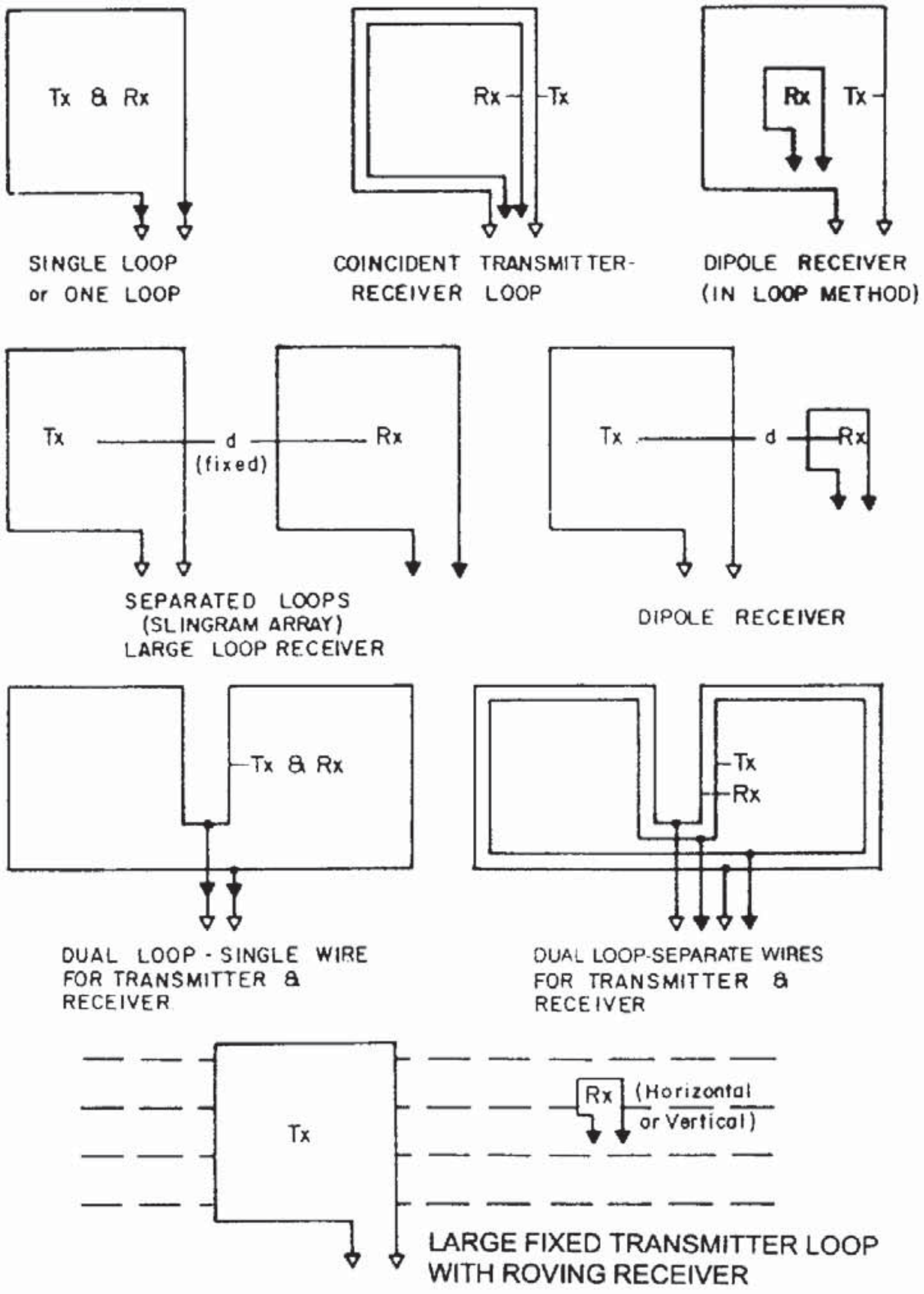

Figure 10.4 Field configurations for time-domain EM surveys. Reproduced with permission from Nabighian and Macnae (1991).

any geological strike. A small receiver coil is moved along transects perpendicular to the long axis of the ungrounded loop to obtain profiles of the measured parameters as a function of distance along the transect. Alternatively, instead of profiling, TEM systems can be used very effectively for depth soundings. Increased depth penetration is achieved by measuring the decay of the secondary field as a function of time. As the secondary field decays, the field parameters are measured at discrete time intervals (typically logarithmically arranged). It is analogous to the induced polarisation (IP) method in resistivity surveying. A specific system (INPUT) was developed in 1958 for airborne work (Barringer 1962). Following 1970, with improvements in technology and computing capabilities, a range of EM systems were developed by both academic institutions and commercial companies. By 1988, all instrument manufacturers had provided fully digital TEM systems.

As a guide, but depending upon the actual configurations and equipment being used, 50 TEM soundings per day is not unreasonable. With increasing pressure to use TEM in environmental applications where depths of penetration of less than 50 m are required, 'very-early TEM' (VETEM) systems are being developed. VETEM could be used in surveys where depths of penetration of less than 25 m but high vertical resolution are required, such as over closed landfills. For more detailed descriptions of TEM systems and of depth sounding, see the reviews by Nabighian and Macnae (1991) and by Spies and Frischknecht (1991) respectively.

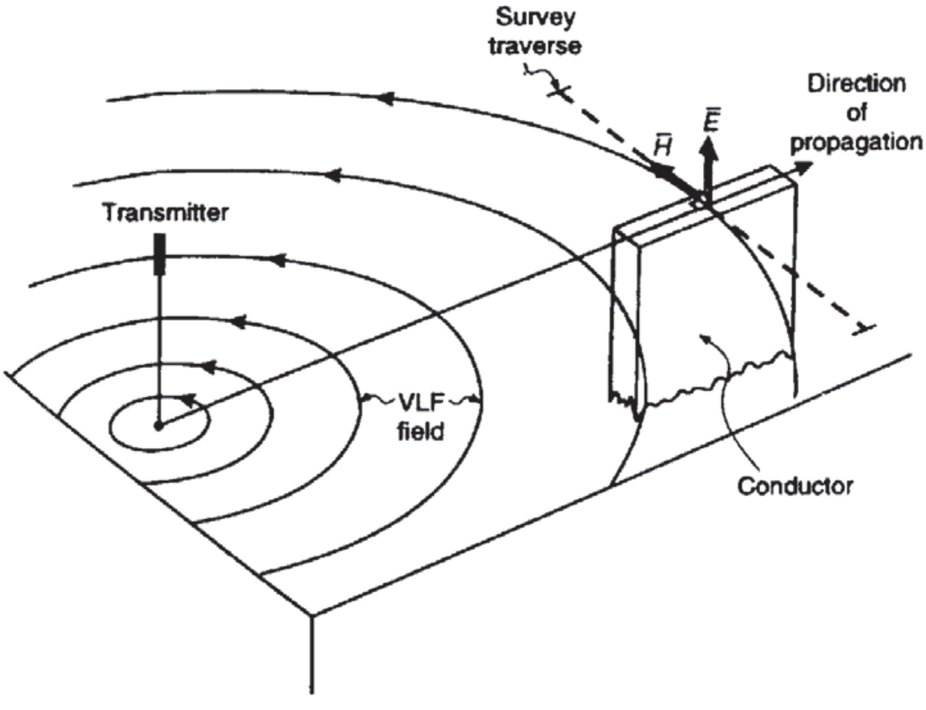

Figure 10.5 Artificial VLF source (e.g. military transmitter) provides a primary EM field which, at a sufficiently large distance, equates to a plane EM wave. Preferred survey directions over a linear conductor are tangential to the VLF field

10.1.3.5 Very low frequency (V.L.F)

High-powered military radio transmitters operating in the 15–24 kHz range (i.e. very low frequency in radio terms) are used to communicate with submarines even when submerged, and for long-range radio positioning. At very large distances from the transmitters, the EM field approximates to a plane wave which is used in geophysical exploration (Figure 10.5). The method can be used either on the ground or from aircraft. The method is discussed in more detail in the next chapter and has been reviewed by McNeill and Labson (1991).

10.2 PRINCIPLES OF EM SURVEYING

10.2.1 Electromagnetic waves

Electromagnetic methods use the response of the ground to the propagation of incident alternating electromagnetic waves which are made up of two orthogonal vector components, an electric intensity (***E***) and a magnetising force (***H***) (Figure 10.6), in a plane perpendicular to the direction of travel. An electromagnetic field can be generated by passing an alternating current through either a small coil comprising many turns of wire or a large loop of wire. The frequency range of electromagnetic radiation is very wide (Figure 10.7), from atmospheric micropulsations at a frequency less than 10 Hz, through the radar bands (10^8 to 10^{11} Hz) up to X-rays and gamma-rays at frequencies in excess of 10^{16} Hz. Of critical importance is the visible band ($\approx 10^{15}$ Hz).

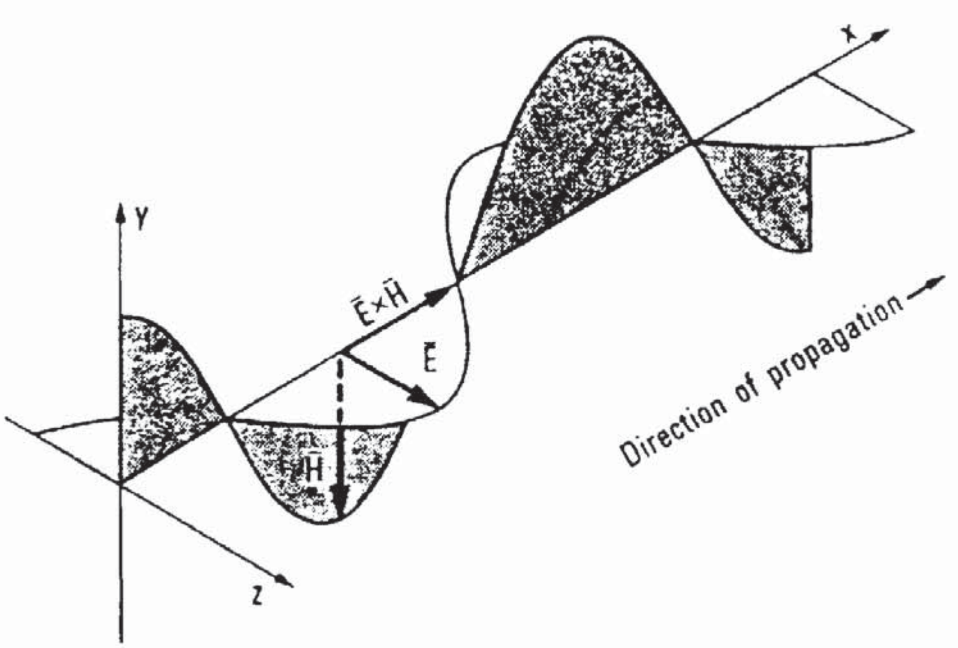

Figure 10.6 Basic elements of an electromagnetic wave, showing the two principal electric (***E***) and magnetic (***H***) components. Reproduced with permission from Beck (1981)

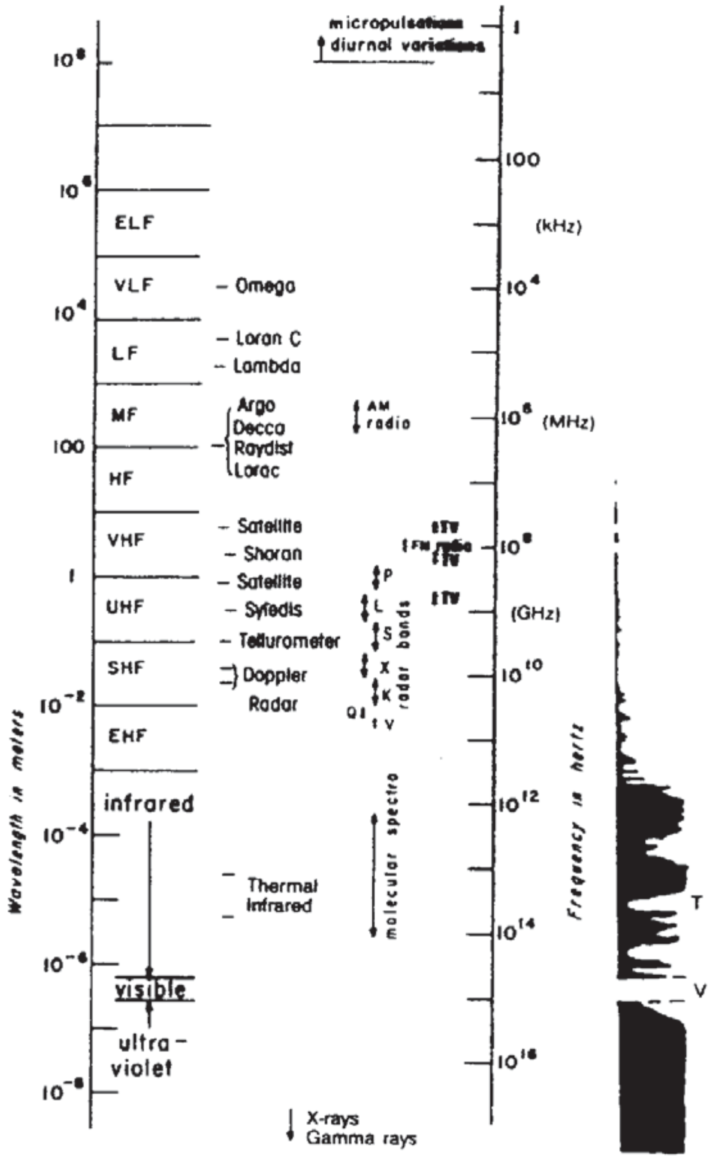

Figure 10.7 The electromagnetic spectrum. (A) designation of the various parts of the spectrum as a function of wavelength in metres. In (B), the dark portion of the graph shows zones of attenuation due to atmospheric absorption. Two windows are evident in the absorption spectrum at T (thermal infrared) and V (visible light). Reproduced with permission from Sheriff (1991)

For geophysical applications, frequencies of the primary alternating field are usually less than a few thousand hertz. The wavelength of the primary wave is of the order of 10–100 km while the typical source–receiver separation is much smaller (≈ 4–$100+$ m). Consequently, the propagation of the primary wave and associated wave attenuation can be disregarded (Figure 10.8).

In general, a transmitter coil is used to generate the primary electromagnetic field which propagates above and below ground. When the EM radiation travels through sub-surface media it is modified slightly relative to that which travels through air. If a conductive medium is present within the ground, the magnetic component of the incident EM wave induces eddy currents (alternating currents) within the conductor. These eddy currents then generate their own, secondary, EM field which is detected by a receiver

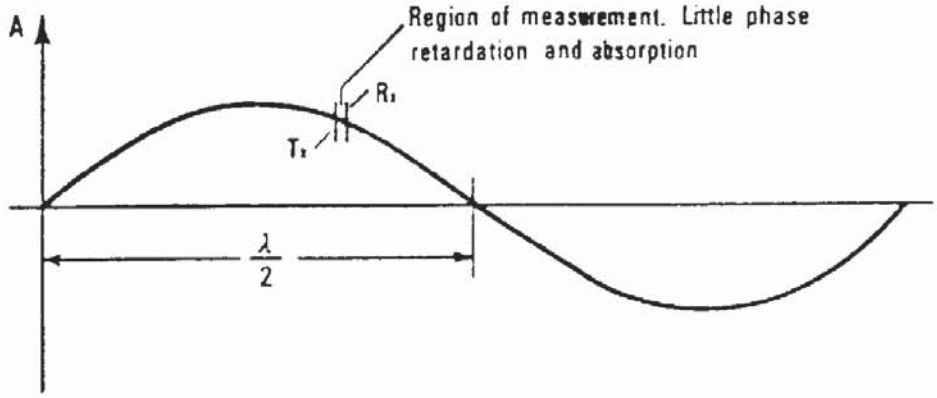

Figure 10.8 The physical separation of a transmitter (Tx) and receiver (Rx) is very small in relation to the wavelength of EM waves with frequencies greater than 3 kHz. Consequently, attenuation due to wave propagation can be ignored. Reproduced with permission from Beck (1991)

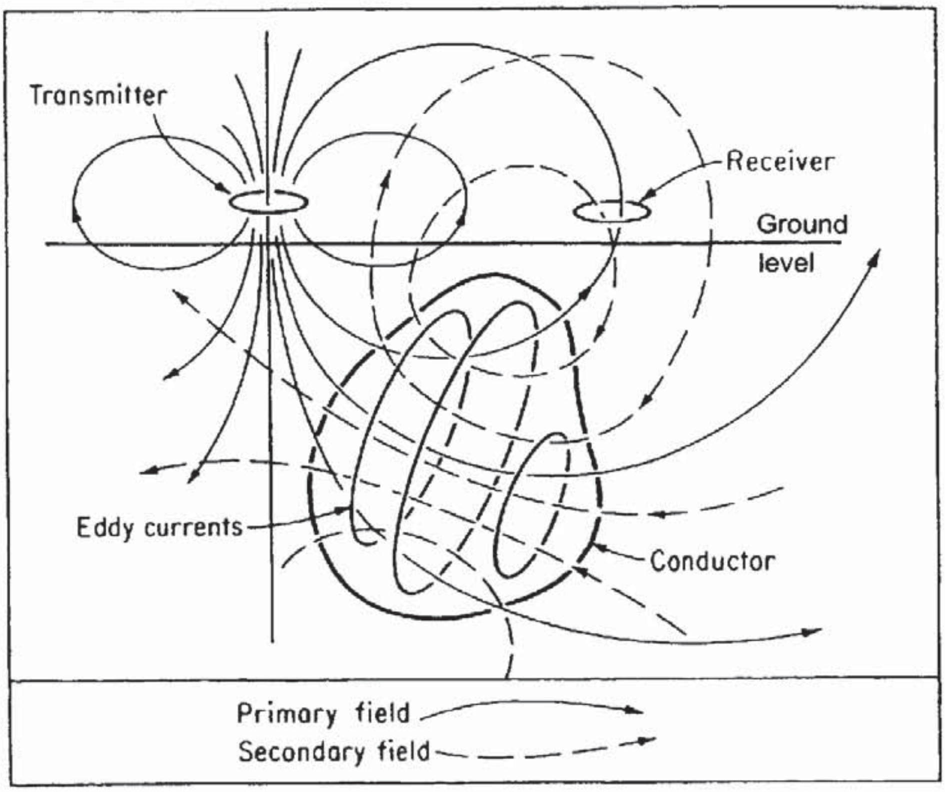

Figure 10.9 Generalized schematic of the EM surveying method. Reproduced with permission from Grant and West (1965)

(Figure 10.9). The receiver also detects the primary field which travels through the air, so the overall response of the receiver is the combined (resultant) effect of both the primary and the secondary fields. Consequently, the measured response will differ in both phase and amplitude relative to the unmodulated primary field. The degree to which these components differ reveals important information about the geometry, size, and electrical properties of any sub-surface conductor. Detailed discussions of electromagnetic theory, which are beyond the scope of this book, have been given by Grant and West (1965), Telford *et al.* (1990), and Ward and Hohmann (1991), among others.

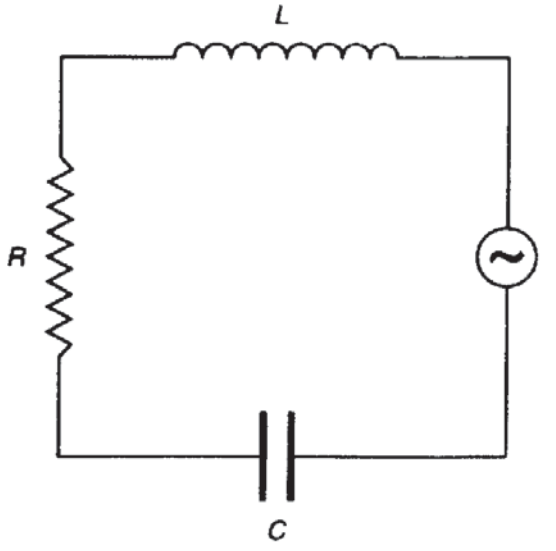

Figure 10.10 Basic electrical circuit containing capacitance (*C*), inductance (*L*) and resistance (*R*), the three electrical components that describe the equivalent behaviour of the ground.

It is useful to regard the ground under investigation as comprising three components: inductive (*L*), resistive (*R*) and capacitive (*C*); the electrical circuit equivalent is shown in Figure 10.10. The applied alternating voltage has the form of a sine wave with an angular frequency of $\omega\ (=2\pi f)$ and amplitude E_0 which varies as a function of time as described mathematically in Box 10.1. The current (I) which flows lags behind the applied voltage by an amount α, the phase lag. In EM exploration, a primary magnetic field is applied (P) which, in accordance with the properties of an EM wave, is in phase with its orthogonal electric component (E) (refer to Figure 10.6). Consequently, the form of the primary magnetic wave is $P = H_0 \sin \omega t$, where H_0 is the peak amplitude of the magnetic wave (Figure 10.11A). The voltage induced into a secondary perfect conductor as a result of the incident primary magnetic field lags behind the primary field by $\pi/2$.

According to Faraday's Law of EM induction, the magnitude of the induced voltage is directly proportional to the rate of change of the magnetic field. The induced voltage is directly proportional to the rate of change of the magnetic field. The induced voltage will be zero when the magnetic field is either at its maximum or minimum (Figure 10.11B). Eddy currents within a conductor take a finite time to generate, arising from an induced voltage. This generation time is manifest as the phase lag α (Figure 10.11C) which depends upon the electrical properties of the conductor. In good conductors this phase lag can be large, and conversely in poor conductors the phase lag is small. Once generated the secondary magnetic field interacts with the primary to form a resultant magnetic field (Figure 10.11D) which has a total phase lag (ϕ) behind the primary field.

Box 10.1 Time varying electrical field

The amplitude (E) of an alternating voltage is given by:

$$E = E_0 \sin \omega t.$$

The current (I) within the equivalent circuit (see Fig. 10.10) is described by:

$$I = E_0\{[\omega L - (1/\omega C)]^2 + R^2\}^{-1/2} \sin(\omega t - \alpha)$$

where

$$\alpha = \tan^{-1}[\omega L - (1/\omega C)]/R$$

and L is the inductance, C the capacitance and R the resistance.

The relationship between the primary, secondary and resultant fields can be represented in vector form (Figure 10.12A). The real (or in-phase) and imaginary (out-of-phase, or quadrature) components are shown on the vector diagram. The primary magnetic field is designated ***P*** and relates to the time-varying wave shown in Figure 10.11A. The induced voltage (cf. Figure 10.11B) lags $\pi/2$ (90°) behind the primary and the secondary current or magnetic field lags behind by α (cf. Figure 10.11C) and has a magnitude ***S***. By normal conven-

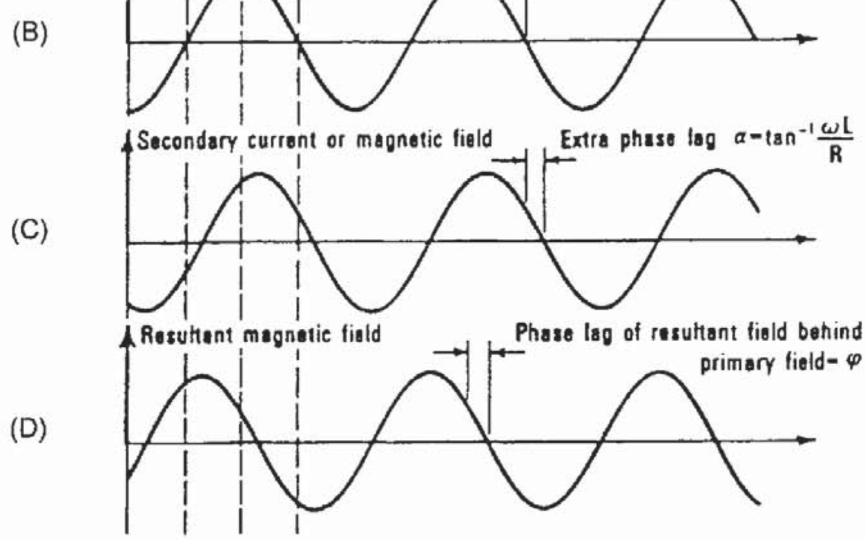

Figure 10.11 Relationships between induced voltages and associated phase lags between primary, secondary and resultant magnetic fields. Reproduced with permission from Beck (1981).

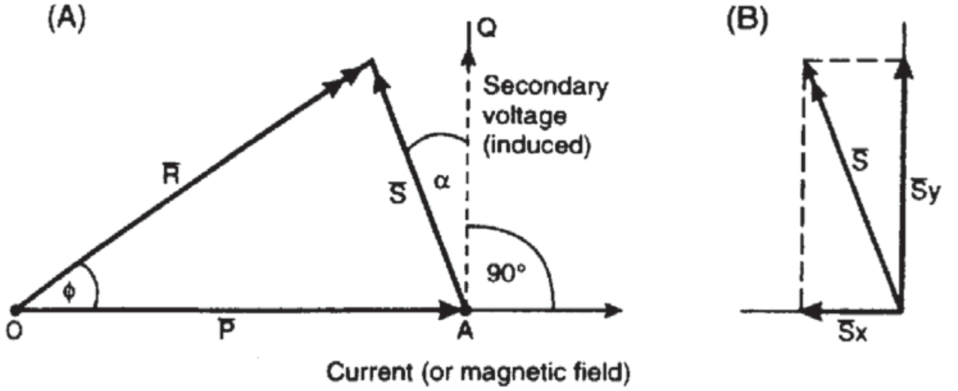

Figure 10.12 (A) Vector diagram defining the magnitudes and phase relationships of the primary and secondary fields. (B) The vectorial components of the secondary field in terms of the secondary voltage (Sy) and the current or primary magnetic field (Sx).

tions of vector diagrams, by completing the vector parallelogram, the resultant $\boldsymbol{R}$ of the primary and secondary fields (Figure 10.12A) is then defined with a total phase lag of ϕ (cf. Figure 10.11D). The secondary field $\boldsymbol{S}$ can be defined by the vectorial summation of its vertical and horizontal constituents (Figure 10.12B). Depending upon which equipment system is used, a number of these components can be measured from which an indication of the electrical properties of the sub-surface materials can be obtained.

10.2.2 Polarisation

It is important to consider two vectors $\boldsymbol{P}$ and $\boldsymbol{S}$ which differ in space by a spatial angle β (Figure 10.13A) and in phase by a phase angle ϕ. In order to calculate the resultant of these two vectors, it is necessary to resolve each into its horizontal and vertical components, denoted by suffices x and y, respectively. The mathematical summation is given in Box 10.2. The consequence of this summation process is that the resultant $\boldsymbol{R}$ always exists but varies continuously in magnitude and rotates in space. The tip of the resultant vector describes an ellipse in space, known as the 'ellipse of polarisation' (Figure 10.13C) which is inclined at an angle θ to the horizontal. The angle θ is known as the tilt or dip angle. Several EM methods (VLF and AFMAG) exploit this parameter and are known consequently as tilt-angle methods.

There are several special cases which should be mentioned. When the angle $\delta = 0$, equation (3) in Box 10.2 reverts to the equation of a straight line. This indicates that $\boldsymbol{R}$ is then a simple alternating vector and that the radiation comprises plane polarised waves. When $\delta = \pi/2$, the ellipse of polarisation is orientated such that axes are coincident with the x- and y-axes. The tilt angle θ becomes either zero or $n\pi/2$ when $\boldsymbol{P}$ and $\boldsymbol{S}$ are at right-angles and $\phi = \pi/2$. A further special case is when $\delta = \pi/2$ and $X = Y$, in which case equation (3) simplifies to the equation of a circle and the radiation is then circularly polarised.

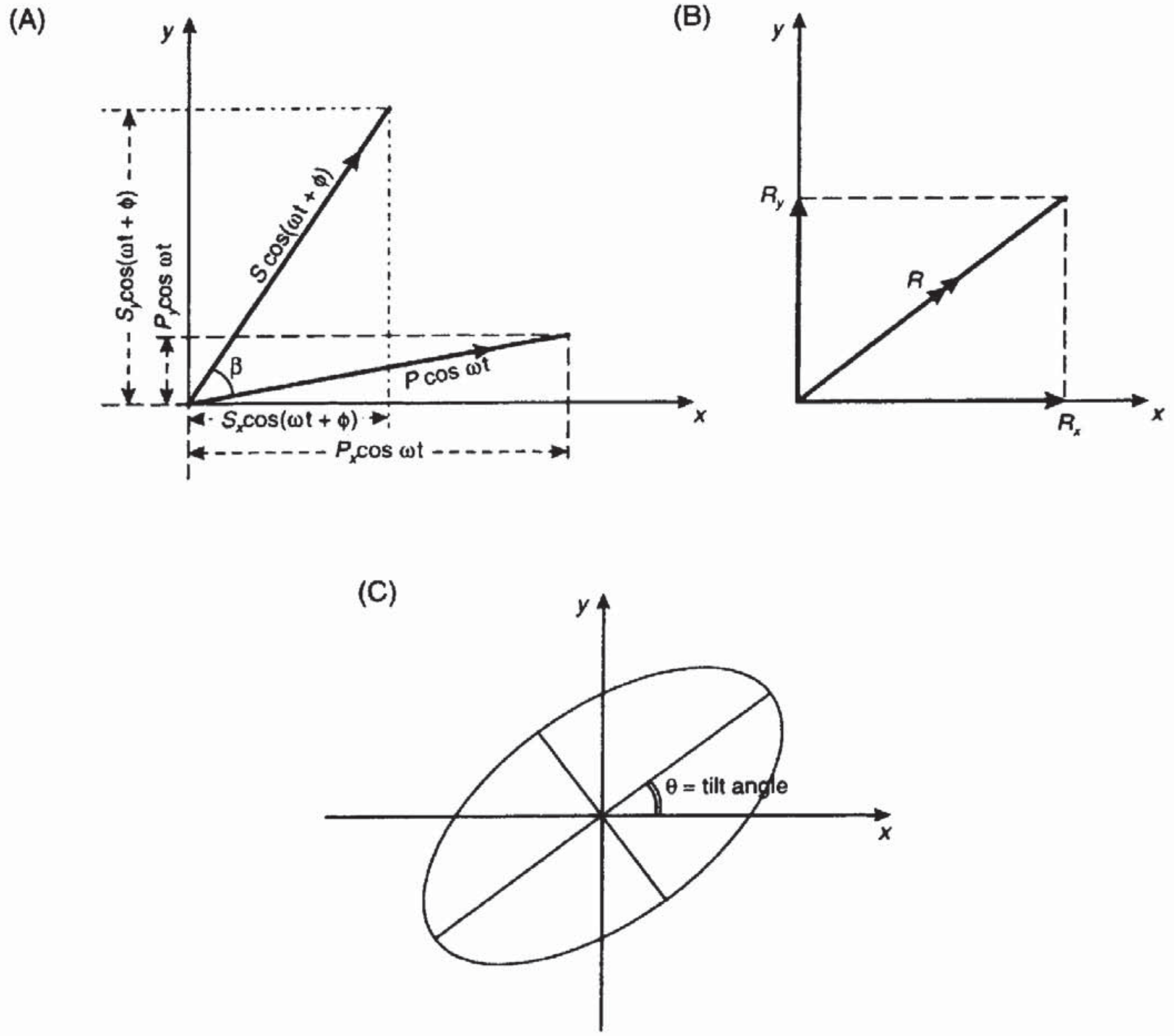

Figure 10.13 (A) Secondary field orientated in space at an angle β to the primary field. (B) The horizontal and vertical components R_x and R_y of the resultant of the summation of primary and secondary fields. (C) The ellipse of polarization inclined at the tilt-angle θ to the horizontal

Box 10.2 Polarisation ellipse

The primary field $\boldsymbol{P}(t)$ is given by:

$$\boldsymbol{P}(t) = \boldsymbol{P} \sin \omega t. \tag{1}$$

The secondary field $\boldsymbol{S}(t)$ is given by:

$$\boldsymbol{S}(t) = \boldsymbol{S} \sin [\omega t - (\pi/2 + \phi)]. \tag{2}$$

The resultant ($\boldsymbol{R}$) can be resolved into its horizontal and vertical components, suffices x and y respectively, where $\boldsymbol{R} = \boldsymbol{i}\boldsymbol{R}_x + \boldsymbol{j}\boldsymbol{R}_y$ and $R^2 = R_x^2 + R_y^2$:

$$R_x = P_x \cos \omega t + S_x \cos(\omega t + \phi) = X \cos(\omega t + \phi_1)$$

$$R_y = P_y \cos \omega t + S_y \cos(\omega t + \phi) = Y \cos(\omega t + \phi_2).$$

continued

continued

By solving the above equations and eliminating ωt, we obtain:

$$\frac{R_x^2}{X^2}+\frac{R_y^2}{Y^2}-\frac{2R_xR_y\cos\delta}{XY}=\sin^2\delta \qquad (3)$$

where

$$\delta=\phi_2-\phi_1.$$

Equation (3) is the equation of an ellipse with its major axis inclined at an angle θ to the horizontal, where θ is defined by:

$$\tan 2\theta=\frac{XY\cos\delta}{X^2-Y^2}.$$

10.2.3 Depth of penetration of EM radiation

Of prime importance in EM surveying are a consideration of the depth of penetrating of the EM radiation and the resolution as a function of depth. In an isotropic resistive medium, EM waves would travel virtually indefinitely. However, in the real world, where surface conductivities are significant, the depth of penetration is often very limited. The depth of penetration is largely a function of frequency and the conductivity of the media present through which the EM radiation is to travel. At the usual frequencies (<5 kHz) used in EM exploration (excluding ground penetrating radar) attenuation effects are virtually negligible, but signal losses occur by diffusion.

A common guide to the depth of penetration is known as the *skin depth*, which is defined (Sheriff 1991) as the depth at which the amplitude of a plane wave has decreased to $1/e$ or 37% relative to its initial amplitude A_0. The mathematical definition of skin depth is given in Box 10.3. Given a known frequency for a particular equipment system, the unknown is the vertical variation of conductivity with depth. Different instrument manufacturers commonly cite effective depths of penetration for their instruments. For example, Geonics Ltd give the depth of penetration of their FEM systems (EM38/EM31/EM34) as a function of the inter-coil separation (see next chapter for details).

Box 10.3 Skin depth

Amplitude of EM radiation as a function of depth (z) relative to its original amplitude A_0 is given by:

$$A_z=A_0e^{-1}.$$

The skin depth δ (in metres) is given by:

$$\delta=(2/\omega\sigma\mu)^{1/2}=503(f\sigma)^{1/2}$$

where $\omega=2\pi f$, and f is the frequency in Hz, σ is the conductivity in S/m, and μ is the magnetic permeability (usually ≈ 1). A realistic estimate of the depth to which a conductor would give rise to a detectable EM anomaly is $\approx \delta/5$.

10.3 AIRBORNE EM SURVEYING

10.3.1 Background

The earliest known airborne EM (AEM) system was developed by Hans Lundberg in 1946 and first used in eastern Canada. It consisted of two coils mounted inside the cabin of a helicopter which had to fly at only 5 m above the ground if any conductors were to be detected!

Figure 10.14 Input TEM system for airborne EM. (A) A primary magnetic field is generated that excites a receiver response (B). The measured response of the receiver is modified by an element (C) that is function of the ground properties. The decay curve (D) is sampled at designated time intervals (channels).

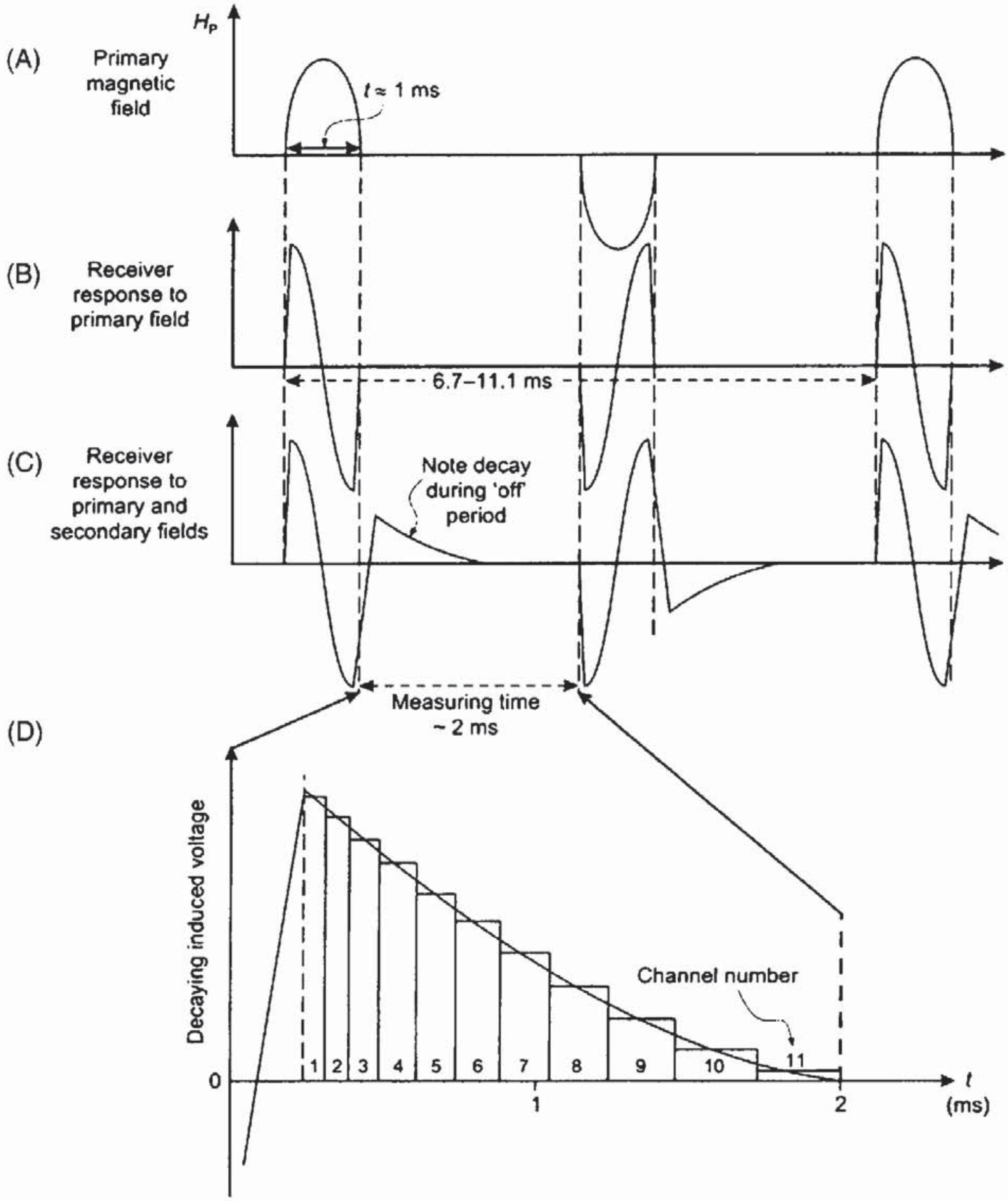

A detailed history of the development of airborne EM has been given by Pemberton (1962), Collett (1986), Becker *et al.* (1990), Palacky (1986) and Palacky and West (1991).

Following on from the early enthusiasm for AEM in the search for strategic base metals (such as copper, lead, zinc and nickel), many other airborne systems were developed. The most successful system was that developed in the late 1950s (Barringer 1962) and known as the INPUT system (INduced PUlse Transient), the principle of operation of which is shown in Figure 10.14. INPUT was developed further in the late 1970s to obtain greater depth penetration required in exploration for uranium and is now operated under the names QUESTEM (operated by Questor Surveys) and GEOTEM (Geoterrex Ltd). Further improvements to these systems were made in the mid-1980s with more powerful transmitters and modern computer technology. At this time an additional system known as PROSPECT became available along with its South African equivalent SPECTRUM; of the INPUT style AEM systems, only SPECTRUM, GEOTEM and QUESTEM are currently operational.

In the late 1970s, two clear styles of instrumentation deployment emerged, high-resolution helicopter surveying using towed instrument sondes and, particularly for deep penetration work, fixed-wing systems using rigid booms fitted to wingtips, mounted above the fuselage or on the nose and tail of the aircraft (Figure 10.15).

Applications of AEM surveying (excluding ground penetrating radar) to other than base metal exploration began in the 1960s with groundwater investigations, and later spread in the 1970s to include other forms of geological mapping, exploration for kimberlites in South Africa, and in the 1980s, mapping of Quaternary deposits in France, coal and lignite prospecting, detection of palaeochannels and salinity mapping in Australia, and shallow-water bathymetry and sea-ice thickness determinations in the USA. Further details of the range of applications of AEM can be found in the symposia edited by Palacky (1986) and Fitterman (1990), for example. Ground penetrating radar in the form of radio echosounding has been used from aircraft in polar regions to investigate major ice sheets since the late 1950s (see also Chapter 12). It is increasingly being used over glaciers at lower latitudes (e.g. Kennett *et al.* 1993).

10.3.2 AEM systems

The general principle of airborne EM surveying is shown in Figure 10.16. A powerful transmitter is mounted on the aircraft to generate the primary field in active systems, with a receiver either towed below in an instrument pod known as a 'bird' or on a separate part of the aircraft. The most commonly used systems are deployed from helicopters as they can be operated most easily at low flying heights and are much more manoeuvrable than fixed-wing aircraft.

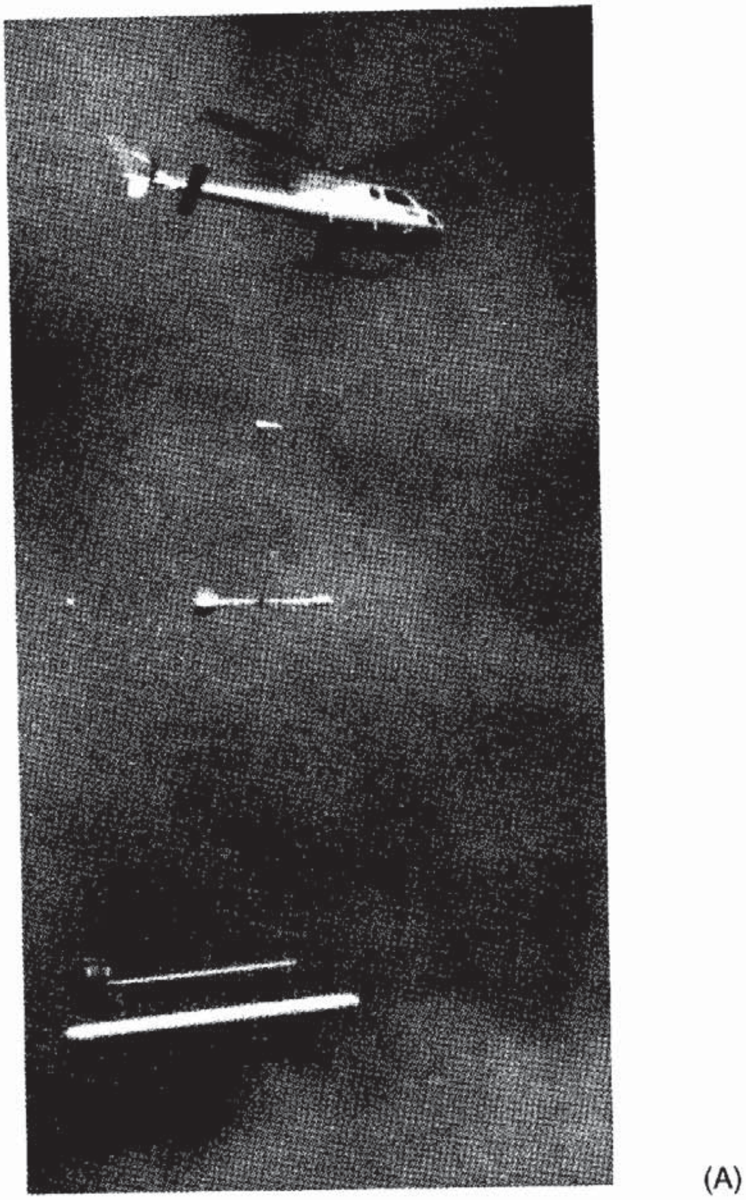

Figure 10.15 (A) Eurocopter AS350B towing three instrument pods. They are (from the top) 2-channel VLF-EM, total-field caesium magnetometer, and a 5-frequency electromagnetic induction system. (B) Cessna 404 fixed-wing aircraft with a total-field magnetometer mounted in a tail stringer. Photographs courtesy of Aerodat Inc., Canada

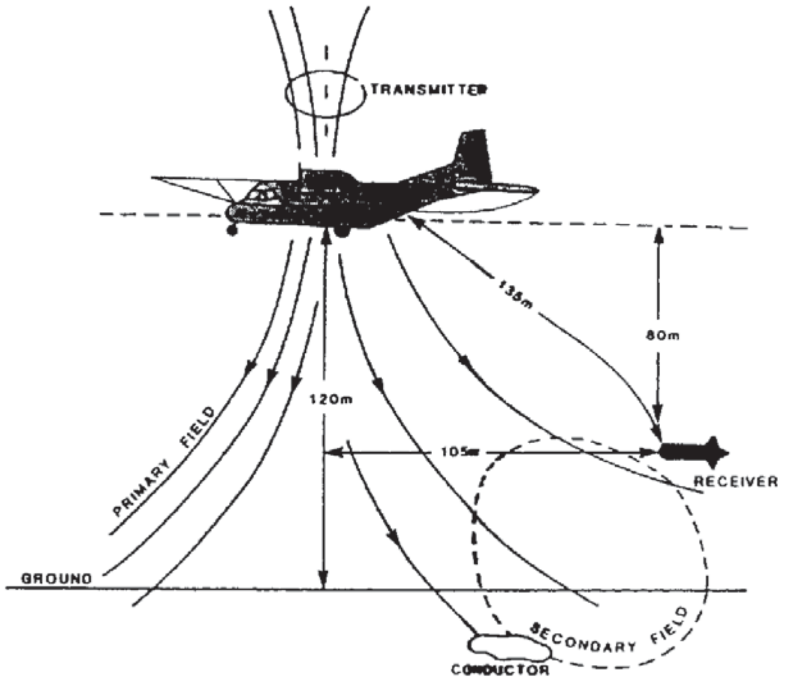

Figure 10.16 Principle of airborne electromagnetic surveying. The system shown deployed is of the towed-bird type. Reproduced with permission from Palacky and West (1991)

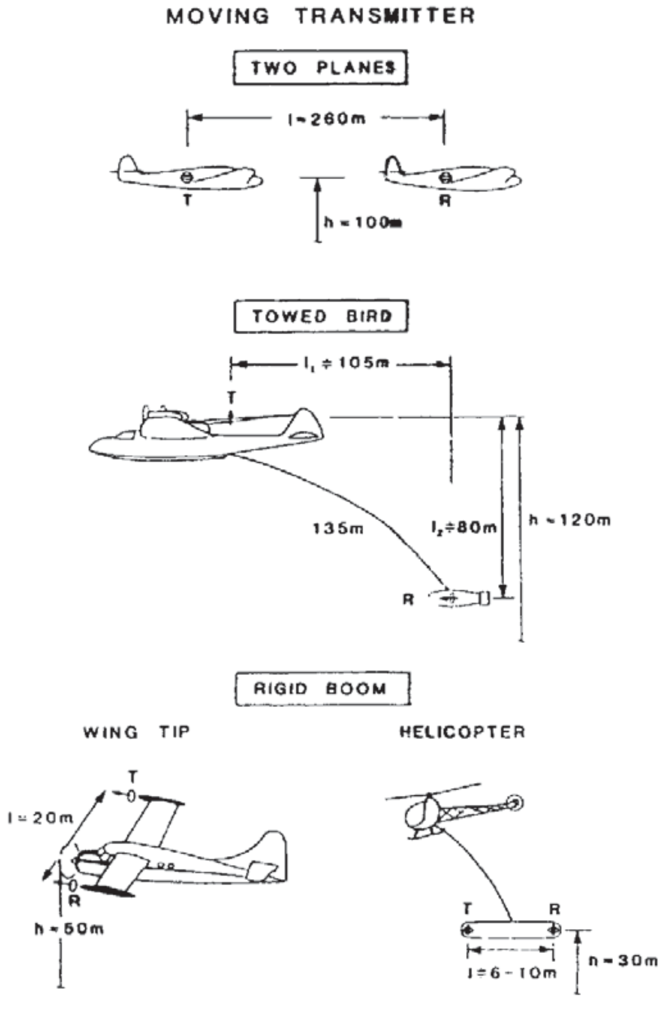

Figure 10.17 Transmitter–receiver geometry of five basic styles of active airborne EM systems. Reproduced with permission from Palacky and West (1991)

The various configurations of deployment of AEM systems are shown in Figure 10.17. There are two main types of transmitter–receiver geometries, towed bird and rigid boom systems. In some helicopter arrangements, the transmitter and receiver are both mounted in an instrument pod which is suspended below the aircraft. Further details of AEM systems have been given by Palacky and West (1991).

10.4 SEABORNE EM SURVEYING

10.4.1 Background

The principal difference between airborne and seaborne EM applications is largely one of scale. Whereas airborne surveys may involve flying heights of typically several tens to hundreds of metres, with transmitter–receiver distances of the order of 20–135 m, seaborne systems may have separations of tens of kilometres. Marine deployment of EM systems is usually for large-scale, crustal investigations and requires specialised instrument packages (Chave *et al.* 1991). There are a few examples of where land-based EM systems, such as a Geonics EM34, have been deployed in rubber inflatable boats and towed over shallow freshwater lakes and rivers in engineering investigations.

The main methods that have been adapted for use in the marine environment are magneto-telluric, magnetometric resistivity, and frequency- and time-domain systems. They have been reviewed in detail by Filloux (1987) and Chave *et al.* (1991).

The critical factor in all marine EM sounding is that the seawater is extremely conductive, and much more conductive than the geological materials at or below the seafloor. Seawater conductivity is strongly dependent upon salinity and temperature. The uppermost sediments under the ocean are usually water-saturated and have conductivities of the order of 0.1–1 S/m. This value decreases with increasing lithification and diagenesis which reduce the *in situ* porosity. Basaltic crust and upper mantle peridotite have conductivities ranging from 0.1 S/m at the base of the overlying sediments to three orders of magnitude less at a depth of about 10 km.

10.4.2 Details of marine EM systems

10.4.2.1 Magneto-telluric (MT) methods

All oceanic MT work has been specifically to probe the deep lithosphere and asthenosphere to obtain a vertical EM structural model to depths of hundreds of kilometres. The MT method is currently the only geophysical method capable of obtaining information about the electrical properties at depths greater than 30 km.

The only commercially available instruments for the measurements of a magnetic field are fluxgate magnetic sensors, with sensitivities of the order of 0.5–1 nT. These sensors are deployed directly on the seabed.

There are two types of device for the measurement of the electric component: (a) long-wire units, and (b) short-arm salt bridges. The long-wire system comprises an insulated wire typically 500 m to 1000 m long with Ag–AgCl electrodes connected to the ends of the wire and to a recording unit (Webb *et al.* 1985). The short-arm bridge apparatus utilises electrodes with spacings of only a few metres and salt bridges. Each salt bridge consists of a hollow tube attached to an Ag–AgCl electrode at one end and open to the sea at the other. The entire electrical unit has four arms (salt bridges and electrodes) which are spread out in the form of a horizontal cross which sits on top of a vertical cylinder housing the recording instruments. The base of this cylinder is located on a detachable tripod which, when lowered to the seafloor, is placed in contact with the seabed. Once measurements have been completed, the instrument module with salt bridges is released from the tripod and rises to the sea surface under slight positive buoyancy for subsequent recovery.

10.4.2.2 Magnetometric resistivity (MMR)

The marine version of MMR developed by Edwards *et al.* (1985), known as MOSES (Magnetometric Off-Shore Electrical Sounding), has been used for deep crustal sounding, mapping sulphide deposits near mid-ocean ridges (Wolfgram *et al.* 1986) and in the study of submarine permafrost below the Beaufort Sea. The general scheme of the MOSES method is shown in Figure 10.18.

The transmitter comprises a vertical long-wire bipole which extends from the sea surface to the seabed. A commutated current is fed

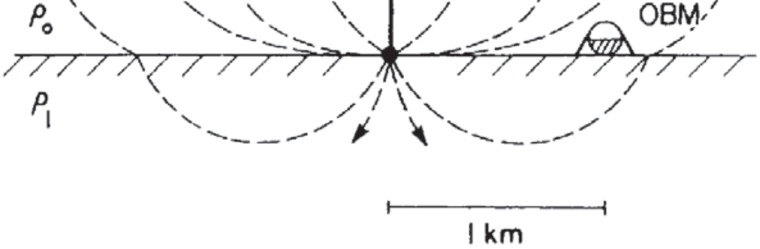

Figure 10.18 Schematic to illustrate the principle of the MOSES method. Current is passed via two electrodes, one at the sea surface and the other on the seafloor. The relatively small amount of current that enters into the resistive crust is proportional to the ratio of the conductivity of the crust to that of seawater. Only this small current contributes to the aximuthal magnetic field measured at a point on the seabed. OBM = ocean bottom monitor. Reproduced with permission from Chave *et al.* (1991).

to two large electrodes at each end of the vertical wire. The return electrical current passes through the seawater and the near-surface materials of the seafloor. A remote receiver located on the seafloor consists of two orthogonal horizontal component fluxgate magnetometers. Two orthogonal components of the magnetic field are measured as a function of frequency and source–receiver distance. The remote receiver consists of a concrete anchor shaped like an inverted cone into which a spherical instrument housing is located. The magnetometers are located within the detachable pressure case which can be released remotely from the concrete anchor for subsequent recovery.

A variation of the above system, called ICE-MOSES, was developed by Edwards *et al.* (1988) for use through sea ice. The sensor design is quite different from the original MOSES version. The sensor is deployed folded (and subsequently recovered) through a 25 cm diameter hole cut in the sea ice. Once through the hole, the unit unfolds to form a horizontal square which is lowered to the seabed. Along two sides at right-angles to each other are located the sensors which consist of coils wound on soft iron laminated cores and housed in stainless steel jackets.

ICE-MOSES is particularly important as it can be used to help define the physical properties of seafloor sediments to a depth of several hundreds of metres. Of particular interest in the Beaufort Sea, where ICE-MOSES was first used, is a seismically important permafrost layer between 100 and 600 m thick under seawater 10–100 m deep. This permafrost horizon is of importance for two reasons. First, a detailed knowledge of this layer is essential if reflection surveys undertaken in the same areas are to be interpreted accurately. Secondly, pockets of gas hydrate can be contained within the permafrost and these can be a possible resource as well as a hazard to drilling to deeper targets.

10.4.2.3 Controlled-source EM methods

Controlled-source EM systems use time-varying electric and magnetic dipole sources of known geometry to induce electric currents in the various conducting media present. The electric or magnetic character of the induced currents can be determined, from which estimates of the vertical electric conductivity structure of the geological materials present can be made. There are four basic source–receiver types but many combinations. The four are: *vertical and horizontal electric dipoles* (VED and HED) and *vertical and horizontal magnetic dipoles* (VMD and HMD).

In contrast to the land-based equivalent, marine controlled-source EM systems have both the source and receiver immersed in a conducting medium, and the electrical structure in both the seawater and the sub-seafloor materials affect the total induction achieved and thus

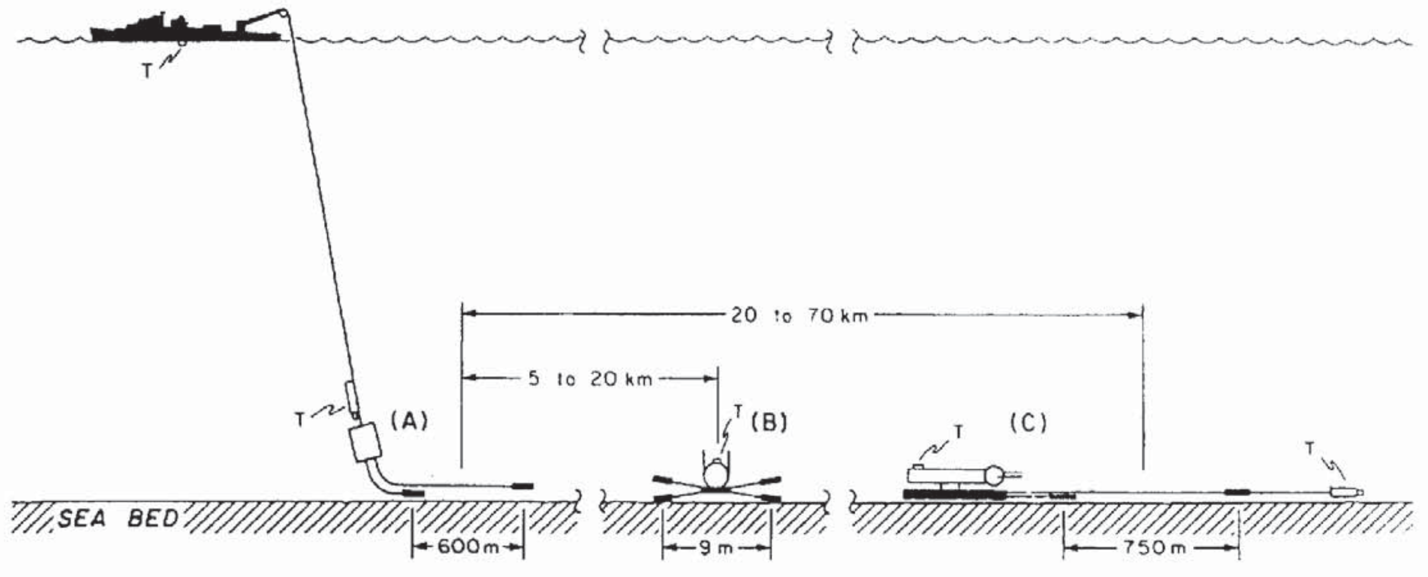

Figure 10.19 Typical layout for a horizontal electric dipole (HED) deep-sounding experiment. Power is supplied from a surface source (e.g. ship) to the seafloor transmitter (A) through a single conductor with a seawater return. The transmitter comprises an insulated antenna (with bare ends) of about 600 m length. Receivers are placed at ranges from 5 to over 70 km from the transmitter. Receivers may by either (B) an electric-field recorder (ELF) with a pair of rigid, orthogonal antennae of 9 m span, or (C) a long-antenna EM recorder (LEM), where the potential is measured between the ends of a 200–300 m insulated copper wire. Acoustics transponders (T) are used to locate all the seafloor components from a surface vessel. Reproduced with permission from Chave *et al.* (1991)

have to be taken into account in the interpretative modelling. In cases involving shallow water, for example over continental shelves, the position of the air/sea surface interface also has to be taken into consideration.

Three systems, two frequency-domain and one time-domain, will be described briefly to illustrate the diversity of systems currently being developed. The first is a submarine horizontal electric dipole (HED) frequency-domain system produced by Scripps Institution of Oceanography for deep sounding of the oceanic lithosphere. The source is a long (0.5–1 km) insulated cable terminating in stainless steel electrodes 15 m long. Receivers to detect the horizontal electric field are placed on the seabed between 1 and 200 km from the source. There are two types of electric receivers (Figure 10.19):

- The ELectric Field (ELF) free-fall recorder consists of a pair of rigid orthogonal antennae, each 9 m long, to the ends of which Ag–AgCl electrodes are fixed. ELF receivers are deployed between 5 km and 20 km from the transmitter.
- The Long antenna EM recorder (LEM) consists of 200–3000 m long insulated copper wire terminated by 0.5 m long Ag–AgCl electrodes. LEM recorders are placed up to 100 km or more away from the source.

The second basic system is also frequency-domain and is produced by Scripps for use over shallow continental shelves (Figure 10.20). The transmitter is made up of two 7 m long copper tubes 7 cm in diameter connected by 50 m of cable and powered directly by the survey vessel. The receiver array comprises a string of Ag–AgCl electrodes along a cable several hundred metres in length, all of which is in contact with the seabed. At the front end of the receiver array is a recording

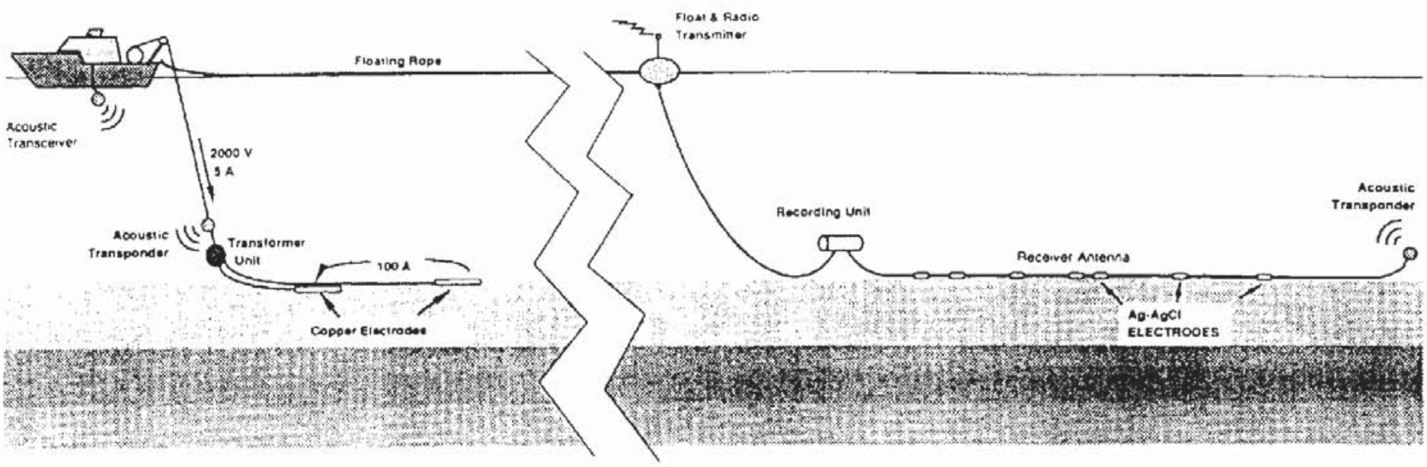

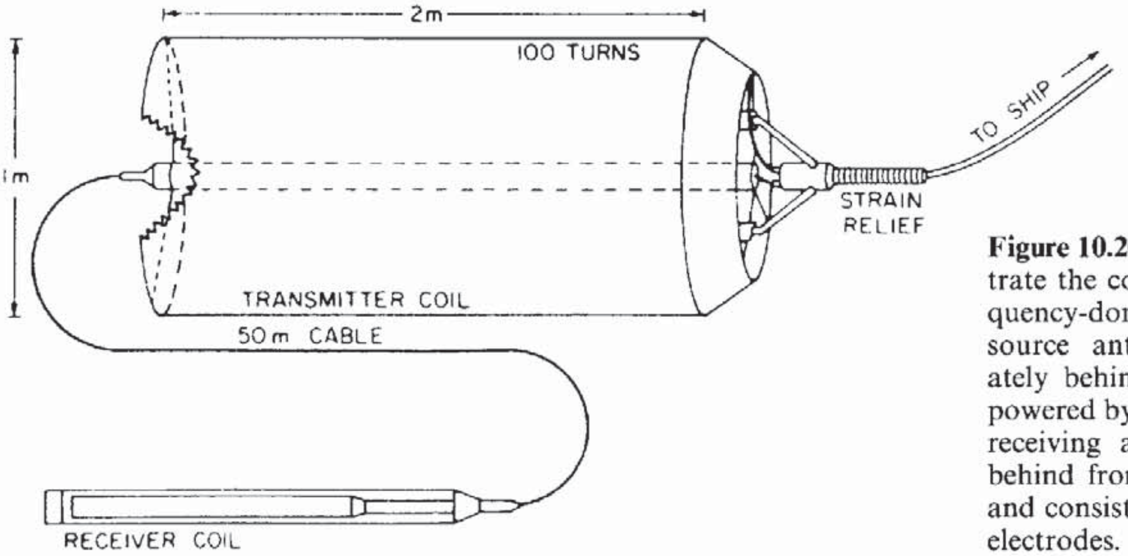

Figure 10.20 (*top*) Schematic to illustrate the components of a towed frequency-domain profiling system. The source antenna is towed immediately behind a research ship and is powered by the ship's generators. The receiving antenna is towed further behind from a radio-equipped buoy and consists of an array of Ag–AgCl electrodes. Acoustic transponders are used for location purposes. Reproduced with permission from Chave *et al.* (1991)

Figure 10.21 (*left*) Schematic of a horizontal magnetic dipole (HMD) transmitter that is connected to a surface vessel by an electric cable. The receiver is made up of a coil wound on an iron core and is encased in a protective plastic sleeve, all of which is streamed 50 m behind the transmitter. Reproduced with permission from Chave *et al.* (1991)

unit which is connected to a float and radio transmitter. The float is connected to the survey vessel by a floating rope, the length of which can be changed to alter the source–receiver separation. The point of having a surface radio transmitter is to allow the real-time relay of measured data from the submerged recorder unit, which also stores the data on to tape, directly to the survey vessel.

The third, time-domain, horizontal magnetic dipole (HMD) system (Figure 10.21) has been constructed by the University of Toronto, Canada. The transmitter comprises a 2 m long, 1 m diameter fibreglass cylinder in which 100 turns of wire are evenly embedded. Current is supplied to the transmitter from two car batteries located on the survey vessel. The polarity of the current is reversed every 5 ms to provide the transient EM signal. The receiver, which is made up of a modified iron core coil encased in a polycarbonate tube, is towed 50 m behind the transmitter. The entire source–receiver array is placed on to the seabed and is stationary during each measurement, which takes 90 s. The survey vessel is able to maintain headway by paying out additional cable during measurement periods and reeling in the extra cable between survey points. An advantage of this system is that the field source–receiver array is relatively small with a consequential improvement in the ease of deployment over some of the larger, and more unwieldy, frequency-domain systems. For any of these systems to become operational commercially, ease of operation is a major factor to be considered.

10.5 BOREHOLE EM SURVEYING

Whereas surface and airborne EM systems have regular geometries of sources and receivers, the addition of the third dimension via a borehole leads to an increased number of possibilities with associated complexities in interpretation. Borehole EM surveying differs from inductive well logging, which is used predominantly within the hydrocarbon industry, by virtue of the ability of being able to detect a conductive body at a significant distance away from the borehole. An induction logging device senses only those features through which the borehole has actually passed or within the near-field around the borehole (Figure 10.22).

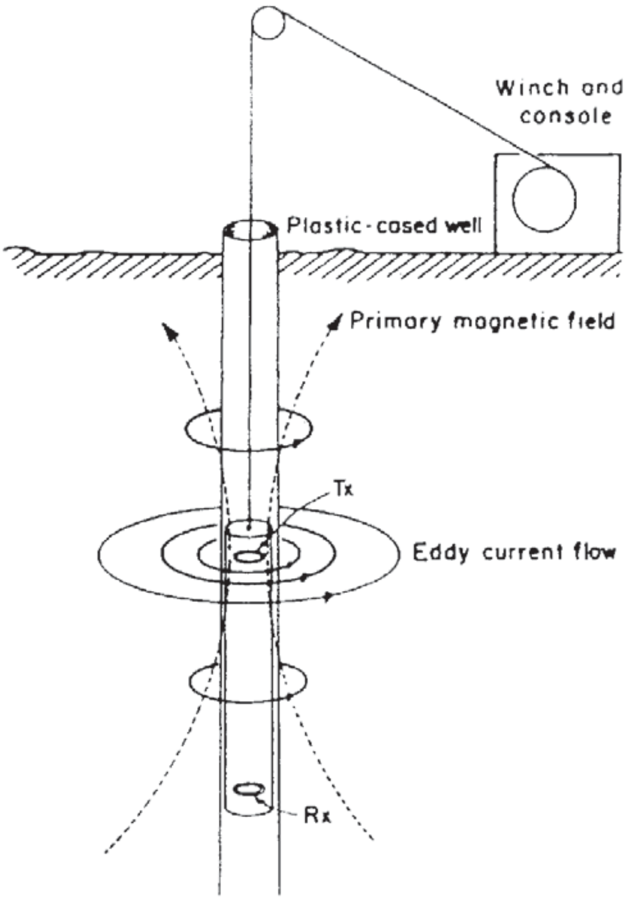

Figure 10.22 The basic principle behind an electromagnetic induction logger for use in boreholes. Reproduced with permission from McNeill (1990)

The principle of operation is the same as for ground conductivity meters. The system is able to measure the conductivity of the materials outside of a plastic cased borehole or well with diameters in the range 5–20 cm. The measurements are insensitive to the usually much more conductive borehole fluid within the casing (McNeill *et al.* 1988). Eddy currents are induced concentrically around the borehole using an intercoil separation of 0.5 m. This configuration provides a reasonable vertical resolution while at the same time maintains an adequate radial range of investigation (McNeill 1990). Drill-hole EM methods have been reviewed by Dyck (1991), and more details can be found therein.

There are three types of system in borehole surveying: dipole–dipole EM, rotatable-transmitter EM, and large-loop EM (LLEM) methods, of which the last is the most commonly used in mineral prospecting. The basic transmitter–receiver geometries are shown in Figure 10.23.

The dipole-dipole system has two coaxial coils separated by fibreglass rods with the transmitter preceding the receiver down the drill hole. Measurement points are taken as being the midpoint between transmitter and receiver. In-phase and quadrature components of the secondary magnetic field are measured as a percentage of the primary field. As the downhole system is deployed on a series of rods, the method can be used in near-horizontal and upwardly inclined holes,

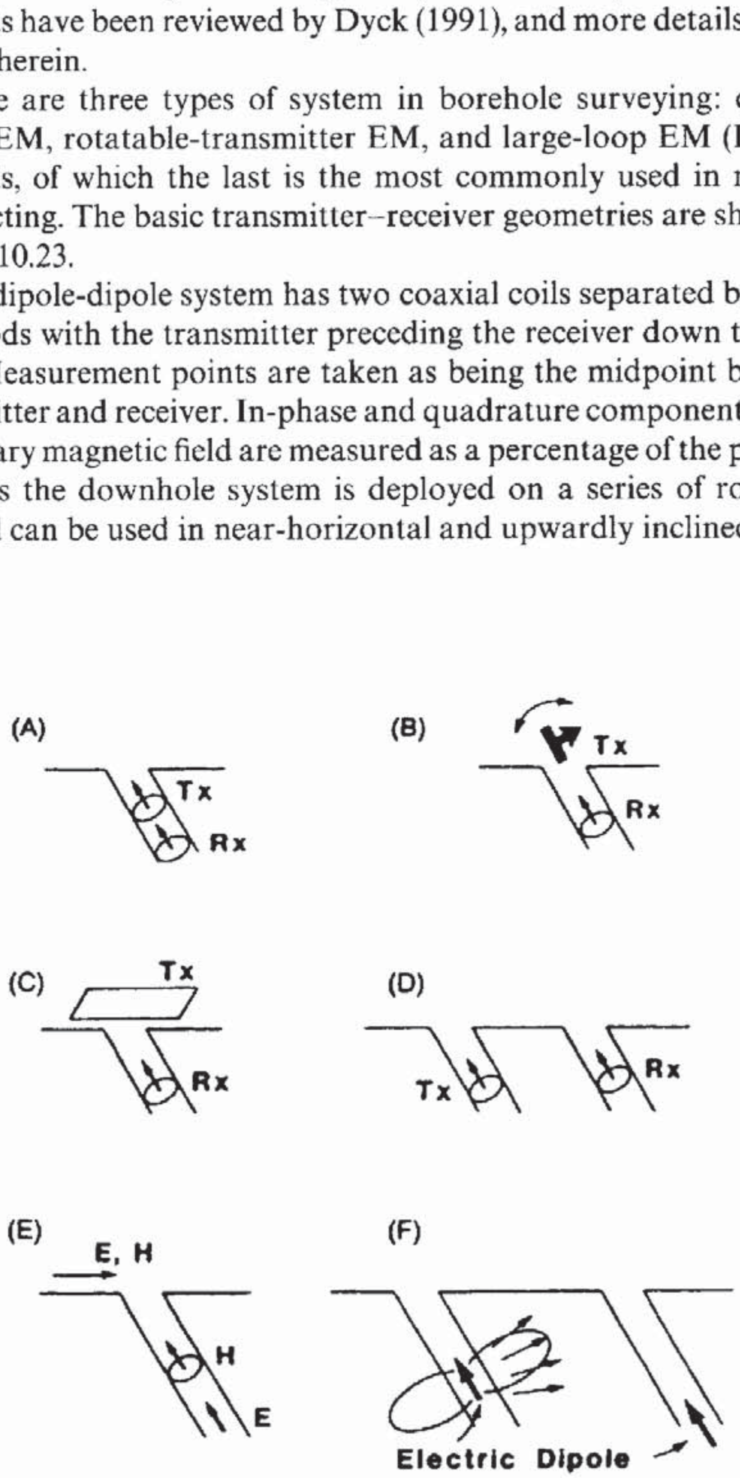

Figure 10.23 Drill-hole EM systems. (A) Dipole–Dipole EM. (B) Rotatable transmitter EM (with transmitter Tx shown side-on). (C) Large-loop EM. (D) Hole–hole dipole EM (variation of (A)). (E) remote transmitter (e.g. VLF radio source) for downhole measurement of electric and/or magnetic field. (F) Hole–hole wave propagation. Reproduced with permission from Dyck (1991)

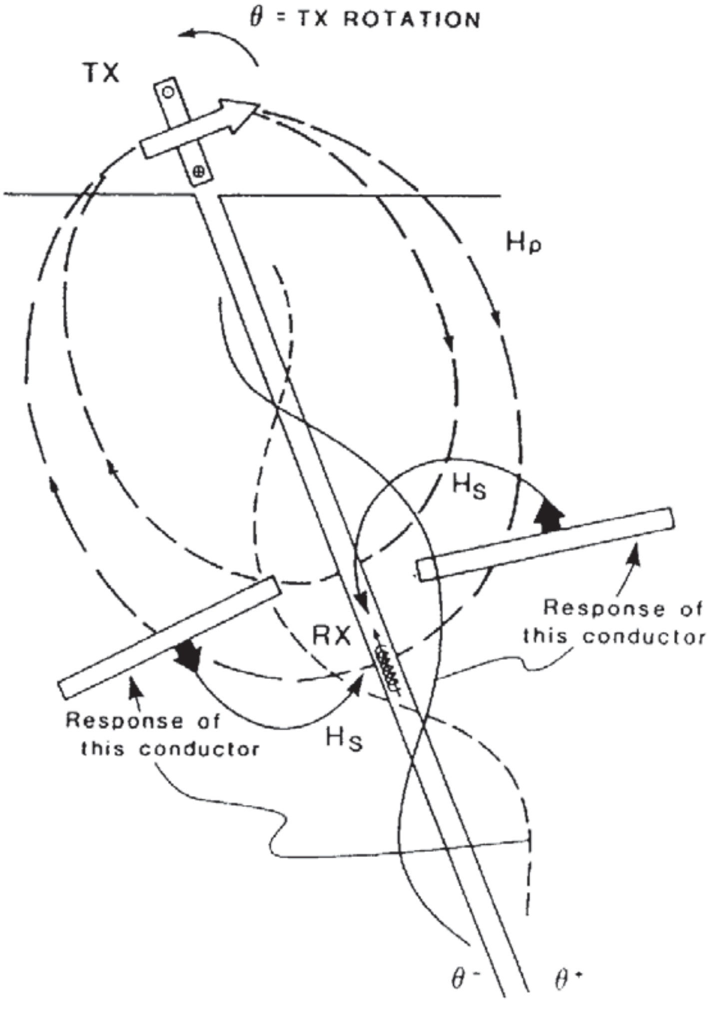

Figure 10.24 Magnetic fields produced by a rotatable transmitter and target conductor. The transmitter coil is rotated about an axis perpendicular to the plane of the diagram. The conductor to the right of the drill hole produces a negative (i.e. downward) component of secondary field H_s at the receiver position shown. A counter-clockwise ($+\theta$) rotation of the transmitter is required to achieve a null by offsetting H_s with a component of H_p, assuming negligible change in transmitter–conductor coupling as the transmitter is tilted. Reproduced with permission from Dyck (1991)

and is then limited only by the ability to move the probes within the hole.

The rotatable-transmitter system is a version of the dipole–dipole method, but the transmitter remains at the drill hole collar throughout the survey while the receiver is moved up and down the hole (Figure 10.24). The receiver probe is moved down the hole in discrete intervals of several metres at a time. At each measurement point, the surface transmitter coil is rotated until a null point in the sensor is reached and the corresponding angle of tilt is recorded. The method is analogous to the surface tilt-angle technique.

The general layout for borehole LLEM surveying is shown in Figure 10.25. A loop transmitter is deployed at the ground surface adjacent to the borehole down which a detector is run to obtain a profile. Typical ground loop dimensions range from 100 m to 1000 m and are comparable to the depth of the drill hole being investigated. One ground loop, in conjunction with profiles down a number of drill holes from the surface and from within a mine gallery, are sufficient to resolve a sub-surface conducting target

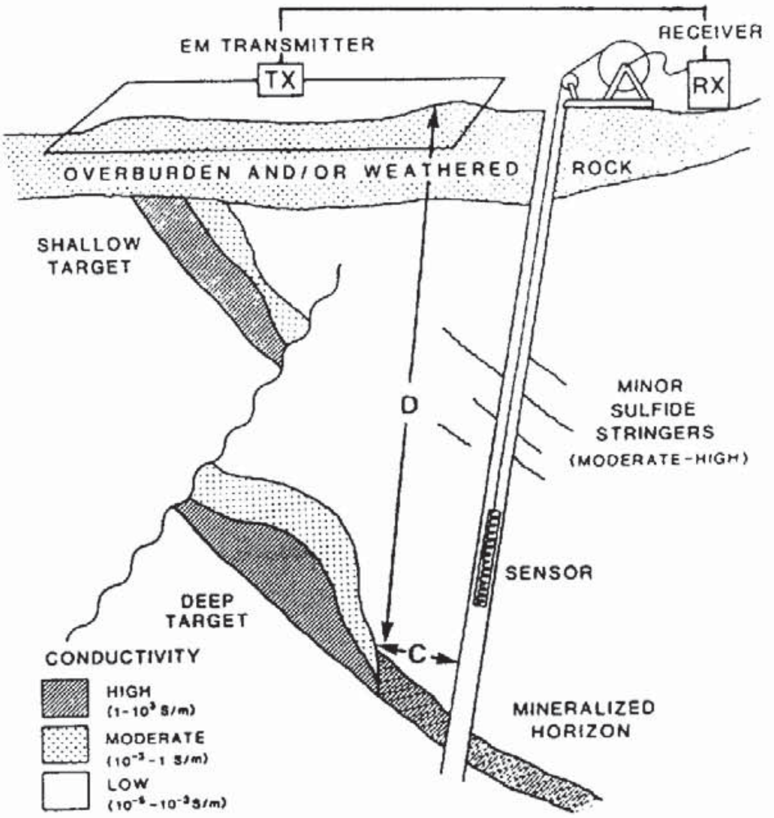

Figure 10.25 Schematic to illustrate the use of the large-loop drill-hole EM method for massive sulphide exploration in highly resistive environments such as Precambrian rocks. The system comprises a transmitter (Tx), a re-Clearance (*C*) is the critical distance in a drill-hole exploration problem involving a highly conductive target buried at depth *D*. There may be other bodies that are also conductive. Reproduced with permission from Dyck (1991)

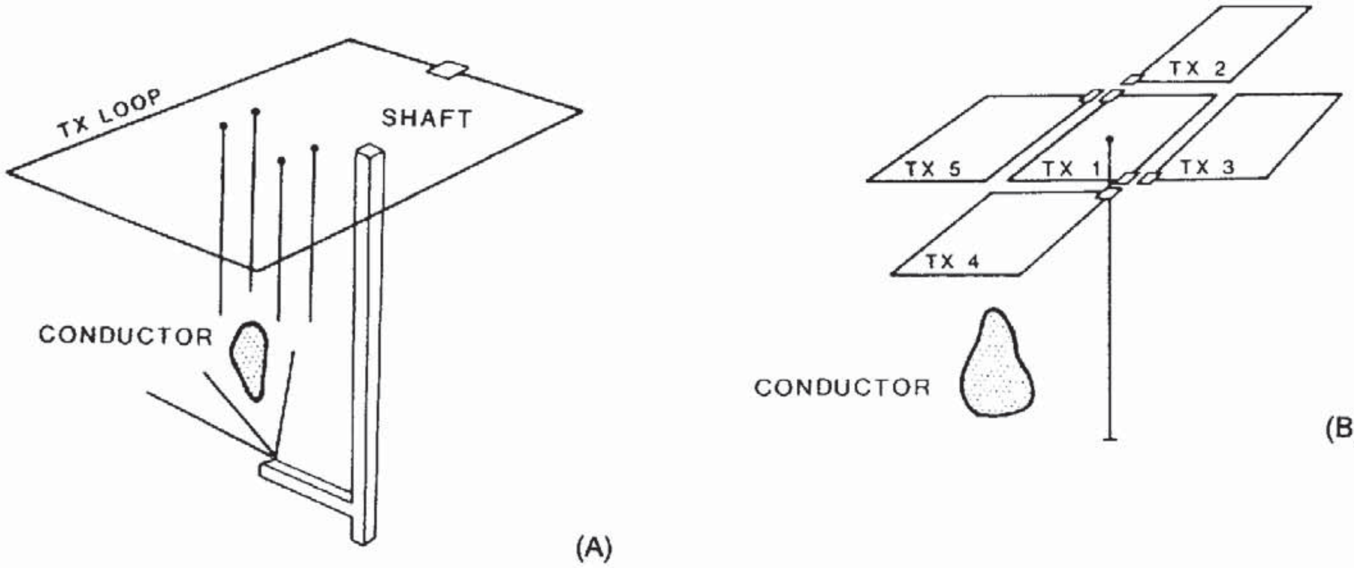

Figure 10.26 Transmitter layouts for surveying (A) a group of drill holes collared underground; and (B) a single isolated drill hole. Tx 1–5 are successive locations of the transmitter loop. Reproduced with permission from Crone (1986).

(Figure 10.26A). In contrast, if only one drill hole is available, one loop on its own does not provide azimuthal information necessary to locate the target. Consequently, a number of loop positions located around a collared borehole (Figure 10.26B) can be used to provide the additional information required.

There are three types of LLEM system depending upon the received primary waveform of system function, namely impulse-type, step-function type (both of which are TEM systems), and multi-frequency (FEM) type. Further details of these systems are given by Dyck (1991). Other systems that are available include down-hole VLF, and inter-hole wave propagation (e.g. Newman 1994) which can include borehole tomographic techniques (see also 'borehole radar tomography' in Chapter 12). Three component (magnetic field) systems are currently under development, although one prototype has been successfully deployed by Boliden Mineral AB, in Sweden (Pantze *et al.* 1986). A 1 × 1 km ground loop was used in an FEM system which operated at two frequencies, 200 Hz and 2000 Hz. Three sensors were mounted in a 32 mm diameter probe with the y-axis always being horizontal, x parallel to the long axis of the probe, and z always at right-angles to x and y. In-phase residuals (computed after the removal of the primary field and the background response caused by the host rock) were plotted as a function of profile distance along the drill hole. The shape and size of the excursion of each component away from a normal value provided information about the location (depth and azimuth) of a sub-surface conductive target.

Chapter 11
Electromagnetic methods: systems and applications

11.1 INTRODUCTION

A basic introduction to the various types of electromagnetic systems and their respective operating principles has been given in Chapter 10. Here, five of the most commonly used types of method are discussed in more detail with case histories to illustrate their various applications. The five types of system can be classified into three groups:

- *near-field systems*, where the source is relatively close to the receiver;
- *far-field systems*, where the source is located at a very large distance from the receiver such that the EM wave can be treated as a plane wave (VLF surveying);
- *natural-source EM systems*, where no active generation of artificial electromagnetic radiation is necessary because naturally occurring ground currents provide the source.

The range of individual instruments is large, especially if airborne, seaborne and drillhole systems are included along with those deployed solely from the ground surface. It is not possible, therefore, to provide as in-depth account of every system that is available. The selection presented here is of those techniques most likely to be used in engineering, environmental and archaeological applications, although in some cases some techniques are used almost exclusively in mineral exploration. More detailed descriptions of specific instrument types have been given, for example, by Nabighian (1987, 1991) and coauthors; technical specifications of individual systems can be obtained from instrument manufacturers.

11.2 CONTINUOUS-WAVE (CW) SYSTEMS

11.2.1 Tilt-angle methods

Tilt-angle methods have been used extensively in both ground and airborne surveys, particularly for mineral exploration. The method obtains its name from the measurement of the angle (tilt) of the resultant of the applied primary field and the induced secondary fields arising from a buried conductive body (Figure 11.1), such as a buried massive sulphide orebody.

Given a horizontal primary field direction, induced eddy currents within a buried conductor generate a secondary magnetic field whose lines of force are concentric around the source of the currents, commonly taken as being the uppermost edge of the body. The secondary field is inclined upwards on the side nearest the transmitter and hence the resultant is also inclined upwards (positive tilt angle). Immediately above the conductive body, both primary and

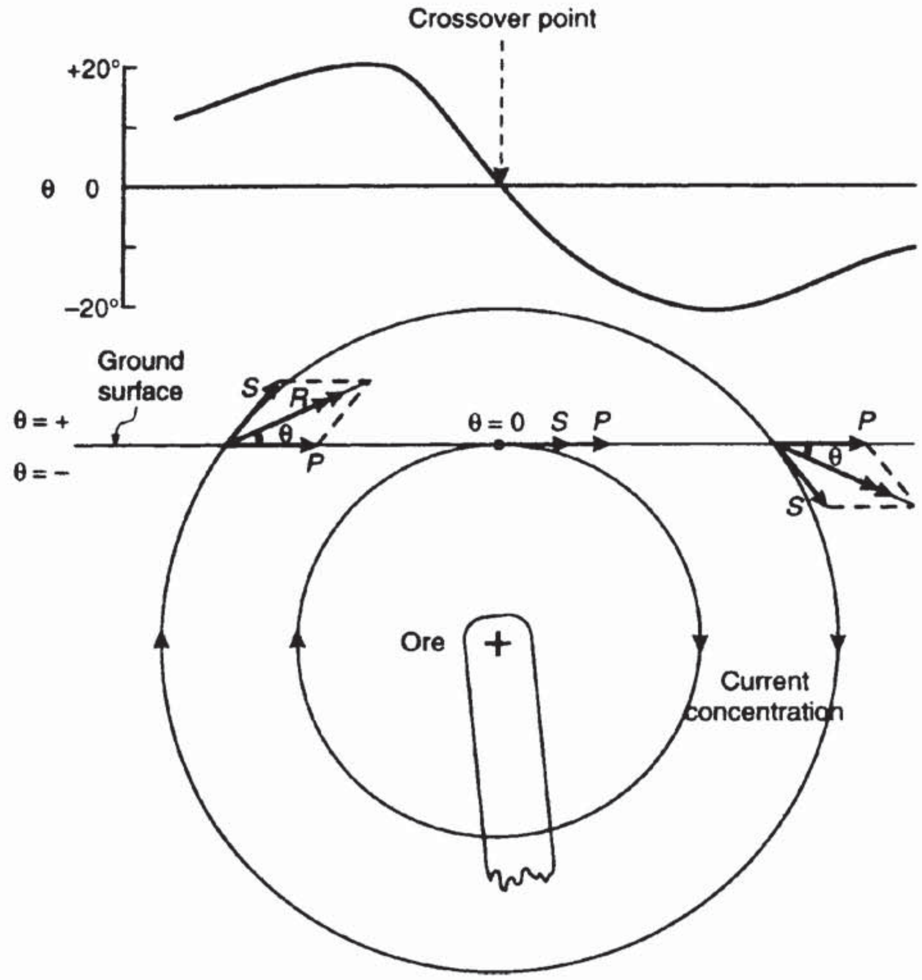

Figure 11.1 Tilt-angle (θ) profile over a conductive orebody arising from a plane EM wave from a remote vertical transmitter. ***P*** indicates the direction of the primary field vector, and ***S*** and ***R*** are the secondary and resultant field vectors, respectively. After Parasnis (1973), by permission

secondary fields are horizontal and in the same direction, hence the tilt-angle is zero. On the side furthest from the transmitter, the secondary field is inclined downwards and thus so too is the resultant (negative tilt angle). From a tilt-angle survey with a vertical coil axis (horizontal primary field), the conductive orebody is located at the point where the tilt angle passes from being positive to negative (the *crossover point*). When the primary field is orientated vertically downwards, the tilt angle passes through a minimum immediately over the conductive body (Figure 11.1).

When a conductive body is close to the ground surface, the steepness of tilt and the horizontal rate of change of tilt angle are greater than would be produced over a deep-seated conductive body. Furthermore, if the conductive body is vertical and the profile surveyed is at right-angles to the sub-surface target, the tilt-angle profile should be symmetrical about the crossover point. If the profile is asymmetrical, then the amount of asymmetry is indicative of the degree of dip of the sub-surface target. As the dip of the conductive target decreases (becomes less vertical relative to the ground), so the amount of asymmetry increases. Principal tilt-angle methods currently in use are the VLF and AFMAG techniques which are described in more detail in Sections 11.4 and 11.6 respectively.

11.2.2 Fixed-source systems (Sundberg, Turam)

Where a fixed source such as a large loop of wire or a long grounded cable is used, as in the Sundberg method, the primary magnetic field is inclined towards the ground (Figure 11.2). In the presence of a vertical, thin, and laterally continuous conductor, eddy currents induced at the top edge of the sub-surface body generate a secondary magnetic field which interferes with the primary field. The resultant or secondary vertical component of the magnetic field is measured by the receiver. In addition, the gradient of the secondary magnetic field can be measured and displayed as a profile.

In the case of a vertical thin conductor, the secondary magnetic field is inversely symmetrical about the crossover point immediately above the top of the sub-surface target (Figure 11.2). At the same location, the gradient of the secondary field reaches a minimum value. If the conductive sheet is not vertical, the anomalies produced increase their degree of asymmetry with decreasing dip angle.

Care has to be exercised when using the Sundberg method because, as with many other EM techniques, topography affects the quality of data acquired. If the ground surface over which a survey is being undertaken is rough, such that the receiver as at an elevation significantly different from that of the source, appropriate topographic

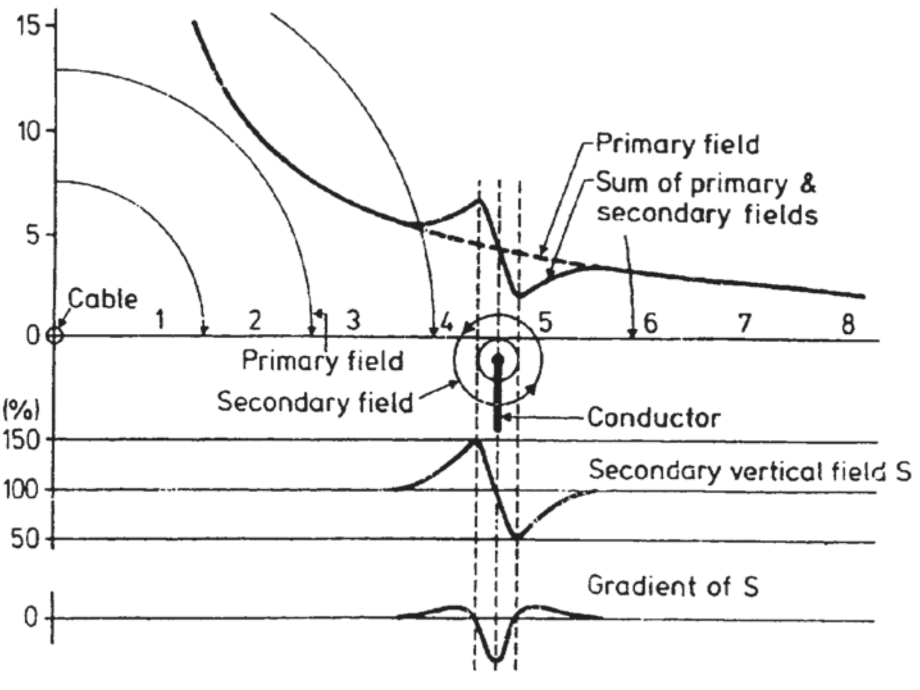

Figure 11.2 In the Sundberg method, the source is a long wire which generates the primary field that produces a secondary field over a sub-surface conductor. The anomaly due to the sub-surface conductor is superimposed on the primary field but can be residualised by the removal of the primary field. The horizontal gradient of the residualised secondary field yields a minimum at a point directly over the top of the conductor. From Parasnis (1986), by permission

corrections have to be applied to the real component data of the vertical primary field in order to compensate.

In the case of the Turam method, two receiver coils (usually placed horizontally) are separated by a fixed distance (c) and are moved along profiles at right-angles to the source wire. Given a number of stations (1, 2, 3, 4,...) at which each coil is located in turn, the amplitude (V) and phase (α) of the vertical electromagnetic field are measured at each location. The ratio of the amplitudes at each successive pair of stations (e.g. V_1/V_2, V_2/V_3, V_3/V_4,...) and the horizontal gradient of the phases ($(\alpha_2-\alpha_1)/c$, $(\alpha_3-\alpha_2)/c$, $(\alpha_4-\alpha_3)/c$,...) are plotted at the location of the midpoint between the coils along the profile. In addition, as the primary field ($\boldsymbol{P}$) decreases in amplitude away from the source, the measured amplitude ratios are divided by the normalised amplitude ratios (P_1/P_2, P_3/P_2, P_4/P_3,...) to give V_1P_2/V_2P_1, V_2P_3/V_3P_2, V_3P_2/V_4P_3,..., which are known as *reduced ratios* (RR). If either or both receiver coils are located at an elevation different from that of the source cable, then a topographic correction has to be applied to the reduced ratios.

It is usual to plot a Turam profile in terms of the reduced ratios and horizontal gradient of phase (e.g. Figure 11.3). As in the case of the Sundberg anomalies, symmetrical anomalies of both measured parameters should be obtained over a vertical conductor. If dip decreases from the vertical, the degree of asymmetry increases; higher values of the reduced ratio and smaller values of horizontal gradient of phase are measured over the downdip side of the conductive target.

Figure 11.3 Reduced-ratio and phase-difference gradient profiles over an inclined conductor obtained using a Turam survey

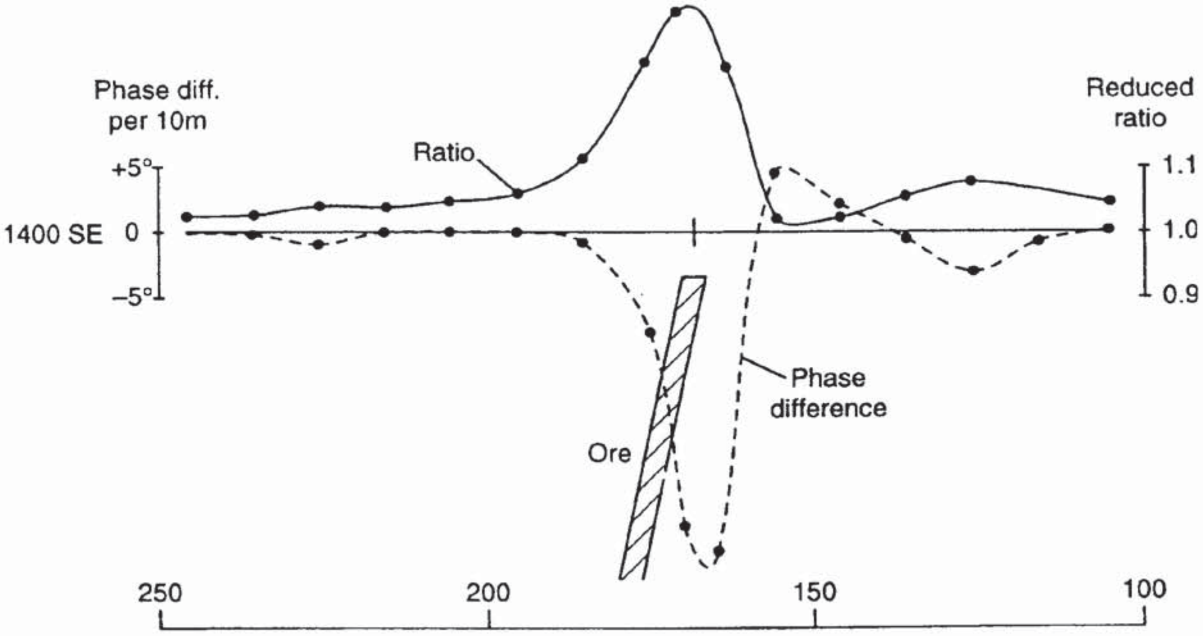

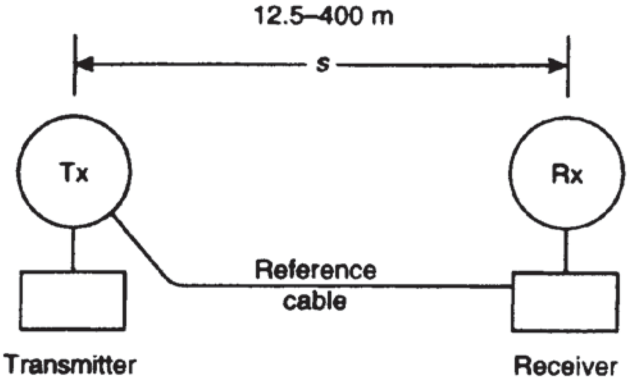

Figure 11.4 Moving dual-coil EM system; circles indicate the transmitter (Tx) and receiver (Rx) coils

11.2.3 Moving-source systems

The most commonly-used EM surveying method in environmental and engineering geophysics is the *moving-source dual-coil method* (McNeill 1990). Two separate coils connected by a reference cable provide the basis of the system (Figure 11.4); one coil serves as a transmitter to generate the primary field and the other acts as a receiver. The inter-coil separation is maintained at a fixed distance and the dual-coil pair is moved along the survey transect in discrete intervals. The point of reference for the measurement is usually the mid-coil position. Typically, dual-coil systems measure the quadrature component only or both the quadrature and in-phase components.

In the case of *ground conductivity meters* (GCM), as manufactured by Geonics Ltd, for example, the instrument provides a direct reading of the quadrature component as the apparent conductivity (σ_a) of the ground in units of millimhos per metre (SI equivalent units are millisiemens per metre (mS/m)). The in-phase component is measured in parts per thousand.

The ratio of the inter-coil spacing (s) divided by the skin depth (δ) is known as the *induction number* (B) (see Box 11.1). Where the induction number is much less than one, then the ratio of the secondary to the primary magnetic fields at the receiver is directly proportional to apparent conductivity (σ_a). If the ground is entirely homogeneous and isotropic, the instrument should give a measure of the true conductivity of the ground. However, real geological materials comprise a mixture of constituents, most notably a solid matrix with pore spaces that may be partially or fully saturated with pore fluids which, in some cases, can be highly conductive. Furthermore, the ground usually is made up of layers (soil over weathered material over bedrock, for example). Each material has its own diagnostic true conductivity and will contribute to the measured apparent conductivity value.

Box 11.1 Apparent conductivity at low induction numbers
(McNeill 1980)

The skin depth (δ) is given by:

$$\delta = (2/\omega\mu_0\sigma)^{1/2} = (2i)^{1/2}/\Gamma$$

and

$$\Gamma s = (2i)^{1/2}\, s/\delta = (2i)^{1/2}B \quad [\text{as } B = s/\delta]$$

where:

$\omega = 2\pi f$ and f is the frequency (Hz)
μ_0 = permeability of free space
$i = \sqrt{-1}$
$\Gamma = (i\omega\mu_0\sigma)^{1/2}$
σ = conductivity
s = inter-coil separation (m).

The ratio of the secondary (H_s) to primary (H_p) magnetic fields at the receiver at low induction numbers (i.e. $B \ll 1$) is given by:

$$H_s/H_p \approx iB^2/2 = i\omega\mu_0\sigma s^2/4.$$

The measuring instrument is designed to ensure that with the selected frequency (f), a given inter-coil separation (s), a designed response of H_p for a given transmitter, the only unknowns are H_s, which is measured by the instrument, and the ground conductivity (σ).

Put another way:

$$\sigma_a = (4/\omega\mu_0 s^2)(H_s/H_p)_q$$

where the subscript q denotes the quadrature phase.

A ground conductivity meter responds to the conductivity composition of the ground, depending upon the orientation of the coils. Typically, there are two modes: horizontal coils with a vertical magnetic dipole (VMD), and vertical coils with a horizontal magnetic dipole (HMD). If a thin semi-infinite horizontal layer is located at a normalised depth z (where z is the actual depth divided by the inter-coil separation), then the relative contribution of that thin layer to the secondary magnetic field (H_s) at the receiver is denoted by the impulse response function (ϕ). The form of this response for both the vertical and horizontal magnetic dipoles (Figure 11.5) is very important. In the case of the vertical magnetic dipole, there is little relative

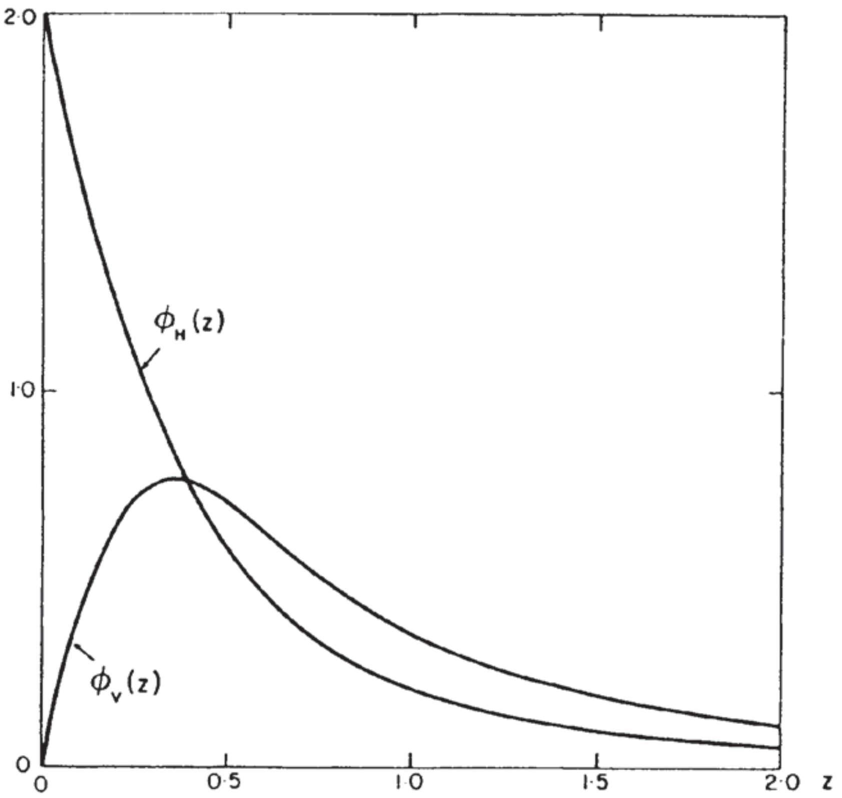

Figure 11.5 Impulse response functions (ϕ) for horizontal and vertical magnetic dipoles as a function of normalised depth (McNeill 1980)

contribution from the very near surface. Consequently, in this configuration, the technique is relatively insensitive to features very near to the surface. The maximum relative contribution arises from a normalised depth of $z = 0.4$. In contrast, the relative response for a horizontal magnetic dipole decreases with depth from a maximum at the surface. In this case, the dipole configuration makes the system very sensitive to near-surface features.

Rather than considering the relative contribution of a single thin layer at a depth z, the relative contributions of all materials within the depth z to the secondary magnetic field (or apparent conductivity) can be calculated. The sum of all the relative impulse responses for all the depths to z is expressed mathematically as the integral of all the impulse response functions. The total contribution so calculated is called the *cumulative response function*, $R(z)$, and has different forms for the VMD and HMD configurations (Figure 11.6).

The graphs of cumulative response function for each dipole orientation can be used in the calculation of true conductivities for simple 2- or 3-layer models. An example of such a calculation is given in Box 11.2.

Consider the case of a model involving two semi-infinite horizontal layers where the inter-coil separation is much less than the skin depth for all layers. The measured apparent conductivity is made up of the contribution of the first layer plus a contribution from the underlying

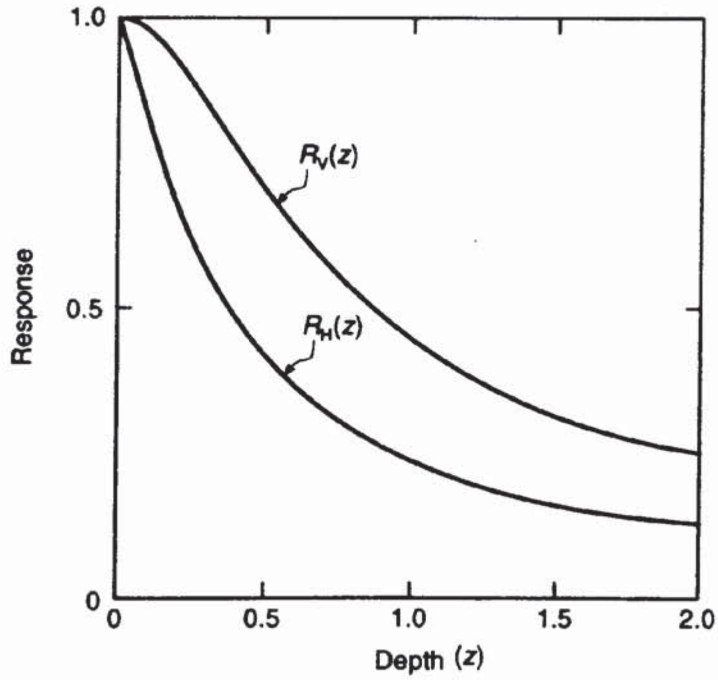

Figure 11.6 Cumulative response functions (R) for horizontal and vertical magnetic dipoles as a function of normalised depth (McNeill 1980)

Box 11.2 Use of the cumulative response function to calculate a layered-earth model from a measured apparent conductivity

In a 2-layer model, the contribution from the upper layer to the measured apparent conductivity σ_a is given by:

$$\sigma_a = \sigma_1(1 - R)$$

where σ_1 is the true conductivity of the first layer and R is the cumulative response function for the appropriate dipole orientation (VMD or HMD). R is a function of normalised depth ($z = d/s$), where d is the actual depth and s is the inter-coil separation.

The contribution arising from the underlying layer is given by:

$$\sigma_a = \sigma_2 R$$

where σ_2 is the true conductivity of the underlying material.

The total contribution to the apparent conductivity is the sum of these two contributions, such that:

$$\sigma_a = \sigma_1(1 - R) + \sigma_2 R.$$

For a 3-layer case:

$$\sigma_a = \sigma_1(1 - R_1) + \sigma_2(R_1 - R_2) + \sigma_3 R_2$$

continued

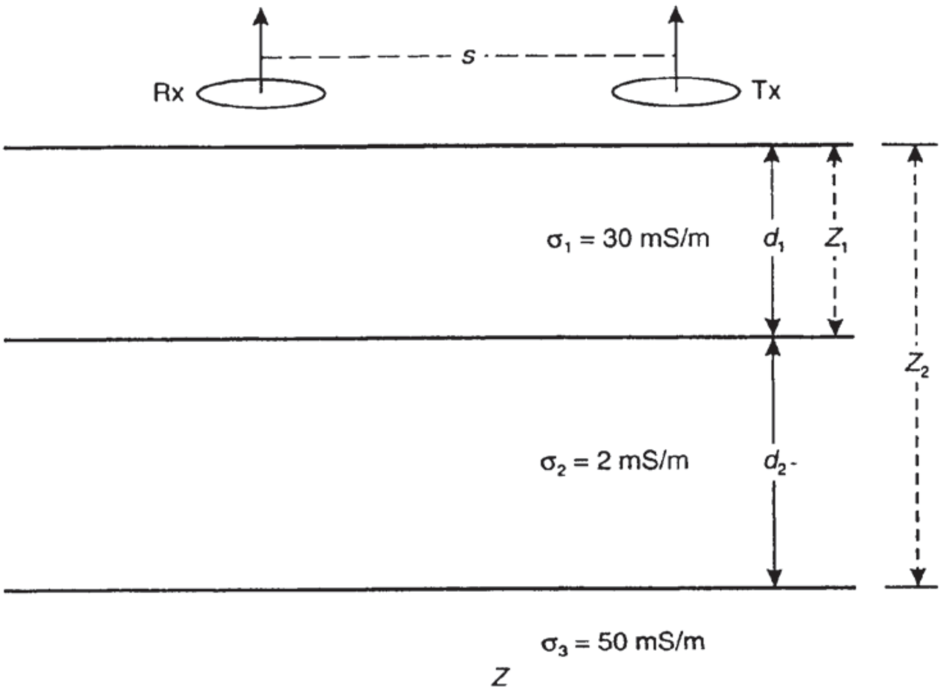

Figure 11.7 Example of the use of cumulative impulse response functions (R) and true conductivities (σ) to calculate a theoretical value of apparent conductivity (σ_a) for a given 3-layer earth model. Given $R_1 = 0.71$ and $R_2 = 0.31$, and using Figure 11.6 for $d_1 = 5$ m and $d_2 = 10$ m, for $s = 10$ m, then: $\sigma_a = 30(1-0.71) + 2(0.71-0.31) + 50 \times 0.31 = 25.0$ mS/m, using the formula for a 3-layer case given in Box 11.2

continued

where $\sigma_{(1,2,3)}$ are the true conductivities and $R_{(1,2)}$ are the cumulative response function values of the first, second and third layers, respectively.

Examples of the calculation are given in the caption to Figure 11.7.

material. The weighting of the conductivity contribution is provided by the cumulative response function. A similar logic follows for a 3-layer case.

This type of calculation is useful if the likely value of apparent conductivity is required over a model where layer conductivities have been estimated along with layer thicknesses. The values of apparent conductivity so obtained are estimates and will be only as accurate as the validity of the assumptions for a given situation. If the ground is not approximated by semi-infinite horizontal planar layers, there is some lateral as well as vertical variation in conductivity and thickness, then the calculation will only be at best a rough guide. If there is a three-dimensional object within the sphere of influence of the EM measuring system, or if the interfaces between layers is sloping or non-planar, then the validity of this calculation will be substantially reduced.

In the case of an APEX MaxMin I-10 dual-coil system, up to 10 different frequencies can be selected (110, 220, 440, 880, 1760, 3250, 7040, 14 080, 28 160 and 56 320 Hz), using one inter-coil separation

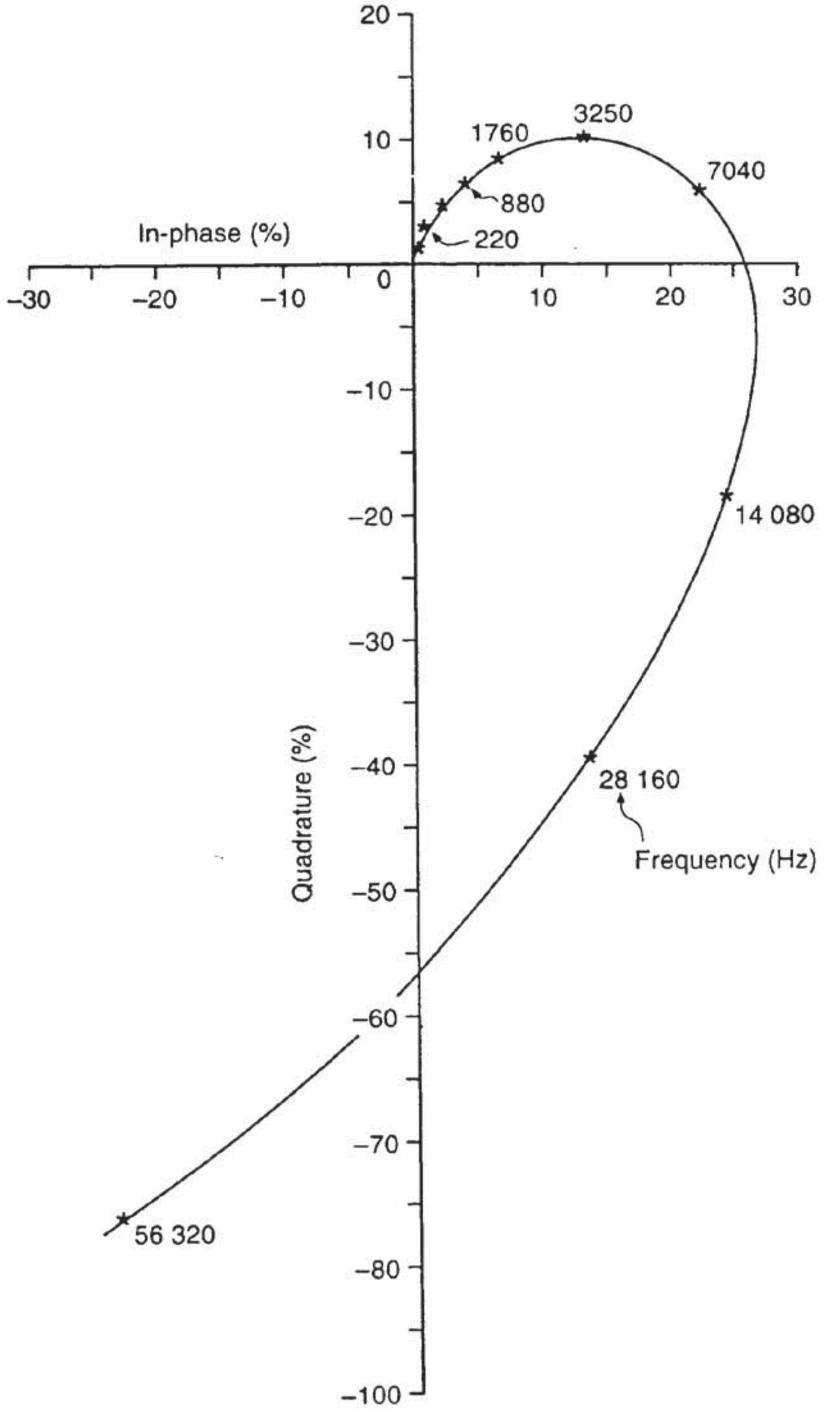

Figure 11.8 Example of a phasor diagram where the in-phase and quadrature data for each frequency (shown by asterisks) are plotted and compared with a best-fit model (solid line) for a horizontal loop EM sounding (Palacky 1991)

which can be selected over the range 20 m to 500 m. The normal mode of operation is referred to as *horizontal loop EM* (HLEM), although measurements can also be made in the perpendicular dipole position and in the tilt-angle configuration (Frischknecht *et al.* 1991). Commonly for mapping Quaternary sediments, an inter-coil separation of 100 m is used. Both the quadrature and in-phase components are measured at each frequency at a given station location and are displayed in a phasor diagram (Figure 11.8). The measured HLEM values depend on a response parameter α (Box 11.3) that is directly proportional to the conductivity of the ground it is desired to measure, and the frequency of measurement (one of the 10 available frequencies) and the inter-coil separation, both of which are chosen by the system operators; other parameters are constants (Palacky 1991). Master-curve phasor diagrams are used in the interpretation of the measured data (see next section).

Box 11.3 Horizontal loop EM response parameter α

The HLEM response parameter α is given by:

$$\alpha = \mu\sigma\omega L^2$$

where μ is the magnetic permeability of free space ($4\pi \times 10^{-7}$ H/m), σ is the overburden conductivity, ω is the angular frequency where $\omega = 2\pi f$, and f is the frequency of measurement, and L is the inter-coil separation (m).

11.2.4 Interpretation methods

11.2.4.1 Profiling and depth sounding

Electromagnetic data can be analysed in a number of different ways, according to the manner in which they have been acquired. Measured parameters may be plotted as profiles or as gridded and contoured maps on which anomalous zones can be identified. These approaches tend to be qualitative and first-order interpretations.

For reconnaissance mapping or ‘anomaly spotting’, qualitative interpretation may suffice. However, there are certain pitfalls that can befall the unwary if the characteristic responses of certain features are not recognised. For example, it is a misconception when using a dual-coil system, such as Geonics EM31, that a target produces only a single peak over a thin conductive target; spotting anomaly ‘highs’ is fraught with danger!

Consider a typical apparent conductivity profile produced over a 10 cm diameter metal gas pipe buried at around 1 m (Figure 11.9A). Two peaks are evident with a strong low or even negative occurring immediately over the target. Note that the distance between the anomaly peaks is the same as the dipole length. Always check the inter-peak distance; if it is curiously similar to the inter-coil separation being used, then the target causing the anomaly is at the midpoint between coils. Depending upon the spatial sampling interval relative to the position of the target, the anomaly peaks and low may be slightly broader or narrower than one dipole length by the sampling being skewed relative to the target (see the sub-sampled profile in Figure 11.9B). The same effects may be more subdued with larger inter-coil separations.

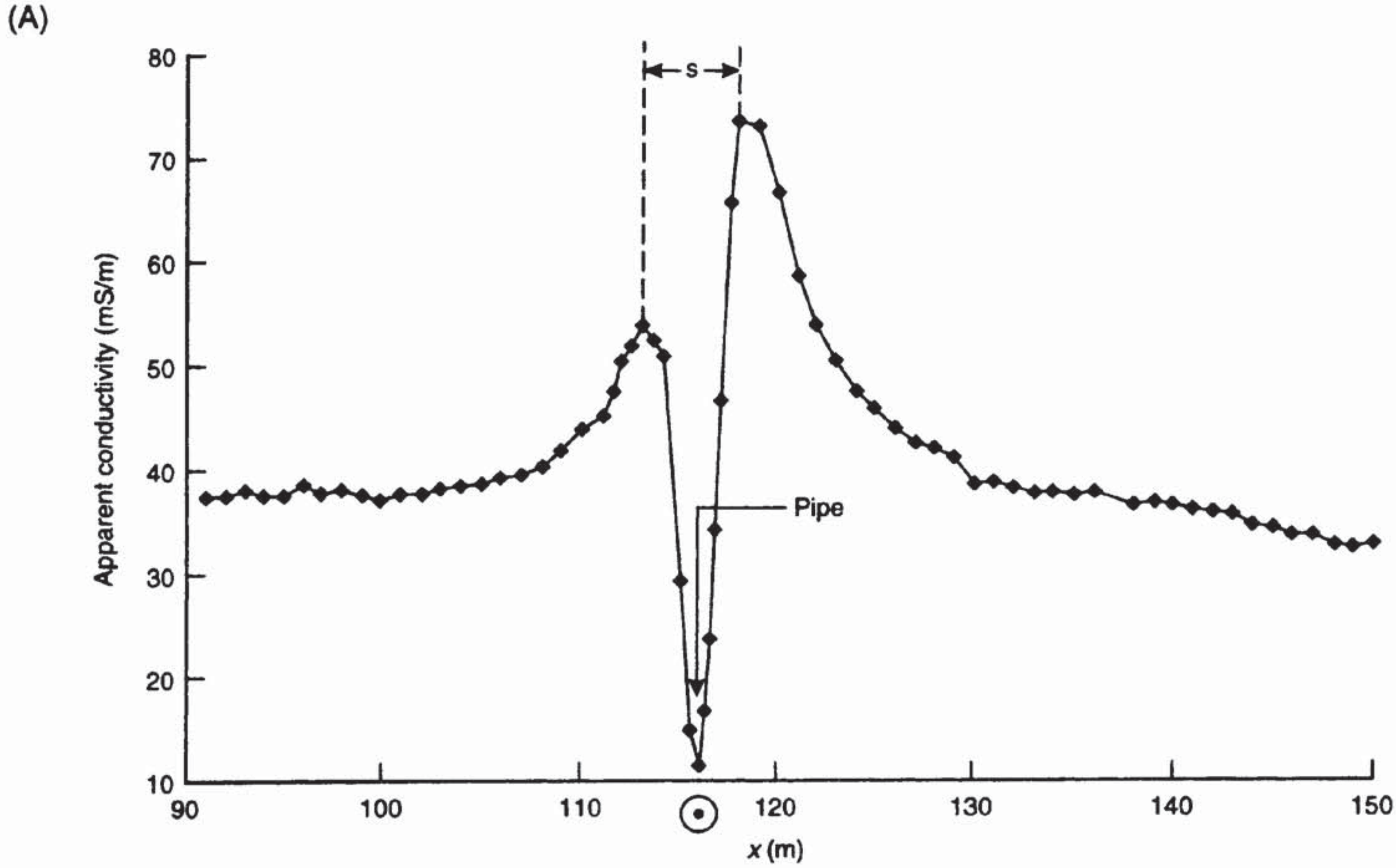
(A)
Apparent conductivity (mS/m)
80
70
60
50
40
30
20
10
90
100
110
120
130
140
150
x (m)
s
Pipe

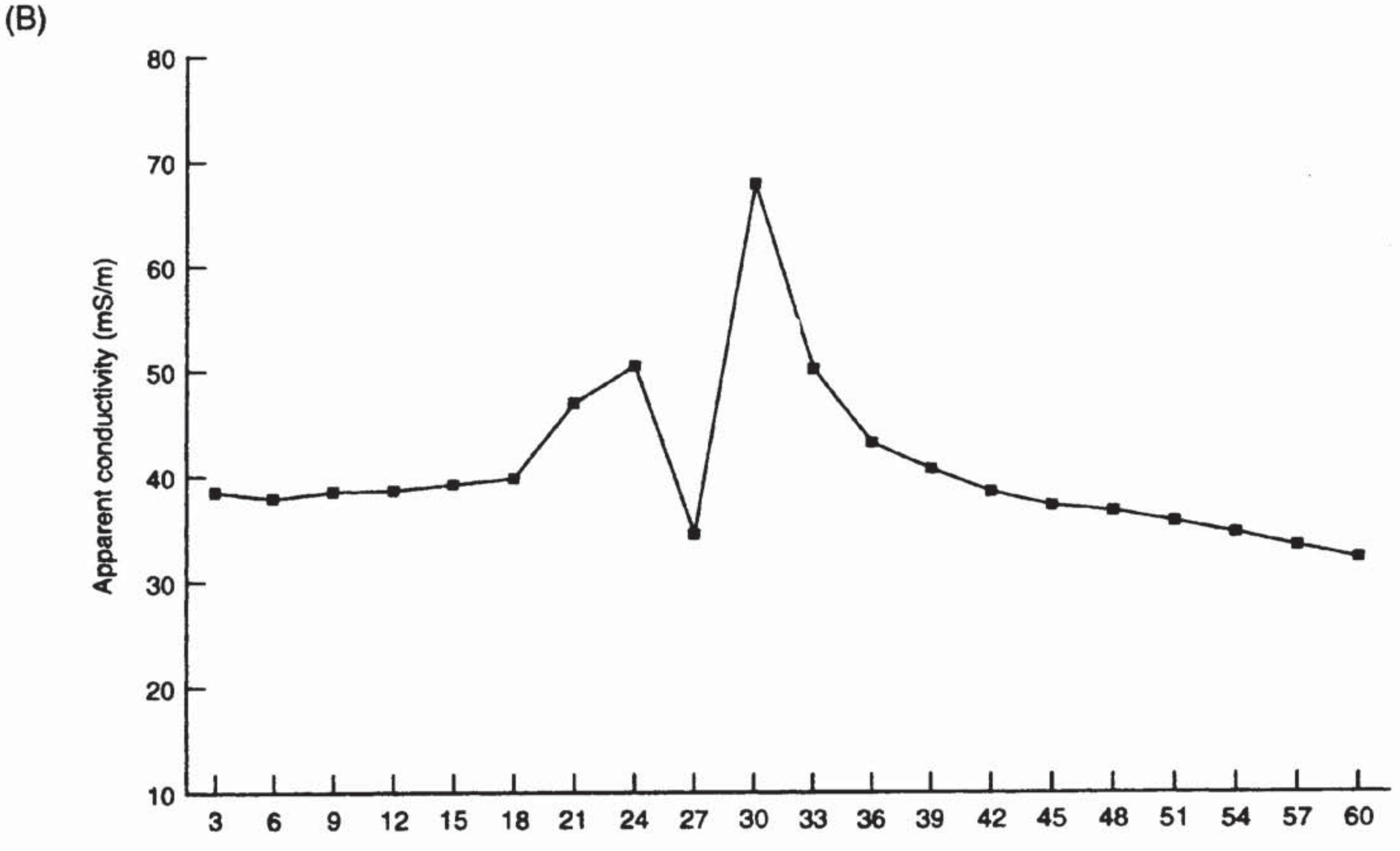
(B)
Apparent conductivity (mS/m)
80
70
60
50
40
30
20
10
3
6
9
12
15
18
21
24
27
30
33
36
39
42
45
48
51
54
57
60
Position (m)

Figure 11.9 (*opposite*) Example of the effect of (A) a metal gas pipe on apparent conductivity data, and (B) the horizontal smearing of the anomaly caused by inadequate spatial sampling. Note that the peak-to-peak distance in (A) is equal to the inter-coil separation

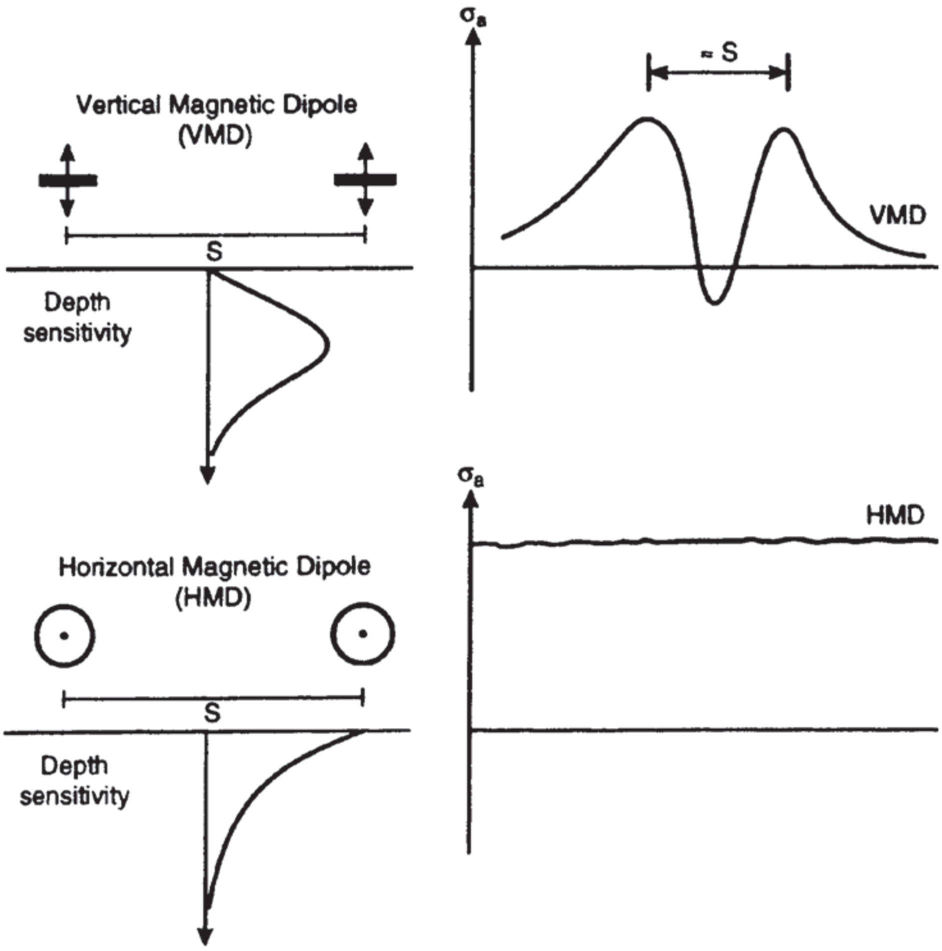

Figure 11.10 Example of the difference in output from both vertical and horizontal magnetic dipoles over a vertical conductor for the same intercoil separation

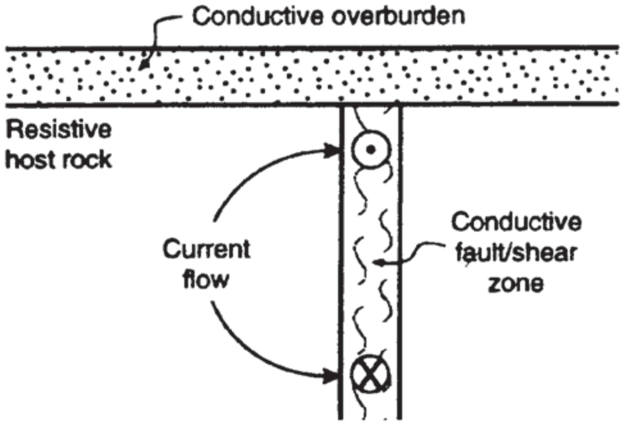

Similarly, the shape of the anomaly will also vary depending upon which dipole orientation is used. An example of the difference of the output from both dipole orientations over a vertical conductor for the same inter-coil separation is shown in Figure 11.10.

The spatial smearing effect is also noticeable in gridded data. If the spatial sampling is too coarse, the anomalies arising from small (particularly 3-D) targets may be effectively smoothed (aliased) and the targets may be missed. The resolution of ground conductivity mapping is discussed in Section 11.2.4.3.

11.2.4.2 Computer analysis

More quantitative analysis can be undertaken using specialist software. Two approaches are possible: (a) using EM data to form a depth-sounding at a single location, and (b) undertaking EM profiling along a line or over a grid to produce a two-dimensional geoelectric cross-section.

In the case of depth-sounding, a limited number of data are obtained as a function of inter-coil separation (which is in itself a function of frequency; greater depth penetration is achieved using the lowest frequencies and greatest inter-coil separations) and dipole orientation. For this discussion, the range of ground conductivity meters made by Geonics Ltd will be used as these instruments are employed commonly in environmental and engineering surveys. Data obtained with other makes of instruments can be interpreted in similar ways.

If a Geonics Ltd EM34-3 ground conductivity meter is used, three inter-coil separations and two dipole orientations are available, giving a maximum number of six data points obtainable using the one instrument at a given sampling point. The apparent conductivity values measured at each inter-coil separation and with each dipole orientation are entered into a program such as EMIX-MM (Interpex Ltd, USA). If an APEX MaxMin I-10 has been used, the 10 pairs of in-phase and quadrature data can be entered into the same software. The program is used to invert the data to produce a layered earth model in which the true conductivity of each layer and its associated thickness are estimated and entered into the program. Synthetic values of apparent conductivity are calculated for the selected model and compared with those actually observed. The computer model is automatically adjusted until the difference between the measured and observed apparent conductivities satisfies some statistical criterion – e.g. an RMS error of less than 2%. The final output of the program is a vertical depth–true conductivity profile. Some versions of the software allow equivalence testing (see also Chapter 7). Correlation with borehole data can help to constrain the model layer thicknesses in order to obtain more realistic values for the layer true conductivities.

While the model so obtained may be statistically adequate, the question of geological reasonableness still has to be asked. For APEX MaxMin data, a series of master-curve phasor diagrams can be produced where the number of layers and their respective conductivity values and thicknesses can be estimated from the fit with the observed phasor diagram. An example of an interpretation is shown in Figure 11.11.

An extension of the depth-sounding interpretation is the profile inversion. Instead of having one set of sounding data, a series of values of apparent conductivity for each inter-coil separation and dipole

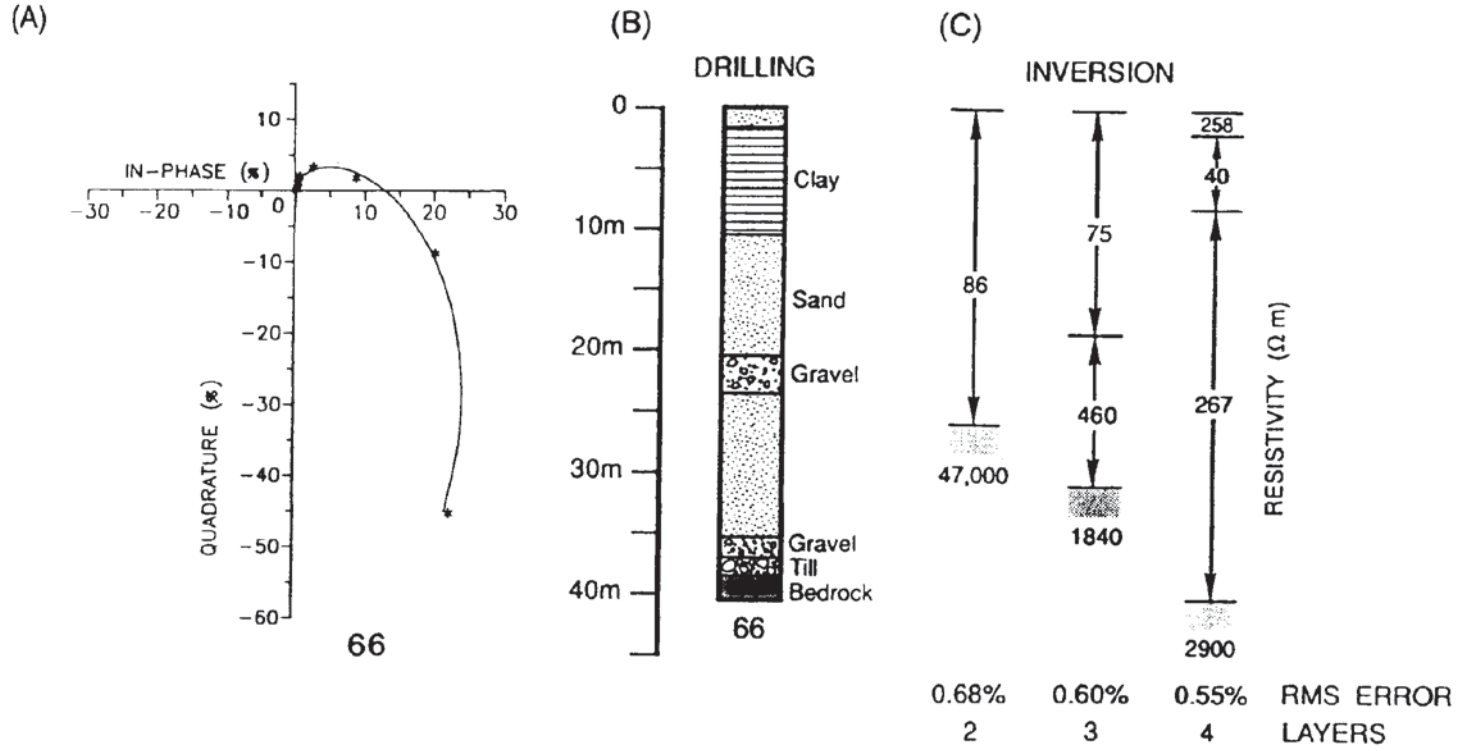

Figure 11.11 Use of model phasor diagrams in the interpretation of HLEM data. (A) Eight frequency HLEM data acquired using an APEX MaxMin instrument; (B) the drilling log; and (C) the various inversions produced using 2-, 3- and 4-layer models. From Palacky (1991), by permission

orientation are obtained along a survey line at discrete intervals. The ensuing apparent conductivity profile can be inverted using a sister programme to EMIX-MM called EMIX34PLUS (Interpex Ltd). The final output is a pseudo-geological two-dimensional section displaying true conductivities and layer thicknesses along the profile line. It is important that sufficient data be collected to provide adequate sampling both spatially and as a function of depth. At least three different inter-coil separations are required for either depth-sounding or profile-inversion to be achieved. Additional data can be obtained by supplementing the Geonics EM34-3 with the EM31 and the EM38, where appropriate. Care has to be taken in the calibration of each instrument when using more than one type on the same survey line, to ensure consistency.

11.2.4.3 Resolution

As with any geophysical technique, consideration has to be given as to the resolution achievable. In the case of dual-coil systems, for example, a number of factors have to be taken into account on any survey if it is to be completed successfully.

Ground conductivity depth-sounding and profiling are best suited to horizontal or sub-horizontal layered structures where the vertical conductivity contrast between horizons is significant. However, in environmental and engineering geophysics, EM techniques are increasingly being used at less than ideal sites. The criterion stated above is seldom applicable and, to complicate matters, the sites may often be cluttered with above-ground structures, old pipes and cables, buildings, tanks, metal fences, metal signposts, etc., each of which may degrade the quality of data and reduce the reliability of, if not negate, any quantitative analysis. In some cases it may be possible to filter out the effects of a power line or pipe if the anomaly due solely to that feature can be identified clearly.

Edge effects associated with changes of slope, or margins of sites contained in old quarries, for example, also affect the data quality. Some of these effects can be reduced in the survey design stage if the presence of these features is known in advance.

A further factor to be considered is the likely resolution of the method for a given type of sub-surface target. The more a target deviates from being a semi-infinite homogeneous horizontal half-space (i.e. one that exists only in textbooks!) the more difficult it is to detect it. For example, consider the case of a steel drum buried at 2 m in an otherwise homogeneous ground. This target should be located readily using an EM31 given a fine enough survey grid. If, however, an EM34-3 is used with 40 m coil separations, the volume of ground being sampled is increased enormously compared with that being sampled by an EM31, and consequently, the drum may be missed. Similarly, a conductive target of 1 m diameter buried at 10 m is unlikely to be resolvable with any EM method unless the utmost care is used and the site is virtually noise-free. Furthermore, a station interval of 1 m would have to be used to stand any chance of providing adequate spatial sampling.

A further consideration in the interpretation of EM data is the position of a sub-surface target with respect to the dual-coil dipoles. If a survey is being conducted with both coils aligned along the survey transect (an 'in-line' configuration) with the transmitter preceding the receiver, and an apparent conductivity anomaly is observed, the source of that anomaly may not actually lie in the line of the transect but to one side (Figure 11.12). This makes the precise identification of the location of a sub-surface target, such as a mineshaft, quite difficult. It is for this reason that one often finds the location of an apparent conductivity anomaly does not necessarily coincide with that of a magnetic anomaly arising from the same metallic conductive target. This apparent lack of coincidence can lead to misinterpretation and the feature being missed. To assist with determining lateral variability in ground conditions, it may be sensible on some sites to rotate the dual-coil system from being 'in-line' to being 'broadside'.

In the case of an EM31, the operator should remember that the instrument has a finite response time if the apparent conductivities are different between the two orientations, and allow the instrument to settle to the correct value before proceeding to the next measurement station. If measurements of apparent conductivity are made too quickly and while the instrument is settling down, inaccurate values

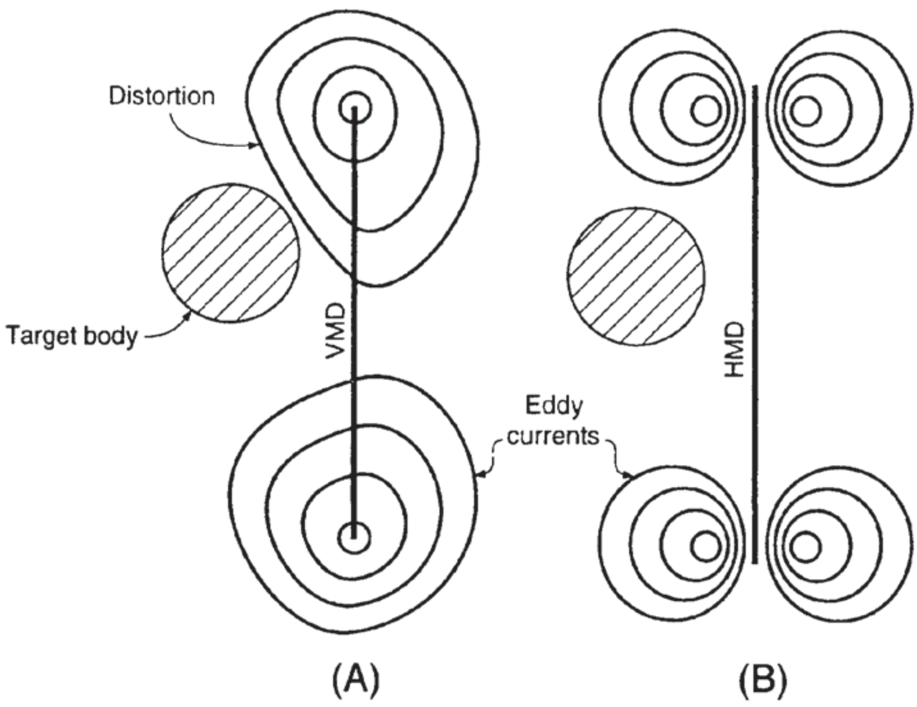

Figure 11.12 Cartoon to illustrate the difference in eddy currents (plan view) produced by (A) the vertical and (B) the horizontal magnetic dipoles (Stoyer 1989). A conductive (or resistive) target in a resistive (or conductive) medium will distort the eddy currents even when off the line of the survey section

will be obtained, thus reducing the value of the entire EM survey. Other aspects of interpretation will be evident by reference to the various case histories presented in the next section.

11.2.5 Applications and case histories

The range of mineral exploration case histories available in the literature is quite large but there are relatively few well-documented environmental examples. While there are a number of different types of EM instruments available, the majority of environmental case histories make reference to EM systems made by Geonics Ltd.

11.2.5.1 Location of orebodies

The most common use of EM profiling is undoubtedly exploration for mineral deposits, mostly as a means of locating possible targets. EM methods have been instrumental in the location of many significant economic orebodies (Frischknecht *et al.* 1991): examples are the Temegami Mine, Ontario; the Poirier deposit, Quebec; the Faro Deposit, Yukon; the Caribou Deposit, New Brunswick; and the Kidd Creek Mine, Ontario, among many others.

EM results on their own are not usually diagnostic of whether a conductive body is economic or not. For example, it may be difficult to distinguish between a carbonaceous, a graphitic or a sulphide body purely on conductivity values alone. Consequently, other geophysical techniques, including other EM methods, are used in conjunction with each other to aid the interpretation.

There are many case histories describing the wide range of EM methods in mineral exploration and a good number have been described by Frischknecht *et al.* (1991). It is important to note that the geophysical responses observed in one geological environment are not necessarily exactly the same in other areas. The specific geophysical responses are determined by the individual blend of mineral and structural associations present at a given site and, in some cases, may be unique to individual geographical locations.

One example is given here to illustrate the combined approach needed to differentiate between target types. Slingram and VLF EM methods were used by Barbour and Thurlow (1982) in exploration where long graphitic zones are common in Newfoundland. In addition, gravity data were used to help differentiate between probable sulphide occurrences and massive sulphide deposits. At the Tulks East deposit, black graphitic shales and mudstones occur within 50 m of more-conductive massive sulphides (Figure 11.13). Both quadrature and in-phase EM components (expressed as a percentage of the primary field) were measured using a MaxMin horizontal loop system. Two frequencies were used (222 Hz and 3555 Hz) but the greatest difference between target types was observed on the higher-frequency dataset (Figure 11.13). The massive sulphide deposit also gives rise to a peak in both the Bouguer gravity profile and the Fraser-filtered VLF transect.

Figure 11.13 (*opposite*) HCP slingram, VLF, and Bouguer gravity profiles across the Tulks East Prospect, Newfoundland. The massive sulphide can be distinguished from 'graphitic' shale at 222 Hz by the larger conductance of the sulphide. From Barbour and Thurlow (1982), by permission

A second example is presented which shows how important adequate signal processing may be to locating a mineral target accurately. A Turam profile across the Kimheden orebody in north Sweden (Parasnis 1991) is shown in Figure 11.14A. Two components (reduced ratio and successive phase difference) are plotted as a function of distance and both show very distinctive positive (RR) and negative (phase difference) anomalies over a steeply dipping pyrite orebody. The point of occurrence of an orebody is usually taken as corresponding with the reduced ratio maximum and phase difference minimum. The secondary fields calculated from the Turam profile in Figure 11.14A and normalised to the local primary field are shown in Figure 11.14B. The reduced ratio maximum is displaced by about 4 m relative to the true position of the current as revealed by the secondary fields. While a 4 m discrepancy in position may have little importance for shallow drilling, in cases where deeper drilling is required, this lateral shift could result in the sub-surface target being missed or inadequately sampled.

An example of the use of HLEM has been presented by Palacky (1991) in an investigation over a conductor buried beneath Quaternary sediments in north-eastern Ontario, Canada. An Apex Max-Min-I (eight-frequency) system with an inter-coil separation of 100 m was used along a 1 km profile south of Fraserdale. In-phase and quadrature components measured at each of eight frequencies are shown in separate families of graphs in Figure 11.15. It is clear that

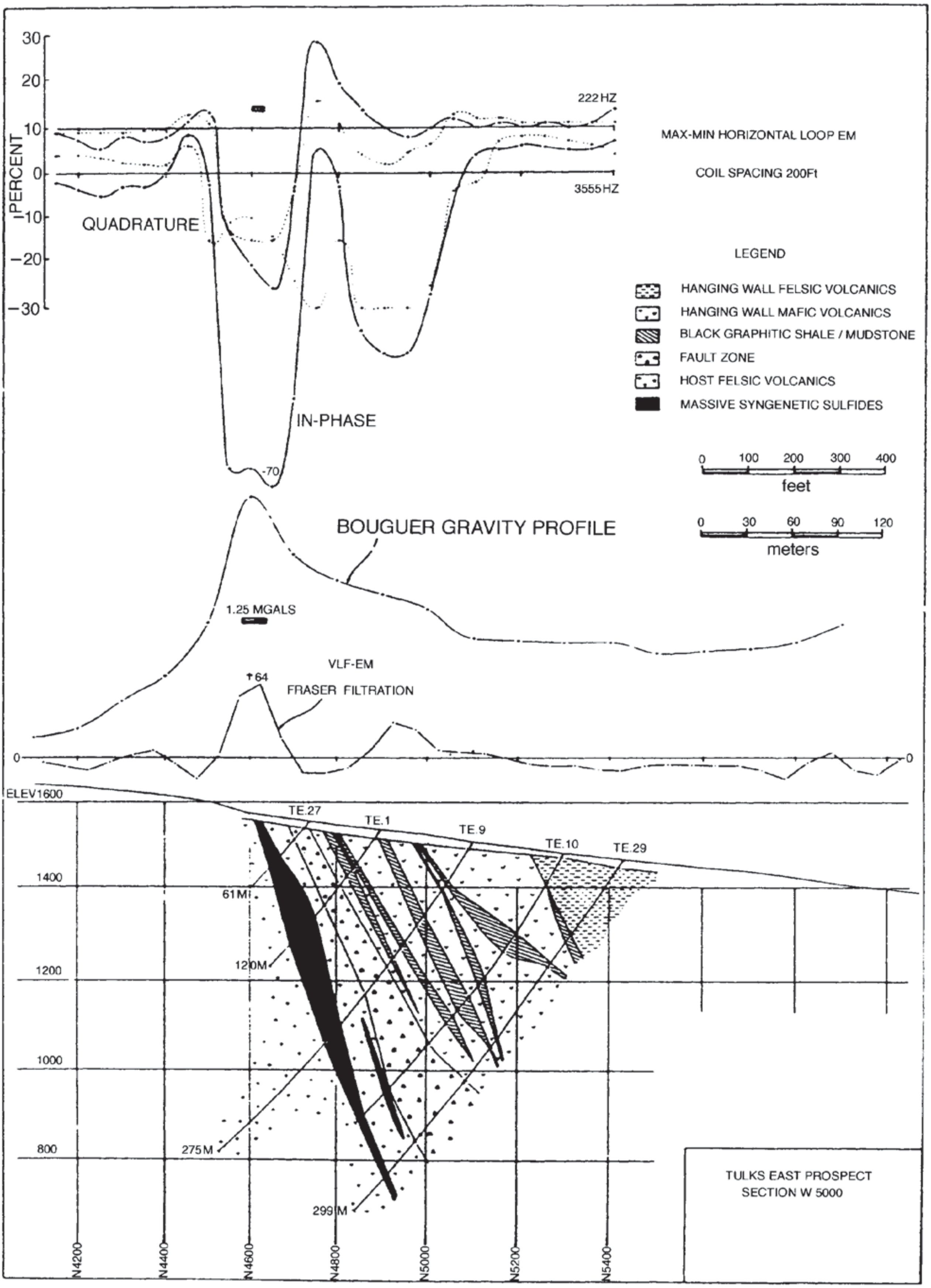
30
20
10
0
−10
−20
−30
PERCENT
QUADRATURE
IN-PHASE
-70
222 HZ
3555 HZ
MAX-MIN HORIZONTAL LOOP EM
COIL SPACING 200Ft
LEGEND
HANGING WALL FELSIC VOLCANICS
HANGING WALL MAFIC VOLCANICS
BLACK GRAPHITIC SHALE / MUDSTONE
FAULT ZONE
HOST FELSIC VOLCANICS
MASSIVE SYNGENETIC SULFIDES
0 100 200 300 400
feet
0 30 60 90 120
meters
BOUGUER GRAVITY PROFILE
1.25 MGALS
VLF-EM
FRASER FILTRATION
64
0
0
ELEV1600
1400
1200
1000
800
TE.27
TE.1
TE.9
TE.10
TE.29
61M
120M
275M
299M
N4200
N4400
N4600
N4800
N5000
N5200
N5400
TULKS EAST PROSPECT
SECTION W 5000

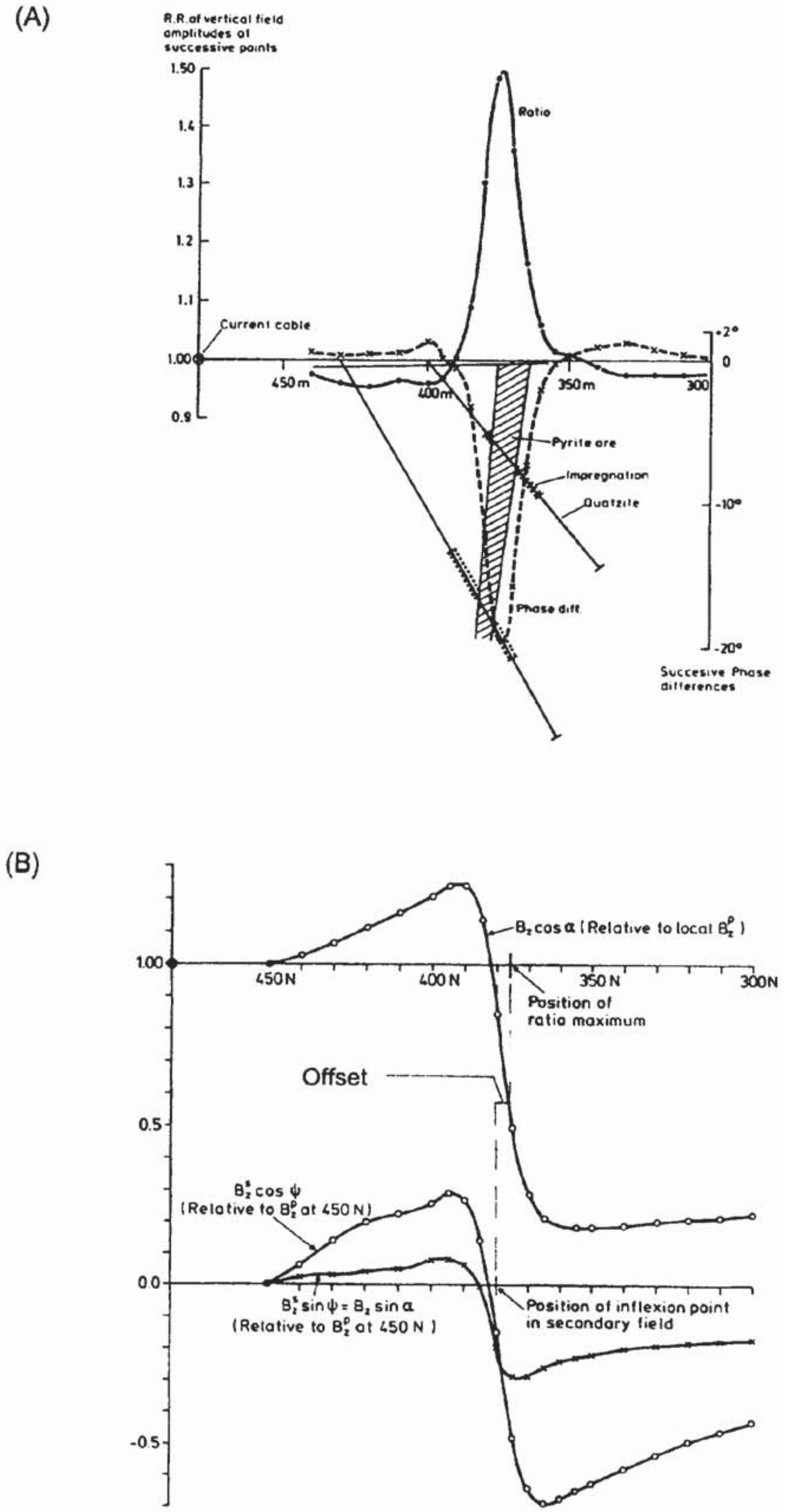

Figure 11.14 (A) Turam profile across the Kimheden orebody in north Sweden, showing reduced ratio (RR) and successive phase differences. (**B**) The secondary field calculated from the Turam profiles in (A). Note the slight offset in location of the position of the RR maximum and that of the point of inflection in the secondary field. From Parasnis (1991), by permission

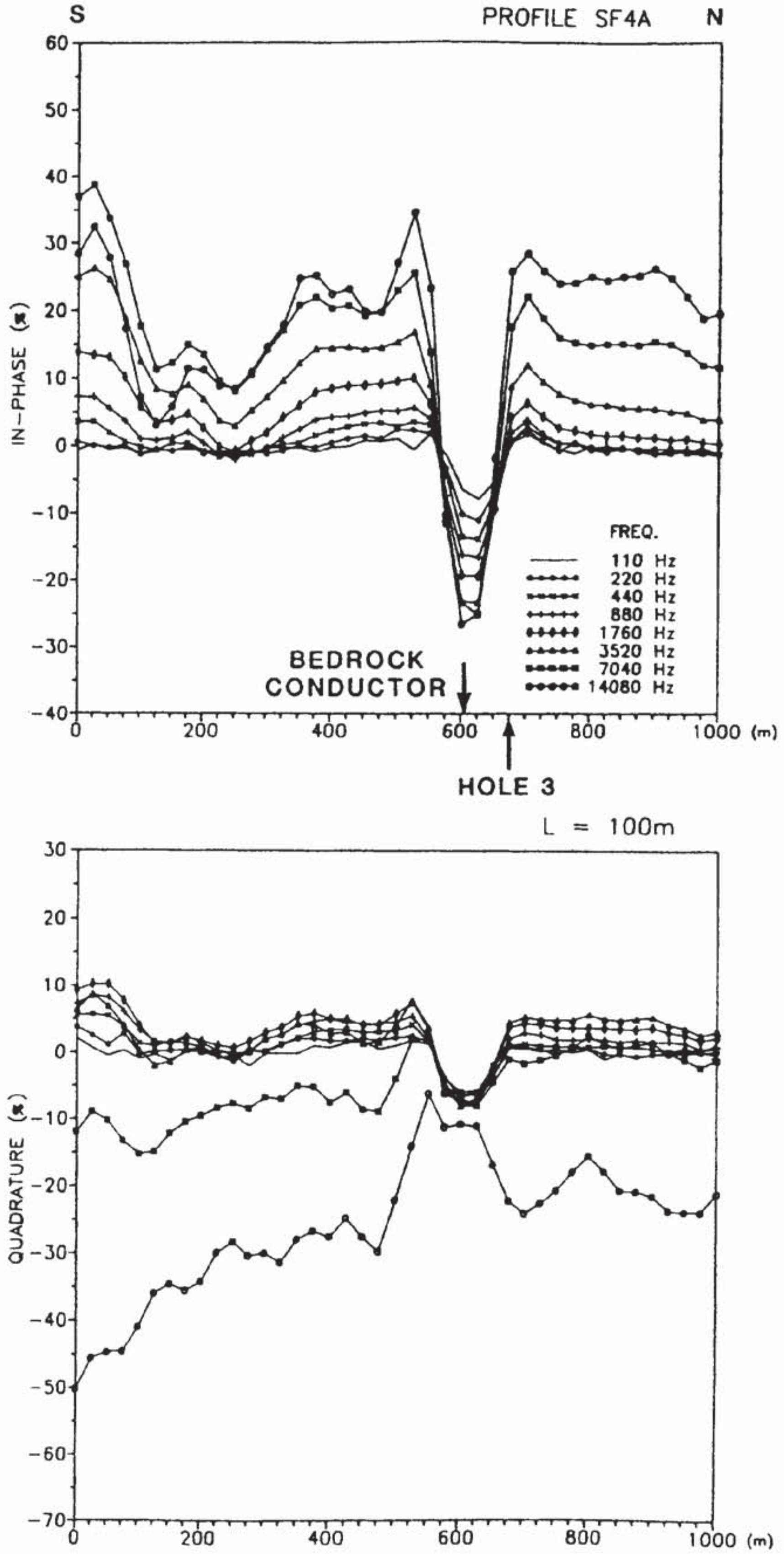

Figure 11.15 HLEM profile over a 1000 m line, 20 km south of Fraserdale, Ontario, over a bedrock conductor (at station 600) covered by Quaternary sediments. In-phase (top) and quadrature (bottom) data were acquired at the frequencies specified. Coil separation is 100 m. The location of borehole 3 is indicated. From Palacky (1991), by permission

around station 600, the in-phase component goes negative and a corresponding trough-shaped anomaly is evident in the quadrature component data. The width of this anomaly at the zero level is equivalent to the inter-coil separation plus the width of the conductor. The character of this particular anomaly is typical of a narrow sub-vertical bedrock conductor of high conductance. In the case of a mineral exploration survey, such an anomaly would be indicative of a possible target zone. The reversal of the trough-shaped anomaly on the quadrature data at 14 080 Hz around station 600 (upside-down with respect to the other graphs) is a result of the presence of moderately conductive overburden. The Quaternary sediments present locally comprised alternating clay–sand units 37 m thick with 2 m of clay over 8 m of sand, 22 m of glacial till and 5 m of sand.

In contrast to the above example, Palacky (1991) also presented a HLEM profile over shear zones covered with thick clay (Figure 11.16) along a 12 km profile south of Kapuskasing, about 80 km south-west of Fraserdale, Ontario. Two shear zones are indicated around stations −375 and −635. A drillhole located at station −500 passed through 35 m of massive clays. The measured amplitudes of both components are much larger than in the previous example and are due to the presence of the very conductive clay. The quadrature data are negative at the four highest frequencies while the in-phase component is negative at 14 080 Hz.

Phasor diagrams obtained for HLEM data at three locations with different sediment types and at which borehole control was available are shown in Figure 11.17, with the simple borehole results. The phasor diagram for borehole 42 (which lies on the profile shown) shows that the fit between the measured data (as indicated by asterisks in Figure 11.17A) and the calculated response of the model (solid line) is imperfect. The overburden thickness was constrained at 35 m (the depth to bedrock as determined by drilling). However, an unconstrained inversion for a 2-layer model produced an interpreted thickness of 42 m and resistivity values of 51 Ω m for the upper layer and 8000 Ω m for the bedrock. The discrepancy of 7 m in depth estimates can be attributed to the effect on the HLEM response of the shear zones nearby.

The phasor diagram associated with the location of borehole 67 (on the profile shown in Figure 11.15) indicated a depth of overburden of 40 m with a resistivity of 210 Ω m from an unconstrained model (Figure 11.17B). The drilled depth to bedrock was 39 m, which is in very close agreement. However, the bedrock resistivity was poorly resolved.

The third phasor diagram (Figure 11.17C) was obtained over thick sand. The best-fit model obtained produced an overburden 41 m thick with a resistivity of 350 Ω m over bedrock with resistivity 500 Ω m. However, when the resistivity values are large and the contrast between layers is small, the determination of layer thicknesses be-

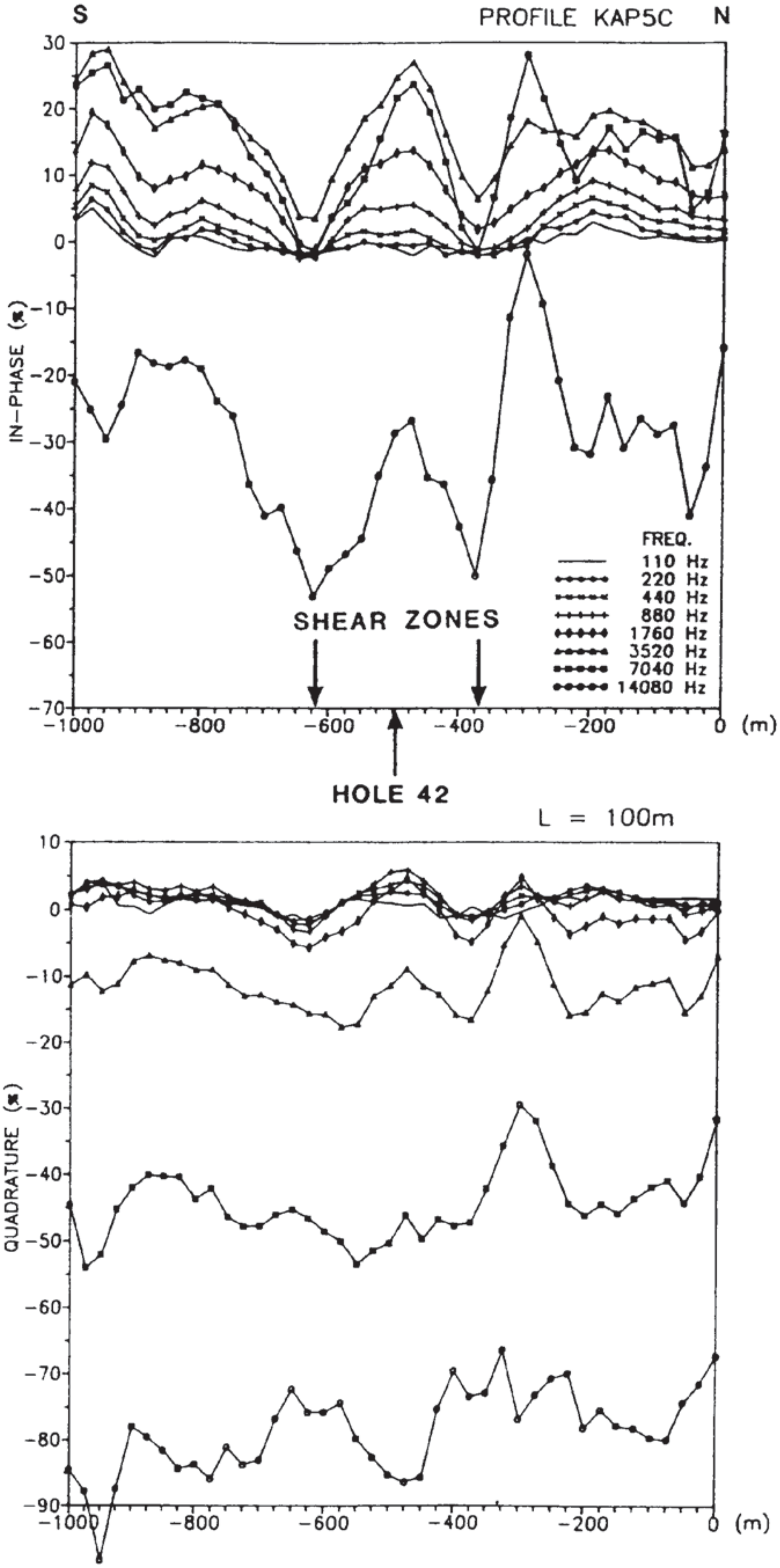

Figure 11.16 HLEM profile over a 1000 m line, 12 km south of Kapuskasing, Ontario, with shear zones concealed by thick clay. From Palacky (1991), by permission

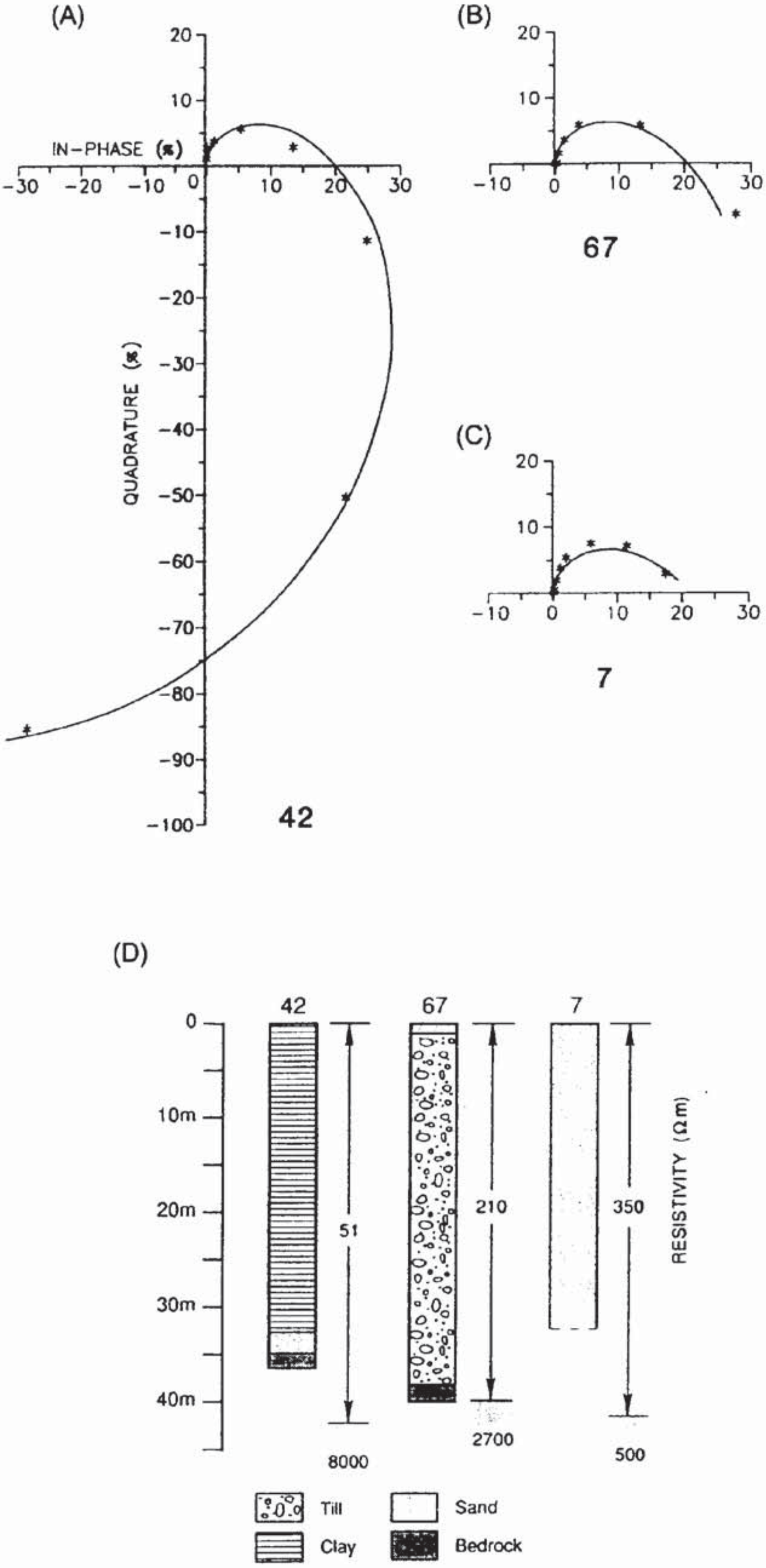

Figure 11.17 (A)–(C) Phasor diagrams, and (D) corresponding borehole results, with HLEM-derived models over three sites with contrasting sediment types. (A) = thick clay adjacent to a shear zone (hence the discrepancy in depth estimates between borehole and HLEM model); (B) = glacial till; (C) = thick sand within a esker. From Palacky (1991), by permission

comes unreliable. Drilling in this case only went through 32 m of sand when the hole was terminated as there was little point in going deeper through an esker where no basal till was expected.

These three examples provided by Palacky demonstrate the effectiveness of the use of HLEM profiling to locate shear zones and conductive targets beneath Quaternary sediments. The method produces phasor diagrams characteristic of the types of sediments present with different associated resistivities. The types of phasor diagrams can be used to help discriminate between different material types and has obvious benefits in geological mapping.

11.2.5.2 Groundwater investigations

Electromagnetic methods have been demonstrated to provide a powerful suite of tools in hydrogeological investigations since the late 1970s. The methods lend themselves to environments where conductivity contrasts are high but the ground surface precludes the simple deployment of DC resistivity methods owing to high surface resistances such as are found in very arid regions.

Two approaches tend to be taken. One is for the general investigation of a groundwater regime, where the groundwater is prevalent within aquifers. The second approach is to search within the local bedrock for fractures which may contain small but usable reservoirs of potable water. The frequency-domain EM methods are generally used for near-surface mapping investigations within a hydrogeological investigation. For deeper investigations, TEM methods are used (see Section 11.3.3.1).

Goldstein *et al.* (1990) have presented a case history where ground conductivity measurements were used to delineate contaminated water emanating from a series of water storage lagoons at Kesterton, Merced County, California. Agricultural drainwater with trace amounts of selenium and other toxic elements had been discharged into 12 unlined storage ponds totalling 5.2 km^2. These ponds provided both a year-round and seasonal habitat to migratory and local waterfowl. The high levels of selenium within the local food chain had resulted in physical deformities within the waterfowl population. A large-scale environmental study to determine the extent and degree of the contamination was initiated so that a plan could be developed for the remediation of the reservoir.

Conductivities of the local unpolluted groundwater were found to be between 300 and 400 mS/m, in contrast to those of the contaminated groundwater which reached 1000–1700 mS/m. From a series of local boreholes it was known that the contamination appeared to be restricted to a depth of less than 40 m, and typically around 20 m.

Ground conductivity measurements were made in 1987 along a series of transects (Figure 11.18A) with GCM instruments made by

Geonics Ltd (EM31 and EM34). Maps of apparent conductivity were produced for each instrument and coil separation (horizontal magnetic dipole configuration) (Figure 11.18B–D). In order to remove the effects of near-surface conductive features, the apparent conductivity values obtained using the 20 and 40 m coil separations were processed using a technique described by McNeill (1985). The conductivity value measured using the 40 m coil separation was doubled and the apparent conductivity value obtained using the 20 m coil separation was subtracted from it to give a new apparent conductivity value which was also displayed in map form (Figure 11.18E). It can be seen that the anomalies shown in the map of the processed data are much more intense than in either of the apparent conductivity maps for each of the two coil separations individually.

The final interpretation of the data is shown in Figure 11.18F. Zone A indicates normal background conductivity values; these values (150–200 mS/m) are high but are consistent with the type of local regional soils known to have a high ambient salinity. The highest apparent conductivity values (>400 mS/m) are found adjacent to Ponds 1 and 2 (area B in Figure 11.18F). The leading edge of the contaminant plume was interpreted to be where the apparent conductivity values measured using the 40 m coil separation declined to background values. This indicated that the plume front was about

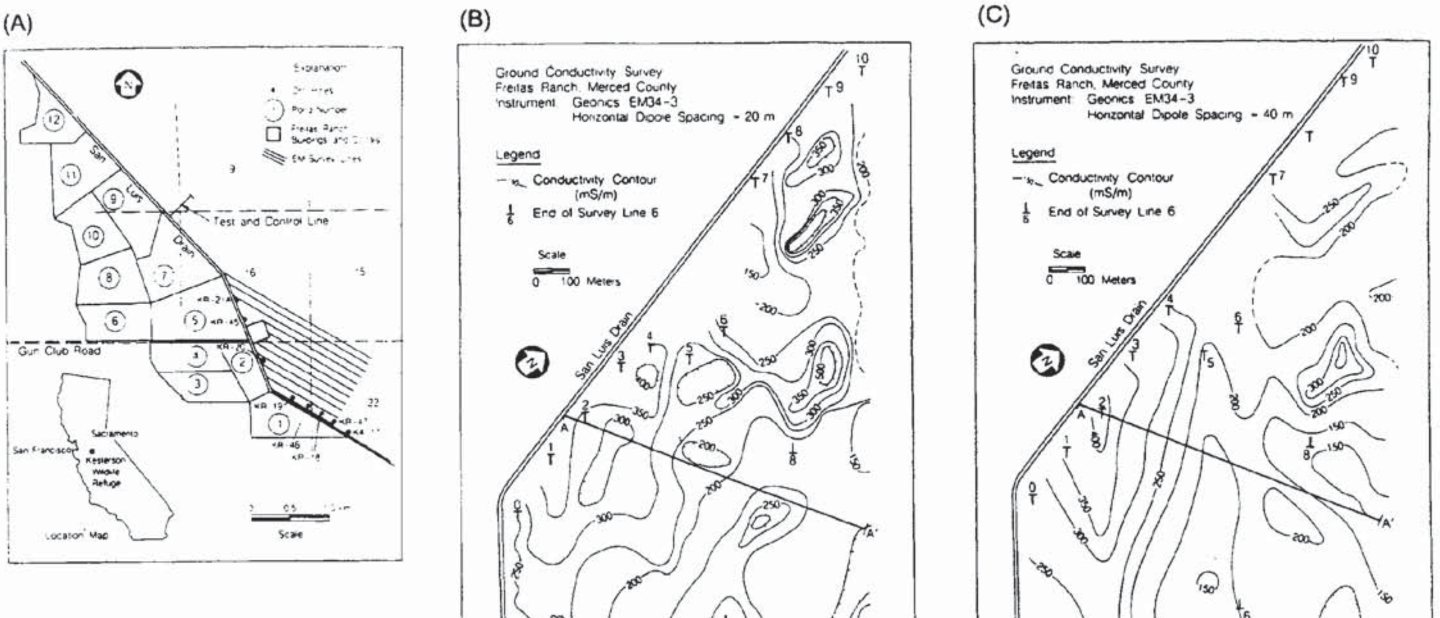

Figure 11.18 (A) Location map, (B)–(D) a series of isoconductivity maps, (E) processed data isoconductivity map, and (F) interpretation map at Kesterton, California. From Goldstein *et al.* (1990), by permission

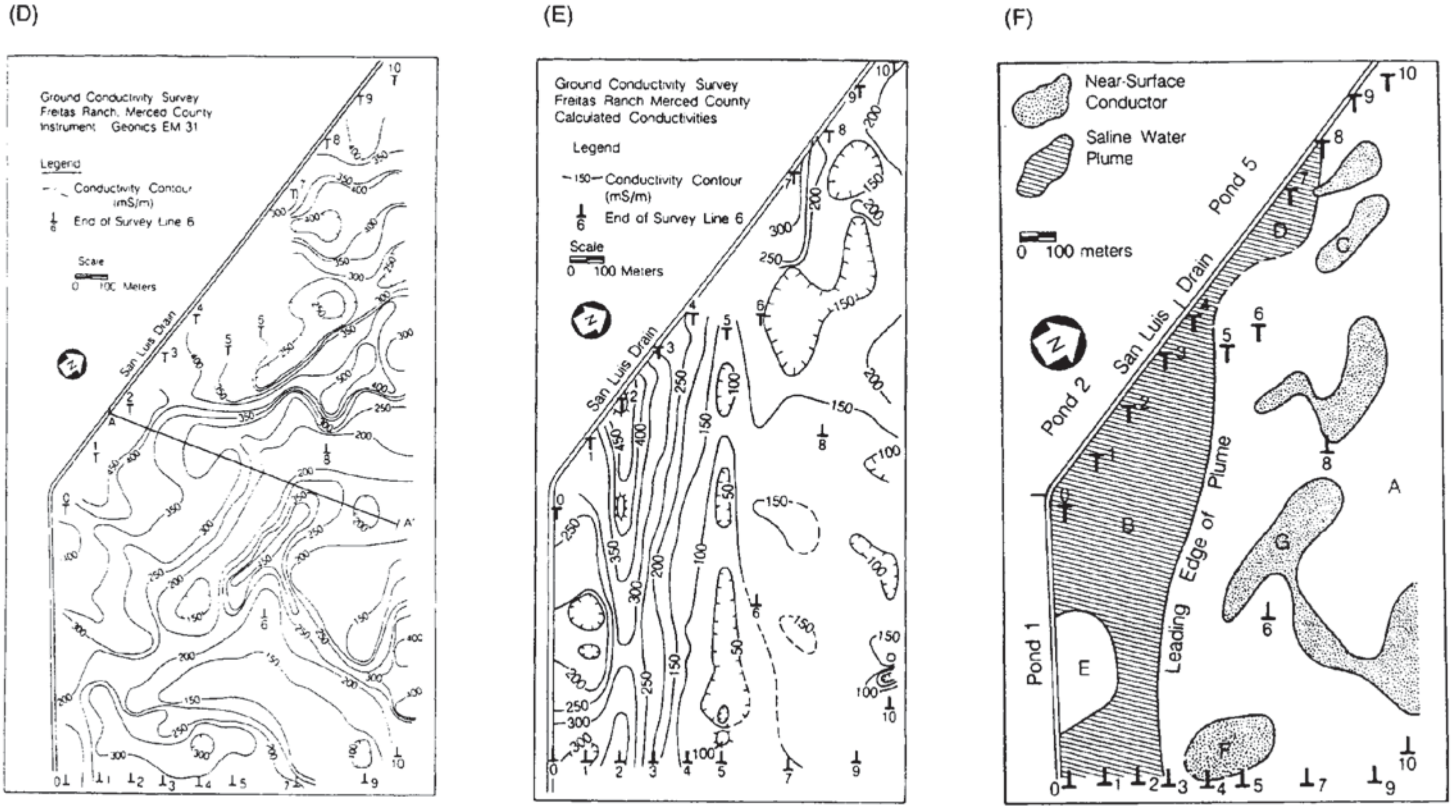

Figure 11.18 (*continued*)

350 m to the east of the San Luis Drain. Anomaly C appears to be related to high-salinity soil and correlated with an area evident on aerial photographs throughout the rainy season as a bleached zone. Area D is part of the saline plume but is confined to the area immediately adjacent to the land drain. A low-conductivity zone (area E) was identified adjacent to Pond 1. This area is thought to have had the effects of the saline plume diluted by local rainwater as drainage water had not been added to Pond 1 during the two years prior to the survey being undertaken. Area F is a deeper-penetrating higher-conductivity zone and is thought to be a plume of contaminant water which is a residual from saline water drainage prior to 1985. Zone G, which has abnormal vegetation cover, appears to be due to a near-surface conductivity feature unrelated to the contaminant plume but probably a function of local soil salinisation processes.

Monier-Williams *et al.* (1990) have described an investigation of a leachate plume emanating from a municipal landfill near Novo Horizonte, a town located 484 km north-west of São Paulo in Brazil. The location of the site is shown in Figure 11.19. The landfill had been in operation for about 5 years prior to the investigation. A well in a local farmhouse located to the north-east of the landfill was contaminated. The local geology comprises unconsolidated

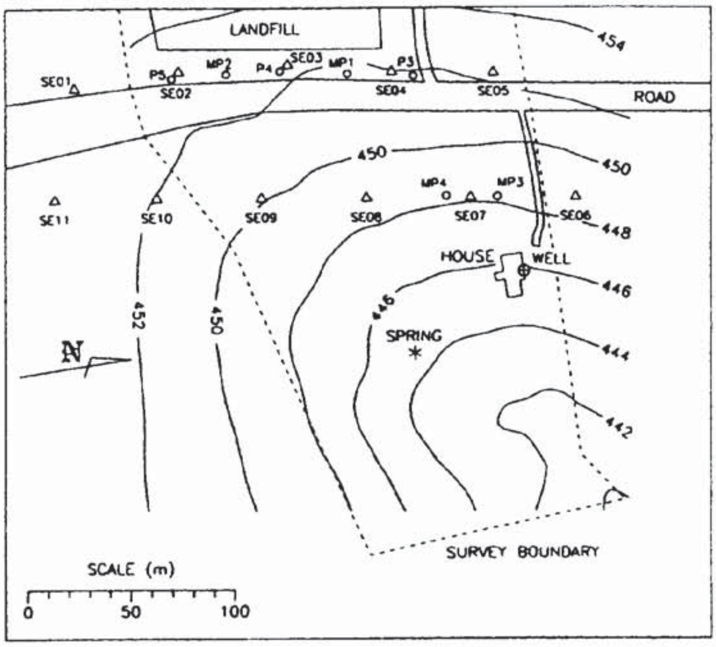

Figure 11.19 Location map of Novo Horizonte municipal landfill and adjacent farm and well. From Monier-Williams *et al.* (1990), by permission

Figure 11.20 (*opposite*) Schlumberger resistivity sounding interpretations and EM ground conductivity profiles, Novo Horizonte, Brazil. From Monier-Williams *et al.* (1990), by permission

Figure 11.21 (*opposite*) (A) Measured EM34-10H data, and (B) the same data topographically corrected, at Novo Horizonte, Brazil. From Monier-Williams *et al.* (1990), by permission

Cretaceous to argillaceous sediments which were thought to have been deposited in a fluvio-lacustrine environment. These sediments lie unconformably on basalts. From the local topography and information from a series of piezometers, the local groundwater gradient was found to be from the landfill towards the farmhouse. Uncontaminated groundwater in the area was known from other borehole information to have conductivities in the range 20–50 μS/cm. Resistivity depth-soundings were also undertaken in the area (at locations depicted by triangles in Figure 11.19).

The results of these soundings and of the EM conductivity surveys along the same lines are shown in Figure 11.20A and B. From these it is clear that, below the soil layer and away from the contamination, high resistivities are found within clay-free sands. A clay horizon is found on each section below an elevation of 432 m. Contamination results in resistivities of less than 40 Ω m in the upper sand, increasing to 200–250 Ω m at the sand–clay interface. The apparent conductivity highs evident on the two EM transects is entirely consistent with a conductive plume emanating from the landfill. Maps showing the observed and topographically corrected apparent conductivity values measured using the EM34-10H (displayed in units of decibels) are shown in Figure 11.21A and B, respectively. The topographically corrected data clearly reveal a more conductive element between the north-eastern corner of the landfill and the farmhouse.

Other examples of the use of ground conductivity meters in the investigation of groundwater contaminant plumes have been given by Monier-Williams *et al.* (1990), Cartwright and McComas (1968), Slaine and Greenhouse (1982), and by Greenhouse and Slaine (1983), among others.

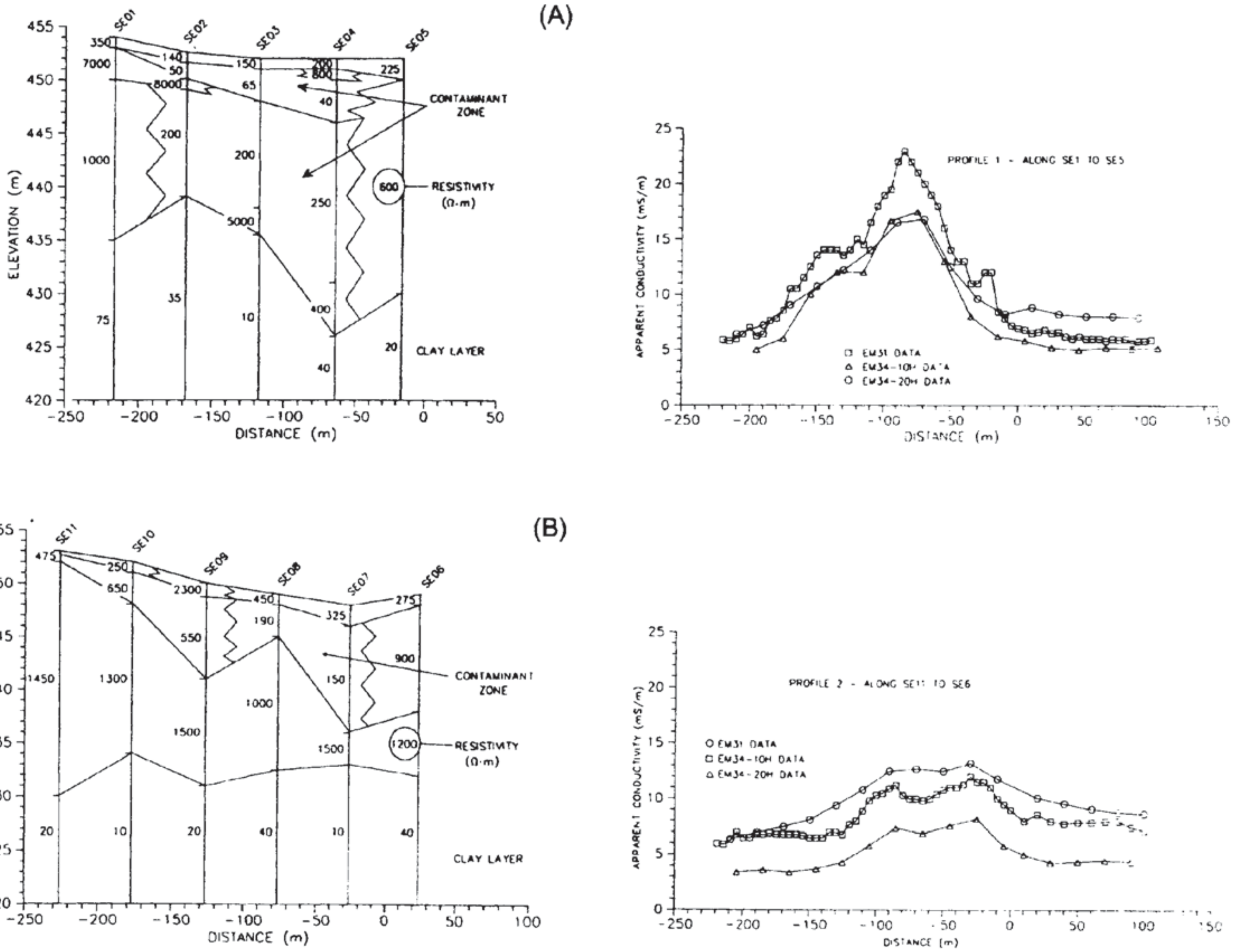

(Figure 11.20)

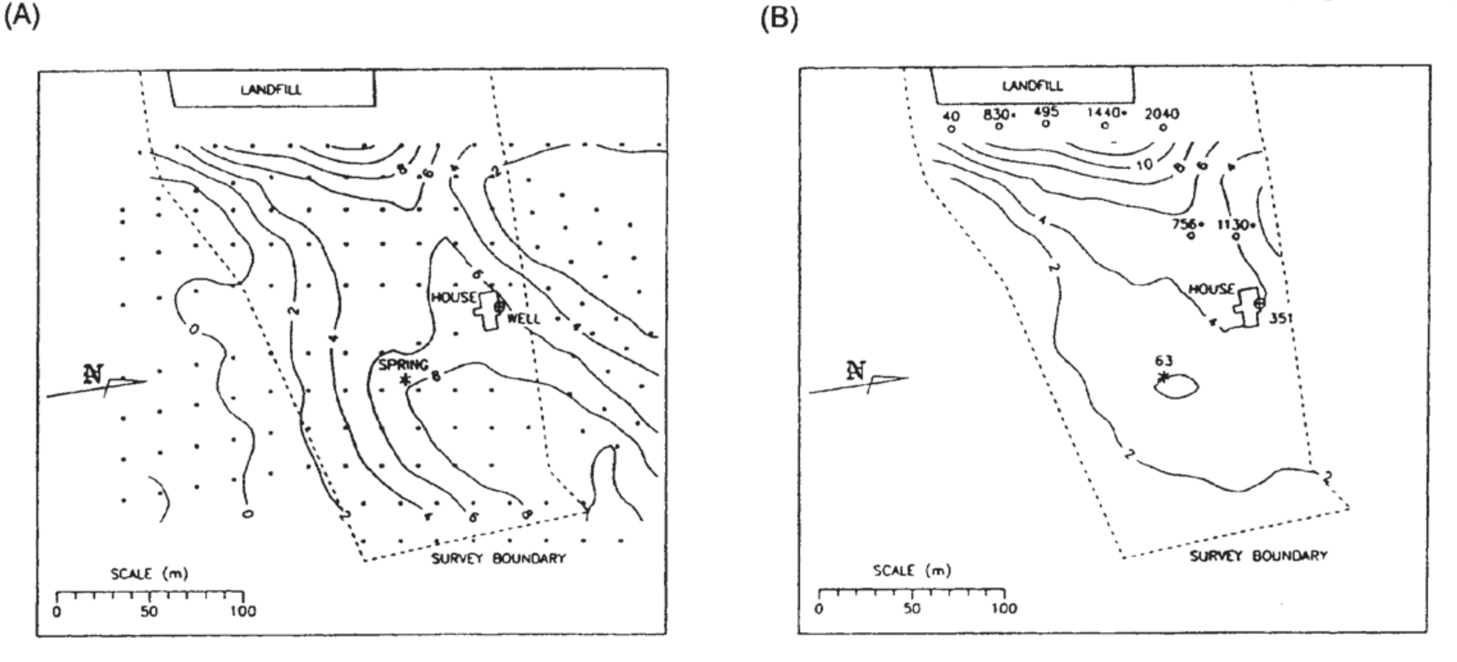

(Figure 11.21)

11.2.5.3 Detection of underground cavities

During a major investigation into the human biological history of the Near East, a Geonics EM31 ground conductivity meter was used as part of an archaeological study at Bab edh-Dhra in Jordan (Frohlich and Lancaster 1986). The aim of the work was to locate and indicate the condition of shafts and tomb chambers. An example of an apparent conductivity profile over what was later found to be a shaft and two burial chambers is shown in Figure 11.22. Where a chamber was silted up, a slightly higher apparent conductivity was observed relative to a background value; where a chamber was intact (air-filled), a low apparent conductivity was observed. By mapping the excavation site with the EM31, various anomalous zones were identified. Of seven examined by direct excavation, all were found to be infilled tomb shafts about 1.5 m wide and about 2 m deep.

Where cavities are large relative to their depth, and there is good electrical contrast between the cavity and the host material, then such a feature should be readily detectable. However, small cavities with low contrasts in conductivity buried at depth are unlikely to be resolvable.

11.2.5.4 Location of frozen ground

In areas affected by extensive permafrost, it is of significant engineering importance to be able to differentiate between frozen and unfrozen ground. In the Arctic, the location of ice-bonded permafrost is vital when planning major projects such as pipelines. Ground frozen

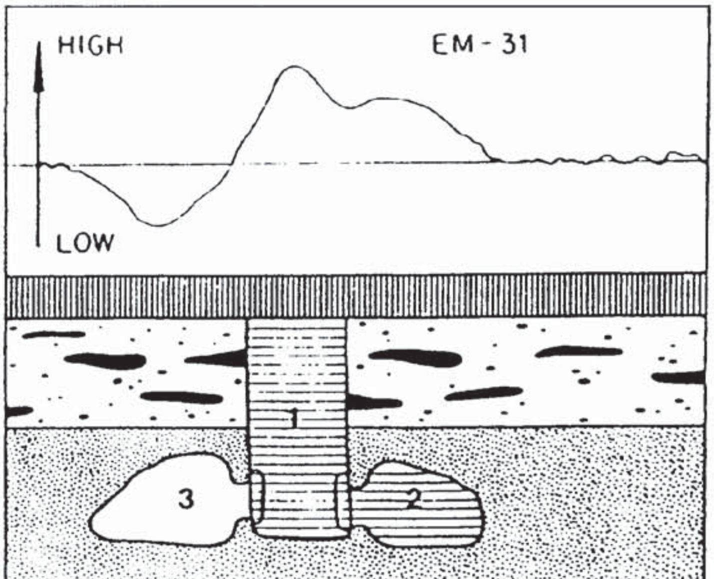

Figure 11.22 An apparent conductivity profile over a shaft tomb at Bab edh-Dhra. The shaft (1) which leads down to the surrounding burial chambers (2 and 3) gives rise to an apparent conductivity high; the silted chamber (2) and the air-filled chamber (3) are associated with intermediate and low apparent conductivities, respectively. From Frohlich and Lancaster (1986), by permission

solid restricts the use of resistivity surveys because of the difficulty in implanting electrodes. Consequently, non-contacting inductive methods are very practical alternatives. This has been demonstrated in the first two case histories. While seismic reflection can be used in overwater surveys, EM dual-coil profiling can be much more rapid in covering the ground. An example of this is given in the third case history. A review of the use of geophysical methods in the investigation of permafrost has been given by Scott *et al.* (1990).

The first case demonstrates the use of a Geonics EM31 in providing a very rapid method of mapping the extent of frozen and unfrozen ground in the Mackenzie River Delta, Northwest Territories (Todd *et al.* 1991). A 5 km traverse was undertaken across the ice of a small channel in the Delta, over frozen tundra and across lake ice over Big Lake. The apparent conductivity profile obtained is shown in Figure 11.23. Apparent conductivity values were found to be around 1.5 mS/m over solidly frozen ground but over 10 mS/m over unfrozen sediments and water. The lateral extents of the frozen/unfrozen portions at and near the surface correlate exactly with the marked changes in the values of the measured apparent conductivity. An example of the use of an EM31 to locate massive ice within frozen silt

Figure 11.23 Apparent conductivity profiles obtained with a Geonics EM 31 ground conductivity meter over part of the Mackenzie Delta, Canada, showing areas affected by permafrost. From Todd *et al.* (1991), by permission

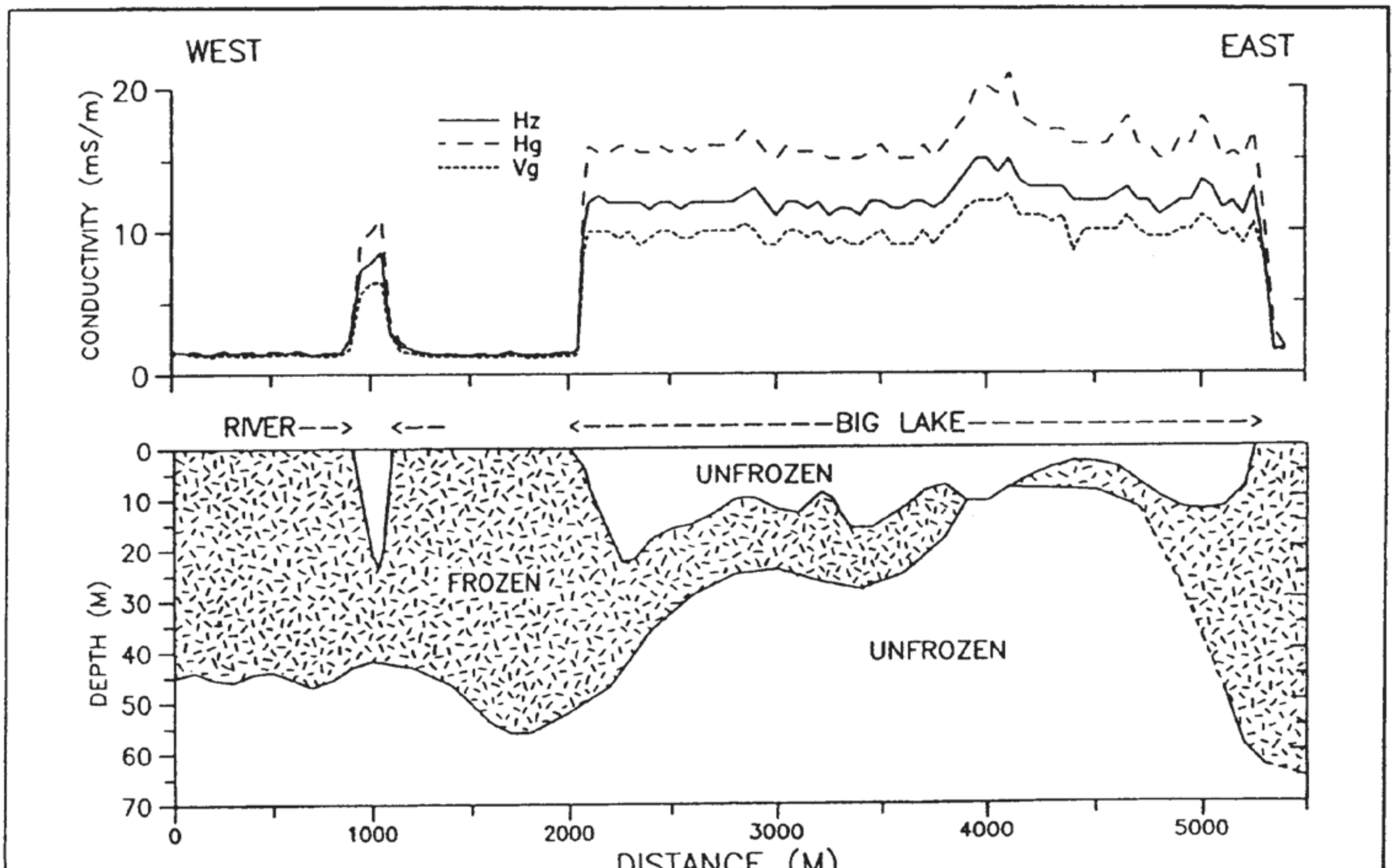

is shown in Figure 7.44 in Chapter 7 in a comparison with electrical resistivity profiling. Massive ice has a lower conductivity than frozen soil and so gives rise to readily identifiable zones along a transect.

The second example, provided by Sinha and Stephens (1983), describes an EM ground conductivity survey over a drained lake at Illisarvik, Northwest Territories. Both an EM31 and an EM34 (with all three coil separations) were used over a 300 × 600 m grid at 25 m centres. The apparent conductivity data from both vertical and horizontal magnetic dipoles for all three coil separations were contoured to give six apparent conductivity maps. Examples of the maps of EM31 and EM34(40) VMD data are shown in Figure 11.24. It is clear that there is an apparent conductivity anomaly centred around (25 mW, 100 mS). This relates in part to a residual pond of water at the surface. Note, however, that the centre of the conductivity anomaly on the 40 m dataset is at (25 mE, 75 mS). This is thought to be related to a zone of partially frozen sediments within the lake bed which have been gradually freezing up after the artificial draining of the lake three years before the geophysical survey was undertaken. Sinha and Stephens undertook some simple modelling of the conductivity data and estimated that the frozen layer was between 11 and 23 m thick in the central part of the former lake area but thicker towards the former shorelines. The draining of the lake has permitted the gradual freezing of the sub-lake sediments.

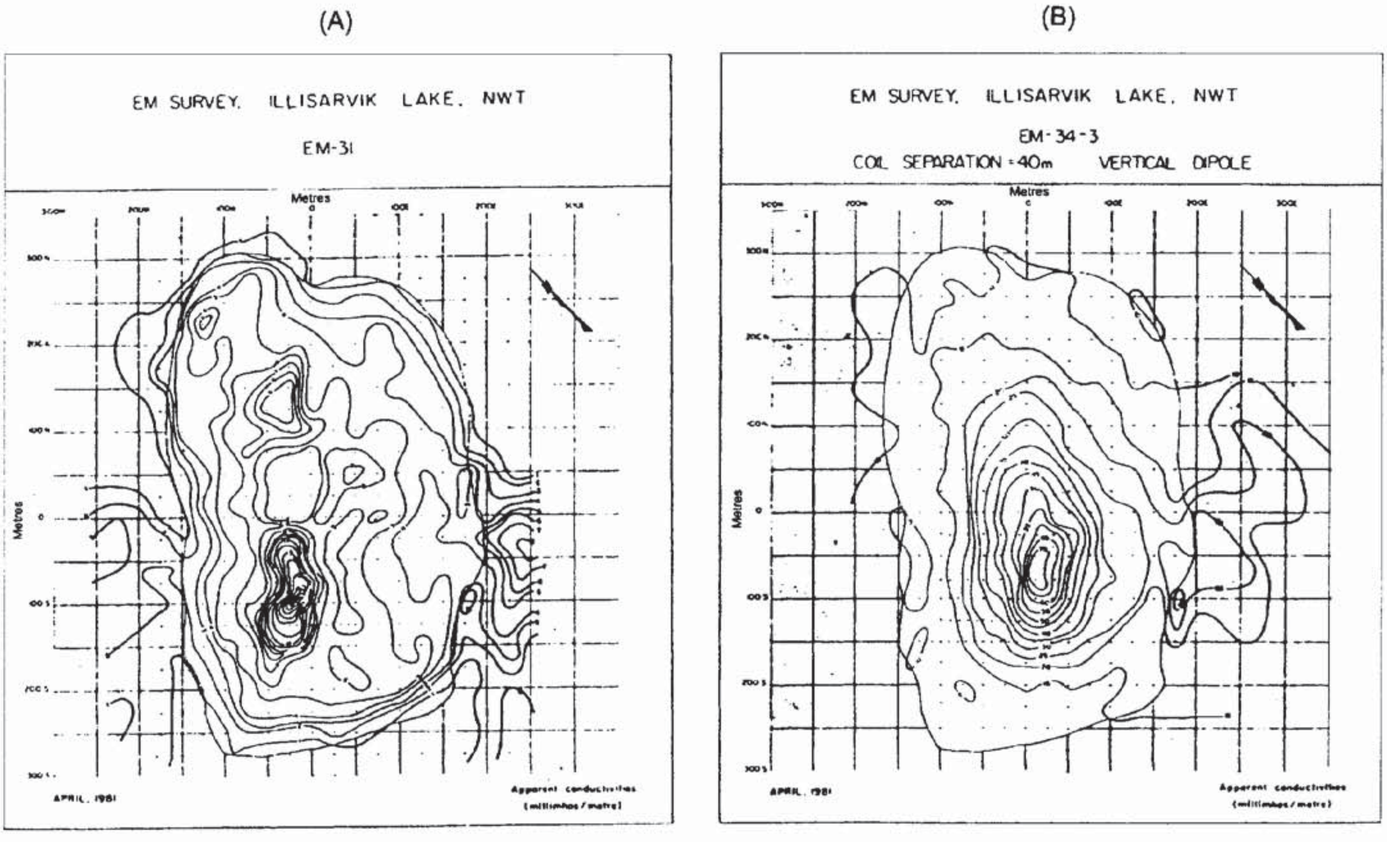

Figure 11.24 Maps of apparent conductivity at Illisarvik, Northwest Territories, Canada, obtained with (A) an EM 31 and (B) an EM 34-3 with a 40 m inter-coil separation. From Sinha and Stephans (1983), by permission

In areas where lake or sea ice is present to provide a safe working platform, ground EM measurements can be made over seawater to determine sub-bottom geological information. An example of where this approach has been taken is in a case history described by Palacky and Stephens (1992). Field experiments using horizontal loop EM (HLEM) were undertaken by the Geological Survey of Canada over sea ice on the Beaufort Shelf. Between 60 and 80 soundings were achieved in a day. To compare results, seismic refraction and reflection measurements were also made along with a number of drillholes. The ice and water layers are readily defined in terms of thickness and conductivity. Sea ice is resistive (5000 Ω m) in contrast to seawater and seawater-saturated sediments (1 Ω m); sub-bottom ice-bonded permafrost is also resistive (5000 Ω m) whereas unfrozen sediments were found to have an average resistivity of 2 Ω m.

An example of one profile is given in Figure 11.25. The seawater and seawater-saturated sediments have not been differentiated as there is insufficient contrast in resistivities for this to be possible. Depths to the top of ice-bonded permafrost are indicated by circled crosses. Seismic reflection data were only of limited use in this area because of shallow accumulations of gas within the near-surface sediments producing acoustic blanking. At one location a drillhole was constructed through 10 m of water to 75 m below seabed. The top 10 m of sediments were found to be water-saturated sandy clays. Ice-bonded permafrost was identified in fine to medium sands between 10 and 36 m below the seabed and was underlain by silty clays and a sandy unit. The borehole was logged using seismic, gamma-ray and EM probes. The borehole EM probe was a Geonics EM39 with two coaxial coils 0.5 m apart.

Figure 11.25 Conductivity section of a 5 km profile over the Beaufort Shelf, Northwest Territories, Canada, obtained using an Apex MaxMin I horizontal loop EM (HLEM) system. Encircled crosses indicate depths interpreted from seismic refraction surveys to the top of the permafrost layer; triangles indicate seismic refraction surveys where no permafrost was found. From Palacky and Stephens (1992), by permission

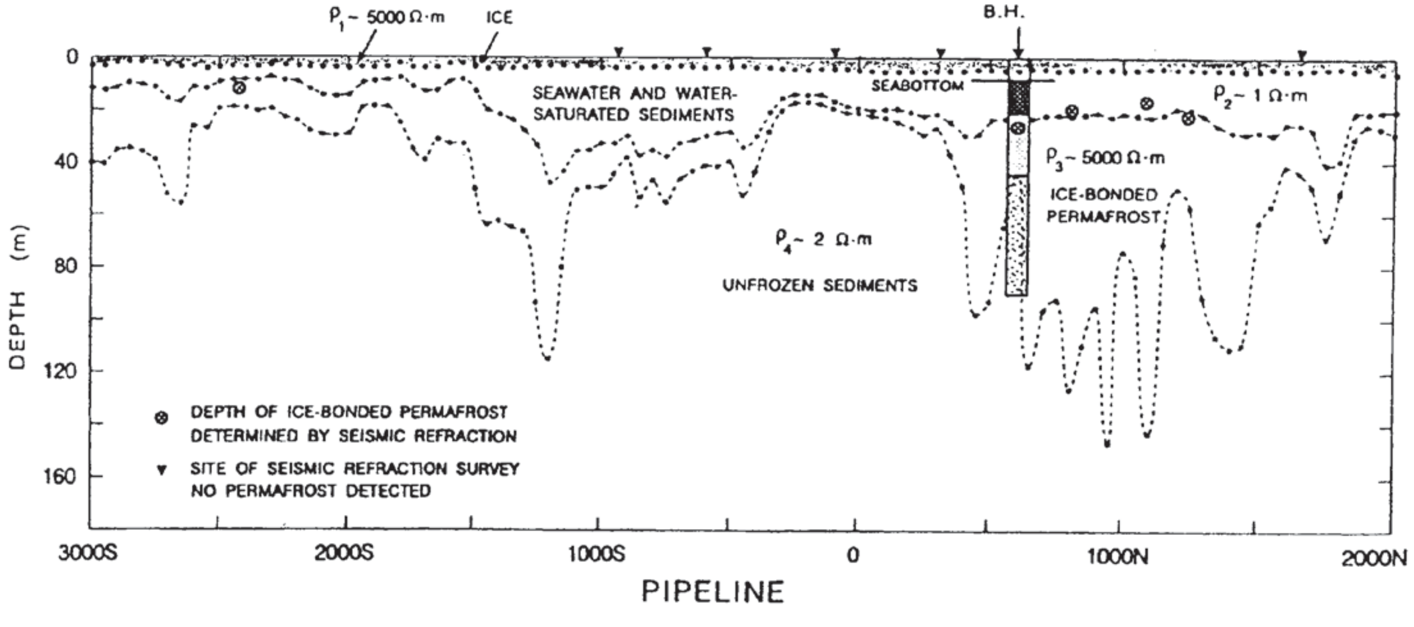

The HLEM interpretation is compared to the results of the EM logging and borehole lithostratigraphy in Figure 11.26 (A to C) respectively. Within the sub-permafrost horizon, the low conductivity values are associated with the sand-rich units while the conductivity highs are associated with silty clay horizons. It is clear that the HLEM interpretation and the drillhole results correlate very well, with all three showing the base of the permafrost horizon to be at a depth of 36 m below the seabed. The seismic refraction depths to the top of the permafrost horizon were in reasonable agreement with the interpretation of the HLEM data. This case history provides an excellent example of the efficacy of the EM method and the reliability of its results over this type of geological environment. From a practical point of view, the HLEM proved to be more rapid and easier to deploy in the extreme cold (down to $-30°C$), although battery power at such low temperatures is always problematic.

11.2.5.5 Contaminated-land mapping

Dual-coil EM mapping provides a rapid means of surveying possibly heavily contaminated sites in a cost-effective and environmentally benign manner. As a trial survey, British Rail Research commissioned a combined EM and magnetometer survey over a trial 50 × 50 m area

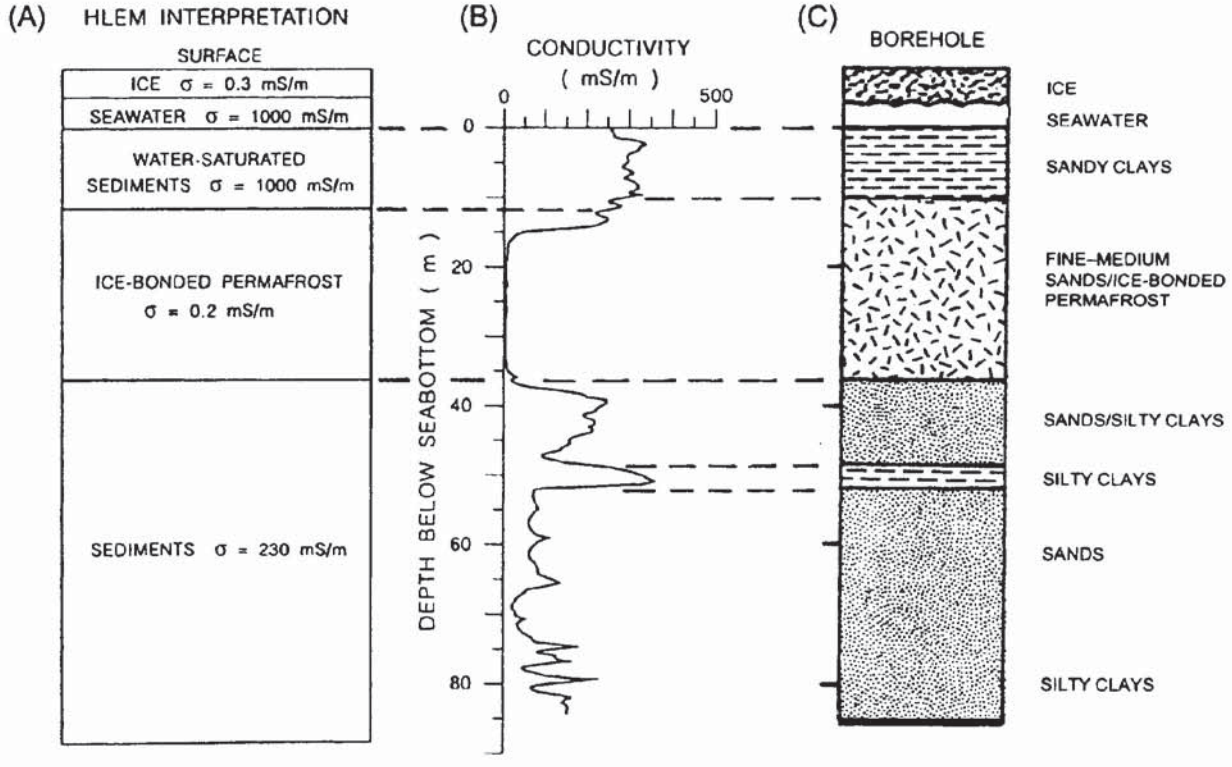

Figure 11.26 (A) HLEM unconstrained conductivity model of the borehole shown in Figure 11.25. (B) Conductivity profile obtained by logging the borehole with Geonics EM 39 dual-coil probes. (C) Composite lithostratigraphic results of the drilling. After Palacky and Stephens (1992), by permission

at a former railway welding yard at Dinsdale, Teeside, UK (Reynolds 1994). It was known that part of the yard had previously been the site of an old iron foundry but the only plans of the works were unreliable. Geophysical methods were deployed to demonstrate what they could find and, in particular, to locate evidence of the iron foundry. The ground was featureless apart from the obvious lines where the railway tracks had once been, but was covered all over in railway ballast made of crushed limestone and dolerite. The two material types were laid in defined lines.

An EM31 was deployed on a 1 × 1 m and 2 × 1 m grid over the area, and both the quadrature and in-phase components were recorded. In addition, the Earth's magnetic field intensity was measured at two different heights above the ground and the difference between the two computed as a vertical gradient. Isometric projections of the apparent conductivity, in-phase component and magnetic gradient are shown in Figure 11.28A–C, respectively. On each, there is clearly an effect due to a major overhead metallic gantry used for moving welded railway track around. It is clear that, in addition to the effects of the gantry, different anomalies are present on each display. For example, in Figure 11.27A (conductivity), six conductive zones were found (lettered A to F). However, only anomaly A appears on the in-phase data, suggesting that the feature causing it is both conductive and metallic (as the in-phase component is particularly sensitive to metallic objects). The other anomalies (B–F) are not evident, suggesting that their cause is due to sub-surface conductive material but which is not metallic. This interpretation is consistent with the results of the magnetic gradiometer survey (Figure 11.27C) on which anomaly A is again clearly evident.

Direct excavation of each of these zones revealed anomaly A to be a series of I-shaped steel girders within reinforced concrete buried at a depth of 1 m. The anomaly width was 12 m and the concrete foundations (with sub-slab void!) was 11 m wide and was contained within the extent of the anomaly. Furthermore, where anomaly A passes into anomaly D, it was found that the concrete foundations stopped and vitrified sulphurous slag was present. Sulphur had leached out from the slag to form yellow crystals on the surface of the slag and presumably giving rise to the elevated conductivities. Anomalies E and F were also found to be due to vitrified but broken-up pieces of sulphurous slag. Anomalies B and C were found to be buried tips of fine ash.

The linear anomalies evident on all three datasets relate to the surface ballast material. The orientation of the anomalies is exactly parallel to the lines of the former railway tracks. One linear feature (L1) was found to correlate with a cable duct which terminated in a metal box evident at the ground surface. On the conductivity data, the effect of this duct diminishes in amplitude towards the metal box. This effect is thought to be due to the increased depth of burial of the

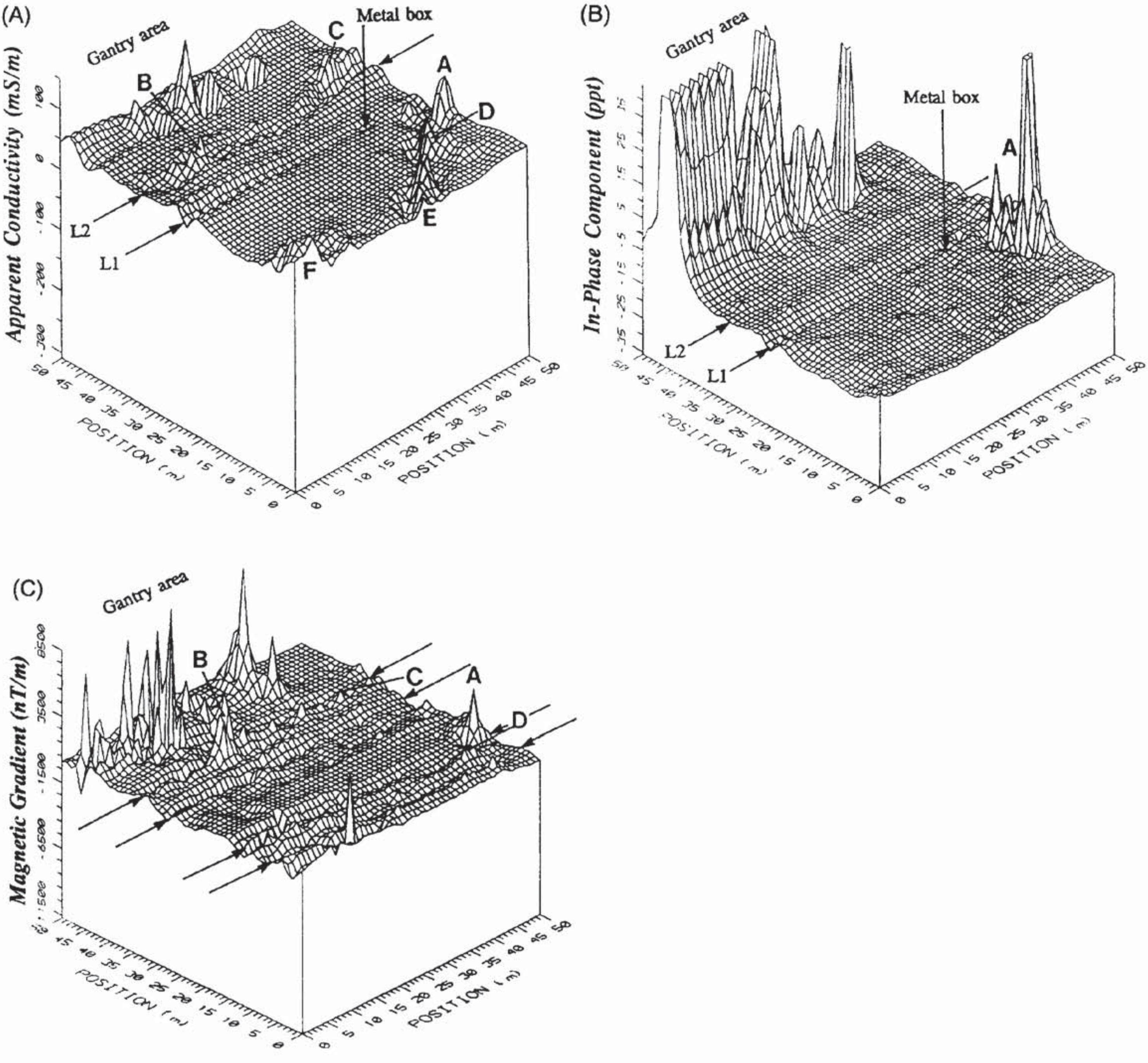

Figure 11.27 Isometric projections of (A) apparent conductivity and (B) in-phase component, both measured using a Geonics EM 31, and (C) vertical magnetic gradient, at a former railway welding yard at Dinsdale, Teeside, UK. Courtesy of British Rail Research (Reynolds, 1994)

ducting below the ballast towards the box. No evidence of the ducting, on either the ground or within the three datasets, was found between the box and the location of anomaly A. In Figure 11.27A, it can be seen that there is no conductivity anomaly over this zone either. Despite the site being so potentially noisy, and with railway ballast covering the area, the EM and magnetic surveys demonstrated that they could be used not only to locate anomalous material within the sub-surface, but to differentiate between material types.

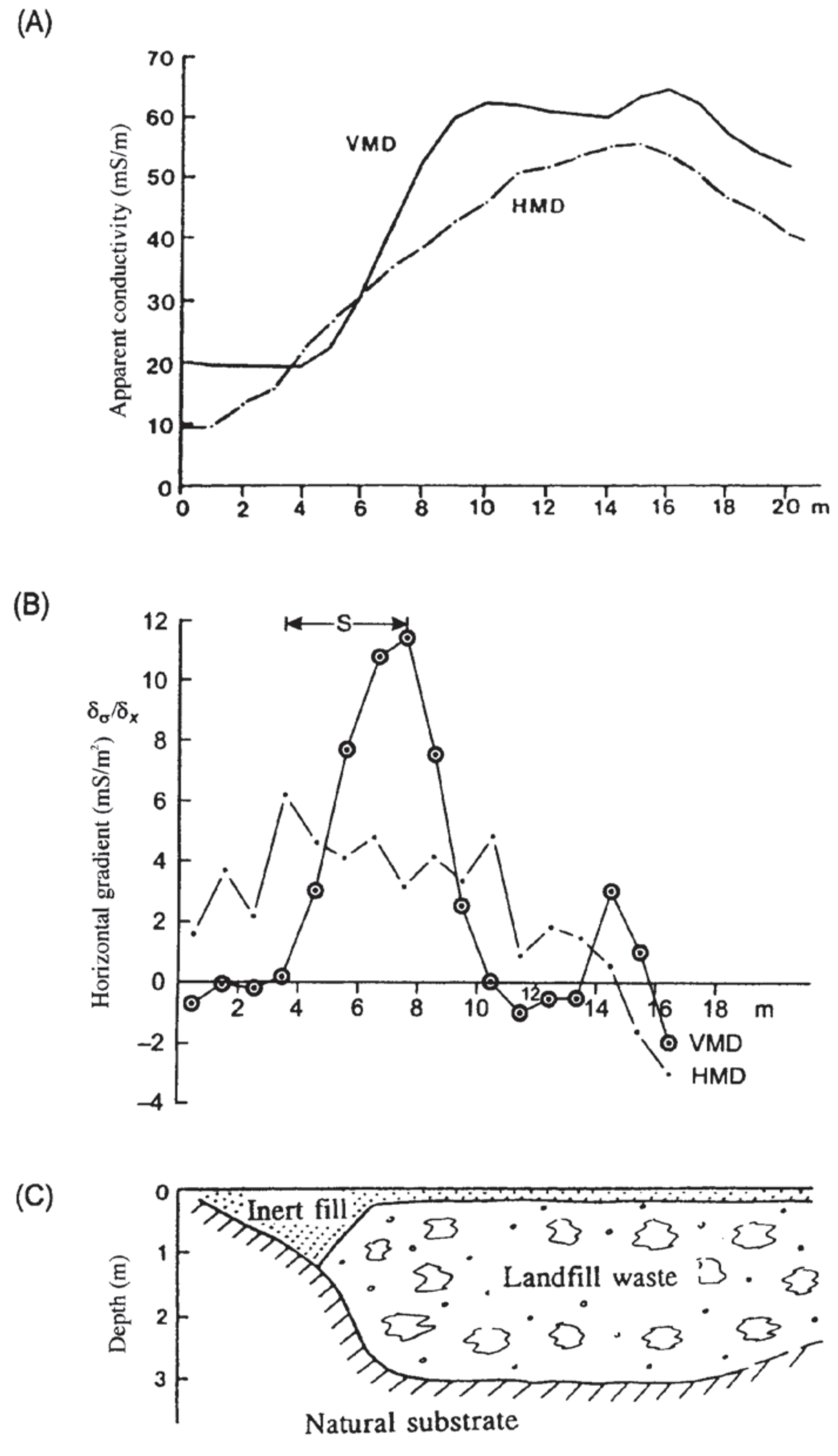

Figure 11.28 (A) EM 31 apparent conductivity profiles with both vertical and horizontal magnetic dipoles (VMD and HMD, respectively) over the edge of a shallow landfill in North Wales. (B) Schematic section of a trenched excavation. (C) Horizontal apparent conductivity gradients for the data in (A). After Reynolds and McCann (1992), by permission

11.2.5.6 Landfill investigations

Not only have FEM methods been used to detect contaminant plumes arising from landfills, they have also been used successfully at three stages in the life of a landfill. These stages are (a) site appraisal prior to the development of the waste facility; (b) investigation of the base of the site during excavation and construction; and, most commonly, (c) over closed landfills.

It is pertinent to consider the factors that need to be taken into account when contemplating undertaking a geophysical survey over any landfill site, at whatever its stage of development. These factors are listed in Table 11.1 (from Reynolds and McCann 1992). The types of waste material, the nature of the base and lining materials, the style of cover, etc., all affect the deployment of geophysical methods. Of particular interest to waste regulatory authorities and those responsible for closed landfill sites, are the location of the edges of the waste material, the depth of waste present, and any information concerning leachate. Three case histories are provided here, one to illustrate a simple method of determining the edge of a landfill, the second to show how EM methods have been used in leachate studies, and the third to demonstrate how ground conductivity meters can be used to provide a wide range of information about the type of fill material.

Of importance to those responsible for old closed landfills is a knowledge of the boundary of the waste. This is often required in relation to building new properties which are not allowed in the UK to be within 250 m of the edge of a waste site for fear of gas and leachate migration. The other problem is that the responsible authority very often has many hundreds of sites within its jurisdiction but insufficient money to investigate them all. What is required is a simple, cost-effective method that can be deployed without interfering with the site in any way.

To detect the edge of a landfill, a Geonics EM31 has been demonstrated to be a useful tool (Reynolds and McCann 1992). A former North Wales landfill containing domestic waste up to 12 m thick and capped with about 1 m of inert soil was investigated using a variety of geophysical methods. The site was about 150 m long by 80 m wide. Trenches through the edges of the landfill had been constructed previously as part of a remediation programme and these provided corroborative evidence against which to check the geophysical interpretation. Short (< 25 m) EM31 profiles were undertaken over the landfill site at right-angles to the perimeter hedge. Both vertical and horizontal dipoles were used but only the quadrature (conductivity) component was measured.

One such profile is shown in Figure 11.28A, with the corresponding trench information (Figure 11.28B). It is clear that the apparent conductivity values increase sharply across the landfill boundary. It is also noticeable that the shallower penetrating EM31H has a less rapid change compared with the data obtained using the vertical dipole. This reflects the slanted edge of the landfill. The EM31H responds to the gradually increasing thickness of the inert fill before finally responding to the refuse itself. The EM31V, however, responds more to the deeper material which changes more abruptly from inert

Table 11.1 Potential unknowns for any landfill (Reynolds and McCann 1992)

- *Type of void space*:
  - Hard-rock quarry
  - Sand/gravel quarry
  - Brickearth quarry
  - Shallow valley
  - Estuarine creek
  - Engineered site
  - Previous industrial site
- *Type of lining*:
  - None
  - Mineral linear (compacted clay)
  - Artificial linear (e.g. HDPE geomembrane)
  - Combination linear (e.g. mineral + geomembrane, double membrane, etc.)
- *Type of capping*:
  - None (natural venting)
  - Clay
  - Artificial (e.g. HDPE geomembrane)
- *Site dimensions*:
  - Areal size
  - Depth
  - Shape, particularly of margins
- *Tipping history*:
  - Types and mixtures of wastes
  - Duration of tipping (likely volumes)
  - Style and degree of compaction and cover during tipping operations
  - Age
- *Geological factors*:
  - Type(s) of substrate
  - Local hydrogeology
  - Sub-site faulting
  - Previous resource activity at or beneath site (e.g. coal mining, quarrying, etc.)
  - Sub-site natural cavities
  - Site (slope) stability
- *Factors related to infill material*:
  - Degree of saturation
  - Gas generation
  - Internal temperature and variability
  - Liquor/leachate generation
  - Mobility and conductivity of lechate
  - Compaction density and variability
  - Material composition (e.g. inert builder's rubble, putrescible material, industrial refuse, etc.)

to refuse material. In order to highlight the effect, the horizontal gradient of each component has also been computed (Figure 11.28C). This demonstrates that the edge of the landfill as defined by the EM31H results lies outside that determined by the EM31V. This is clearly consistent with the observations within the trench.

By carrying out a series of short EM31 transects at right-angles to the site boundary, and using the criteria described above, the edge of this landfill site was determined accurately (to within 1–2 m) using a survey which took one person about one day to execute. The results could be interpreted on site and the landfill boundary marked with reasonable confidence. The approach taken here is very similar to that demonstrated by Zalasiewicz *et al.* (1985) for the interpretation of EM31 data in mapping geological boundaries at shallow depth.

A major problem with many landfills is the formation of leachate. As long as the liquor remains on site and is treated it poses no significant problems. However, should leachate begin to migrate away from a site it may cause potential contamination of local potable water supplies. A further difficulty is in the treatment of wastes from some coal workings. Oxidation of pyrite associated with coal and coal-bearing strata causes increased acidity of minewater which also typically contains high concentrations of iron, sulphates and trace metals, especially manganese and aluminium. Ladwig (1983) has described several case histories associated with acid mine drainage (AMD). One of these examples relates to an abandoned strip mine in Butler County, Pennsylvania. The 8-hectare site was thought to have been mined in the 1950s but detailed records were no longer available.

In 1981, the mine was reclaimed and a lake previously filling the mine was drained and the void space backfilled with mine spoil and regraded. Up to 7 m of soil was placed over the high-wall of the mine grading down to less than 2 m in the central and eastern parts of the site. A limestone-lined sub-surface drain was built along the base of the high-wall to take away seepage. Following completion of the reclamation, discharge from the sub-surface drain had been slightly acidic (acidity 20 mg/litre with iron 18 mg/L and sulphate 200 mg/L). Furthermore, an intermittent seep of acid water had occurred on the south-eastern side of the site.

Over a 1.6-hectare part of the site near to where the seep was observed, a series of EM ground conductivity profiles was undertaken using a Geonics EM34 with a 10 m coil separation and 10 m station interval. The field survey took $1\frac{1}{2}$ days. The resulting map of apparent conductivity values is shown in Figure 11.29. The closely spaced contours (14–24 mS/m) to the west and east of the site correspond to the edges of the mine. The rapid increase in apparent conductivity observed over these areas is indicative of passing from resistive bedrock into conductive regarded spoil. The apparent conductivity

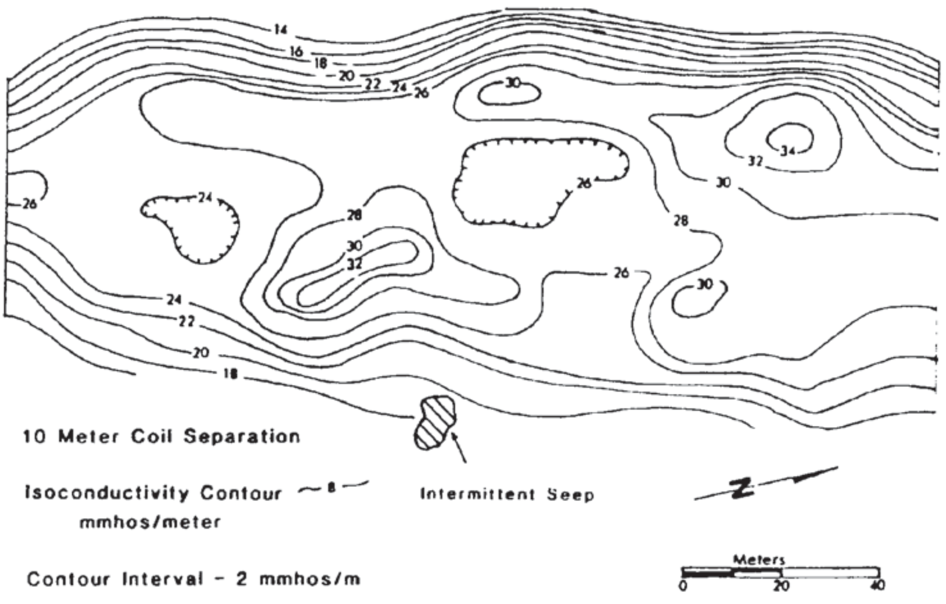

Figure 11.29 Apparent conductivity map over a backfilled former strip mine, Butler County, Pennsylvania, USA. From Ladwig (1983), by permission

highs (30 and 34 mS/m) in the north-west part of the site are associated with the sub-surface drain. The distribution of apparent conductivities (apart from the features already described) is related to the infiltration of conductive acid minewater moving downgradient towards the lower eastern part of the site and ponding within the spoil. This is thought to be the cause of the conductivity high of 32 mS/m in the southern part of the site. Further migration of contaminated groundwater is restricted by the presence of the low-wall of the mine and what is interpreted to be a more-resistive bedrock ridge of unmined material separating the southern conductivity anomalous zone from a smaller one to the north. The location of the intermittent seep occurs downslope of the main conductivity anomaly, giving credence to the ponded groundwater model. A summary of the interpretation of the EM survey is shown in Figure 11.30. As a consequence of this survey, the physical model was used as a basis for siting injection and observation wells installed as part of a remediation test using AMD inhibiting agents.

While the station interval (10 m) chosen was quite coarse, it provided sufficient spatial detail to meet the objective of the survey. However, if the edges of the mine were to have been mapped, a closer station interval would have been necessary. In this case, the mine high-wall could possibly have been located to better than ±2 m. Given the speed of the EM survey, it demonstrates how much useful information can be obtained in such a short time.

The third example is of a combined EM31 and EM34 survey over a site near Manchester at which a landfill facility was being constructed. The objective of the survey was to determine and map the

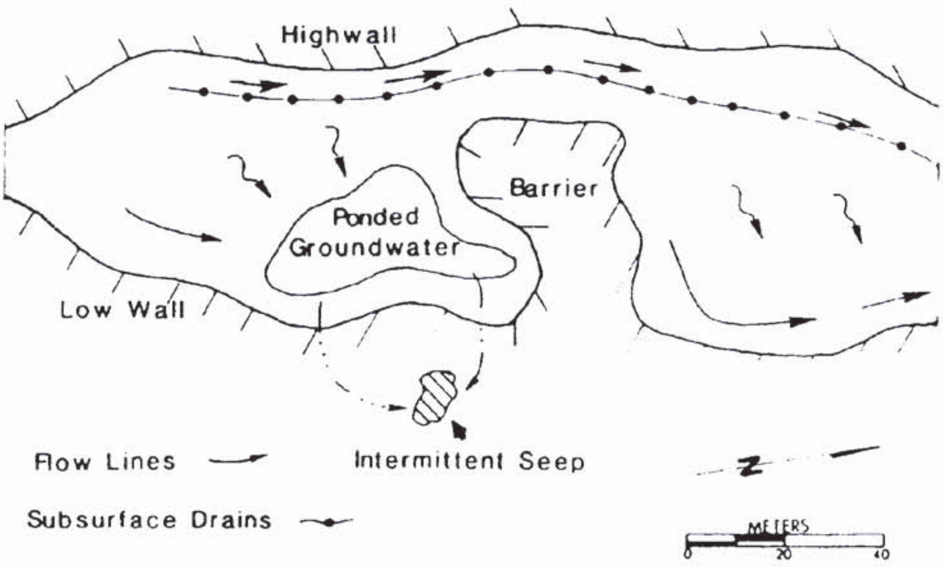

Figure 11.30 Schematic of the interpretation of the EM data shown in Figure 11.29. From Ladwig (1983), by permission

thickness of the boulder clay underlying the site, because a requirement for the site licence was a certain thickness of boulder clay to act as an impermeable mineral liner. The survey was undertaken over a series of parallel traverses using both magnetic dipole orientations and 10 and 20 m coil separations with the EM34. The resulting six values of apparent conductivity per station were entered into EMIX34PLUS (Interpex Ltd) to produce two-dimensional interpreted cross-sections through the site. The general stratigraphic sequence was boulder clay over a saturated fine sand over bedrock. There was a reasonable conductivity contrast between the various layers which were delimited on the interpreted models. One such profile (reproduced courtesy of RUST Environmental) is shown in Figure 11.31.

Borehole information available at the edge of the site was used to constrain the EM models. The interpreted thicknesses along each survey line were correlated between adjacent lines and an isopachyte map of clay thickness and a map of the elevation of the base of the clay layer were produced. As the landfill design required that a certain void volume be available to accommodate waste for the site to be commercially viable, a knowledge of the thickness of the clay and the elevation of its base were essential. As a consequence of the EM survey, various cell walls within the landfill were relocated. The geophysical survey provided the site operator with information of sufficient quality and reliability that he was able to modify his landfill design and construction appropriately, thereby avoiding potential problems later had the clay liner been too thin.

These three case histories are but a small representation of what ground conductivity meters can be used for. It is worth reiterating, however, that in all cases, careful survey design is essential if the

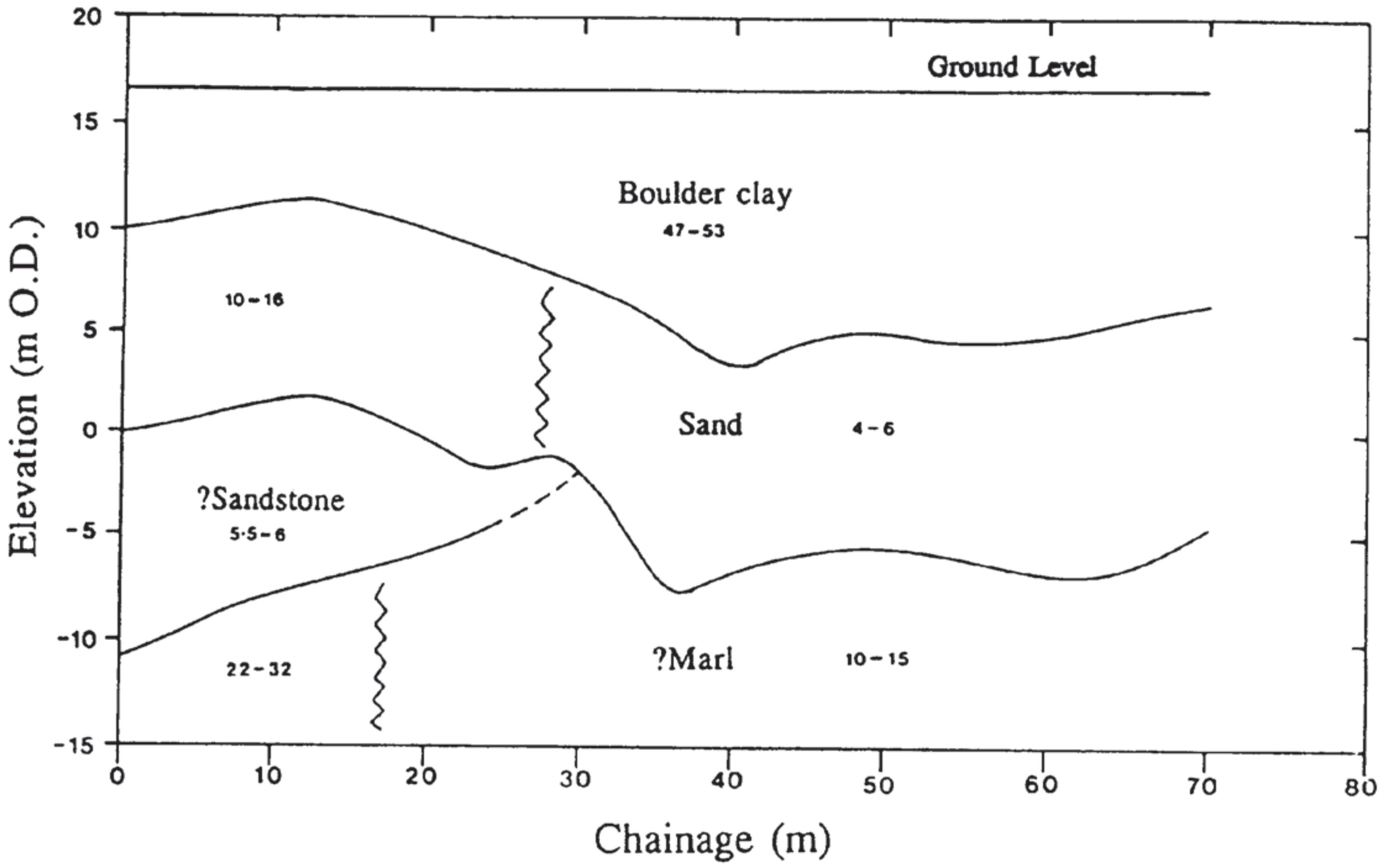

Figure 11.31 Pseudo-geological cross-section derived from electromagnetic ground conductivity data derived from an EM 31/34 survey over a base of a landfill being engineered with a natural clay liner. Values cited for geological materials are true conductivities in units of mS/m. From Raynolds and McCann (1992), by permission

objectives of a survey are to be met. In addition, while isoconductivity maps can provide excellent qualitative spatial information about a site, detailed quantitative analysis using specialist software can give highly reliable two-dimensional models. When used as part of a grid of survey lines, the models along each line can be correlated between lines to produce a pseudo-three-dimensional model of the subsurface, under the right conditions. There are situations where no satisfactory model can be computed which then suggests that there may be three-dimensional targets present within the ground. This in itself is useful information. For example, when modelling some EM data over an old colliery in the north-east of England, consistent layered models were successfully produced over much of the site. However, along one line, the data became erratic over a very short distance and no satisfactory models were producible. This effect was thought to be due to the presence of pillar and stall mine workings at shallow depth (<10 m). When the location of the anomalous zone was drilled, soft ground indicative of partially collapsed mine workings was found, thus confirming the inference derived from the modelling.

11.3 PULSE-TRANSIENT EM (TEM) OR TIME-DOMAIN EM (TDEM) SYSTEMS

11.3.1 TDEM/TEM surveys

In a typical TDEM survey, a large direct current is passed through a large ungrounded loop transmitter to energise it. After a discrete period of time (a few tens of milliseconds), during which any effects due to switching the current on would have died away (known as 'turn-on transients'), the applied current is interrupted abruptly. If a conductor is present within the vicinity, the sharp change in the primary field will induce eddy currents within the conductor, initially at its surface only. This is known as the 'early-time' stage of the transient process. These surface currents then start dissipating through ohmic losses. The zone immediately within the conductor then experiences a decreasing magnetic field with a consequential flow of eddy currents through it. Effectively, this is the start of the inward diffusion of the current pattern caused by the eddy currents towards the interior of the conductor. This is the 'intermediate-time' stage of the transient process. The final or 'late-time' stage of this process is reached when the induced current distribution is invariant with time. The only change observed is a decrease in the overall amplitude with time. If the conductor present is very large relative to the dipole source being used, the eddy currents may spread out laterally as well as diffuse into the interior of the conductor. The rate of change of these currents and of their respective magnetic field depends on the size and shape of the conductor and on its conductivity. In contrast, the initial distribution of surface current is dependent only on the size and shape of the conductor as this is a geometrical phenomenon, not one due to the conductivity of the body. The whole process of the step-wise excitation of the current loop is repeated many times (Figure 11.32) and the data stacked for a given location. A detailed description of TEM prospecting methods has been given by Nabighian and Macnae (1991) which has been used as the basis for this section.

The transient electric field reaches a maximum at a distance known as the diffusion depth (d), which is to TEM what the skin depth δ is to frequency-domain EM (see Box 11.4). In the time domain the diffusion depth is directly proportional to $\sqrt{t}$, whereas in the frequency domain it is inversely proportional to $\sqrt{\omega}$ (where $\omega = 2\pi f$). This local maximum propagates downwards with a finite velocity (v).

In the case of a semi-infinite half-space, i.e. uniform horizontally layered media, the 'early-stage' surface currents are located primarily in the vicinity of the transmitter loop. With the passage of time, diffusion occurs by the downward and outward spreading of the induced current loop, much like the downward movement of a system of smoke rings (Figure 11.33), with a consequential decay of the

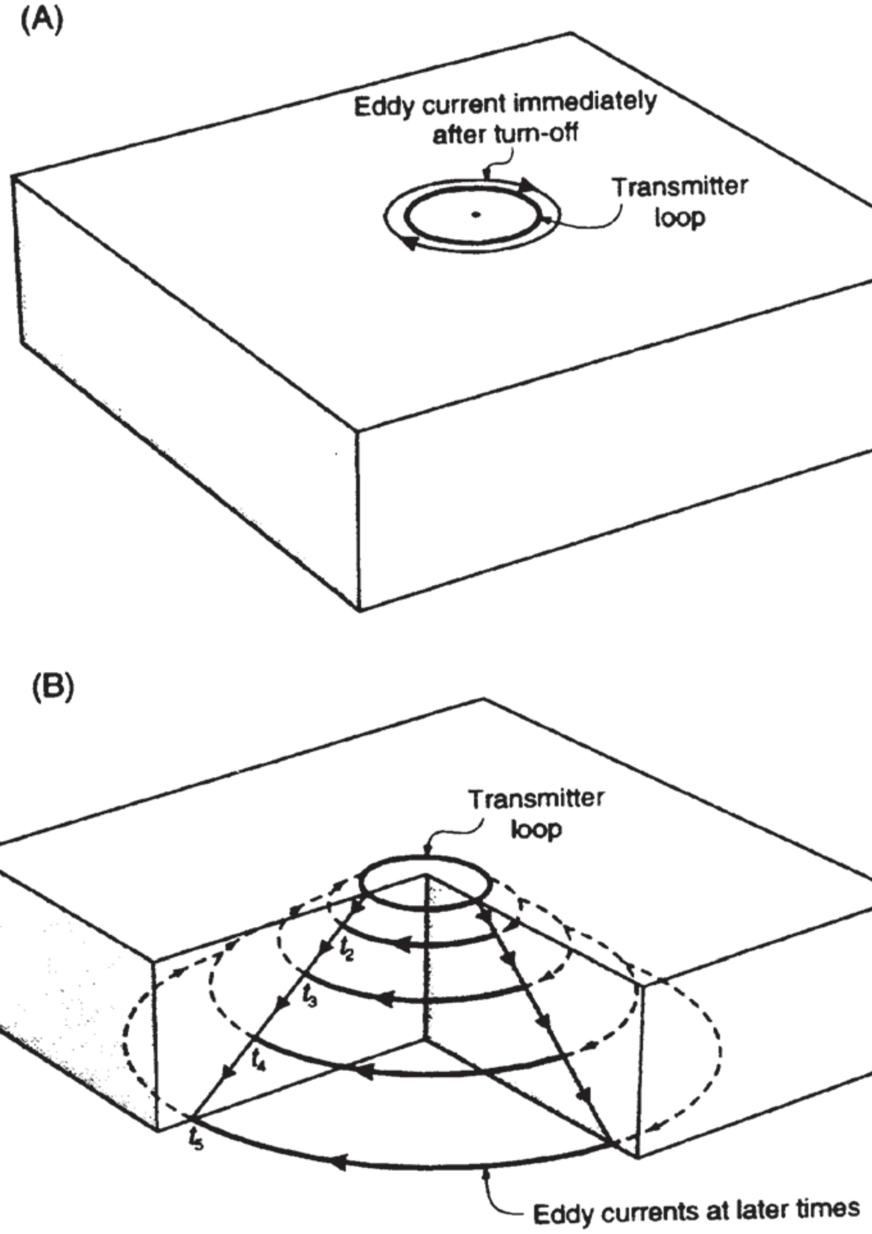

Figure 11.32 (A) The form of an eddy current immediately after turn-off of the primary field. (B) Downward and outward propagation of the eddy current filament at successive intervals of time ($t_2, \cdots$) over homogeneous ground, rather like smoke rings

amplitude with time. The same principle applies in the case of a horizontally layered earth. Normally, the ground materials are assumed to be non-polarisable and conductivity is taken to be independent of frequency or delay time. These induced polarisation effects affect the reliability of interpretation.

Where materials within the ground have slight variations in magnetic permeability, typically of the order of 1% of the Earth's magnetic field intensity (e.g. 550 nT in a field of 55 000 nT), small TEM effects may be detectable. The TEM response is likely to be enhanced by about 1% in such cases. Where lateritic soils are present, super-paramagnetic effects may cause anomalous transient recordings with the SIROTEM system. It manifests as a $1/t$ dependence which results

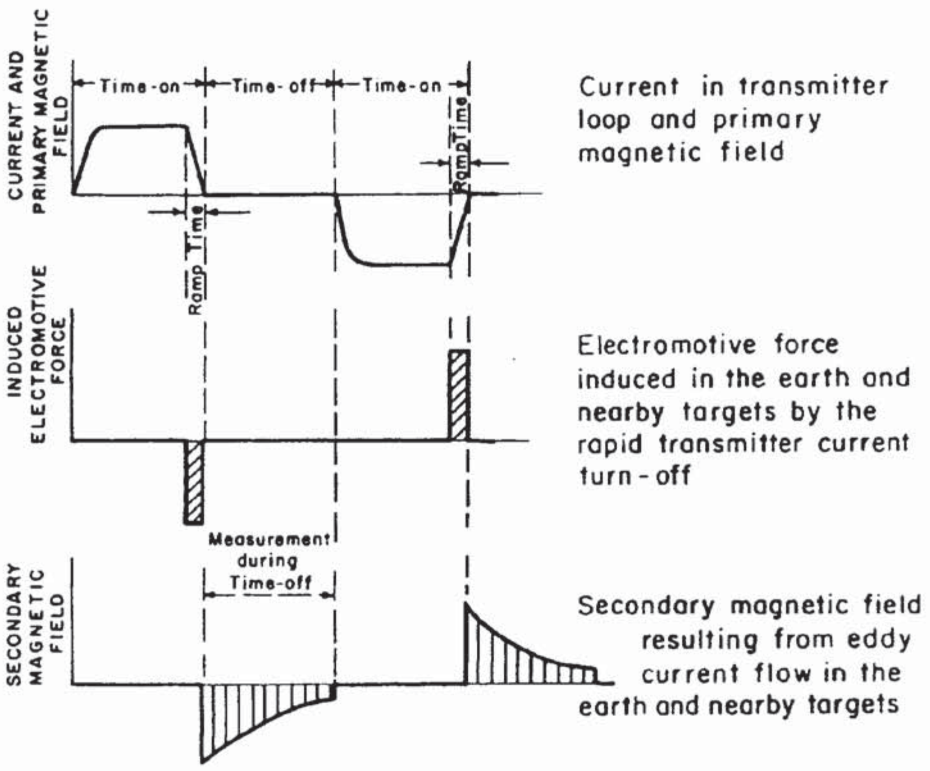

Figure 11.33 Time-domain EM waveforms. From McNeill (1990), by permission

Box 11.4 Diffusion depth (*d*) and velocity (*v*)

In a uniform conducting medium, the transient electric field achieves a maximum at the diffusion depth (*d*) such that:

$$z = (2t/\sigma\mu)^{1/2} = d$$

where σ and μ are the conductivity and the magnetic permeability of the medium. The maximum travels downwards with a velocity (v) such that:

$$v = (2\sigma\mu t)^{-1/2}.$$

In a conducting half-space, the downward velocity is given by:

$$v = 2(\pi\sigma\mu t)^{-1/2}.$$

in erroneous determinations of apparent resistivity with time. Similar effects are also likely to occur where either the conductivity or the magnetic permeability of the ground varies as a function of frequency. Removal of superparamagnetic effects can be achieved by displacing the receiving loop by 2–3 m relative to the transmitting loop where deployed in a coincident loop configuration.

There are three principal sources of error in TEM measurements: (a) geometric errors in transmitter–receiver positions and topographic effects; (b) static cultural noise; and (c) dynamic cultural noise.

Most TEM methods are largely insensitive to geometrical errors and, in the case of a resistive ground, are also relatively insensitive to topographic effects. However, where a conductive overburden is present, topography can produce severe coupling errors and deliberate procedures need to be followed to correct for such effects (Nabighian and Macnae 1991).

Static cultural noise arises from the presence of pipes and cables, metal fences or other utilities present in the survey area. Some metallic utilities serve as current channellers which can cause distortions in the TEM data. Live electric cables have distinctive effects at particular frequencies and their harmonics, but these can be readily removed by notch filtering. The effect of channelling can be reduced by laying the transmitter loop symmetrically over the utility.

Dynamic cultural noise is caused by a number of sources. At frequencies less than 1 Hz, the source is geomagnetic signals from within and above the Earth's ionosphere. At frequencies above 1 Hz, typically in the 6–10 Hz range, signals generated by distant lightning discharges produce sferics which are natural EM transients. Higher frequency sources of noise are AC power lines (50–60 Hz) and VLF transmitters (10–25 kHz). Of particular importance in airborne EM and in surveys undertaken in wide open spaces is wind noise which causes motion of magnetic field sensors within the Earth's magnetic field. The fields used in TEM work are typically five orders of magnitude smaller than the Earth's magnetic field.

11.3.2 Data processing and interpretation of TEM surveys

There are many ways in which TEM data can be processed and these are largely dependent upon which instrument system is used to acquire the original data. Most TEM systems record the transient voltage at a number of discrete intervals during the voltage decay after the applied current is switched off. Each time the current is applied and then stopped, measurements are taken; when the current is applied again and switched off, a repeat set of measurements is taken. This process may be repeated many tens of times at a given location with all the data being logged automatically. Consequently, these many data can be processed to improve the signal-to-noise ratio. At the same time, the field data are checked for repeatability. Commonly, the data are normalised with respect to the transmitter current or other system parameter, and the effects of the time decay may be amplified in compensation by normalising the observed field at each point with the respective primary field value at the same point.

As the field measuring systems become more sophisticated and the amount of data increases, more careful thought needs to be given to the often quite involved data processing sequences now available. For example, Stephan *et al.* (1991) describe a data processing sequence for 'long offset transient EM' (LOTEM) sounding undertaken in Germany. Three data processing stages were formulated: (a) prestack processing; (b) selective stacking; and (c) post-stack processing. Prestack processing was used to remove unwanted periodic noise using filtering such as a notch filter to remove noise associated with AC power lines and the German electric railway grid. A selective stacking algorithm was applied to average only a percentage of the data around the median of the individual time samples. The consequence of this was to reduce the noise content, thereby improving the signal-to-noise ratio. The final stage was to apply a slight time-variable smoothing filter. The culmination of this processing was the production of logarithmic plots of apparent resistivity as a function of decay time.

A variety of plots of processed data can be produced, such as transient decay (logarithmic) plots of voltage (in mV) versus decay time (in milliseconds); response profiles (graphs of measured voltage at a selected decay time at all stations in a survey area); response contours (the response profile data plotted in map form); apparent resistivity plots, either as profiles or maps; and vector plots, display components of the data in different orthogonal planes (*xz* or *yz* planes).

Interpretation methods are as varied as the different types of data plots and systems used to acquire the data. Typically, the interpretation is undertaken in two stages. The first is to locate a possible sub-surface target on the basis of the shape, size and location of anomalies evident on profiles and maps of relevant parameters. The second, more quantitative, stage is to determine the 'quality' of the conductor using time constants determined from decay plots of the field intensity at one or more locations.

Various types of display parameter are useful for different applications. For example, apparent resistivity soundings can be extremely useful in hydrogeological investigations and in geological mapping but provide very little information appropriate for mineral exploration. In the latter application, time-decay rates are more valuable as the curves produced can be characteristic of specific types of conductor. For example, the decay curve of an isolated conductor in a resistive medium shows a rapid decrease in amplitude in the 'early-time' stage but this changes to a straight-line segment at late delay times. The gradient of this straight-line segment is used to derive a characteristic time constant (τ) when plotted logarithmically. These time constants are indicative of different types of causative bodies; examples of time constants for four target types are listed in Table 11.2. An analytical approach to the calculation of time constants is given in Box 11.5. For mineral exploration, time constants in the range 0.5–20 ms are of particular interest. Pyrrhotitic bodies often have very

Table 11.2 Time constants for four common target types

Conductor type	Time constant τ
Sphere of radius a	$\sigma\mu a^2/\pi^2$
Cylinder of radius a	$1.71\,\sigma\mu a^2/\pi^2$
2-D conducting plate of finite depth extent (l)	$2t\sigma\mu l/\pi^2$
Thin prism of thickness t and average dimesion L	$\sigma\mu Lt/10$

Box 11.5 Analytical approach to the calculation of time constants

The general expression for a time constant τ of a conducting target is given by (Nabighian and Macnae 1990):

$$\tau = K\sigma\mu A$$

where K is a numerical coefficient and A is proportional to the effective cross-sectional area of the conductor (see Table 11.2).

The time constant of a conducting target can be obtained from the straight-line segment of a TEM decay graph plotted on semi-log axes. The cotangent of the slope angle (in degrees) gives directly the value of the conductor's time constant.

Analytically, given an initial amplitude A_0, then the decayed amplitude at a time t (A_t) is given by:

$$A_t = A_0 \exp(-t/\tau).$$

Taking the logarithm of both sides, this can be rewritten as:

$$\ln(A_t) = \ln(A_0) - t/\tau$$

which is the equation of a straight line with negative gradient of $1/\tau$.

If the amplitudes at two times t_1 and t_2 are measured, the expression for the time constant becomes:

$$\tau = (t_2 - t_1)/\ln(A_1/A_2).$$

large time constants (several tens of milliseconds). With the exception of nickel associations, such targets are often of little economic interest. However, time constants alone should not be used to attach either geological or economic significance to any particular target.

The sense and degree of dip can be gauged from the asymmetry in measured components when plotted as functions of lateral distance along survey traverse lines.

While computer modelling is being used increasingly in the interpretation of TEM data, classical inversion is notoriously difficult to apply to three-dimensional models. Software for such processing is largely still research-based and requires inordinately long computer execution times on mainframe computers. Consequently, such processing has yet to be applied routinely to commercial TEM projects when three-dimensional modelling is required.

However, for engineering and environmental applications, TEM-sounding interpretation is carried out routinely using personal computers; appropriate software is available commercially. Very detailed discussions of data processing and modern interpretational methods for a wide variety of EM systems have been given by Spies and Frischknecht (1991) and Nabighian and Macnae (1991), among others.

11.3.3 Applications and case histories

11.3.3.1 Groundwater investigations

Electromagnetic methods have long been used in hydrogeological investigations. Most commonly, frequency-domain systems have been used for shallow investigations and electrical resistivity depth-sounding for greater depth penetration. However, development during the 1980s of TEM systems with faster shutoff rates and earlier time sampling resulted in an increased use of TEM in hydrogeology. A theoretical approach has been described by Fitterman and Stewart (1986) which provides a range of hypothetical TEM responses for a range of commonly found hydrogeological problems. One advantage with TEM is that with the relatively small loop sizes available, measurements can be made on sites, such as public open space and sports fields, whose size may preclude the use of resistivity soundings, for example. Furthermore, in urban areas with high ambient dynamic electrical noise, the signal stacking capability of modern digital systems helps to improve the signal-to-noise ratio and recovery of the all-important signals from background noise.

TEM measurements have found increasing application in the mapping of saline–freshwater interfaces in coastal regions. A good case history describing such an application has been published by Mills *et al.* (1988) and Hoekstra and Blohm (1990). It describes the mapping of four overlapping aquifers shown schematically in Figure 11.34. These comprise a perched aquifer in which the groundwater has been heavily contaminated by fertilisers; a 60 m thick aquifer (known as the '180 ft') into which saltwater has intruded a significant distance inland; a 123 m thick aquifer (known as the '400 ft') into

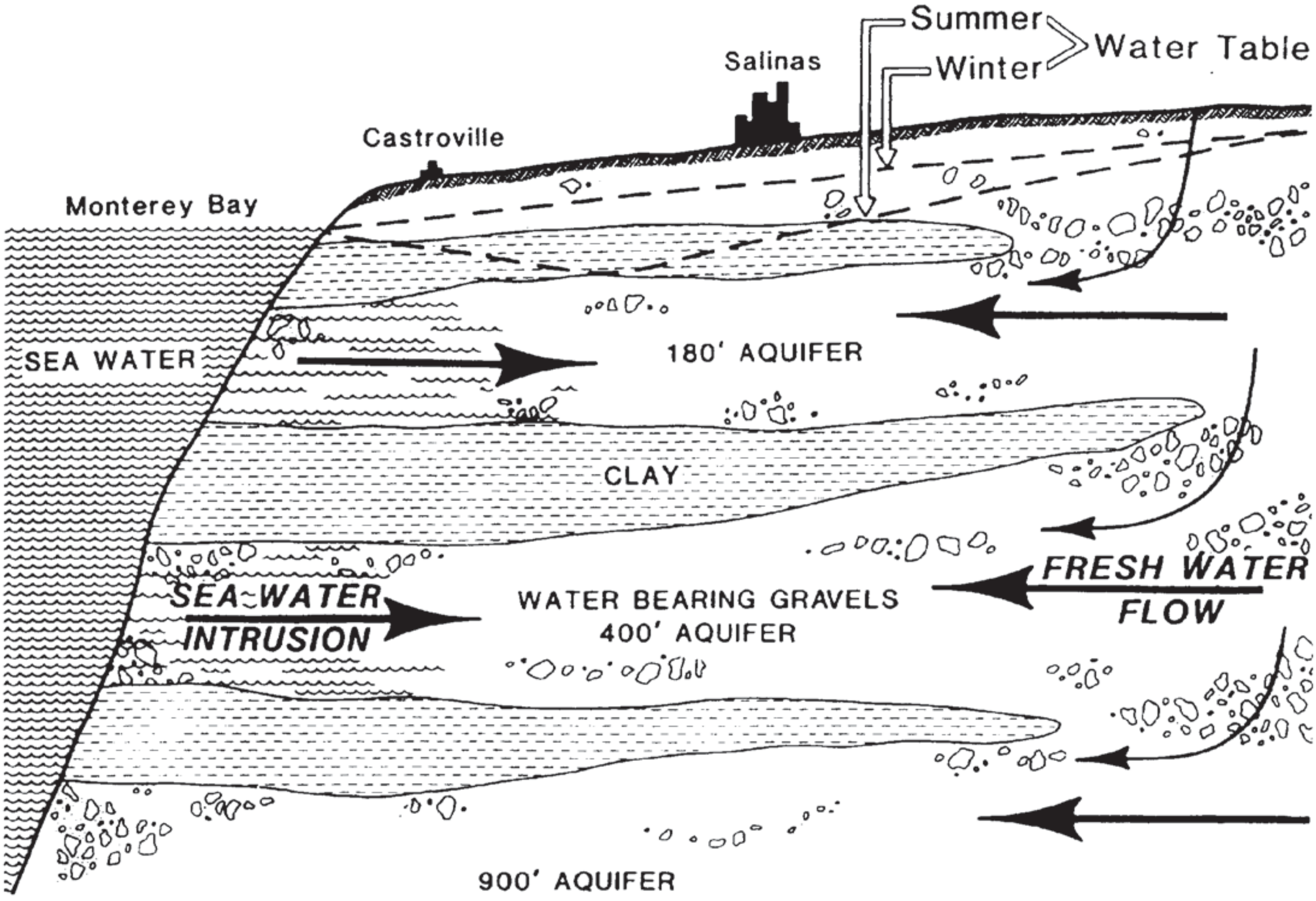

Figure 11.34 Schematic hydrogeological section in the Salinas Valley, California. From Hoekstra and Blohm (1990), by permission

which saltwater has penetrated less far; and the deepest ('900 ft') aquifer which was untainted by saltwater at the time of the surveys. The layer-cake sequence of contaminated aquifers provided a difficulty in penetrating through the upper, more extensive, saline intrusions to detect the lower ones. To this end, a TEM system employing 100 × 100 m transmitting loops was used to map the '180 ft' acquifer; for the deeper aquifers, a 200 × 200 m transmitter loop was used.

Four late-stage apparent resistivity sounding curves are shown in Figure 11.35, with the corresponding one-dimensional inversions. These soundings relate to the positions on the interpreted geoelectric section B–B′ shown in Figure 11.36. As an aid to interpretation, information from monitoring wells was used to constrain the number of layers used in the TDEM data inversion process. This information was also used to correlate derived true resistivities with equivalent chloride concentrations. It was found that a resistivity of approximately 8 Ω m correlated with a 500 ppm chloride concentration. Using this information, and the spatial information provided from the TDEM surveys, interpreted positions of the 500 ppm isochlor contours were plotted in map form for both the '180 ft' and '400 ft' aquifers and are shown in Figure 11.37. Also shown are the locations

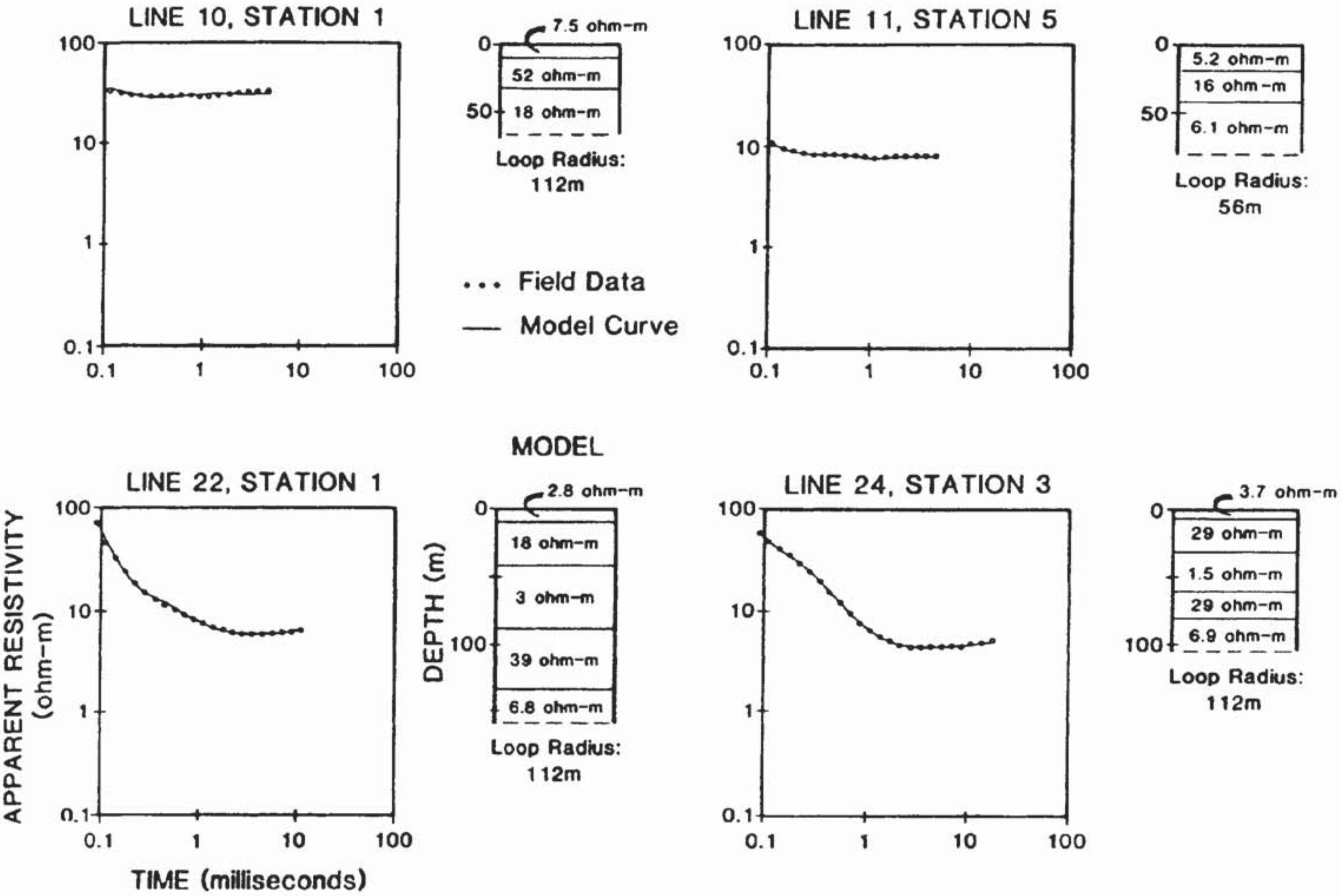

Figure 11.35 Four late-stage apparent resistivity curves and their corresponding one-dimensional inversions along section B–B′ (see Figure 11.36). From Hoekstra and Blohm (1990), by permission

of the 500 ppm isochlor contours derived from monitoring wells. The greater detail on the TDEM-derived contours is a consequence of the greater spatial sampling provided by the TDEM survey compared with that of the monitoring wells.

A very similar application has been described by Goldman *et al.* (1994) to map saline intrusion within the coastal strip immediately to the west of the Dead Sea in Israel. They carried out TDEM sounding using a Geonics PROTEM 37 with inversion and equivalence testing with TEMIXGL software (Interpex Ltd, USA). A feature of this example was the use of TDEM to image the transition zone between the fully saline intrusion and the freshwater above.

An example of the use of TDEM mapping in conjunction with resistivity, magnetic and gravity mapping in the Murray Basin, New South Wales, Australia, was given by Dodds and Ivic (1990). In addition to a Geonics EM34 (FEM) system, a SIROTEM time-domain system was used with 100 × 100 m loop transmitter with a multiturn receiver at its centre. Delay times used were in the range 0.4 ms to 52 ms. An example of the SIROTEM pseudosection along one traverse is shown in Figure 11.38, with the corresponding interpreted geoelectric section. The results of the inversion of four electri-

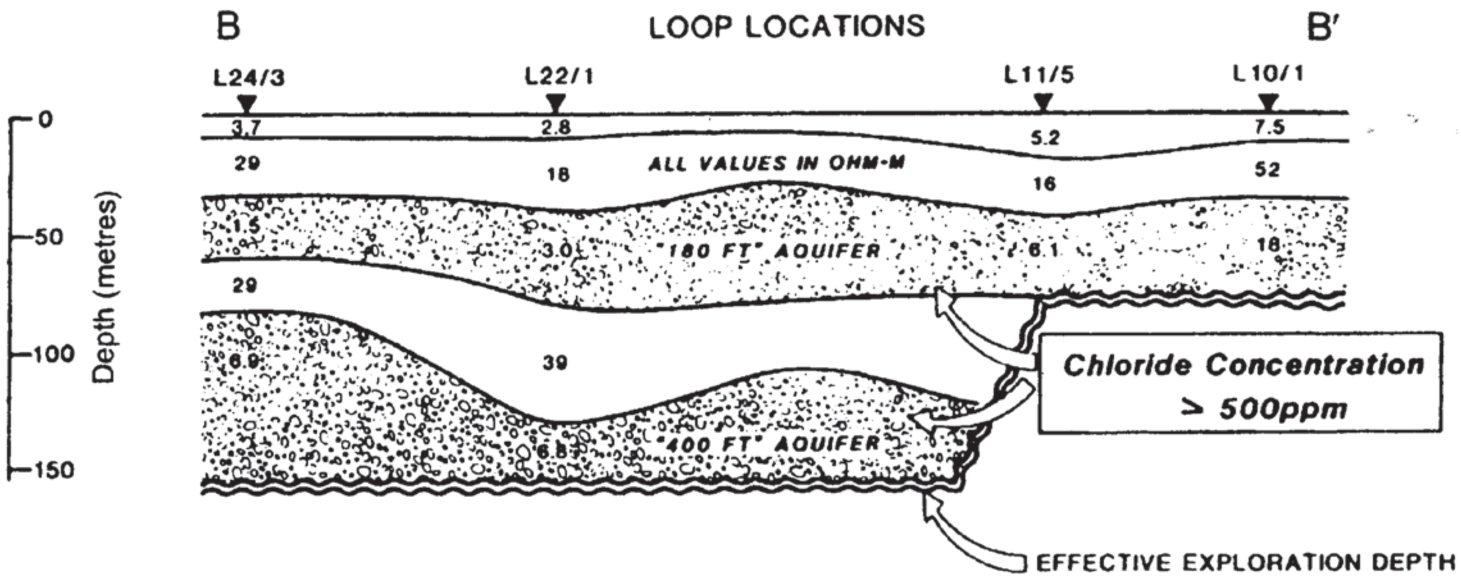

Figure 11.36 Interpreted geoelectric section B–B′ derived from TDEM soundings illustrated in Figure 11.35. From Hoekstra and Blohm (1990), by permission

cal resistivity depth-soundings are also shown on this figure for comparison. A zone (shaded in Figure 11.38B) with a true resistivity in the range 0.6–2.5 Ω m is interpreted as being due to saline groundwater. There is a clear zone where saline groundwater was not found and this zone was interpreted to be a basement high. This interpretation, which was also consistent with the results of the gravity and magnetic surveys, was subsequently proven by drilling. One aspect of this investigation is that the VES inversions were then used to fix the layer parameters for the top two layers in the TEM inversion routine. Examples of this are shown in Figure 11.39.

These case histories demonstrate the usefulness of TEM soundings and profiles constructed with closely spaced soundings in hydrogeology. With the right combination of transmitter sizes and closely spaced soundings, profiles can be produced with a high degree of vertical and lateral resolution. Such spatial sampling, and the

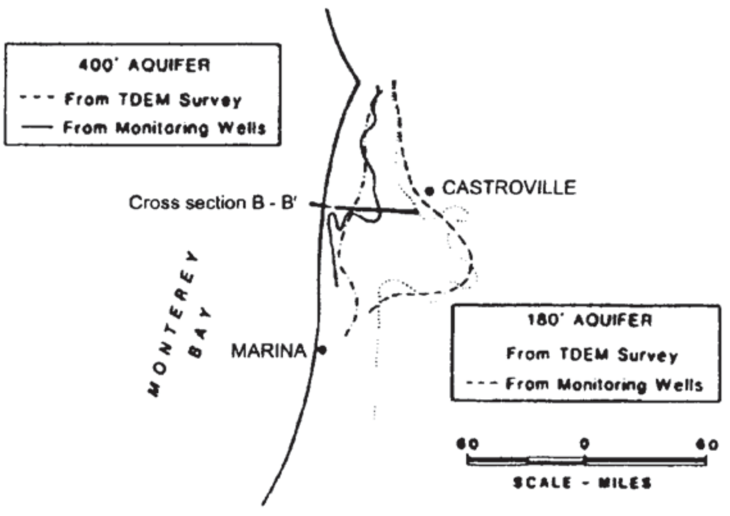

Figure 11.37 Comparison of the position of the 500 ppm isochlor within the '180 ft' and '400 ft' aquifers derived from monitoring wells and TDEM soundings. From Hoekstra and Blohm (1990), by permission

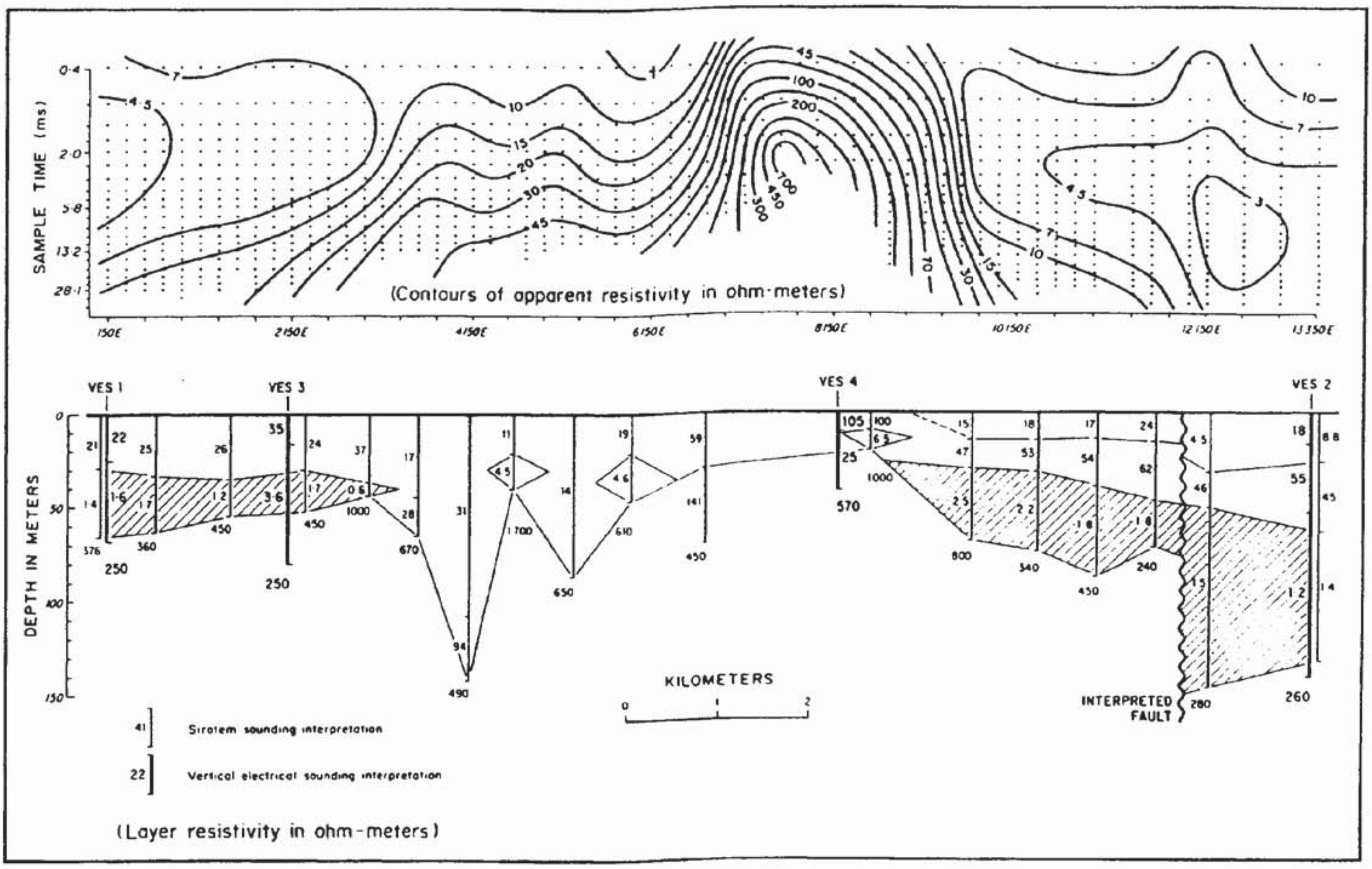

Figure 11.38 (A) SIROTEM apparent resistivity pseudosection in New South Wales, Australia, with (B) the corresponding geoelectric section. Saline groundwater (shaded zone) is evident each side of the bedrock high. From Dodds and Ivic (1990), by permission

increasing reliability of the inversion process, enables detailed two-dimensional geoelectric sections to be produced much more cost-effectively than could have been achieved with boreholes alone.

11.3.3.2 Contaminant plume mapping

Hoekstra *et al.* (1992) have provided a case history which demonstrates the benefit of a combined deployment of both FEM and TEM soundings. The survey was conducted in the vicinity of a brine lagoon in south-west Texas, USA. A Geonics EM34-20H FEM system was used to map variations in apparent conductivity around the brine pit. It is obvious from the resulting contour map (Figure 11.40) that elevated apparent conductivities are evident a considerable distance away from the brine pit. However, a single dipole configuration with a single inter-coil separation can provide only a qualitative impression of the distribution of this conductive contaminant plume. If both dipole orientations had been used with the 10 m and 40 m inter-coil separations, quantitative inversion would have been possible to determine the depth of the plume.

Instead of increased number of measurements with the EM34, TEM soundings were undertaken using a Geonics EM-37 with

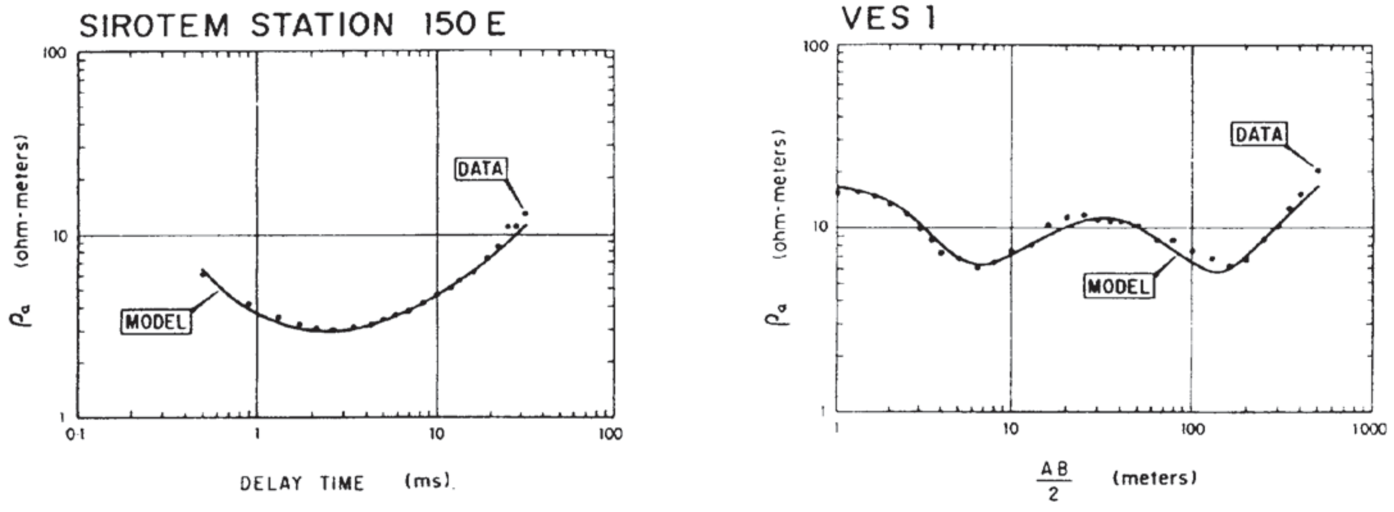

LAYER	THICKNESS (meters)	RESISTIVITY (ohm-meters)
1	1·5 *	17 *
2	3·0 *	3·1 *
3	24 **	21
4	36 **	1·4 **
5		380

* Fixed parameter

** Influential parameter

LAYER	THICKNESS (meters)	RESISTIVITY (ohm-meters)
1	1·5	17
2	3·0	3·1
3	20·0	22·0
4	43·0	1·6
5		250·0

Figure 11.39 (*top*) Combined TEM and resistivity inversion using vertical electrical soundings (VES) to fix the layer parameters for the top two layers in the TEM inversion. From Dodds and Ivic (1990), by permission

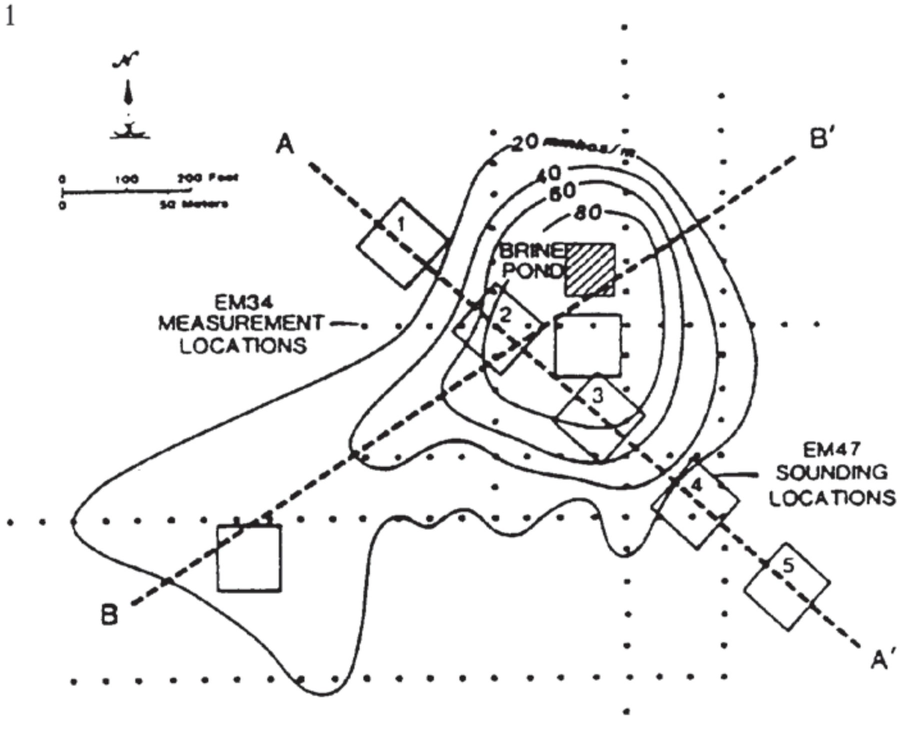

Figure 11.40 Location map and apparent conductivity contour map derived from measurements made with a Geonics EM34 at 20 m coil separation, horizontal magnetic dipole, around a brine evaporation pit. Numbered squares indicate the locations of Geonics EM47 loop soundings. From Hoekstra *et al.* (1992), by permission

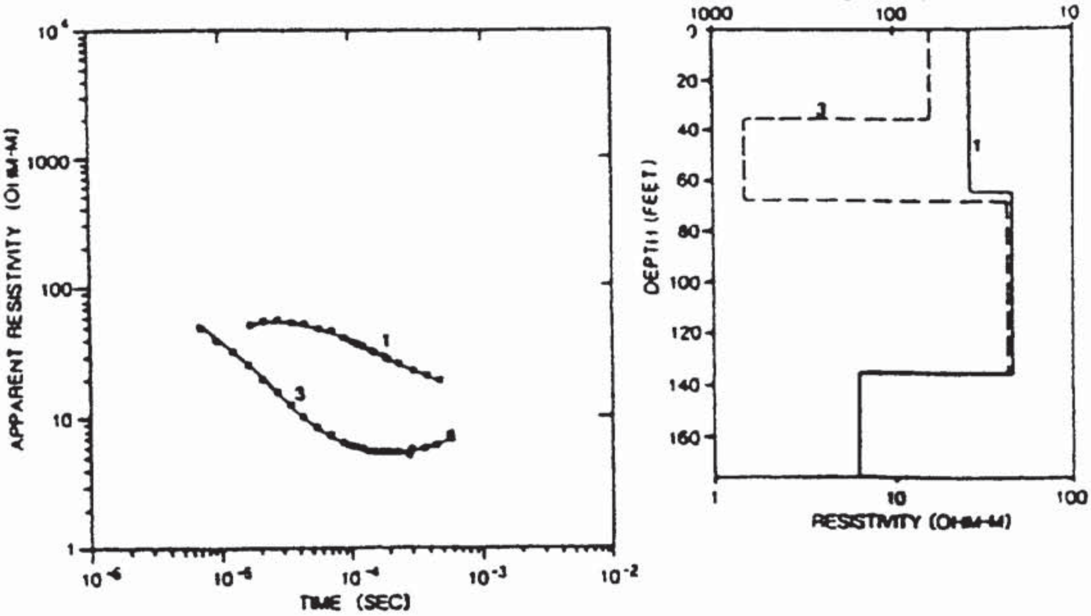

Figure 11.41 TDEM apparent resistivity sounding curves and their corresponding one-dimensional inversions along cross-section A–A′ (see Figure 11.40). From Hoekstra *et al.* (1992), by permission

a transmitter loop side length of 100 ft (30 m). Examples of two TEM soundings are shown in Figure 11.41 with their respective one-dimensional inversion results. It is clear that a layer about 10 m thick with a high conductivity is present on sounding 3 but is not seen on sounding 1, although the conductivities for deeper layers are the same for both. This high-conductivity zone is attributed to the saline contaminant plume. Using a series of soundings, a geoelectric section has been produced (Figure 11.42) on which the position of the contaminant plume is obvious (shown as the shaded area). The advantage of the TEM soundings in this case history is that a model of the probable migration pathways of the contamination can be developed using the TEM models (Figure 11.43). Not only can the EM data be used to map the contaminant plume spatially, but they have been

Figure 11.42 Geoelectric section derived from one-dimensional inversions of TDEM soundings along A–A′ (see Figure 11.40). From Hoekstra *et al.* (1992), by permission

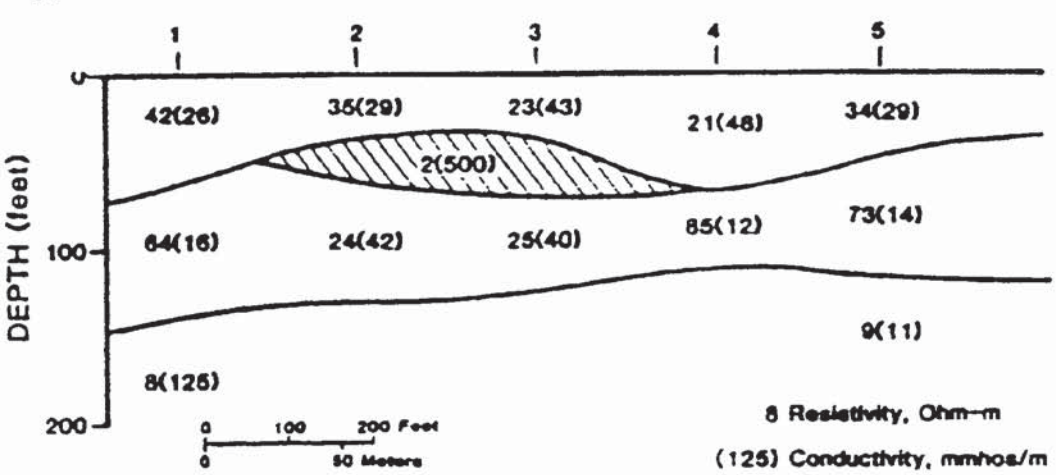

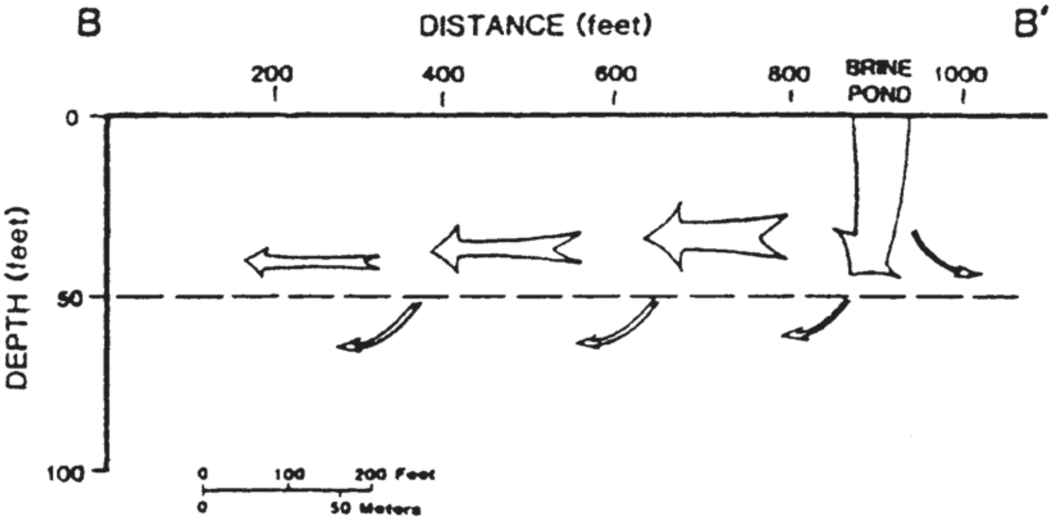

Figure 11.43 Model of probable pathways of brine migration along cross-section B –B′ (see Figure 11.40) constructed from geophysical surveys. From Hoekstra *et al.* (1992), by permission

demonstrated to provide an indication of the thickness too. Furthermore, and perhaps more fundamentally, they provide important information for the development of a model of migration pathways. This knowledge is vital if any remediation is to be undertaken successfully.

Buselli *et al.* (1990) have provided examples of the use of TEM in mapping contaminant plumes near Perth in Western Australia. One of these has been selected for discussion here.

A waste disposal facility had been established at Morley, near Perth. Sand was quarried from the Pliocene–Holocene sequence of surficial sand formations and the resulting pit was then filled with domestic solid waste. The area underlain by the predominantly clay Osborne Formation (Figure 11.44) was found to have a resistivity of $10\,\Omega\,\mathrm{m}$. The unsaturated zone within the sand was found to have a resistivity of $3600\,\Omega\,\mathrm{m}$ and to be up to 50 m thick. The saturated zone of the surficial sand formation was between 20 and 30 m thick with a resistivity of $50\,\Omega\,\mathrm{m}$. The sand formations consist of unconsolidated very fine to medium sand which coarsens progressively with depth to become gravely at the contact with the Osborne Formation. The general direction of groundwater flow is towards the south-west.

TEM measurements were made using a SIROTEM system with a transmitter loop of either 25 m or 50 m side length with an in-loop geometry with a dipole receiver of $10^4\,\mathrm{m}^2$ effective area placed in the centre of the transmitter loop. The instrument had a capability of measuring the response in a delay time range of 49 μs to 160 ms. The locations of all TEM loop centres are shown in Figure 11.44 and borehole locations in cross-section in Figure 11.45.

The results of the TEM survey are shown in Figure 11.46, in which values of resistivity of the sand formation derived from the TEM inversion are contoured. The contaminant plume arising from landfill

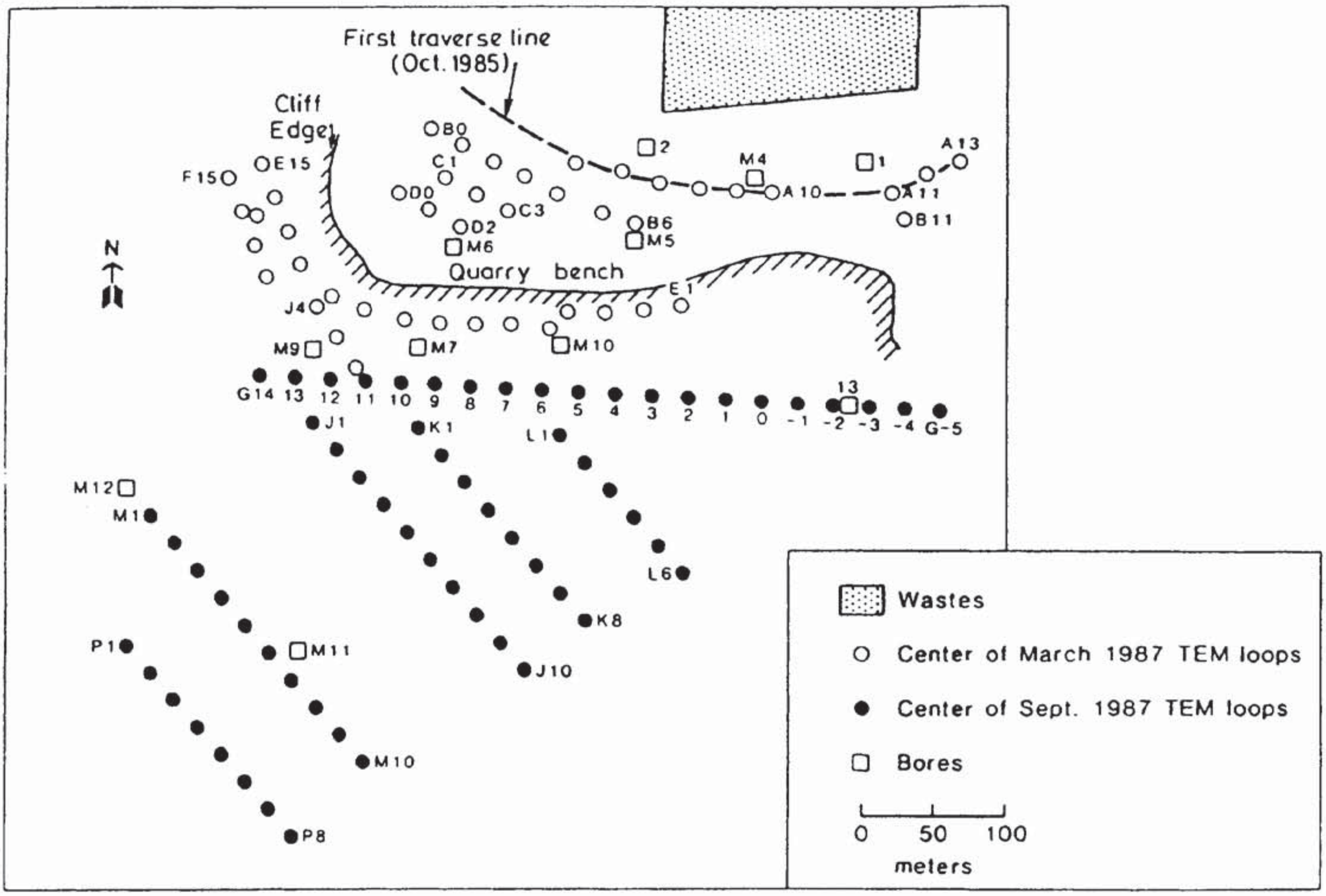

Figure 11.44 Plan of the Morley landfill and survey area with centres of the 25 m TEM transmitter loops and borehole locations indicated. From Buselli *et al.* (1990), by permission

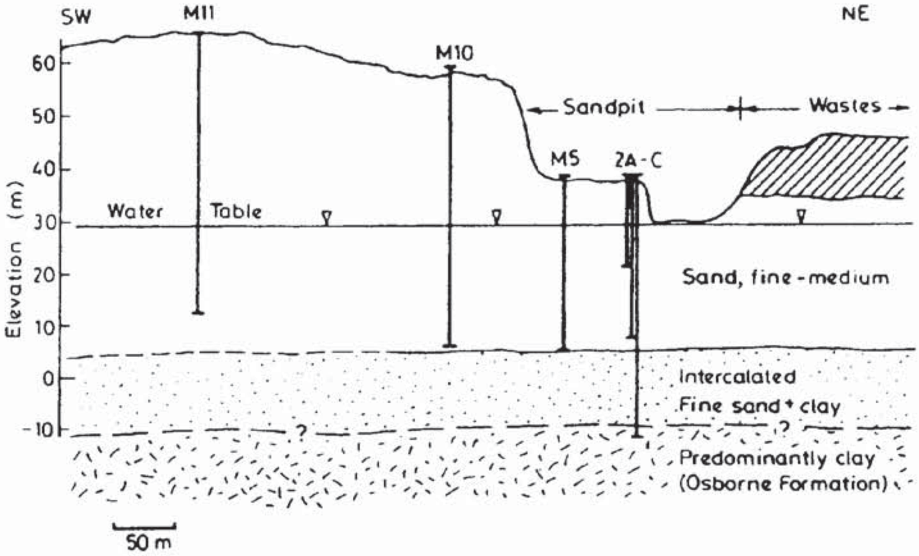

Figure 11.45 Cross-section through the sequence of boreholes M11, M10, M5 and 2A–C and the landfill at Morely, Perth, Western Australia. From Buselli *et al.* (1990), by permission

has been interpreted to be where resistivity values less than or equal to 75 Ω m were determined (tinted area in Figure 11.46). The general orientation of this anomalous zone is the same as the direction of general groundwater flow. This is further confirmed by superimposing

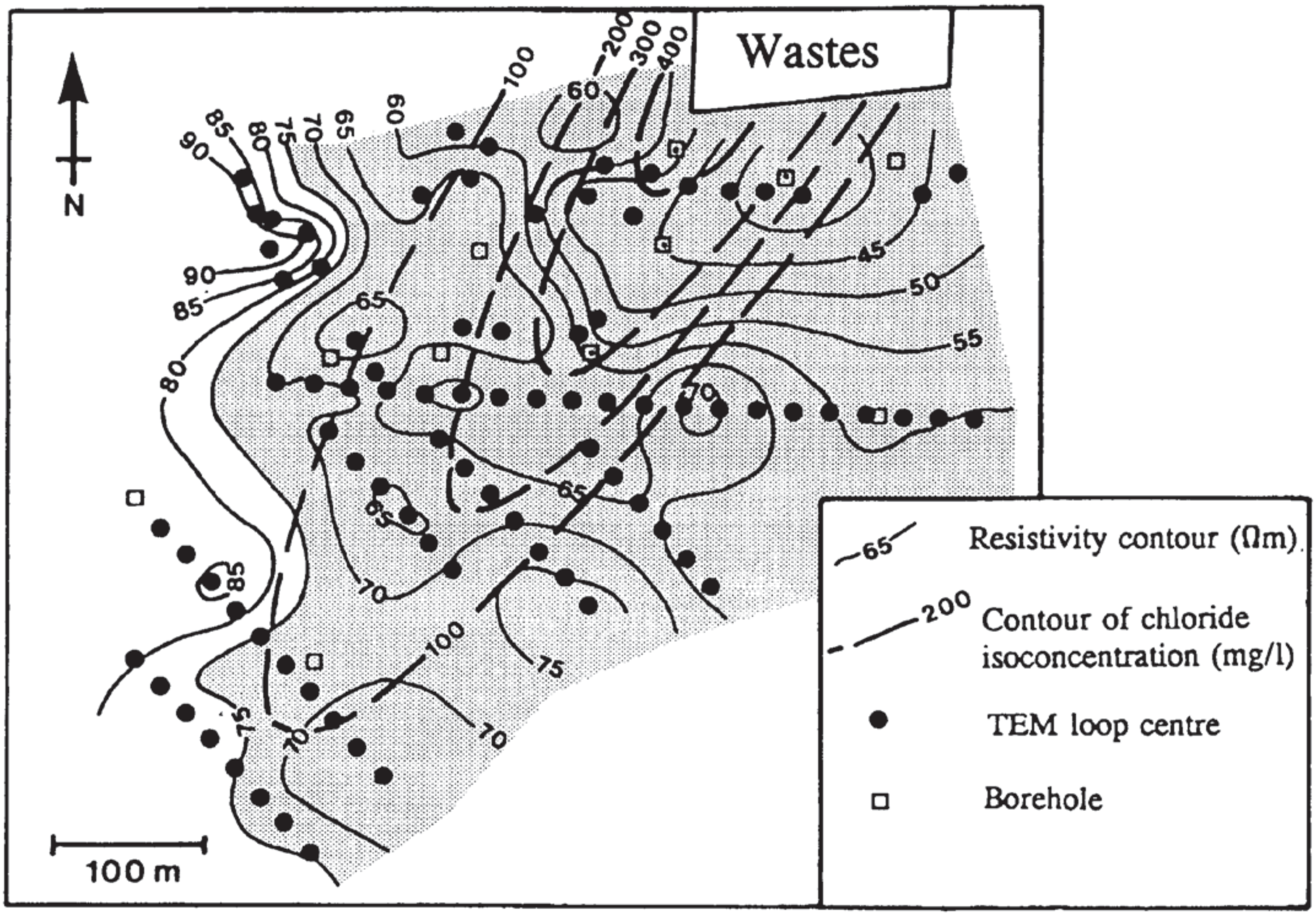

Figure 11.46 Isoresistivity map derived from TEM sounding data with contours of isochlor concentrations determined from chemical analysis of water samples from the boreholes. The contaminant plume is indicated by a tint, as determined by resistivity values $\leqslant 75\,\Omega\,\mathrm{m}$. After Buselli *et al.* (1990), by permission

the isochlor concentrations as determined from chemical analyses of water samples from the various boreholes over the resistivity map.

The ease with which TEM measurements can be made makes it very simple to re-occupy the same survey locations after discrete intervals of time, such as every 3–6 months, in order to observe changes in the resistivity values. This provides a means of monitoring the flow of a contaminant plume not only with respect to space but also in time. The natural extension of this is the use of TEM to monitor any remediation undertaken.

11.3.3.3 Mineral exploration

A surface DEEPEM survey was undertaken by Crone Geophysics Ltd for Cogema Canada Ltd in the Athabasca Basin, Saskatchewan, Canada. As a consequence of this survey, in conjunction with other techniques, a high-grade uranium deposit was discovered (Crone 1991). The uranium deposit, which is a typical Athabasca type, comprises a long horizontal 'tube' of cross-sectional width less than 100 m of high-grade uranium mineralisation which occurs at the base

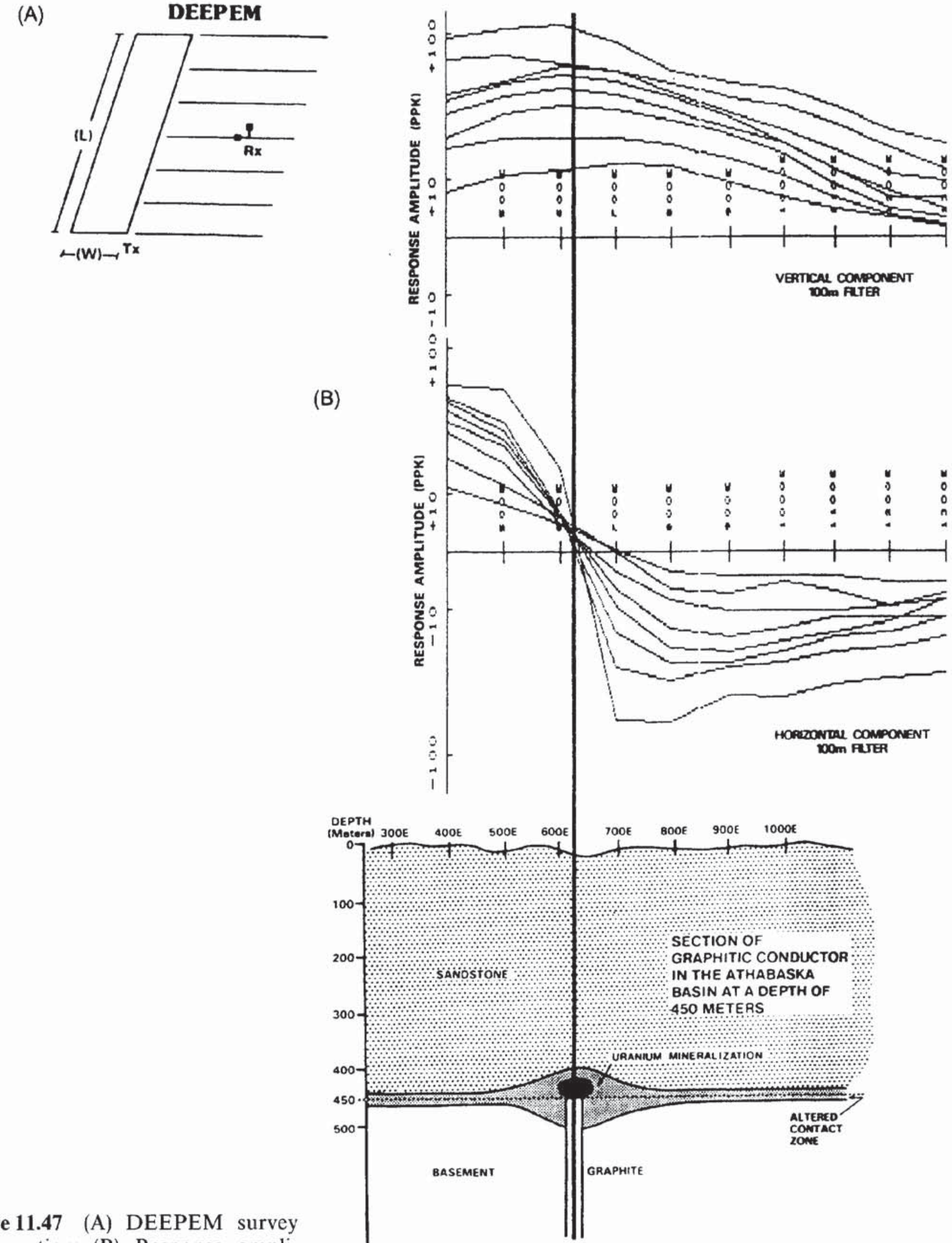

Figure 11.47 (A) DEEPEM survey configuration: (B) Response amplitudes for both horizontal and vertical components (Fraser filtered with a 100 m station interval filter gate). From Crone (1991), by permission

of flat-lying sandstone. The mineralised 'tube' is commonly associated with the upper interface of a large near-vertical graphitic structure that occurs in Archaean basement rocks. The EM surveys may be employed to locate the graphitic conductors. Between the basement and the sandstone is an altered contact zone up to 100 m thick which is made up largely of clay and which is commonly found in areas of uranium mineralisation.

In this survey, a large-loop (400 × 800 m) pulse EM system was used, powered by a 2 kW waveform generator. Horizontal and vertical component measurements were made by the receiver coil at each survey location (Figure 11.47A). The data were filtered using a Fraser filter to emphasise selectively the response from currents at up to a depth of five times the filter station interval. A 100 m station interval was used in the filter in order to pinpoint the location of the graphitic conductor. The filtered results of the survey are shown in Figure 11.47B. The data for the horizontal component are particularly revealing, with the location of the graphitic conductor being indicated by the node of the family of graphs as indicated in the figure.

Not all massive sulphide mineral deposits are necessarily good EM targets. For example, Cyprus-type massive sulphide deposits, which occur as silicically altered mineralisation in altered conductive pillow lavas, present very small physical parameter contrasts with the host rocks. Experiments using TEM over known mineral deposits in Cyprus failed to detect the orebodies (Cooper and Swift 1994). Even when induced polarisation was used, only the true chargeability could discriminate between highly silicified structures and mineralised targets. Even chargeability was found to be an unreliable exploration parameter. The occurrence of extensive local disseminated pyrite masks electrical mineralisation anomalies at a survey scale typical of that used for mineral exploration. However, despite the lack of direct success with TEM in locating orebodies, it was used to help to delineate geological detail (faults, determination of lithology thicknesses, trends, etc.) which in turn can be used to build up a three-dimensional structure of a given area (Cooper and Swift 1994).

11.3.3.4 Mapping sub-surface voids

A SIROTEM system was used in the investigation of a series of sink holes along the route of the proposed Alice Springs to Darwin railway across the Wiso Basin, Northern Territories, Australia (Nelson and Haigh 1990). The occurrence of sinkholes in this area was well known, but the sudden collapse of part of the Buchanan Highway into a sinkhole in 1982 highlighted the engineering hazard which then prompted a full-scale investigation.

Various geophysical methods were tested as to their effectiveness over terrain which was undulating and irregular, and which was covered with lateritic soils. Intuitively, air-filled cavities should give rise to resistive anomalies, but the contrasts found were sufficiently small that the method was not considered practicable for the required coverage of large tracts of land along the proposed railway route. It was found, however, that the walls and floors of known dolines tended to contain electrically conductive clay-rich material. Furthermore, the process of doline (sinkhole) formation was associated with leaching of silica, which produced pipes or structures with leached, weathered, transported or altered detritus that were also found to be charactristically conductive. Consequently, the target type for which the geophysics was selected was not the more intuitively obvious 'hole-in-the-ground' but the conductive secondary targets. Indeed, TEM would not have been suitable for air-filled voids owing to the diffusion velocity through the void being of the same order as the velocity of light. Similarly, these same silica-leached features also caused significant and detectable anomalies on time delays, relative amplitude attenuation and spectral content of seismic waves.

Following a considerable amount of trial work with a variety of methods, it was established that coincident-loop SIROTEM was the best method for rapid reconnaissance with the seismic surveys being used over specific features. The seismic work, in addition to the SIROTEM investigation, has been described in considerable detail by Nelson and Haigh (1990).

Of several test areas, the Buchanan Highway Test Site, located 60 km west of the Stuart Highway, was known to be a major zone of doline formation. As part of this work, 25 m coincident-loop SIROTEM surveys were undertaken, with four turns of wire per loop to improve the signal strength. The rate of surveying with this system was up to 4 km per day. Two lines parallel to each other but 25 m apart were surveyed, with additional parallel lines with greater offset being investigated as required to help delimit the extent of features identified.

The general findings of the SIROTEM investigation were that the local geology was characterised by a generally uniform resistivity distribution, with apparent resistivities in the range 50–100 Ω m, and with a gently dipping and consistently layered structure. In contrast, areas affected by dolines were found to have lateral resistivity fluctuations of up to 20 Ω m with a complex heterogeneous geometrical appearance. A map of apparent resistivity values obtained using the SIROTEM system for part of the test site, where two dolines were known to occur, is shown in Figure 11.48. Sinkholes HV4 and HV5 were the two that occurred suddenly overnight in 1982. A car that drove into the newly formed hole was totally wrecked but the driver escaped with only minor injuries! As a consequence of this incident, the highway was diverted along the route shown in Figure 11.48. However, a prominent apparent resistivity low (to 10 Ω m) was found at coordinates (90 m E, 40 m N) almost on the diverted highway. This same feature correlated with seismic arrival time anomalies and is interpreted to be an imminent doline collapse feature!

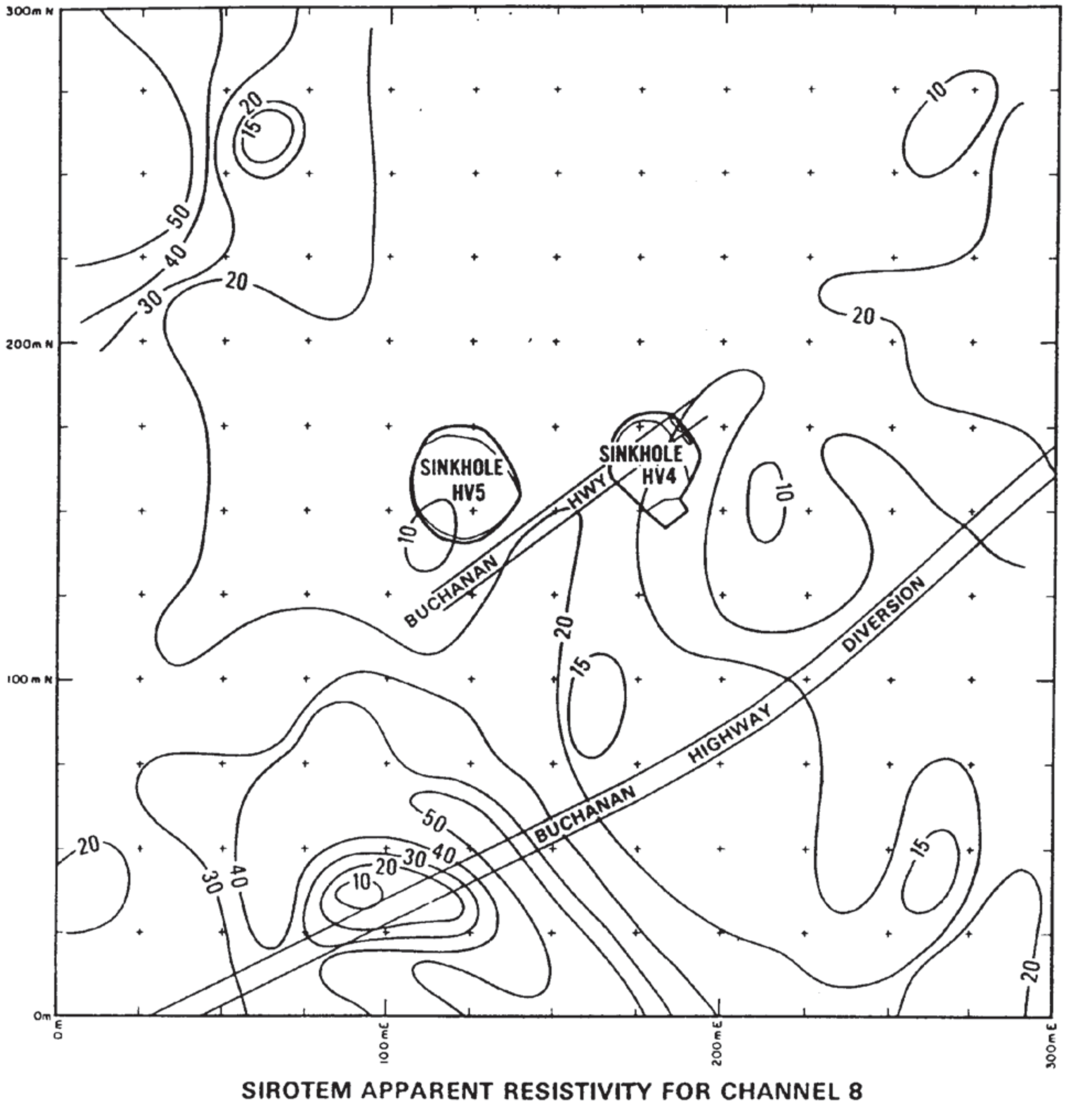

Figure 11.48 SIROTEM apparent resistivity anomaly map over part of the Buchanan Highway test site, Northern Territory, Australia. From Nelson and Haigh (1990), by permission

Figure 11.49 shows composite results of the two parallel SIROTEM traverses 25 m apart as contoured apparent resistivity values. A complex anomalous zone is evident between 89 900 N and 90 200 N on both traverses; in comparison with anomaly shapes over known dolines, this anomaly is characteristic of sinkhole-prone terrain. The SIROTEM anomaly is also consistent with the interpretation of seismic refraction results in terms of amplitude decay and travel-time delay over the anomalous feature. This combined correlation of the anomalous zone provides increased confidence in the overall interpretation. The full scope of the investigation carried out by Nelson and Haigh (1990) and co-workers deserves being read in

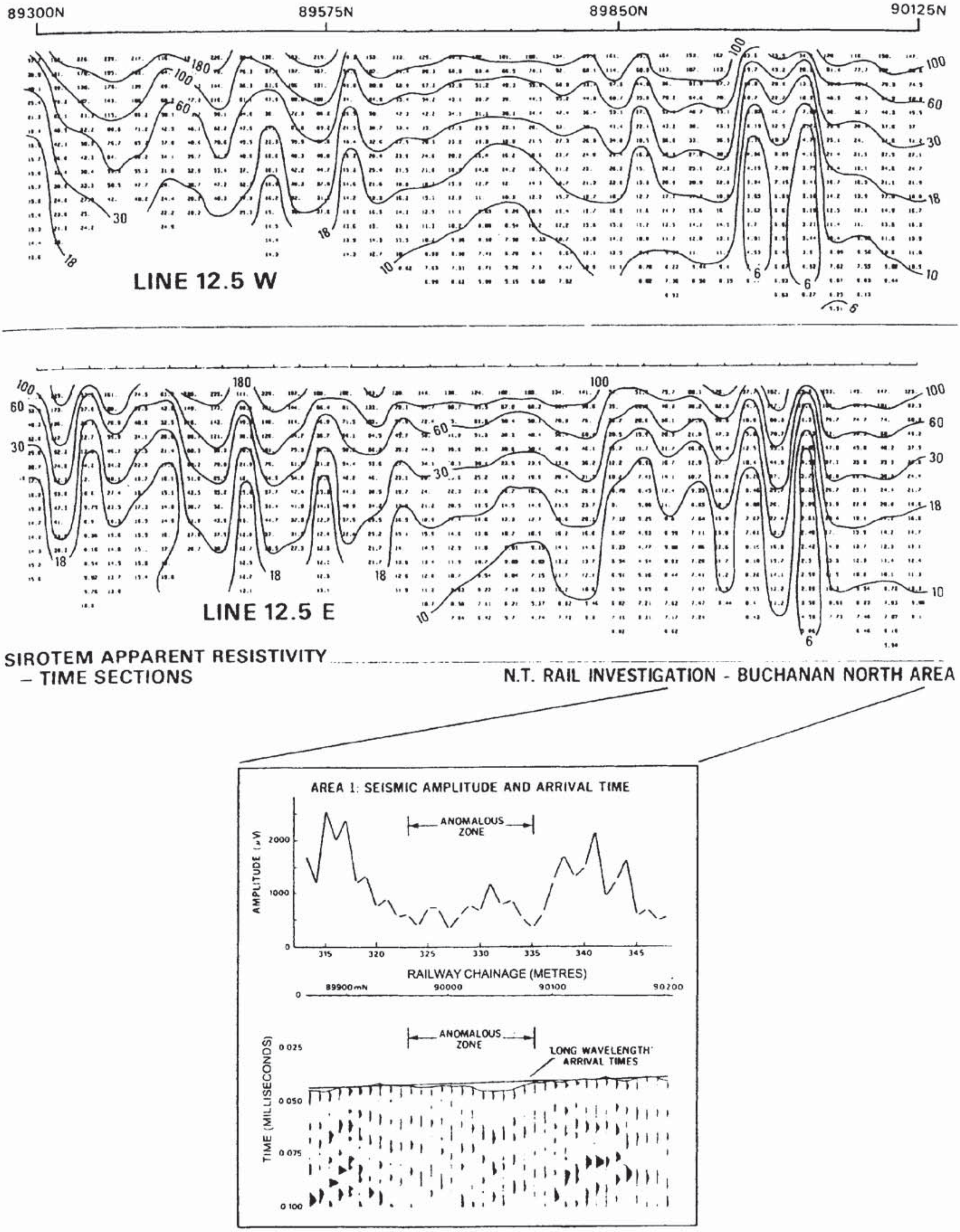
89300N
89575N
89850N
90125N
100
60
30
18
10
6
180
LINE 12.5 W
LINE 12.5 E
SIROTEM APPARENT RESISTIVITY – TIME SECTIONS
N.T. RAIL INVESTIGATION - BUCHANAN NORTH AREA
AREA 1: SEISMIC AMPLITUDE AND ARRIVAL TIME
AMPLITUDE (μV)
2000
1000
0
ANOMALOUS ZONE
315
320
325
330
335
340
345
RAILWAY CHAINAGE (METRES)
89900mN
90000
90100
90200
TIME (MILLISECONDS)
0.025
0.050
0.075
0.100
'LONG WAVELENGTH' ARRIVAL TIMES

detail as it is an excellent example of a well-thought-out investigation that was well executed. As with so many projects like this, lack of finance at a critical stage denied the final conclusive direct investigative work. A series of appropriately sited boreholes could have helped test the geomorphological model for the formation of these features. Considering the major engineering significance of these features over a very large tract of land in the Northern Territory of Australia, the incomplete funding of such work is a major oversight.

Figure 11.49 (*opposite*) SIROTEM 25 m coincident-loop apparent resistivity pseudosections along two lines 25 m apart, either side of the centreline of a proposed railway route at Buchanan Highway. Seismic amplitude and waveform sections over the SIROTEM anomalous zones confirm the probability of this region being indicative of sinkhole-prone terrain. From Nelson and Haigh (1990), by permission

11.3.3.5 Geological mapping using airborne EM

Huang and Palacky (1991) have described the use in 1983 of airborne EM surveying for geological mapping in Dongling, Anhui Province, China. The survey was undertaken using an INPUT-type system made in China (the M-1 instrument) which uses a transmitter made up of a seven-turn vertical axis loop mounted on a fixed-wing aircraft. The receiver used was a towed bird, nominally 90 m behind and 63 m below the aircraft. Although designed for an optimum flying height of 120 m, the system was flown at significantly greater heights. The channels at which the signals were measured were 0.3, 0.5, 0.8, 1.2, 1.7 and 2.3 ms after the transmitter switch-off.

The survey area was known to contain lead–zinc mineralisation of the replacement type in Mesozoic limestones. The objective of the AEM survey was to locate previously unknown mineralised bodies and to determine the thickness of fluvial clays in the Yangtze River plain and the extent of the weathering in areas underlain by Mesozoic rocks. The line spacing was 500 m with a NW–SE flight line direction.

Figure 11.50 shows the AEM data and the corresponding geological section with the altimeter trace (top), and measured amplitudes at six channels with indicated base levels for each. The fiducial markers are at approximately 500 m intervals. The geological section was derived from the interpolation of drilling data. The peak observed on the AEM data at fiducial 54 for channels 1 and 2 (arrowed) is thought to be due to the change in flying height. Strong AEM anomalies evident on the early-time channels (1–3) are due to conductive fluvial clays. Resistivities of the local geological materials were obtained from ground-based electrical soundings with the fluvial clays having a resistivity in the range 5–15 Ω m and the weathered material, up to 50 Ω m with the underlying Mesozoic strata having resistivities of hundreds to thousands of ohm-meters. The inversion results of the same data are shown in Figure 11.51. The apparent resistivity (ρ_a) was derived from the inversion of the AEM data from all six channels, assuming a homogeneous half-space model. The marked increase in apparent resistivity near fiducial 51 is associated with the transition from the fluvial clays to Mesozoic sediments. The segments of the resistivity graphs shown dotted are indicative of less reliable results owing to the higher noise levels within the system.

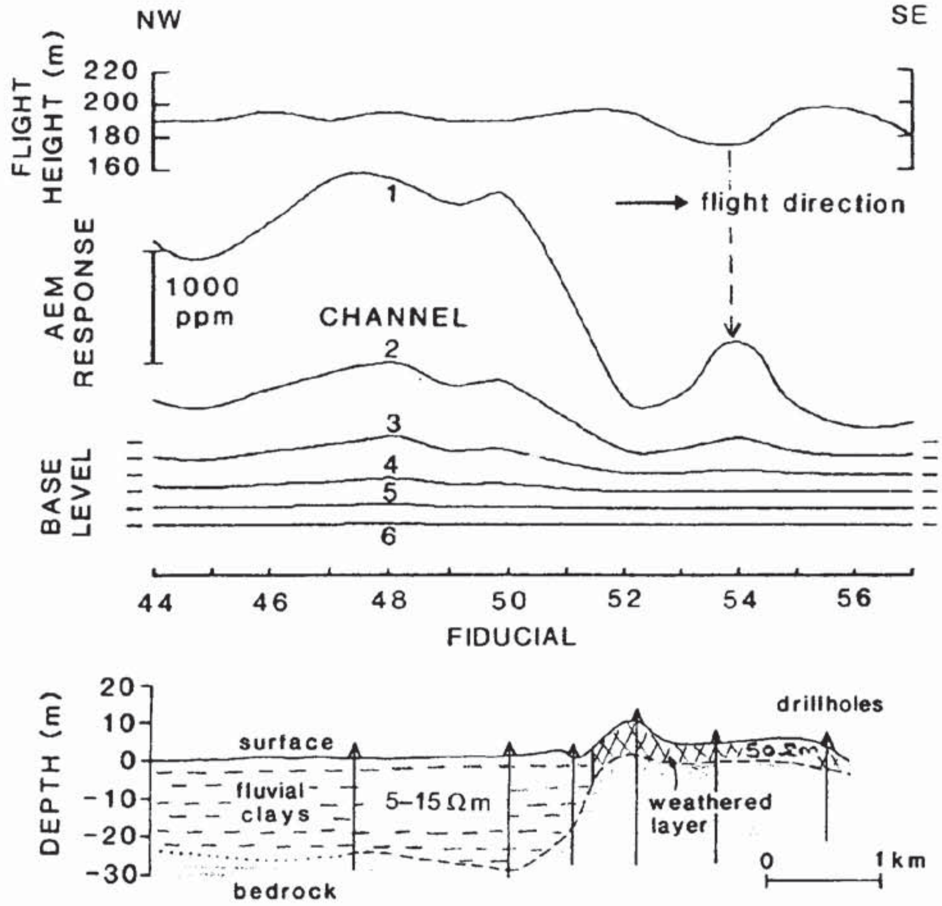

Figure 11.50 (A) Altimeter trace for an airborne EM (AEM) survey at Dongling, Anhui Province, China. (B) AEM responses at six channels with respective base levels for each channel with fiducial fix numbers. (C) Interpreted geological section derived from AEM data and borehole information. The true resistivity ranges (in Ω m) of the superficial materials are indicated. From Huang and Palacky (1991), by permission

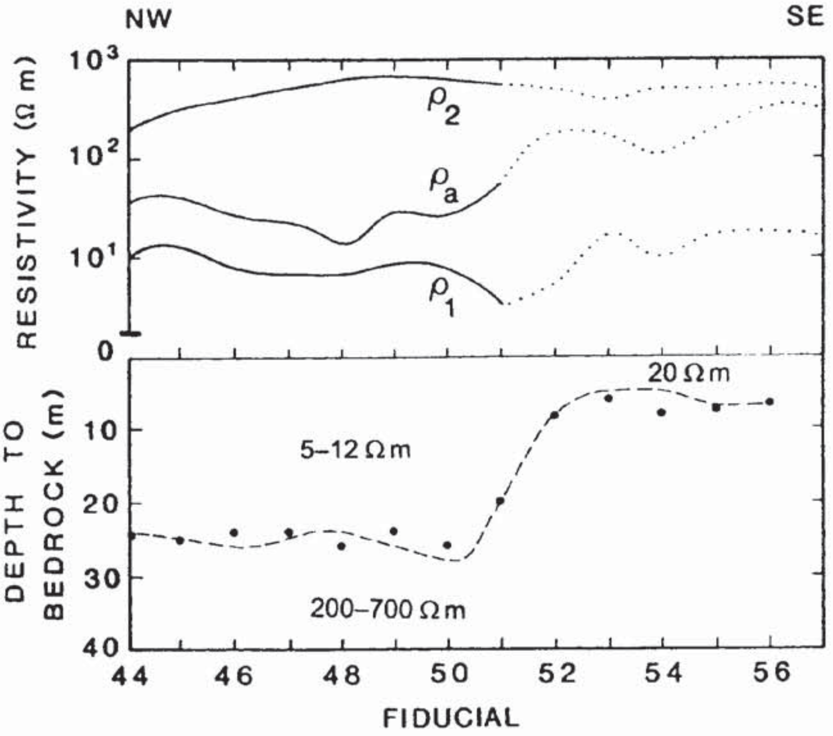

Figurer 11.51 Apparent resistivity (ρ_a) and first- and second-layer resistivities (ρ_1 and ρ_2) obtained by inversion of the AEM data shown in Figure 11.50. The interpreted depth to bedrock at each fiducial position derived from the AEM inverion (dots) and from drilling (dashed lines) are shown for comparison. From Huang and Palacky (1991), by permission

The inversion was carried out using a 2-layer model for which resistivities were found to be 200–700 Ω m for the Mesozoic strata, 5–12 Ω m for the Cenozoic fluvial clays and about 20 Ω m for the weathered Mesozoic sediments, all of which are in good accord with the results of the ground-based investigations. Furthermore, the depths derived from the inversion (dots) are in very good agreement with those found from drilling (dashed line) as shown in Figure 11.51. This example demonstrates the effectiveness of the AEM method coupled with appropriate inversion processing in mapping significant geological boundaries. The method shows that it is particularly the early-time responses that are sensitive to the conductivity contrasts in the near-surface.

11.4 VERY-LOW-FREQUENCY (VLF) METHODS

11.4.1 Introduction

The first commercially available ground VLF instrument was made in 1964 by Ronka (Paterson and Ronka 1971) with others being manufactured within the following few years. The most widely accepted ground survey instrument has undoubtedly been the Geonics EM16. Its resistivity mapping mode is also very well used in the EM16R configuration. In recent years, new VLF instruments have been produced such as the WADI from ABEM, EDA's integrated magnetometer/VLF system called the OMNI IV, the 'VLF-3' and 'VLF-4' from Scintrex, and the 'VLF-2' from Phoenix, among others. Although VLF measurements can also be made from the air, only ground-based systems wlll be considered here. A comprehensive review of VLF methods has been given by McNeill and Labson (1991).

The VLF method has remained an excellent, cheap and rapid tool for reconnaissance mapping of conductive mineralised bodies and water-bearing fractures. Its use in engineering and environmental work has as yet remained small. However, with the advent of modern VLF systems with integrated data-loggers, auto-selection of appropriate transmitters and enhanced display and interpretation methods, the technique is gradually being tried for non-exploration purposes such as in cavity detection and in mapping landfills.

11.4.2 Principles of operation

There are eleven major VLF transmitters distributed around the world used primarily for military communications. These provide very powerful EM waves which, when sensed from a distance greater than a few tens of kilometers, behave as plane waves propagating outwards horizontally. Signal level contours for two of the major VLF transmitters are shown in Figure 11.52. Areas enclosed within the 54 dB contours have good signal strengths while those within the 48 dB contour have only marginal signal strength. Areas left unshaded have signal strengths too weak for the method to be used effectively or without special techniques being used.

If a vertical sheet conductor is orientated such that its long axis lies on a radial direction from an active transmitter, the magnetic vector acts tangentially (as depicted in Figure 10.5 in the previous chapter) across the conductor. Eddy currents are induced within the conductor to produce a secondary electromagnetic field. For a conductor not so aligned, the production of eddy currents is much less efficient and the strength of the induced secondary field is much reduced.

For a vertical sheet conductor in a resistive medium, for example, and a profile direction aligned along the magnetic vector, then the tilt-angle response obtained is derived from the vector summation of the primary and secondary components, as shown in Figure 11.53. The primary magnetic vector is horizontal. The induced electromagnetic field varies in amplitude and direction with position relative to the target. On one side of the target, the angle between the two vectors reaches a maximum and then passes to a minimum on the other side before returning to zero beyond the influence of the target. The point at which the tilt angle passes through zero from the positions of the maximum and the minimum, known as the 'cross-over' point, lies immediately above the conductive target. If the target dips, then the anomaly shape is distorted with either the positive or negative element being emphasised at the expense of the other component.

The largest amplitudes of the various electric and magnetic components lie at the ground surface and diminish with depth (Figure 11.54). VLF surveys are used largely for spatial mapping of sub-surface targets, not for depth determination as the depth penetration is generally restricted to the near-surface only.

The VLF instrument contains one or more aerials whose characteristics are appropriate for specific transmitters. The VLF EM16 requires the correct crystal aerial for a given transmitter to be physically plugged into the device. To use the instrument, the operator holds the device out horizontally and then rotates it around a vertical axis until a null position is sensed using an audio signal. The direction in which the device is then pointing is along the line of the horizontal component of the electric vector. Survey profiles are conducted at right-angles to this direction, i.e. along the line of the magnetic vector for the given transmitter. Once aligned along the profile direction, at each station, the device is rotated about a horizontal axis. The operator holds the device to his/her eye and views the tilt of the instrument through an eyepiece. The operator rocks forwards and backwards to sense a null in the audio signal, at which

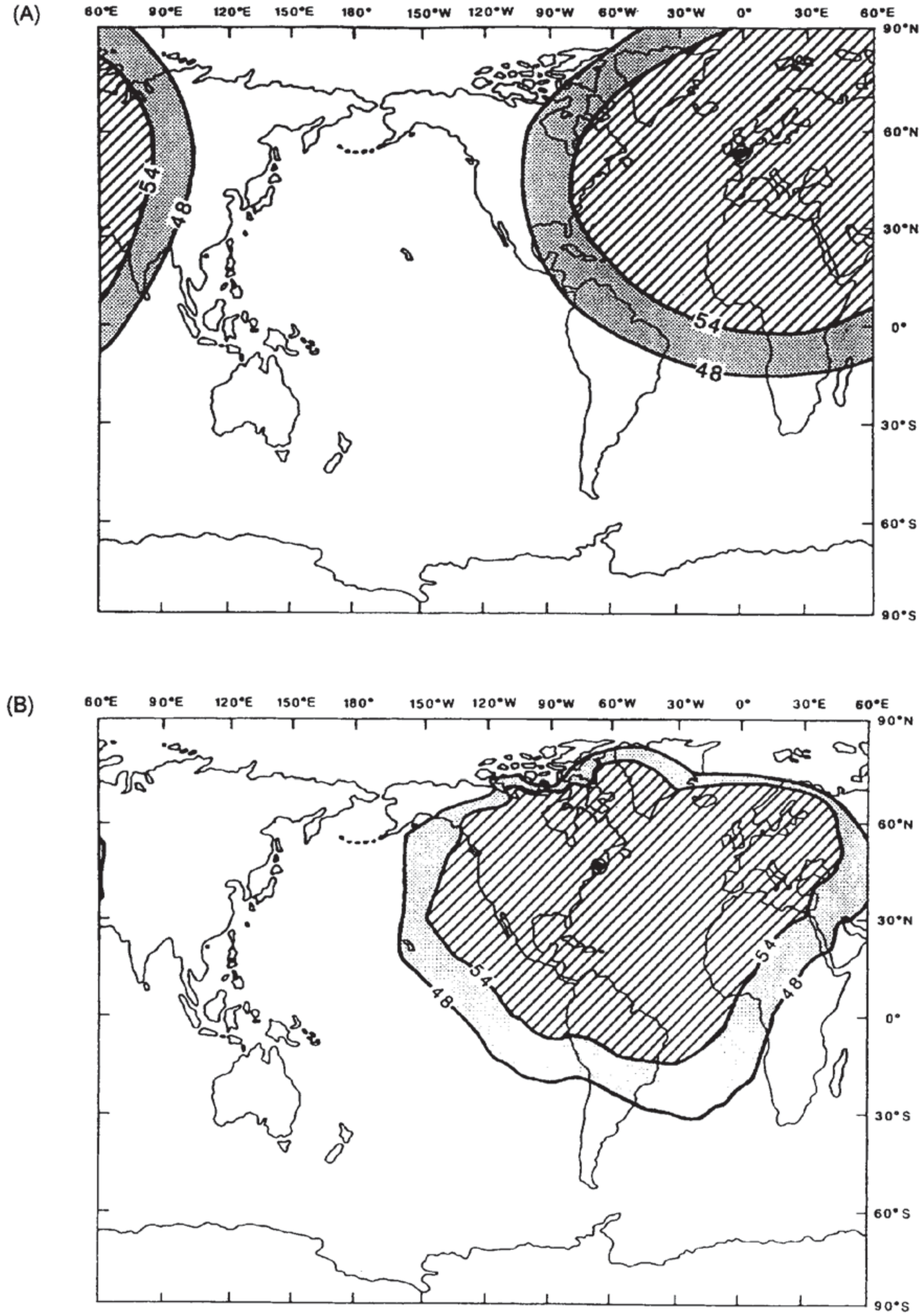

Figure 11.52 Signal level contours for VLF transmitters at (A) GBR, Rugby, UK, and (B) NOAA, Cutler, USA. From McNeill and Labson (1991), by permission

point the tilt angle is then read from the instrument. VLF devices can also be used to measure the electric component by using a grounded dipole up to 5 m long made up of a piece of wire connected to the ground at each end. In this configuration (VLF-R) the apparent

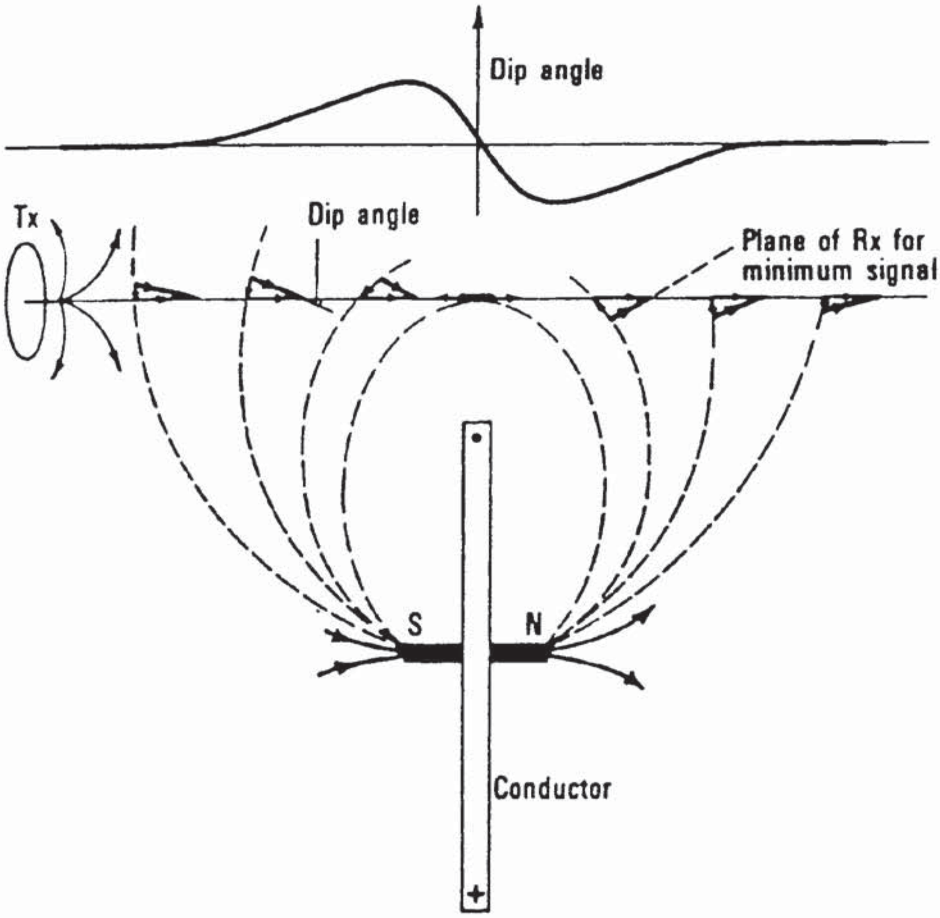

Figure 11.53 Tilt-angle profile over a vertical sheet conductor. From Beck (1981), by permission

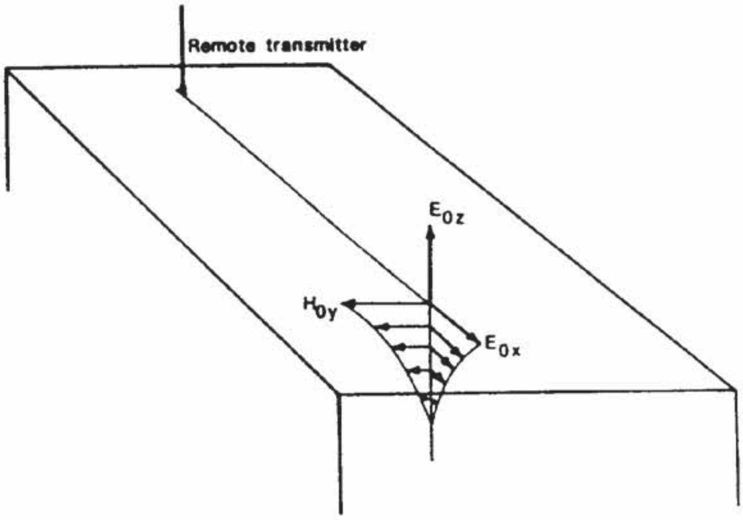

Figure 11.54 Schematic of the diminution of the amplitude of field components with depth. From McNeill and Labson (1991), by permission

resistivity and phase of the horizontal electric field in the ground can also be determined.

In a modern instrument, such as the ABEM WADI, three different frequencies are used simultaneously and the device is able to sense from which transmitter the strongest signal is emanating. Without having to orientate the instrument, the operator walks along the chosen profile line and takes readings. While this has obvious benefits in reducing setup time, there is one major disadvantage with autotuning devices. Repeatability of measurements is sometimes difficult along the same profile when surveyed on different occasions as the transmitter with the strongest signal may be different each time. Thus survey parameters are difficult to keep constant.

Another drawback with any VLF system is that the method is totally dependent on there being an appropriate transmitter operational. There are occasions when transmitters are off-air and no source signal from a transmitter with an appropriate azimuth to the target is available. Sometimes, a given transmitter can be switched off while an operator is in mid-survey. There is nothing within the control of that operator that can be done to rectify the situation unless another transmitter is available with a suitable azimuth and the instrument being used has the appropriate aerial.

With modern instruments it is now possible to measure the respective fields from two orthogonal transmitters with one instrument in the same pass along the survey line. The direction to one transmitter is parallel to the strike of the target with the other at right-angles. These two orientations are then referred to as the E- and H-polarisation modes. Thus with modern instruments in both VLF-EM and VLF-R modes using two orthogonal transmitters, eight parameters can be obtained at each station (in-phase and quadrature components in VLF-EM mode; resistivity and phase in the VLF-R mode for each transmitter).

11.4.3 Effect of topography on VLF observations

VLF measurements can be adversely affected by topography, and so some sort of topographic correction may have to be applied before a target anomaly becomes obvious. If a topographic high, such as a ridge, is parallel to the strike direction of the target body, and thus is at right-angles to the survey direction, the topographic effect is a subdued version of the actual topography. That is, on rising up the slope, the tilt angle is increased slightly, and on descending down the slope the other side, it decreases. If the survey is conducted parallel to the survey direction along the ridge, then no association with topography may be evident. The actual topographic response can be complex and depends on the resistivity of the local materials. If the tilt-angle profile mirrors the actual topography, then this is strongly suggestive that topographic effects are present. Similarly, if positive polarity anomalies correlate with topographic highs and negative polarity anomalies are located at the bottoms of valleys, this also indicates the presence of topographic effects.

If the survey has been conducted over topography with a wavelength much longer than the width of the target along the survey line, topographic effects may be removed by the application of an appropriate filter.

11.4.4 Filtering and interpretation of VLF data

VLF tilt-angle data are commonly interpreted only qualitatively. The point where the tilt angle crosses over from being positive to negative polarity is usually interpreted as being immediately above the top of the conductor causing the anomaly. In profile, this crossover is usually quite clear. When plotted spatially in map form, however, the locus of all zero-points (a line joining the crossover points from each profile) is not as easy to identify.

One way by which this problem has been resolved is the use of a filter, such as that devised by Fraser (1969). His filter was designed to shift the tilt-angle data by 90 degrees so that crossover and inflection points become peaks. The filter also attenuated long spatial wavelengths to help overcome some aspects of topographic effects and also to reduce the slow temporal variations in signal strength of the transmitter. Furthermore, his filter was designed not to increase the noise content of the data and, importantly, to be simple to apply.

The Fraser filter uses four consecutive data points, where the data have been acquired at a regular interval and can be applied very simply using a hand calculator or spreadsheet. The sum of the first and second data points is subtracted from the sum of the third and fourth values and plotted at the midpoint between the second and third tilt-angle stations (see Box 11.6). It is important to remember to take account of the polarity of the tilt angle, whether positive or negative, in the calculation of the filtered values.

Box 11.6 Fraser filtering VLF tilt-angle data

Given a sequence of tilt-angle data, $M_1, M_2, M_3, \ldots, M_n$, measured at a regular interval, then the Fraser filter F_i is applied as follows:

- The first filtered value, $F_1 = (M_3 + M_4) - (M_1 + M_2)$ and is plotted half-way between stations 2 and 3.
- The second filtered value, $F_2 = (M_4 + M_5) - (M_2 + M_3)$ and is plotted half-way between stations 3 and 4, and so on along the profile.

For interpretation, it is arguably better to use both the raw and filtered data. The effect of filtering the data can result in the anomaly peak being displaced laterally along the survey line. Thus for more accurate target location, the raw data should be used.

For more quantitative interpretation, two approaches can be taken. One is to use a set of *master curves* and associated interpretational aids published by Madden and Vozoff (1971). However, these curves have not been widely used as most interpreters appear to favour their own empirical approach based on experience or on nomograms calculated for simple dipping sheet-like conductors (Sinha 1990). For more detailed interpretation, especially in connection with two-dimensional and three-dimensional targets, numerical modelling can be used (e.g. Nissen 1986; Ogilvy and Lee 1989), although this tends to be undertaken more in research work rather than mainstream commercial surveys. A detailed discussion of the quantitative analysis of VLF data has been given by Telford *et al.* (1990) and by McNeill and Labson (1991). The main value in VLF surveying lies in its simplicity of use in the field for reconnaissance work for which qualitative interpretation is usually adequate.

11.4.5 Applications and case histories

11.4.5.1 Detection of orebodies

A VLF profile acquired across mineralised metasediments at Sourton Tors adjacent to the Dartmoor granitic intrusion, Devon, is shown in Figure 11.55. The VLF profile shows a marked change in polarity at about 210 m along the survey line. This location correlates with a known area of stratabound mineralisation within the chert/shale zone marked 'MZ'. For comparison, profiles obtained using SP and magnetometry are also shown. Both of these reveal anomalies around the same location and with the shapes of anomalies consistent with a conductive magnetic target dipping towards the north-west. Another section across Sourton Tors is shown in Chapter 2 (Figure 2.43). The VLF data were acquired using a Geonics EM16 with GBR, Rugby, as the transmitter.

11.4.5.2 Location of sub-surface cavities

Ogilvy *et al.* (1991) have described a VLF survey undertaken near Alcala de Henares, about 20 km east of Madrid, Spain. In medieval times, artificial galleries were constructed at a depth of 2–4 m to drain superficial Quaternary gravel terrace deposits which overlie an impermeable Tertiary clay formation in order to provide the town of Alcala with fresh water. The location and the lateral extent of these galleries were uncertain. The shallowness of the galleries meant that they posed a potential for collapse. Indeed, one road subsided as a direct consequence of being constructed over one of these galleries.

An example of a geological cross-section through a typical gallery is shown in Figure 11.56A. The galleries are on average 1 m wide and 2 m high and are largely free-standing and straddle the gravel–clay

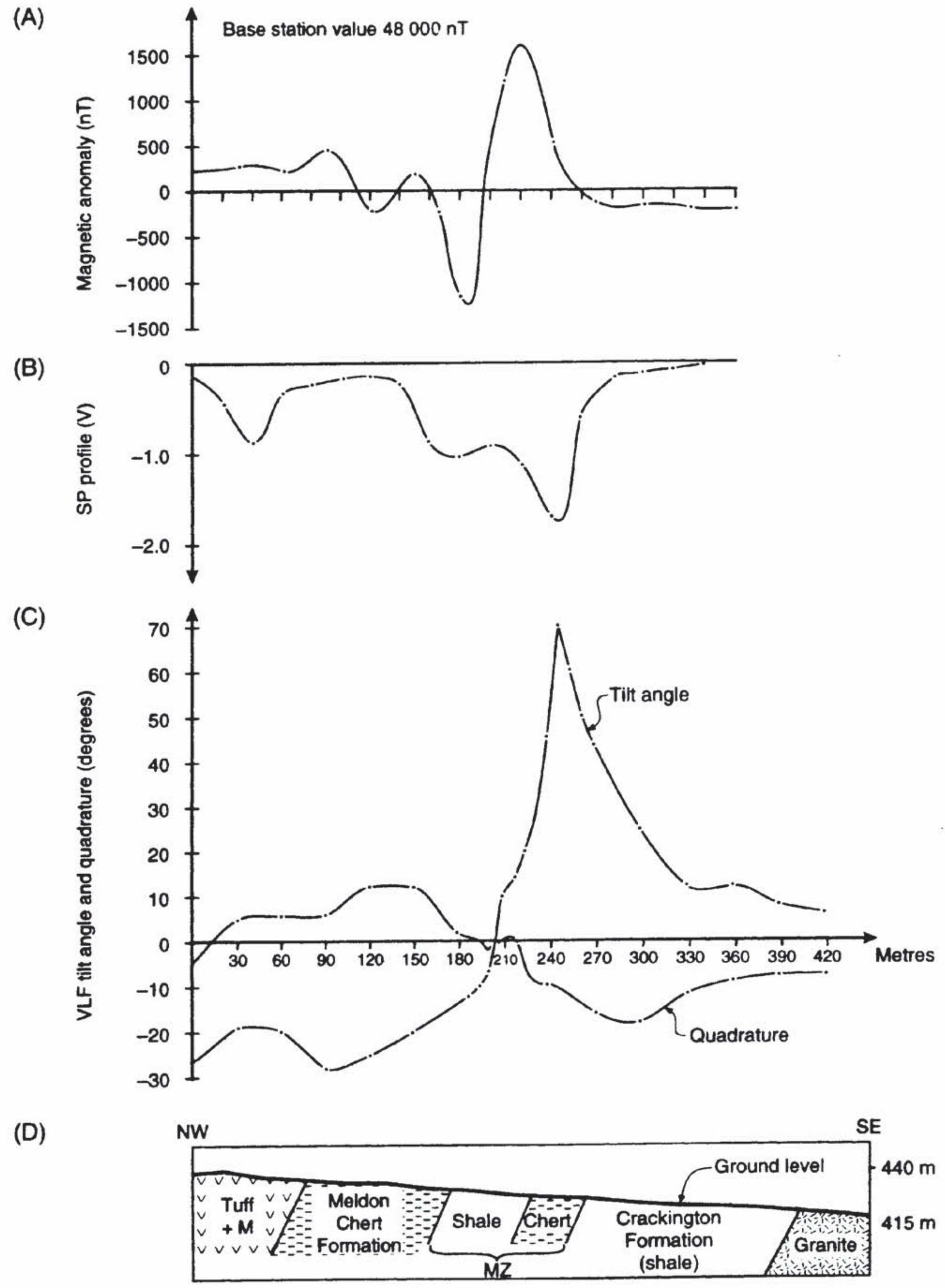
(A)
Base station value 48 000 nT
Magnetic anomaly (nT)
1500
1000
500
0
−500
−1000
−1500
(B)
SP profile (V)
0
−1.0
−2.0
(C)
VLF tilt angle and quadrature (degrees)
70
60
50
40
30
20
10
0
−10
−20
−30
Tilt angle
Quadrature
30
60
90
120
150
180
210
240
270
300
330
360
390
420
Metres
(D)
NW
SE
Ground level
440 m
415 m
Tuff + M
Meldon Chert Formation
Shale
Chert
MZ
Crackington Formation (shale)
Granite

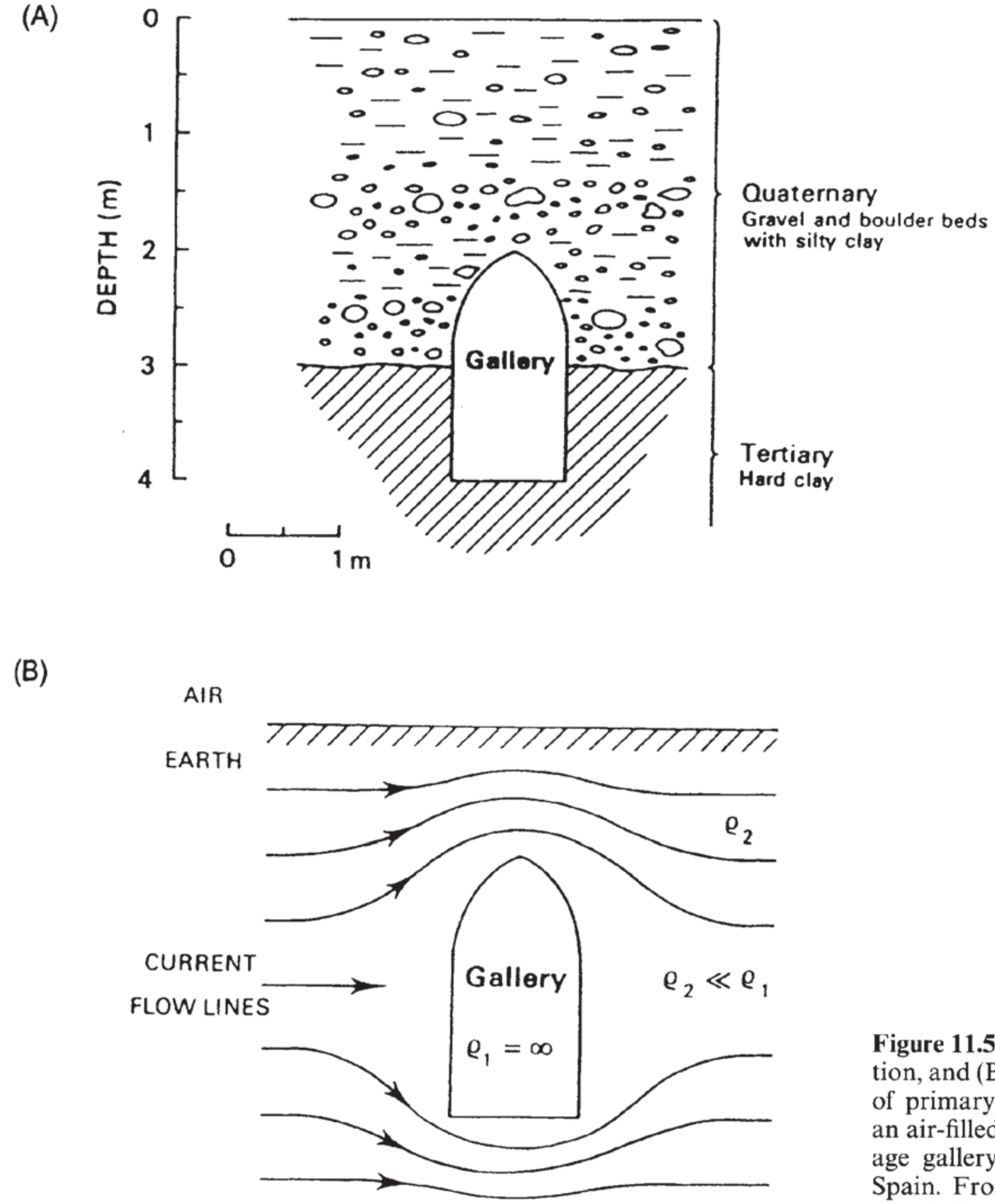

Figure 11.56 (A) Typical cross-section, and (B) schematic representation of primary current flowlines around an air-filled (infinitely resistive) drainage gallery at Alcala, near Madrid, Spain. From Ogilvy *et al.* (1991), by permission

interface. At the time of the survey, the galleries were dry and thus constituted air-filled tunnels.

A 100 × 100 m grid was established over one part of the known gallery system with lines orientated at right-angles to the direction of the galleries with an inter-line separation of 10 m or less. Station intervals along the lines varied between 5 m and 1 m, as required to sample the observed anomalies spatially. The position of the gallery system was also mapped underground by theodolite and compass so as to provide information with which to compare the VLF results.

Figure 11.55 (*opposite*) A variety of geophysical profiles acquired using different geophysical methods over mineralised metasediments at Sourton Tors, Devon, UK: (A) magnetic total field; (B) SP; (C) VLF, and (D) the geological cross-section

The VLF instrument used was a Scintrex VLF-3 in both VLF-EM and VLF-R modes using two orthogonal VLF transmitters: NAA, USA (24 kHz) and Ste Assise, France (16.8 kHz) providing the H-polarisation and E-polarisation data, respectively. The type of current flow around an infinitely-resistive two-dimensional void, such as provided by the galleries, over a conductive substrate is shown in Figure 11.56B. There is obvious current channelling occurring as indicated by the closeness of the current flowlines around the gallery.

Figure 11.57 (A) VLF-R apparent resistivity, and (B) phase profiles over a known drainage gallery: H-polarisation mode using the NAA, USA, transmitter (24 kHz). From Ogilvy *et al.* (1991), by permission

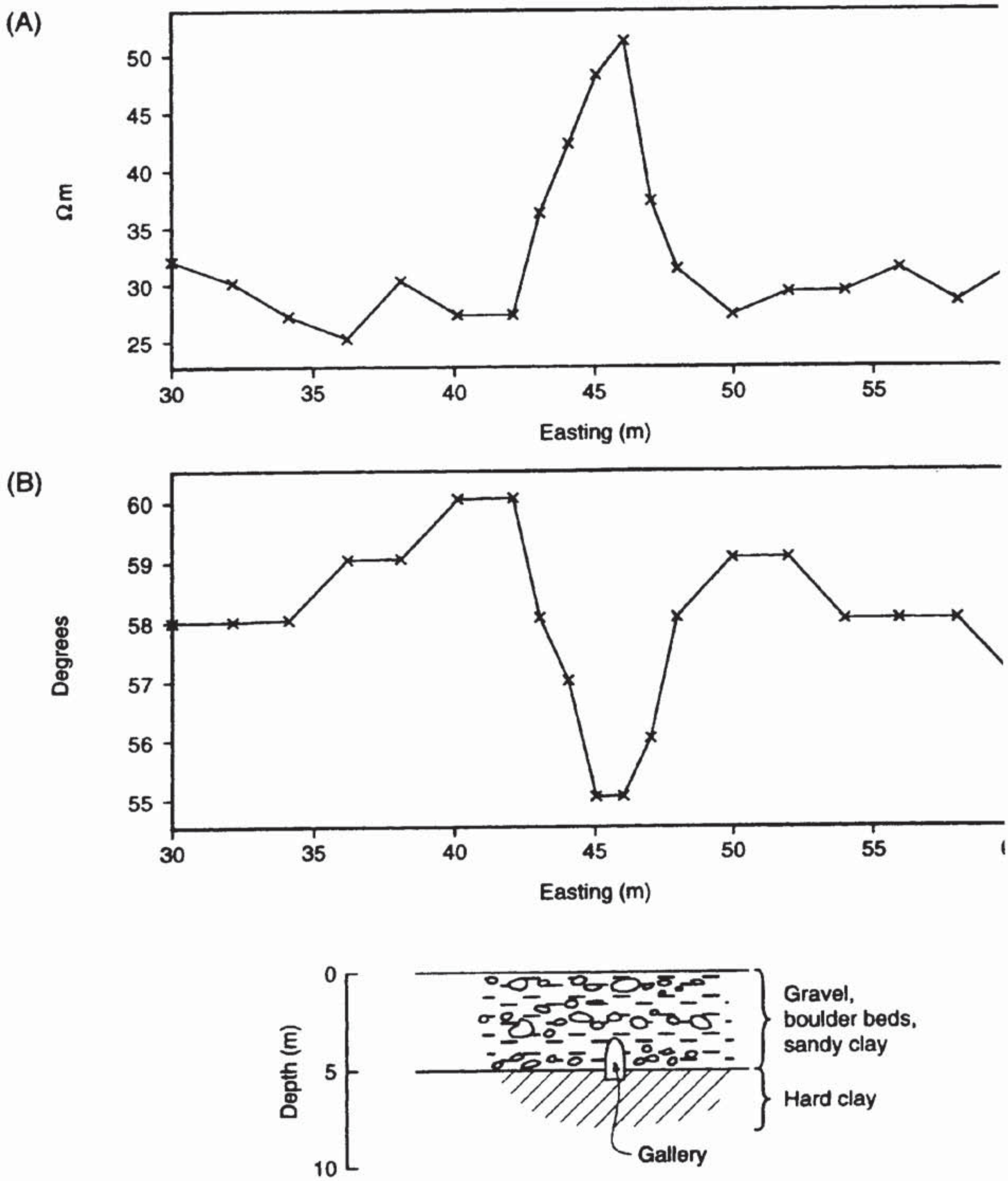

The VLF-EM survey produced absolutely no response from the gallery system. Given the true resistivities of the gravel beds (200 Ω m) and the underlying clays (10 Ω m), and the geometry of the gallery with respect to the H-polarisation, no vertical magnetic gradient is generated by such a structure.

In contrast, however, the VLF-R H-polarisation results produced anomalies which could be directly correlated with the gallery system and which could be modelled using two-dimensional inversion routines. Pronounced apparent resistivity (52 Ω m) and phase (5° peak-to-peak) anomalies were observed directly over a known gallery position (Figure 11.57). The decrease in phase above the gallery is indicative of a resistive structure below the uppermost layer. As it is known that the substrate is conductive clay, the only resistive target available is the gallery. This demonstrates the effectiveness of H-polarisation VLF-R measurements in the detection of air-filled voids over conductive media.

This example also demonstrates the importance of using orthogonal transmitters. The absence of any detectable VLF-EM magnetic field response for H-polarisation suggests that the observed anomaly must be caused by the electric field component E_x of the complex impedance ratio E_x/H_y. It is also a good example of the dominance of galvanic currents over vortex current flow arising from the deviation and concentration of current flow lines around the air-filled gallery. Such current flow results in larger-than-normal primary electric fields, with a consequent increase in apparent resistivities; hence the observed apparent resistivity high immediately over the target.

11.5 THE TELLURIC METHOD

11.5.1 Principles of operation

As a consequence of the presence and fluctuation of the Earth's magnetosphere (see Chapter 1), natural low-frequency magnetotelluric fields occur which induce alternating currents within the ground. These currents flow parallel to the ground surface and cover huge areas and are known as 'telluric' currents – named after Tellus, the Earth Goddess in Roman mythology. The electric current fields fluctuate continuously in direction and magnitude at any point in response to the temporal variations in the ionosphere and magnetosphere caused by extraneous influences (solar wind, etc.). Distant lightning gives rise to frequencies in the range 1–400 Hz, and changes in density of conductive plasma (solar wind) impinging on the Earth's magnetic field generate frequencies between 0.0005 and 1 Hz. The magnitude of the electric field gradient is of the order of 10 mV/km. Electrical noise is also present, generated by electric storms, seawater currents, sferics, and man-made sources, such as electrified railway and tram lines.

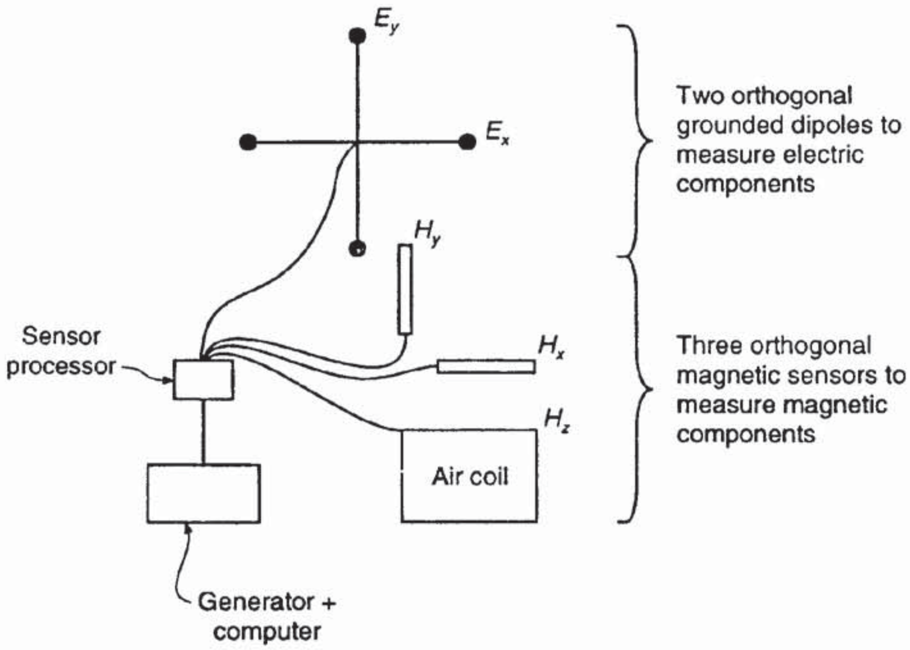

Figure 11.58 Telluric current flow around a sub-surface structure

In a uniform conductive earth, the telluric currents flow parallel to the ground surface with decreasing amplitude with depth. If there is a large-scale resistive sub-surface structure present, such as a salt dome or anticline, then the telluric current flow will be distorted and directed into the more conductive material above; similarly, if a large conductive target is present, such as a massive orebody, then the current will flow towards the more conductive material (Figure 11.58). The exploration method is designed to locate the distortions of the telluric fields. Historically, the telluric method has been used in the location of salt domes in exploration for hydrocarbons, particularly in Russia, Europe and North Africa. It has not been used widely in the USA as the salt domes there are generally too small to give rise to significant telluric anomalies. The method has also been used in the search for massive sulphide deposits and in geothermal resource evaluation.

11.5.2 Field measurements

The potential gradient is measured across two pairs of orthogonal non-polarisable electrodes, at a base station located over ground that is thought to be electrically uniform or remote from the type of target being sought. A second pair of orthogonal non-polarisable electrodes are used as mobile search dipoles. The potential gradient across each dipole within each pair is measured at both the mobile and base stations simultaneously over a period of several minutes. If the ground is electrically uniform below the base station, the two horizontal components of the electric field measured at right-angles should be the same, irrespective of azimuth. The locus of the electric vector at the base station should, therefore, describe a circle.

In actuality, with the presence of various components of electric noise in addition to the telluric currents, the base-station field vector does not describe a circle. However, a mathematical function can be applied to the data to constrain the results to conform to a circle with unit radius. This same mathematical function is applied to the dataset measured simultaneously at the mobile pair of dipoles in order to correct for the electric noise and time-variant field. By referring the measured signals at the mobile dipoles to those at the base station, the data from the mobile station are normalised. If there is no perturbation to the flow of telluric currents, the electric vector at the mobile station also describes a circle. If, however, there is some distortion due to the presence of a sub-surface target, the field vector at the mobile station describes an ellipse. The orientation of the major axis of the ellipse at the mobile station is aligned to the direction of maximum current flow at that point. The ratio of the area of the ellipse to that of the base-station circle gives a relative indication of the amplitude of the telluric anomaly.

Interpretation of telluric results can be qualitative, especially when the method is used for reconnaissance purposes. For more quantitative analysis, the effect of certain simple two-dimensional geological structures, such as an anticline, fault or horizontal cylinder, and three-dimensional shapes, such as a sphere or ellipsoid, can be calculated theoretically. Model curves can be produced against which measured anomalies can be matched. Detailed discussions of such procedures have been given by Keller and Frischknecht (1966) and by Telford *et al.* (1990).

11.6 THE MAGNETO-TELLURIC (MT) METHOD

11.6.1 Principles of operation

The magneto-telluric method uses measurements of both the electric and magnetic components of the natural time-variant fields generated as described in Section 11.5.1. The major advantage of this method is its unique capability for exploration to very great depths (hundreds of kilometres), as well as in shallow investigations, all without the use of an artificial power source (with the exception of 'controlled-source' versions of the method).

The *natural-source magneto-telluric* method uses the frequency range 10^{-3} to 10 Hz, while the *audio-frequency MT* (AMT or

AFMAG) method operates within the higher range 10–10^4 Hz using sferics as the main energy source. The main disadvantage with the natural-source MT methods is the erratic signal strength. The variability in source strength and direction requires substantial amounts of stacking time (5–10 h) per site, thus making MT soundings expensive and production rates slow. AMT measurements can be made faster owing to the slightly higher frequencies, but variability of local thunderstorm sources and signal attenuation around 1 Hz and 2 kHz can degrade data quality. For an example of the relative speed of measurements, three AMT soundings were made in six hours within the crater region of White Island, an active volcano 50 km to the north of North Island, New Zealand (Ingham 1992).

In the early 1970s, David Strangway and Myron Goldstein (Goldstein and Strangway 1975), at the University of Toronto, introduced the principle of an artificial signal source which was dependable and strong enough to speed up data acquisition and improve the reliability of results. The *controlled-source MT* methods typically operate within the frequency band 0.1 Hz to 10 kHz. The first commercial systems were produced by Zonge Engineering and Research Organization Inc., from 1978. Excellent overviews of the range of methods included within the MT family have been given by Vozoff (1986, 1991), and for controlled-source audio-frequency MT (CSAMT) by Zonge and Hughes (1991).

Table 11.3 Applications of controlled-source audio magneto-telluric (CSAMT) surveying

---

Exploration for:
- Hydrocarbons
- Massive sulphides
- Base and precious metals
- Geothermal resources

Geological mapping:
- Structure
- Lithology

Environmental applications:
- Mapping brine leakage from wells
- Mappings brine plumes from leaking tanks, etc.
- Mapping spilled petroleum products
- Monitoring leachate solution in *in-situ* copper recovery projects

Geotechnical applications:
- Structural analysis in mine planning
- Void detection in underground mines
- Mapping burn fronts in underground coal mine fires
- Monitoring enhanced oil recovery

References to all published sources have been given by Zonge and Hughes (1991)

AMT has been used in groundwater/geothermal resource investigations and in the exploration for major base metal deposits over the depth range from 50–100 m to several kilometres. The main application of the MT method, however, has been in hydrocarbon exploration, particularly in extreme terrain and to penetrate below volcanic materials, both types of areas where reflection seismology is either extremely expensive or ineffective. It has also been used recently to investigate a meteoric impact structure in Brazil (Masero *et al.* 1994).

Since the mid-1970s, CSAMT has been used in an increasing range of applications, and especially since the early 1980s within geotechnical and environmental investigations (Table 11.3). It is considered that CSAMT is an under-utilised method with many potential applications in the future. For this reason, CSAMT is described in some detail here.

11.6.2 Field measurements

The general field layout for a magneto-telluric survey is shown in Figure 11.59. It comprises two orthogonal electric dipoles to measure the two horizontal electric components, and two magnetic sensors parallel to the electric dipoles to measure the corresponding magnetic components. The magnetic sensors are made up of coils with several tens of thousands of turns around highly permeable iron cores with a total sensor length typically 2 m long. A third sensor measures the vertical magnetic component. Thus at each location, five parameters are measured simultaneously as a function of frequency. By measuring the changes in the magnetic (H) and electric (E) fields over a range

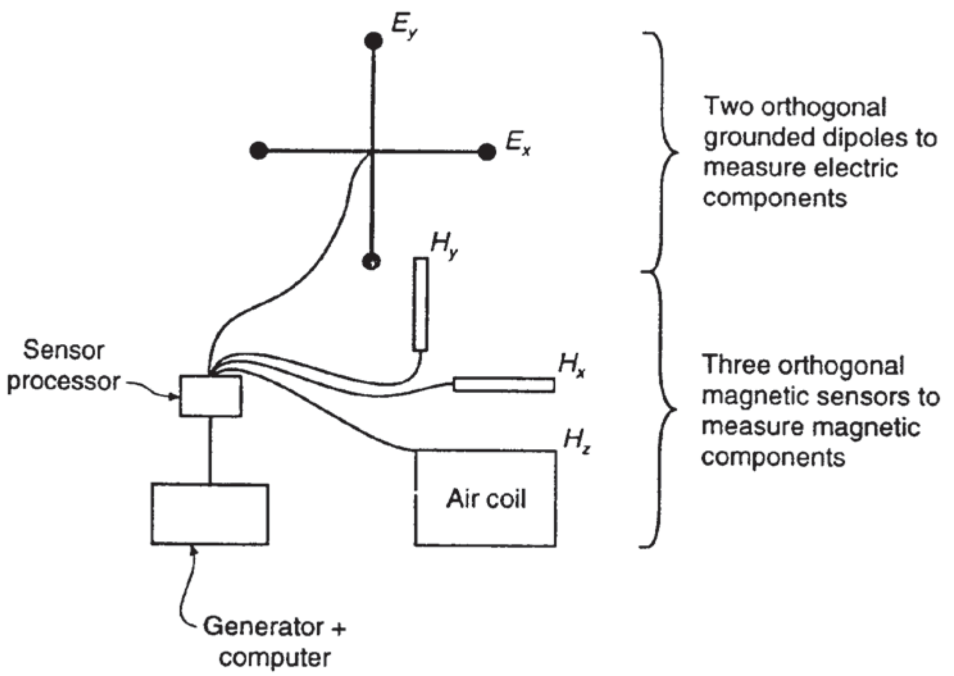

Figure 11.59 Generalised field layout for a magneto-telluric survey

of frequencies, an apparent resistivity sounding curve can be produced, analogous to that produced for electrical resistivity sounding but measured as a function of frequency rather than inter-electrode separation (Box 11.7). The lower the frequency, the greater is the depth penetration.

The data are displayed on log–log plots as apparent resistivity versus either frequency (f) or period ($1/2\pi f$). Over a uniform earth, the phases of the two orthogonal components differ by $\pi/4$, with the magnetic component lagging behind the electric component. If, however, the measured phase difference (θ) is not $\pi/4$, this is indicative of the ground being non-uniform. The basic definitions of apparent resistivity using magneto-telluric parameters were formulated by Cagniard (1953) whose name is given to the apparent resistivity and the impedance term which is the ratio of the orthogonal electric and magnetic horizontal components. The definitions apply to a layered earth; for more complex structures the full tensor impedance must be used (see later in this section).

Box 11.7 Determination of apparent resistivity from magneto-telluric data

Apparent resistivity (ρ_a) is approximated by:

$$\rho_a = \frac{0.2}{f}\left|\frac{E_x}{B_y}\right|^2 \equiv \frac{0.2}{f}\left|\frac{E_x}{H_y}\right|^2 = \frac{0.2}{f}|Z|^2$$

where E_x (nV/km) and B_y are the orthogonal electric and magnetic components, respectively. B_y is the magnetic flux density in nT, which is numerically equal in these units to the magnetising force H_y (A/m). The term Z is the *Cagniard impedance.*

For controlled-source MT surveys, either a loop or grounded dipole is used as a transmitter (the controlled source) with the same measurement configuration as described above. The grounded dipole is typically between 1 km and 3 km long; commonly two orthogonal grounded dipoles are used to provide two different source polarisations (Figure 11.60). The source may be several kilometres away from the receiver sensors. The location and orientation of the bipole source are important in determining the response of the ground at the receiver and have implications for the style of interpretations appropriate. Particular aspects of source polarisation effects have been discussed by Kellett *et al.* (1994) with respect to two massive sulphide deposits in Australia.

A variety of different field configurations are available, ranging from the simple scalar CSAMT, which provides a measure of the two

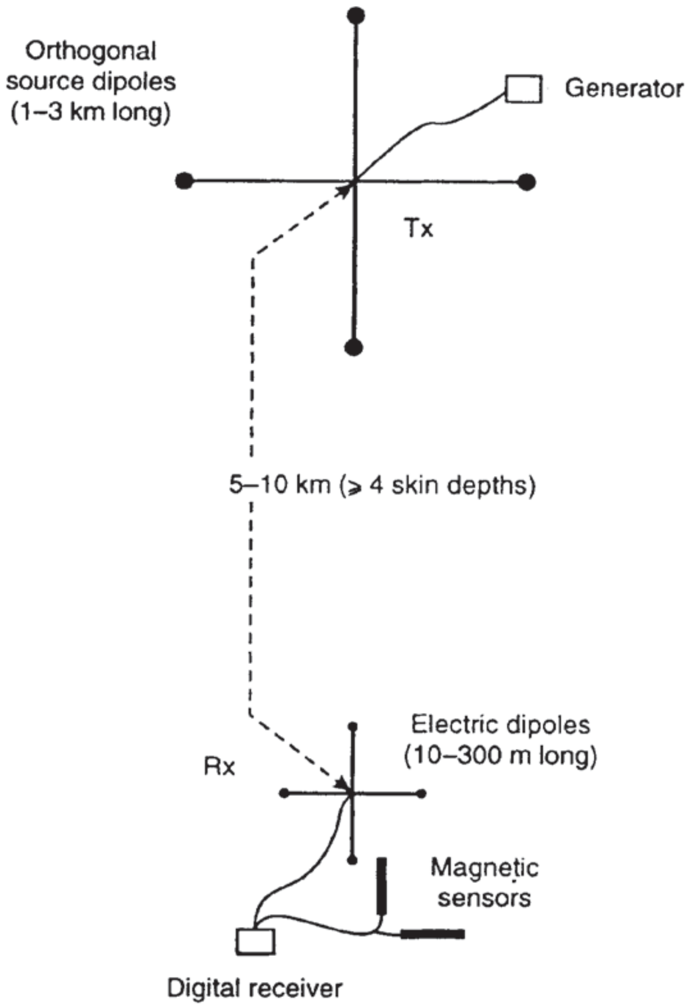

Figure 11.60 Generalised field layout for a controlled-source magneto-telluric survey

orthogonal electric and magnetic components as shown in Figure 11.61A, to vector CSAMT with one source and two sets of orthogonal components (Figure 11.61B), and full tensor CSAMT with either coincident or separated sources (Figures 11.61C and D, respectively).

11.6.3 Interpretation methods

Since the early 1980s there has been a tremendous advance in the interpretation of both magneto-telluric and controlled-source MT soundings, particularly in relation to the computer inversion of sounding curves. Detailed discussions of interpretational methods have been given by Telford *et al.* (1990), Vozoff (1991), and Zonge and Hughes (1991).

Two examples of magneto-telluric soundings are shown in Figure 11.62. It is evident that the combined interpretation of phase difference as well as apparent conductivity can yield important information. As frequency decreases, phase anticipates the resistivity behaviour. For example, Model A in Figure 11.62 is for a resistive basement. With decreasing frequency, the phase difference increases

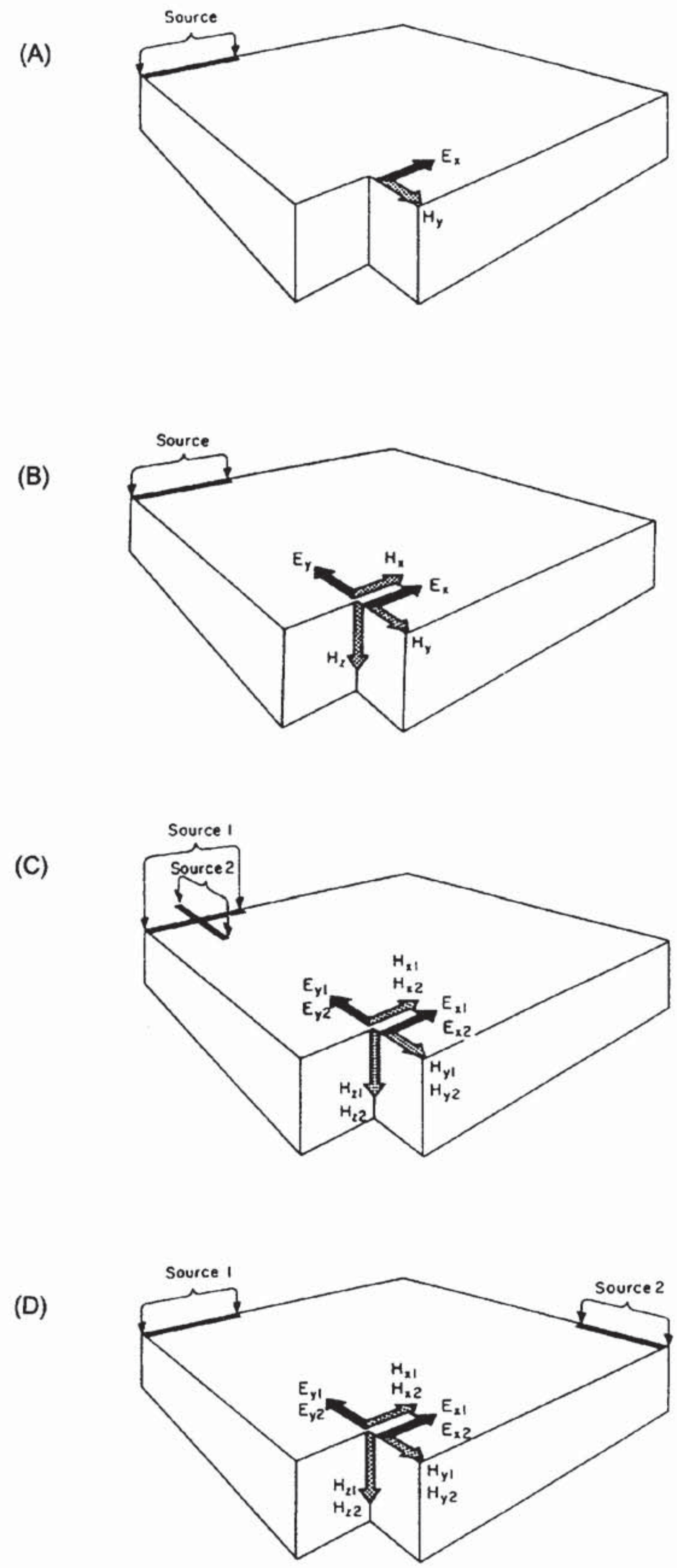

Figure 11.61 Schematics of: (A) scalar controlled-source audio-magneto-telluric sounding (CSAMT); (B) vector CSAMT; (C) tensor CSAMT with coincident sources; and (D) tensor CSAMT with separated sources. From Zonge and Hughes (1991), by permission

to achieve a peak at mid frequencies while the apparent resistivity increases to reflect the basement value. Conversely, in the case of a conductive basement, the phase passes through a minimum while the apparent resistivity decreases with increasing depth penetration.

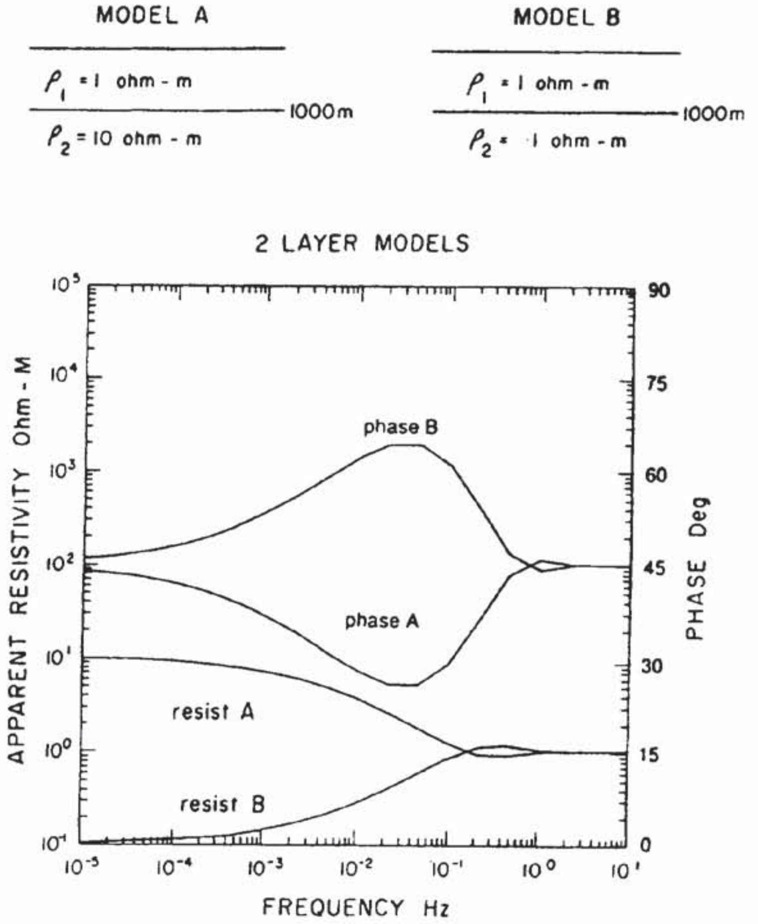

Figure 11.62 Magneto-telluric apparent resistivity and phase responses of 2-layer models. Model A = resistive basement; Model B = conductive basement. From Vozoff (1991), by permission

As long as the apparent resistivity is asymptotic to a constant value at low frequency, then phase difference should revert to 45° ($= \pi/4$). The apparent resistivity profile, however, is sensitive to near-surface inhomogeneities which may reduce the reliability of a resistivity-only inversion. Furthermore, at middle and higher frequencies the phase difference is more sensitive to deeper structures than apparent resistivity. Very shallow features may not be evident on the phase difference sounding while they may be seen on the apparent resistivity data.

In CSAMT surveys, considerable amounts of data processing may be necessary prior to inversion (see Figure 11.63). The processing is usually undertaken in two stages: pre-processing and interpretative processing.

Pre-processing conditions the acquired data by the removal of errors and noise. Interpretative processing includes optimising plotting conventions for the particular measured or derived parameters. In addition, certain data enhancement processes may be applied such as normalising, static correction, filtering and derivative calculations. As explained by Zonge and Hughes (1991), normalisation removes the effects of layering by subtracting, dividing or other means of deconvolving equal-frequency or equal-depth average values from a set of data. Regional effects can be removed by deconvolution,

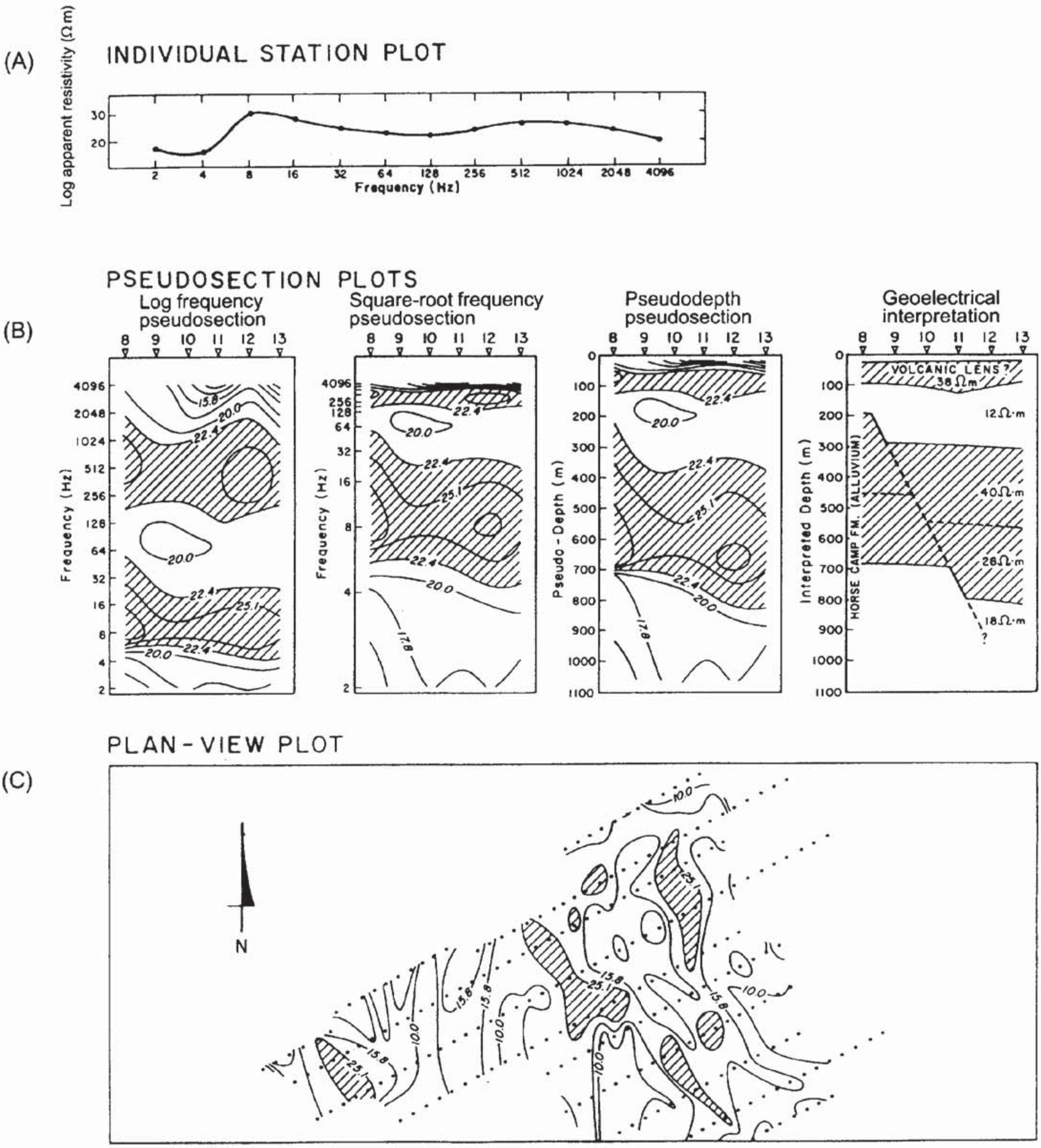

which can be used as well to enhance subtle lateral effects in survey areas with complex layering.

With multistep processing it is important to compare the processed results with the original resistivity and phase information in order to maintain a sense of reality in the processing. If the basic trends evident in the original data cannot be observed in the processed results, then this suggests that something is wrong with the processing. The interpretative processing stages should emphasise particular trends in the original dataset, not create new ones.

11.6.4 Applications and case histories

Zonge and Hughes (1991) have provided a selection of excellent case histories, several of which are abstracted here.

11.6.4.1 Mineral exploration

In central Washington, USA, gold mineralisation occurs in hydrothermally altered, silicified zones (reefs) within arkosic sandstones and conglomerates. The silicified zones occur in linear, steeply dipping bodies and are mostly concealed beneath surface cover.

A CSAMT apparent resistivity pseudosection (shown in Figure 11.64) was obtained across a known silicified reef several kilometres from Cannon mine, which is a major gold producer. A strong electrically resistive feature is associated directly with the silicified reef which outcrops at the surface along this transect. Each side of this feature are two conductive zones thought to be due to conductive clay alteration surrounding the silicification. Similar CSAMT lines were acquired over areas with surface cover and the resistive feature was mapped along strike. Such information was used to identify specific drill targets, thereby reducing the overall cost of the exploration drilling programme.

Another example of the use of CSAMT in gold exploration was that undertaken by Phoenix Geoscience in north-central Nevada, USA. The geology (Figure 11.65A) consists of alluvium over 60 m

Figure 11.63 (*opposite*) Display types for CSAMT data. (A) Plot of log apparent resistivity versus frequency. (B) Pseudosection displays with the corresponding geoelectric interpretation. (C) Plan-view plots. Other parameters, such as phase, may be plotted in similar ways. After Zonge and Hudges (1991), by permission

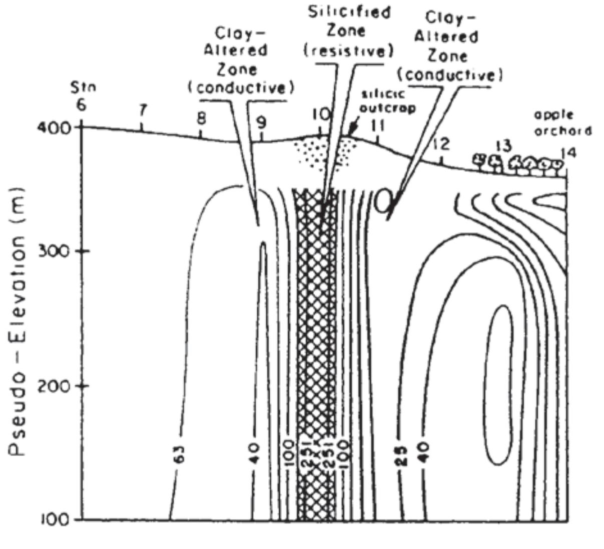

Figure 11.64 CSAMT apparent resistivity pseudosection over a silicified reef several kilometres from a gold mine which exploits this same structure. From Zonge and Hudges (1991), by permission

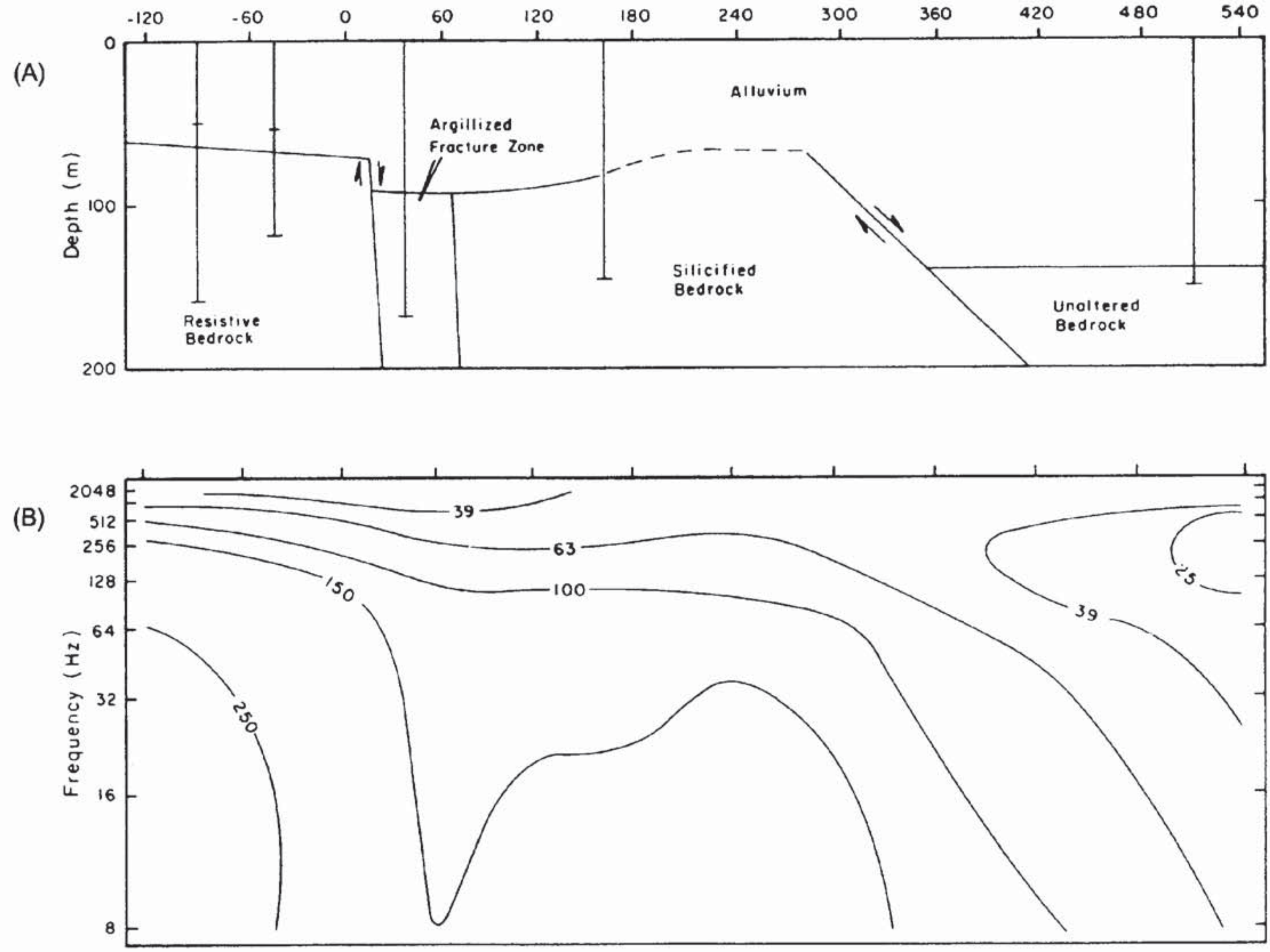

Figure 11.65 CSAMT results of a survey over a buried basement structure associated with a hydrothermal gold deposit: (A) geology and CSAMT results, and (B) CSAMT Cagniard resistivity data, courtesy of Phoenix Geophysics. From Zonge and Hughes (1991), by permission

thick overlying silicified Palaeozoic sediments. Graben faulting has resulted in the bedrock interface varying considerably in depth. The gold deposit occurs in a steeply dipping fracture zone which exhibits argillic alteration. The gold deposit has been proved by drilling but has not been mined since 1988.

An example of a CSAMT Cagniard resistivity pseudosection, obtained using 60 m dipoles, across the above structure is shown in Figure 11.65B. The general level of the bedrock interface is well imaged by the 63 Ω m and 100 Ω m contours and shows a dipping trend beyond position 300 with low-resistivity material at greater depth beyond this point. The 150 Ω m contour shows a prominent cusp around position 60, indicating the presence of a conductive feature. This correlates with the clay-rich fracture zone known to contain gold. The results of one-dimensional inversion of the resistivity data agree closely with basement depths obtained by drilling.

11.6.4.2 Hydrocarbon investigations

CSAMT surveys have been used predominantly for hydrocarbon exploration where either the terrain is unsuitable for seismic reflection surveys or where volcanic sequences obscure deeper structure from being imaged seismically. One such example is the Trap Spring Field in Railroad Valley, east-central Nevada, USA. Within the area, there are many graben-type sub-basins, each with its own unique lithology, structure, reservoir and source rocks, thermal history, etc. Fractured Oligocene ignimbrites source the oil which is trapped by the truncation of volcanics in an up-dip direction by a high-angle, basin-margin fault. The volcanics are overlain by 300 m to 3000 m of unconsolidated valley fill material. The material below the volcanics consists of Palaeozoic shales, dolomites and limestones. The top seal to the oil trap is a heavily argillized, unwelded zone at the top of the volcanics. There is only limited drilling information. Seismic reflection surveys are very expensive to procure, and the results less than satisfactory given the cost. Volcanic lenses produce unwanted multiples, unresolvable complex structures, a lack of predictability of target type and, occasionally, poor signal coupling.

A single line of scalar CSAMT was surveyed across the southern portion of the field and the Cagniard resistivity and phase data obtained (shown in Figure 11.66A and B, respectively). The resistivity versus frequency data reveal a characteristic shape with a cusp occurring below a frequency of 8 Hz. The steepness of the cusp sides increases as a result of a tuning effect associated with an extreme 2-layer low-over-high resistivity contrast which occurs at the top of the volcanics where a conductive argillized zone overlies resistive ignimbrites. This electrical marker is particularly sensitive to changes in layering and fault-related displacements, making the CSAMT method an effective structural tool with which to map the resistive basement.

In detail, a significant lateral discontinuity can be seen, especially on the 8 Hz data in Figure 11.66A (Cagniard resistivity plot), at position −2. This termination is associated with the basin-margin fault which bounds the western margin of the field. The overall interpretation utilising both CSAMT and drillhole information is shown in Figure 11.66C. The conclusions arising from the combined interpretation are: (1) the basin-margin fault dips moderately steeply to the east and (2) probably extends to the ground surface; (3) the eastern block is downthrown approximately 200 m with respect to the western side; and (4) the eastern block deepens consistently to the east as a result of successive step-faulting.

The trial CSAMT survey across the Trap Spring Field demonstrated that the method is an effective reconnaissance approach at only a quarter of the cost of reflection seismology. More detailed seismic surveys could be targeted on the basis of further CSAMT surveys.

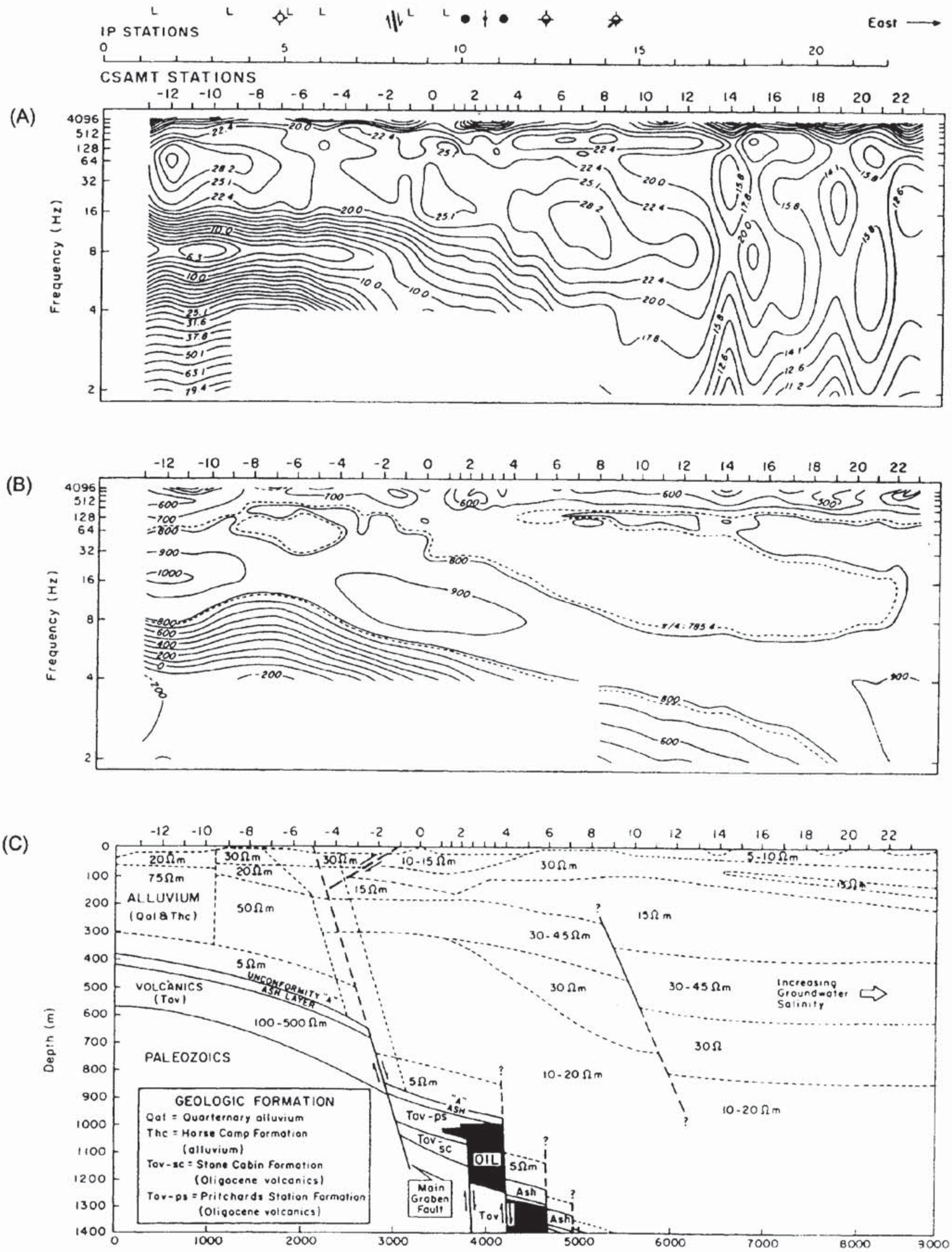
IP STATIONS
East
CSAMT STATIONS
(A)
Frequency (Hz)
(B)
Frequency (Hz)
(C)
Depth (m)
20 Ωm
75 Ωm
ALLUVIUM
(Qal & Thc)
30 Ωm
20 Ωm
50 Ωm
10-15 Ωm
15 Ωm
30 Ωm
5-10 Ωm
15 Ωm
30-45 Ωm
5 Ωm
UNCONFORMITY "A"
ASH LAYER
VOLCANICS
(Tov)
30 Ωm
30-45 Ωm
Increasing Groundwater Salinity
100-500 Ωm
30 Ω
PALEOZOICS
5 Ωm
10-20 Ωm
"A" ASH
Tov-ps
Tov-sc
OIL
5 Ωm
Ash
Main Graben Fault
Tov
10-20 Ωm
GEOLOGIC FORMATION
Qal = Quarternary alluvium
Thc = Horse Camp Formation (alluvium)
Tov-sc = Stone Cabin Formation (Oligocene volcanics)
Tov-ps = Pritchards Station Formation (Oligocene volcanics)

11.6.4.3 Environmental applications

Zonge and Hughes (1991) have provided several case histories of environmental applications of the use of CSAMT surveys. Space constraints at typical sites, high ambient cultural noise, lack of experienced CSAMT operators, and significant survey costs have precluded the use of the CSAMT method for environmental applications within the UK particularly, and to a lesser extent within western Europe. However, with a greater awareness of the effectiveness of the CSAMT method, applications at suitable sites may be forthcoming in the future.

An engineering company was commissioned to undertake a hydrogeological investigation over a 2.5 km^2 site of a potential commercial development of a desert area north of Phoenix, Arizona, USA. The supply of water to the development was of major concern; to have imported water via a surface pipeline would have resulted in enormous cost and potential legal problems. To have a water supply at the site would have significant benefits.

The local geology, knowledge of which was very limited at the start of this project, comprises granitic outcrops trending N50°W with basaltic lava flows, tuffs, agglomerates, and cinders, and separate schistose units, all laterally discontinuous suggestive of some structural control in the area. Apart from some basic regional gravity data and limited surface geological information, little else was known.

Two boreholes were constructed at the southern part of the property to a depth of about 150 m and approximately 450 m apart. In one hole, water was found at a depth of 91 m and at 43 m in the other, but pressure heads were minimal and the saturated zones were thin.

At this stage, three survey lines of CSAMT were acquired to provide additional information about the sub-surface hydrogeological environment. All three lines showed similar features on the apparent resistivity pseudosections, one of which is shown in Figure 11.67. A significant near-vertical feature is evident around station 8 which is thought to be due to a fault.

The apparent resistivity versus frequency data display the presence of a cusp at low frequencies (less than 128 Hz) as shown in Figure 11.68. The data show a spatial dispersion with the resistivity profile away from the supposed fault as indicated by line A in Figure 11.68 with a cusp at 64 Hz. Survey stations near the fault exhibit type-B behaviour with a much steeper cusp, the side slopes of which are increased owing to the focusing effect of decreased resistivity at depth near the fault. (This same type of behaviour was described in Section 11.6.4.2.) Computer modelling indicated the presence of a conductive layer at a depth of around 300 m, which could have been caused by a previously unknown aquifer at depth. Consequently, it was decided to deepen one borehole to investigate the interpreted conductive target. A significant water-saturated zone was encountered by the

Figure 11.66 (*opposite*) (A) Cagniard resistivity (Ω m), (B) phase difference (mrad) and (C) CSAMT/drillhole interpretation over the Trap Spring Field, Nevada, USA. From Zonge and Hughes (1991), by permission

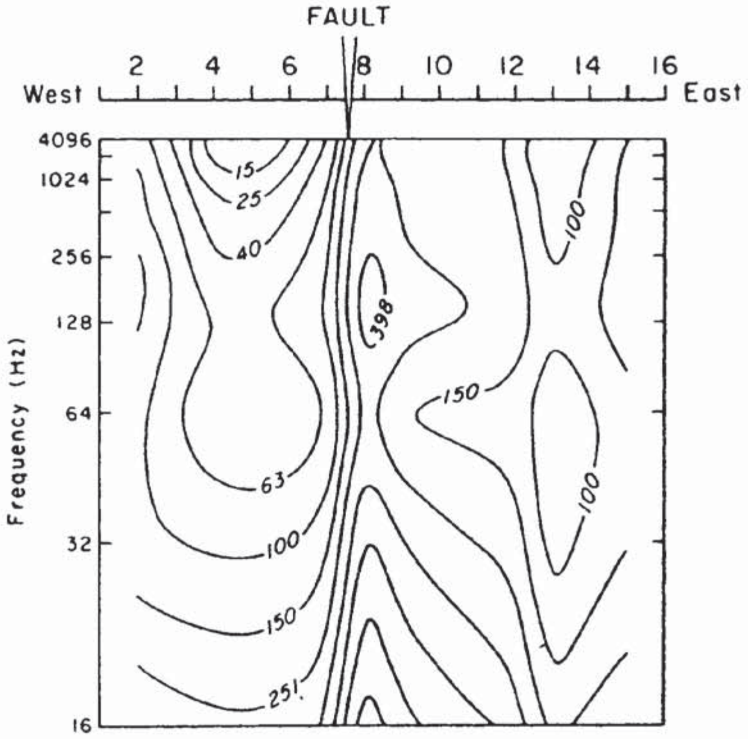

Figure 11.67 Apparent resistivity pseudosection across a fault zone; lower frequencies correspond to greater depth penetration. From Zonge and Hughes (1991), by permission

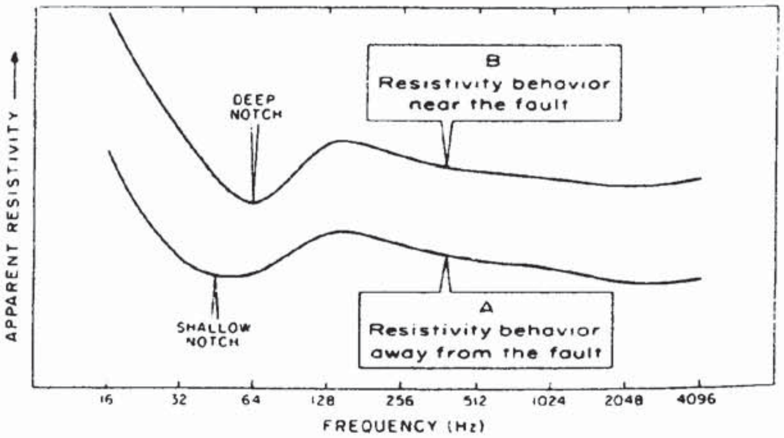

Figure 11.68 Comparision of resistivity responses adjacent to, and removed from, the fault. From Zonge and Hughes (1991), by permission

extended drilling at a depth of 317 m. The saturated zone was at least 61 m thick and had a pressure head of 360 psi on a 6-inch borehole. With a 17-inch diameter well, it was thought that the hole would have yielded between 600 and 1000 gallons per minute.

The successful use of CSAMT at this site helped avoid the premature abandonment of the property or the instigation of expensive and legally complicated surface pipeline option.

In the USA, there are thousands of abandoned, improperly plugged oil and gas wells. Where the producing horizon is overpressurised following secondary hydrocarbon recovery techniques, these wells can allow injected oilfield brines to migrate up the borehole and into shallower potable-water aquifers. For example, at one oilfield at Sac and Fox tribal lands of Lincoln County, Oklahoma, USA, oil has

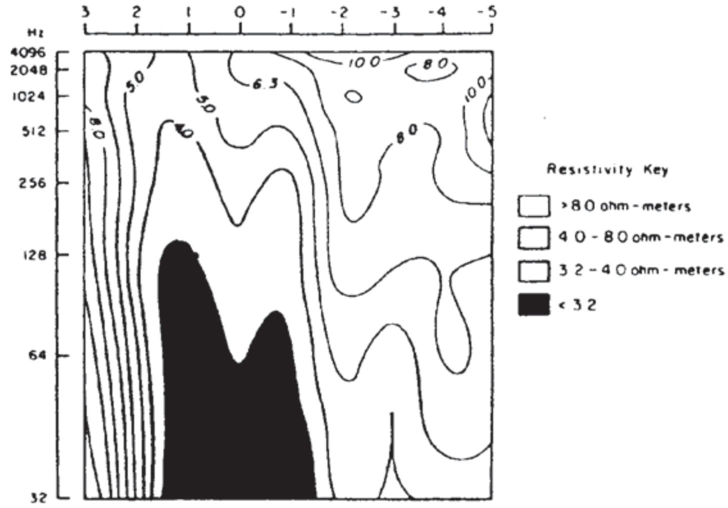

Figure 11.69 Apparent resistivity pseudosection near an abondoned injection well, showing the conductive plume (shaded) associated with upwardly migrating brine. From Zonge and Hughes (1991), by permission

been recovered from the Prue Sand Unit since the 1930s. Brine injection has been used since the 1950s for enhanced oil recovery. At the same location, the Vamoosa Formation is the major source of drinking water and its base occurs at depths of between 45 m and 135 m. Test wells drilled in 1979 indicated significant brine concentrations.

CSAMT surveys in the area indicated the presence at depth of plumes of conductive material around abandoned injection wells. One such apparent resistivity section is shown in Figure 11.69 on which the conductive plume is self-evident. Some plumes were found to reach shallow depths. Following the CSAMT survey two additional test wells were constructed, and bromide/chloride ratios established that the source of the contamination was undoubtedly the Prue Sand brines, as previously suggested by the CSAMT surveys.

In a similar vein, the migration of conductive fluids for *in situ* mining tests as well as injection tests have been mapped using CSAMT methods. In one example, an *in situ* leaching project was losing 90% of the injected fluid and it was important, therefore, to identify where the remainder of the injected material was going. A CSAMT survey was instigated and the resistivity results processed to provide depth-level resistivity slices (Figure 11.70). Conductive areas are shown shaded.

It is evident from Figure 11.70 that the main body of conductive material was centred at the 1600 level (as the areal extent is greatest at this level). It appeared that the fluid had migrated more slowly than hydrologists had suspected. Two CSAMT surveys were undertaken over exactly the same ground but one month apart to map the migration of the conductive plume. It was found that in some areas the apparent resistivity was changing by as much as 1% per day.

As with many geophysical methods, the use of the appropriate method(s) can yield valuable information about the three-dimensional

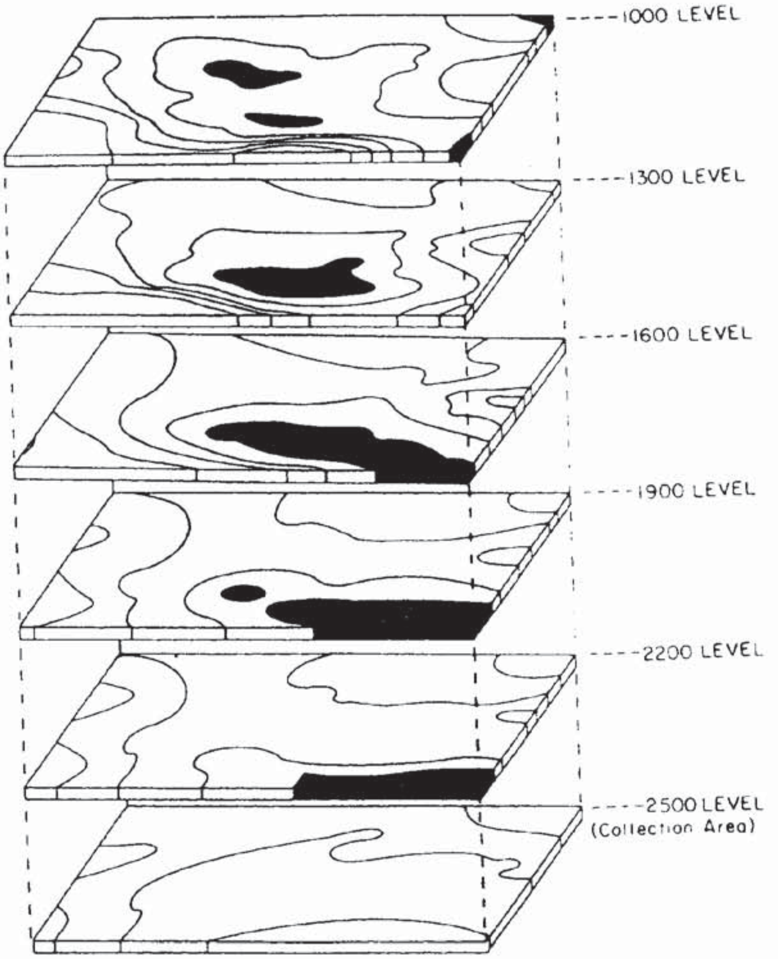

Figure 11.70 CSAMT depth-level resistivity slices; conductive zones are shown shaded. The largest areal extent of contamination can be seen at the 1900 level. From Zonge and Hughes (1991), by permission

spatial distribution of sub-surface features. In environmental applications particularly, the spatial changes as a function of time are increasingly important. Where appropriate, CSAMT along with other EM and electrical methods can provide valuable information cost-effectively and without any environmentally detrimental effects.

Chapter 12
Ground penetrating radar

12.1 INTRODUCTION

Since the mid-1980s, *ground penetrating radar* (GPR) has become enormously popular, particularly within the engineering and archaeological communities. However, radar has been used for geological applications since the 1960s, especially in connection with the development of *radio echosounding* of polar ice sheets. Glaciological applications of radar are now very well developed. Despite the recent upsurge in interest in the method, general experience in data processing and interpretation within the engineering community in particular has not kept pace with advances in technology or computer capabilities. There is enormous scope for the application of ground penetrating radar and it is extremely exciting to anticipate what might be achieved in the near future.

GPR applications can be divided into two virtually discrete classifications based on the main antenna frequencies. For geological applications, where depth penetration tends to be more important than very fine resolution, antennae with frequencies less than or equal to 500 MHz are used. For engineering or non-destructive testing (NDT) applications, antennae with frequencies of 500 MHz and greater are used, typically as high as 900 MHz or 1 GHz. A list of the range of applications of GPR is given in Table 12.1.

The first use of electromagnetic (EM) signals to locate remote buried objects is attributed to Hülsmeyer in a German patent in 1904, but the first published description of such investigations was by Leimbach and Löwy (1910), also in German patents. The systems used in these investigations employed continuous wave (CW) transmission. Hülsenbeck (1926) developed the first use of pulsed radar to investigate the nature of buried features.

Pulsed techniques were developed substantially over the following five decades. Its early civilian development was in radio echosounding of polar ice sheets (Cook 1960; Evans 1965; Swithinbank 1968). The first use of impulse radar for glaciological purposes was in the early 1970s (Watts *et al.* 1975). There is much pioneering research work being carried out in the glaciological field (for example, see papers by Wright *et al.* (1990), Hammond and Sprenke (1991) and Narod and Clarke (1994)). A useful review has been published by Bogorodsky *et al.* (1985). There has been wide acceptance of the radar method in certain areas of civil engineering, such as road pavement analysis and void detection behind tunnel linings. There has also been an expanding role for the method in geological applications, particularly in the rapid assessment of superficial deposits, location of swallow holes, etc. In archaeological studies, too, GPR has been used on many sites to identify potential excavation areas.

Many uses of ground penetrating radar have been described in the literature. These include the determination of permafrost thickness (Annan and Davis 1976); the detection of fractures in rock salt

Table 12.1 Range of applications of ground penetrating radar

Geological:
Detection of natural cavities and fissures
Subsidence mapping
Mapping sand body geometry
Mapping of superficial deposits
Soil stratigraphy mapping
Glacial geological investigations
Mineral exploration and resource evaluation
Peat thickness mapping and resource evaluation
Permafrost investigations
Location of ice wedges
Fracture mapping in rock salt
Location of faults, dykes, coal seams, etc.
Geological structure mapping
Lake and riverbed sediment mapping

Environmental:
Contaminant plume mapping
Mapping and monitoring pollutants within groundwater
Landfill investigations
Location of buried fuel tanks and oil drums
Location of gas leaks
Groundwater investigations

Glaciological:
Ice thickness mapping
Determination of internal glacier structures
Ice movement studies
Detection of concealed surface and basal glacier crevasses
Mapping water conduits within glaciers
Determination of thickness and type of sea and lake ice
Sub-glacial mass balance determination
Snow stratigraphy mapping

Engineering and construction:
Road pavement analysis
Void detection
Location of reinforcement (rebars) in concrete
Location of public utilities (pipes, cables, etc.)
Testing integrity of building materials
Concrete testing

Archaeology:
Location of buried structures
Detection and mapping of Roman Roads, etc.
Location of post-holes, etc.
Pre-excavation mapping
Detection of voids (crypts, etc.)
Location of graves

Forensic science:
Location of buried targets (e.g. bodies and bullion)

(Thierbach 1974; Unterberger 1978; Nickel *et al.* 1983; Olsson *et al.* 1983); and archaeological investigations (Bevan and Kenyon 1975; Imai *et al.* 1987; Bevan 1991). Examples of civil engineering and of other geological applications have been described by Darracott and Lake (1981), Leggo (1982), Ulriksen (1982), Leggo and Leech (1983), Davis and Annan (1989), Moorman *et al.* (1991), Doolittle (1993), and Huggenberger *et al.* (1994), among others. Cross-hole radar systems for use in crystalline rock have been described by Nilsson (1983), Wright and Watts (1982) and Olsson *et al.* (1990). GPR has also been used in police investigations to help locate buried bodies, such as in a double murder inquiry on Jersey, Channel Islands, in the 1980s, and in a gruesome search for human remains at two houses in Gloucester in 1994. In the latter, radar was instrumental in detecting where the corpses of 10 murdered women had been hidden within thick concrete inside the buildings, and in locating the remains of two other victims buried in a nearby field.

For regional and large-scale investigations, radar measurements have been made increasingly from aircraft and satellites. Such *remote sensing techniques* are beyond the scope of this chapter. Nevertheless, for sub-surface mapping in arid regions for hydrogeological purposes, for example, satellite radar imagery has been used to locate important features that would otherwise be extremely difficult to locate using ground-based surveys. An example of this is the identification of an ancient river drainage system now buried beneath desert sands in Africa and which was later proven to be an important source of potable water.

Ground radar was developed further by the US Army during the Vietnam War. Systems were constructed in order to locate labyrinths of tunnels excavated and used by the Viet Cong. At the end of the Vietnam War, the potential of GPR for civilian purposes was identified by Geophysical Survey Systems Inc. (GSSI), who are still the largest ground radar manufacturer internationally. In recent years other manufacturers have developed GPR systems, such as the PulseEKKO (Sensors & Software Ltd, Canada) and a range of systems produced by ERA Technologies Ltd, UK. Other companies are developing antennae to add on to existing radar systems, such as Radarteam AB (Sweden). Following the Falklands conflict in 1982, a radar system was developed with the aim of locating plastic mines that had been sown indiscriminately from the air.

12.2 PRINCIPLES OF OPERATION

A radar system comprises a signal generator, transmitting and receiving antennae, and a receiver that may or may not have recording facilities or hardcopy graphical output. Some advanced systems have an onboard computer that facilitates data processing both while acquiring data in the field, and post-recording.

The basic constituents of a radar system are shown in Figure 12.1. The radar system causes the transmitter antenna (Tx) to generate a wavetrain of radiowaves which propagates away in a broad beam. As radiowaves travel at high speeds (in air 300 000 km/s or 0.3 m/ns),

Figure 12.1 Simplified diagram of (A) the constituents of a radar system with (B) the interpreted section of (C) the radargram display. Adapted from Butler *et al.* (1991) and Daniels *et al.* (1988)

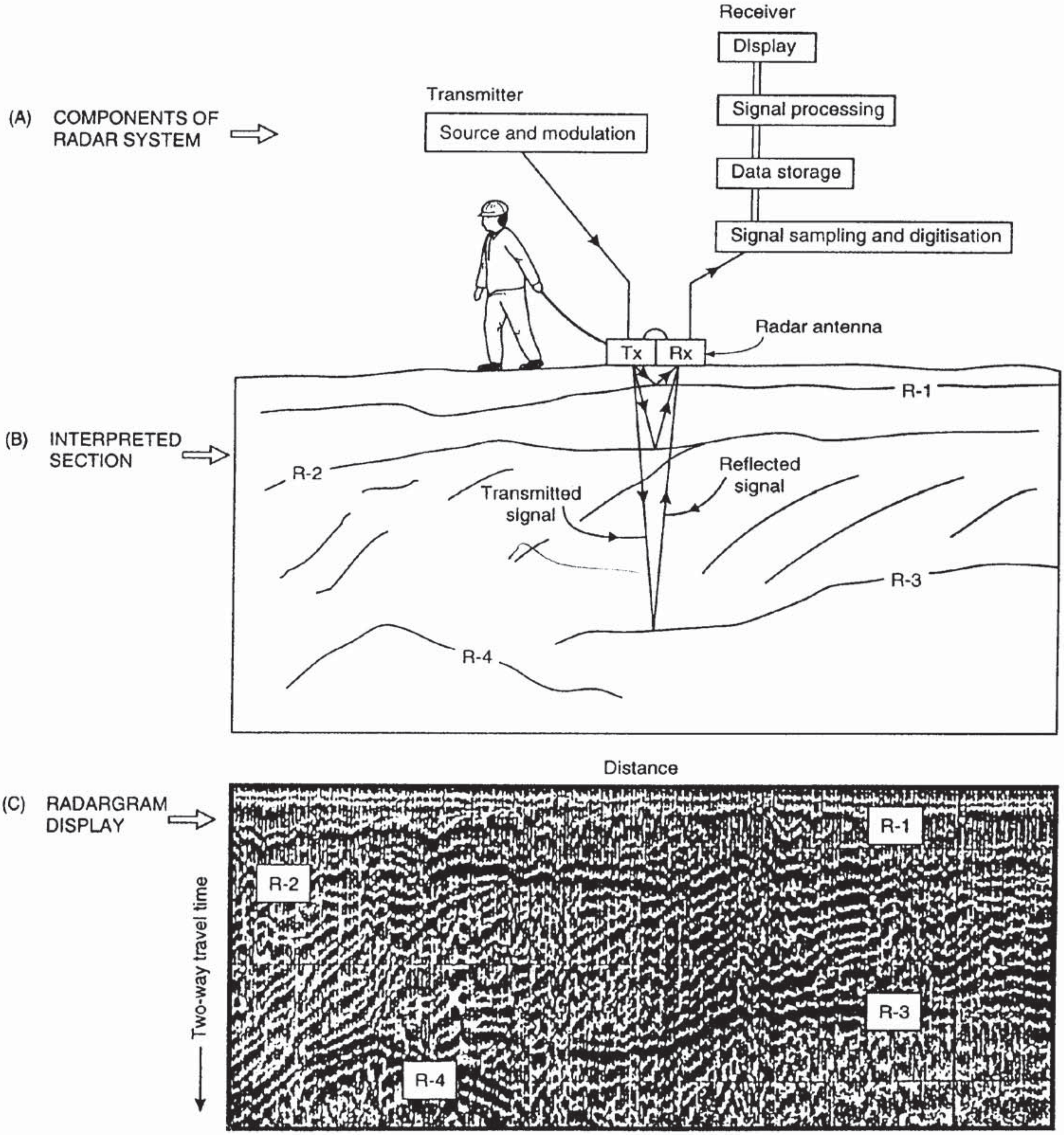

the travel time of a radiowave from instant of transmission through to its subsequent return to the receiving antenna (Rx) is of the order of a few tens to several thousand nanoseconds (ns; 10^{-9} seconds). This requires very accurate instrumentation to measure the transmit instant precisely enough for the final accuracy of the system to be reasonable with respect to the travel times in question. The antennae are used in either a monostatic or bistatic mode. *Monostatic mode* is when one antenna device is used as both transmitter and receiver, whereas *bistatic mode* is when two separate antennae are used with one serving as a transmitter and the other as a receiver. There are specific cases (such as in *wide-angle reflection and refraction* (WARR) measurements) when the bistatic mode is advantageous over the monostatic mode. The PulseEKKO system uses only bistatic antennae. For the majority of this chapter it can be assumed that any antennae are deployed in monostatic mode unless indicated otherwise.

The transmitter generates a pulse of radiowaves at a frequency determined by the characteristics of the antenna being used at a repetition rate of typically 50 000 times per second. The receiver is set to scan at a fixed rate, normally up to 32 scans per second, depending upon the system being used. Each scan lasts as long as the total two-way travel time range, which can be set from a few tens to several thousand nanoseconds. Each scan is displayed on either a video screen or a graphic recorder or both. As the antenna is moved over the ground, the received signals are displayed as a function of their two-way travel time, i.e. the time taken from instant of transmission to time of detection by the receiver, in the form of a *radargram*. This display is analogous to a seismic section (seismogram).

The pulse length of the transmitted radiowave should be short enough (typically <20 ns, depending upon antenna frequency and type) to provide resolvable reflections. It is important, therefore, that the shape and characteristics of the transmitted radiowave are both determinable and highly repeatable. The significance of this point will be discussed below (see Section 12.5). The manner in which the recorded signals are displayed on a graphic recorder, for example, are determined by the operator; a simplified output is illustrated in Figure 12.2. Signals with amplitudes greater than the set threshold are printed dark on the radar section as illustrated. In some cases, it may be most suitable to print both positive and negative, or when just positive or just negative. Displays can also be output in terms of *variable area wiggle* or wiggle trace only (just as in seismic data displays). Commonly, the more sophisticated digital recording systems display the amplitudes of the signals according to a grey scale or colour menu; for example, the strongest reflections can be picked out by the brightest colours.

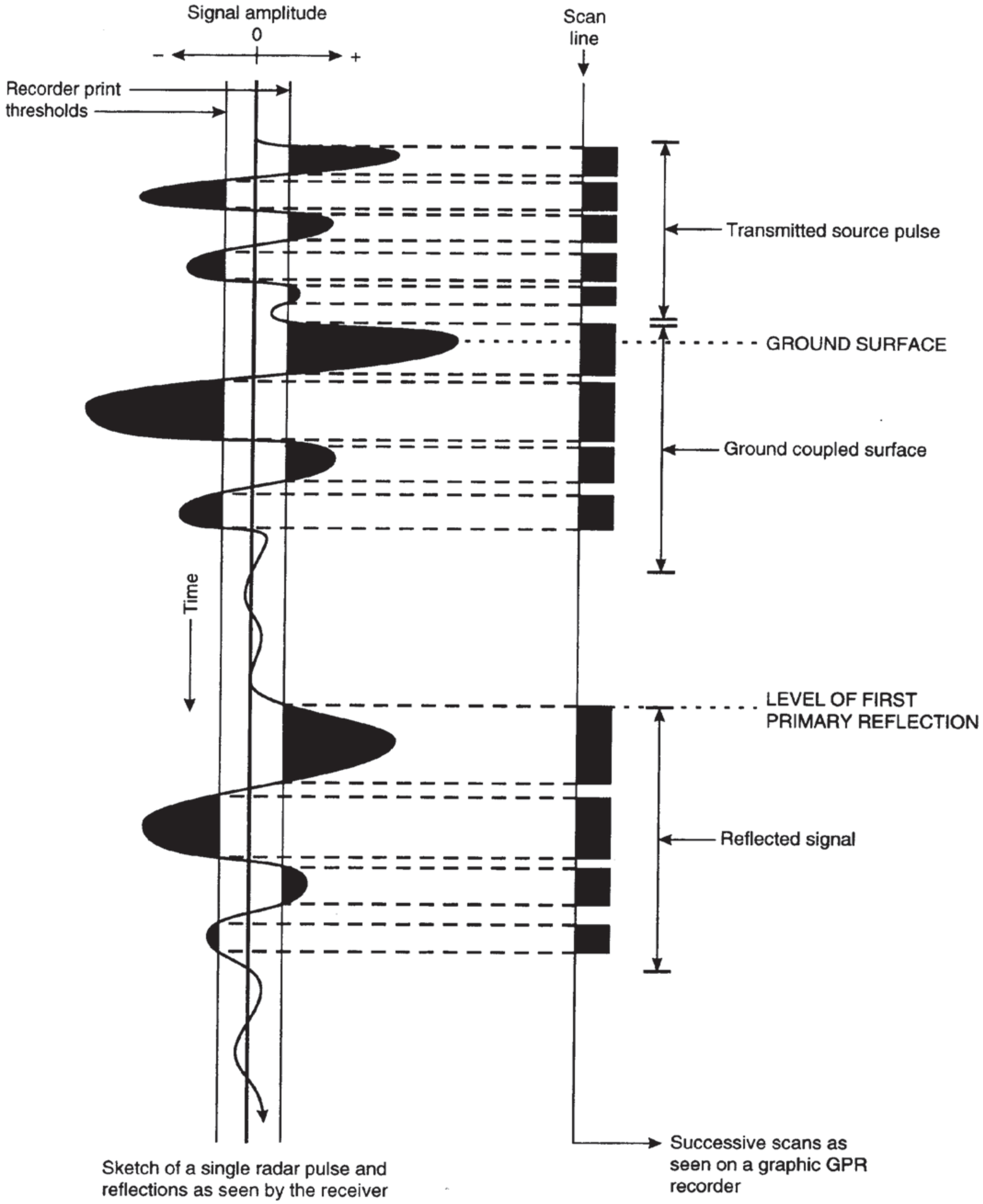
Signal amplitude
0
–
+
Recorder print thresholds
Scan line
Transmitted source pulse
GROUND SURFACE
Ground coupled surface
Time
LEVEL OF FIRST PRIMARY REFLECTION
Reflected signal
Sketch of a single radar pulse and reflections as seen by the receiver
Successive scans as seen on a graphic GPR recorder

Note that the source pulse consists of more than one wavelength and that it may have a complex waveshape. Ground coupling affects the shape and duration of the downgoing wavelet and thus the waveshape of any reflection is equally complex, but with a pulse-broadened duration due to attenuation of the higher frequency components of the signal. The reflection event consists of several wavelets, not just one, and it is imperative that this be borne in mind during the interpretation of radar data.

The measurement system should have sufficient dynamic range and sensitivity to be able to detect the low signal strengths associated with the returning radar pulses. It should also be able to produce printouts with adequate clarity for interpretation.

While the manufacturer's specifications may indicate the measurement accuracy of the timing within the instrument (e.g. to ±1 ns), this should not be interpreted as being equivalent to the resolution capability of interpretation. Vertical and horizontal resolution are discussed in Section 12.5.

Figure 12.2 (*opposite*) Schematic example of the translation of the received waveform (one scan) on to a graphic recorder output

12.3 PROPAGATION OF RADIOWAVES

12.3.1 Theory

The electromagnetic properties of materials are related to their composition and water content, both of which exert the main control over the speed of radiowave propagation and the attenuation of electromagnetic waves in materials.

The speed of radiowaves in any medium is dependent upon the speed of light in free space ($c = 0.3$ m/ns), the relative dielectric constant (ε_r) and the relative magnetic permeability ($\mu_r = 1$ for non-magnetic materials) (see Box 12.1). The success of the ground radar method relies on the variability of the ground to allow the transmission of radiowaves. Some materials, such as polar ice, are virtually transparent to radiowaves. Other materials, such as water-saturated clay and seawater, either absorb or reflect the radiowaves to such an extent that they are virtually opaque to radiowaves. It is the contrast in relative dielectric constant between adjacent layers that gives rise to reflection of incident electromagnetic radiation. The greater the contrast, the greater will be the amount of radiowave energy reflected. The proportion of energy reflected, given by the *reflection coefficient* (R), is determined by the contrast in radiowave velocities, and, more fundamentally, by the contrast in the relative dielectric constants of adjacent media (see Box 12.2). In all cases the magnitude of R lies in the range ± 1. The proportion of energy transmitted is equal to $1 - R$. The equations given in Box 12.2 apply for normal incidence on a planar surface assuming no other signal losses and refer to the amplitude of a signal. The power reflection coefficient is equal to R^2.

Box 12.1 Speed of radiowaves

The speed of radiowaves in a material (V_m) is given by:

$$V_m = c/\{(\varepsilon_r \mu_r/2)[(1+P^2)+1]\}^{1/2}$$

where c is the speed of light in free space, ε_r is the relative dielectric constant, and μ_r is the relative magnetic permeability (=1 for non-magnetic materials). P is the *loss factor*, such that $P = \sigma/\omega\varepsilon$, and σ is the conductivity, $\omega = 2\pi f$ where f is the frequency, ε is the permittivity $= \varepsilon_r \varepsilon_0$, and ε_0 is the permittivity of free space (8.854×10^{-12} F/m).

In low-loss materials, $P \approx 0$, and the speed of radiowaves, $V_m = c/\sqrt{e_r} = 0.3/\sqrt{\varepsilon_r}$.

It should always be remembered when dealing with ground radar that the radiation is electromagnetic and its propagation is described by Maxwell's equations with the electric (E) component orthogonal to the magnetic (H) component (Figure 12.3). The specific shape and size of the directivity pattern lobes are functions of the dielectric constant(s) of the host media. There is a danger in making the comparison of radargrams to seismograms that the vector nature of radar may be overlooked, so that incorrect assumptions are made about the way the radiowaves behave in geologic media. While seismic data processing can be used effectively in most cases, the electromagnetic polarisable characteristics of the radiowaves are more analogous to seismic S-waves than to P-waves.

Box 12.2 Amplitude reflection coefficient

The amplitude reflection coefficient is:

$$R = \frac{(V_1 - V_2)}{(V_1 + V_2)}$$

where V_1 and V_2 are the radiowave velocities in layers 1 and 2 respectively, and $V_1 < V_2$. Also:

$$R = \frac{\sqrt{\varepsilon_2} - \sqrt{\varepsilon_1}}{\sqrt{\varepsilon_2} + \sqrt{\varepsilon_1}}$$

where ε_1 and ε_2 are the respective relative dielectric constants (ε_r) of layers 1 and 2, applicable for incidence at right-angles to a plane reflector. Typically, ε_r increases with depth.

٢٥

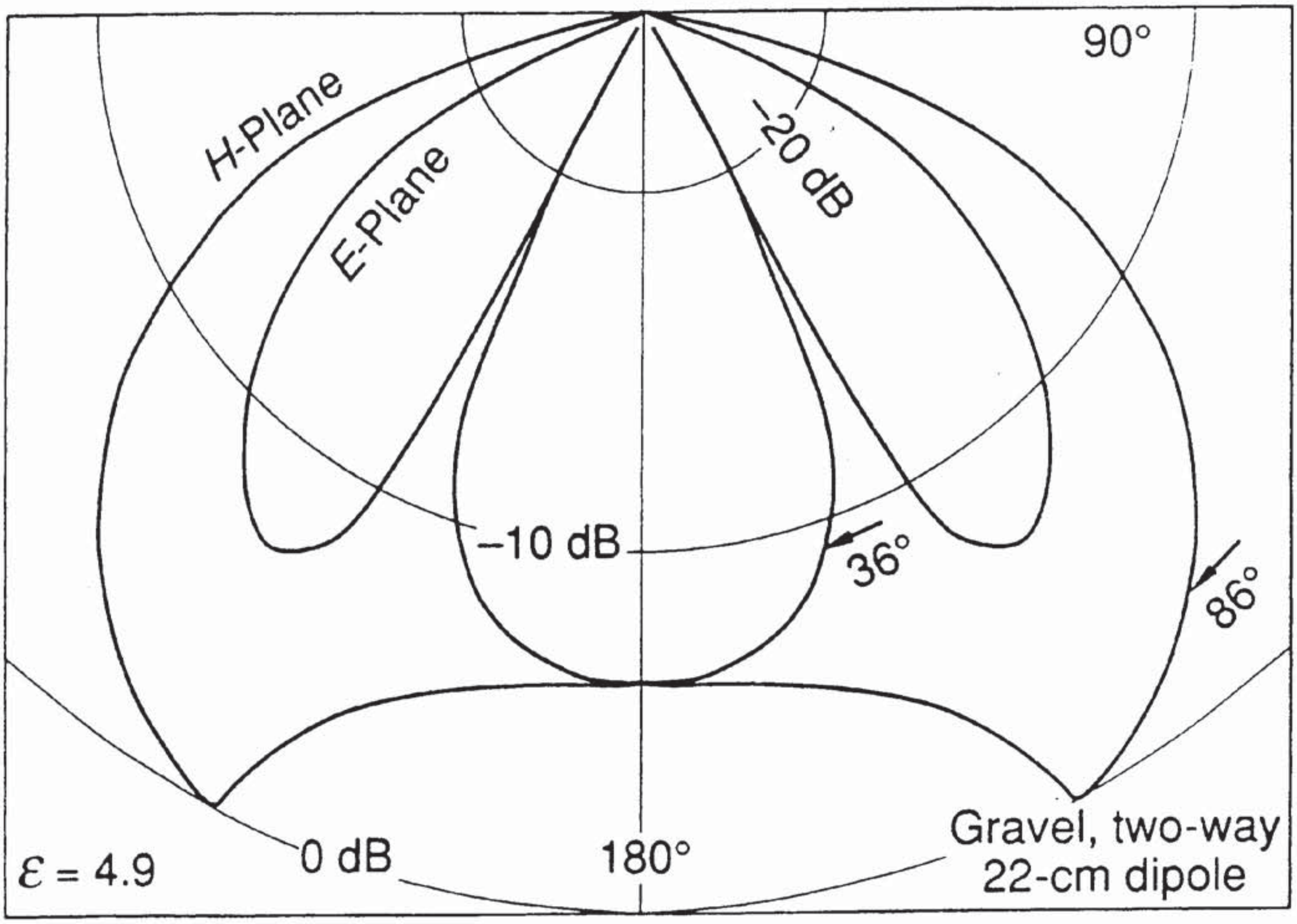

Figure 12.3 Theoretical *E*- and *H*-plane radar directivity patterns for a 22 cm resistively-loaded dipole situated over a medium with $\varepsilon = 4.9$. From Acrone *et al.* (1993), by permission

12.3.2 Energy loss and attenuation

Factors that result in a decrease in signal strength as radiowaves propagate through sub-surface media are illustrated schematically in Figure 12.4. Energy loss occurs as a consequence of reflection/ transmission losses about each interface and occur each time the radiowaves pass through a boundary. Furthermore, if there are objects with dimensions of the same order as the wavelength of the radar signal, these objects will cause scattering of energy in a random manner. This is known as *Mie scattering* and causes 'clutter' noise on the radar section. It is analogous to the noise seen on marine radar screens caused by the backscatter from seawaves in rough weather.

In addition to reflection/transmission losses at interfaces, energy is lost by *absorption* (turning the electromagnetic energy into heat). This is best pictured by analogy with a microwave oven which uses high-power radiowaves to cook food. A further loss of energy is caused by the geometrical spreading of the energy. The radar signal is transmitted in a beam with a cone angle of 90°. As the radio signals travel away from the transmitter, they spread out causing a reduction in energy per unit area at a rate of $1/r^2$, where r is the distance travelled.

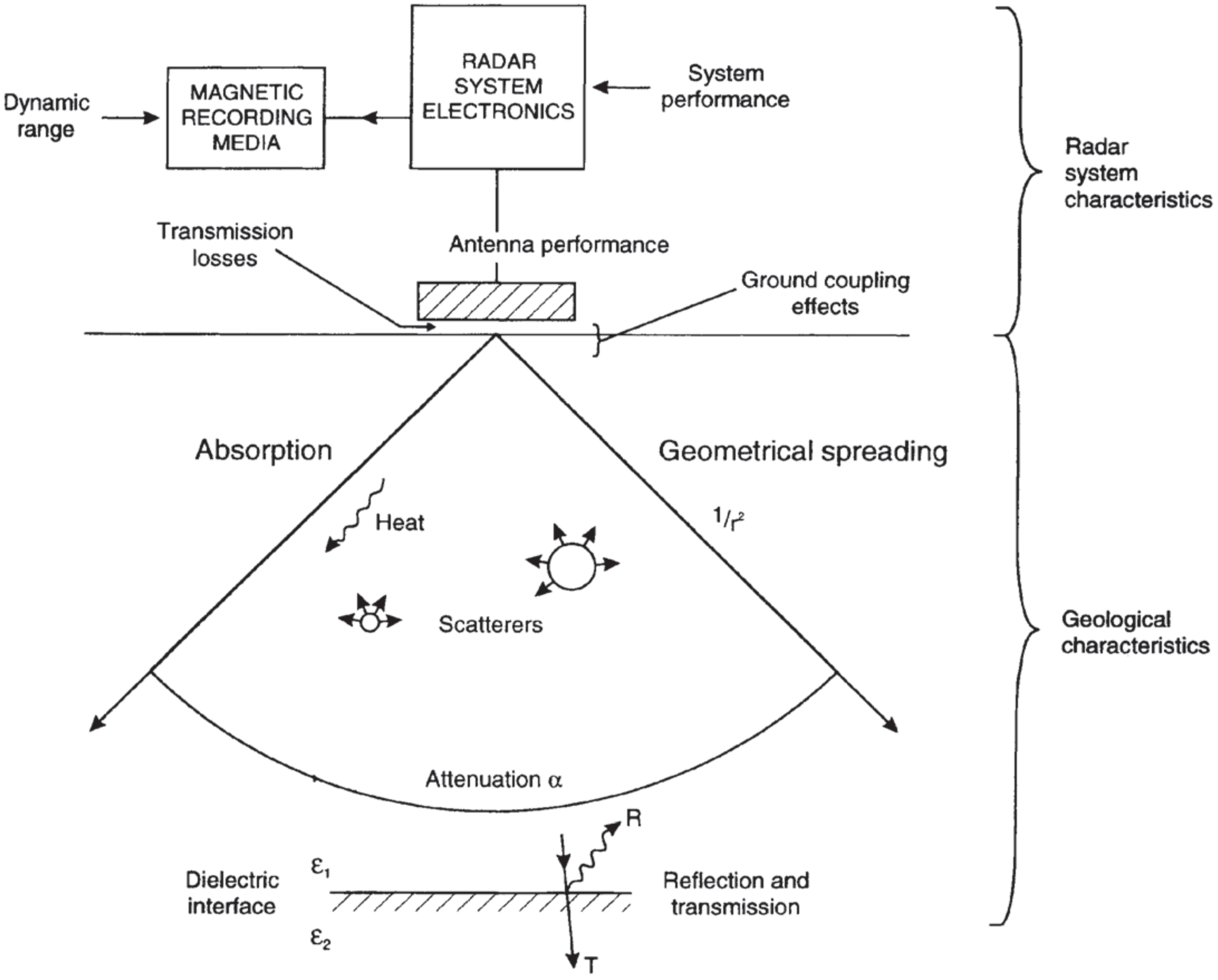

Figure 12.4 Processes that lead to reduction in signal strength

A fundamental cause of the loss of energy is *attenuation* which is a complex function of the dielectric and electrical properties of the media through which the radar signal is travelling. The attenuation factor (α) is dependent upon the electric (σ), magnetic (μ) and dielectric (ε) properties of the media through which the signal is propagating as well as the frequency of the signal itself ($2\pi f$). The bulk behaviour of a material is determined by the corresponding physical properties of the various constituents present and their respective proportional abundances.

As with other electromagnetic waves, the depth by which the signal has decreased in amplitude to $1/e$ (that is, to 37%) of the initial value is known as the skin depth (δ) and is inversely proportional to the attenuation factor (i.e. $\delta = 1/\alpha$). Mathematical definitions of the attenuation factor and skin depth are given in Box 12.3. Using the final term for the skin depth, and substituting typical values for seawater, it can be seen that the skin depth in seawater is only 1 cm, and for wet clay it is only 0.3 m. Where fresh dry rock is encountered, the conductivity term decreases substantially and hence the skin depth increases, and much greater depth penetration is likely. The variation in skin depth is shown in Figure 12.5 as a function of ground resistivity at the extremes of expected *in situ* relative dielectric constants (McCann *et al.* 1988).

Box 12.3

If the peak electric field strength on transmission is E_0, and at a distance x away it has reduced to E_x, the ratio of the two amplitudes is given by:

$$E_0/E_x = \exp(-\alpha x)$$

where α is the attenuation coefficient;

$$\alpha = \omega\left\{\left(\frac{\mu\varepsilon}{2}\right)\left[\left(1+\frac{\sigma^2}{\omega^2\varepsilon^2}\right)^{1/2} - 1\right]\right\}^{1/2}$$

where $\omega = 2\pi f$ where f is the frequency (Hz), μ is the magnetic permeability ($4\pi \times 10^{-7}$ H/m), σ is the bulk conductivity at the given frequency (S/m), and ε is the dielectric permittivity where $\varepsilon = \varepsilon_r \times 8.85 \times 10^{-12}$ F/m and ε_r is the bulk relative dielectric constant. The formula is valid for non-magnetic materials only.

The term $(\sigma/\omega\varepsilon)$ above is equivalent to the *loss factor* (P), such that:

$$P = \sigma/\omega\varepsilon = \tan D.$$

Also, skin depth $(\delta) = 1/\alpha$. When $\tan D \ll 1$, $\delta = (2/\sigma)(\varepsilon/\mu)^{1/2}$. Numerically:

$$\delta = (5.31\sqrt{\varepsilon_r})/\sigma, \text{ where } \sigma \text{ is in mS/m.}$$

It is important to remember that the simplified version of skin depth is valid only when the loss factor is considerably less than one. In order to determine when such conditions are valid, the graph shown in Figure 12.6 should be used. The figure shows the theoretical conductivity values (in mS/m) when the loss factor is equal to one. Thus the observed conductivity for the condition of being much less than unity to apply should be of the order of 0.05 of the theoretical conductivity. For example, if the observed true conductivity is 15 mS/m, then the loss factor needs to be considered in its full form in all cases other than when a 900 MHz antenna is being used, as long as the relative dielectric constant is greater than or equal to 6. If the full form of the attenuation factor is not used under these circumstances, the derived value of skin depth will be overestimated.

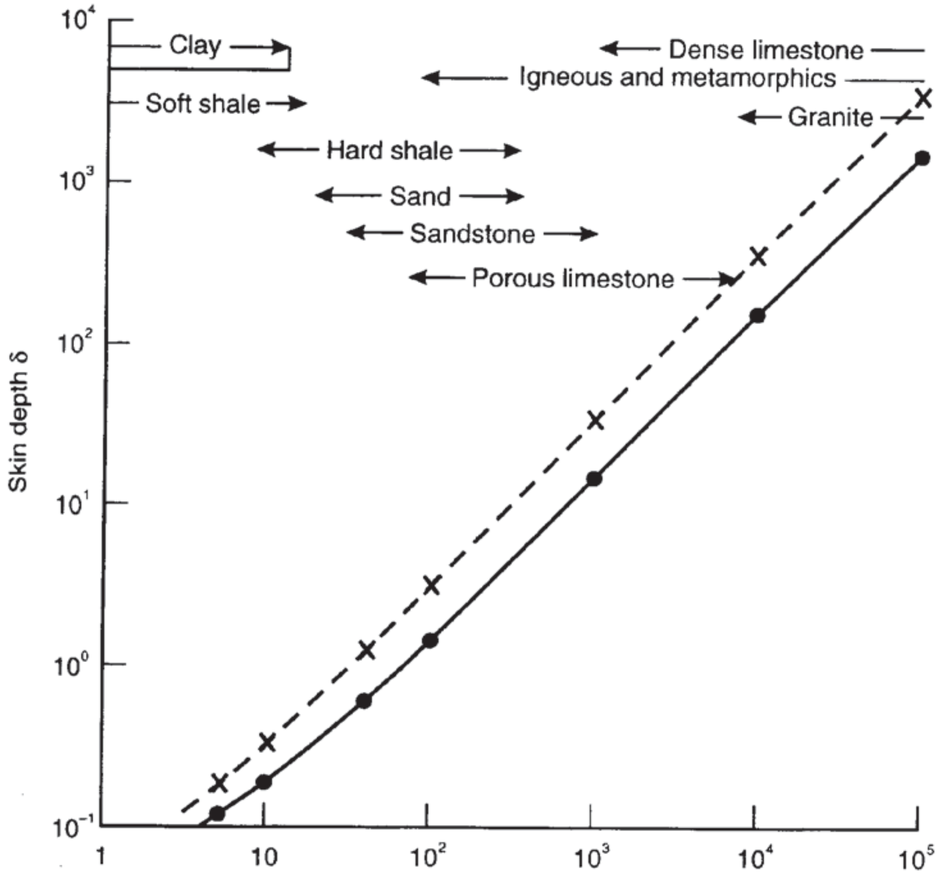

Figure 12.5 Variation of skin depth (δ) as a function of resistivity for $\varepsilon_r = 8$ and 40. After McCann *et al.* (1988), by permission

It should be noted that the skin depth does not equate to the depth of penetration of the ground radar. To determine radar range, instrumental factors also need to be taken into consideration in addition to those related to the sub-surface target and to the media through which the radiowaves travel. The total path loss for a given distance is made up of five terms: antenna losses; transmission losses between the air and the ground; losses caused by the geometrical spreading of the radar beam; attenuation within the ground as a function of the material properties; and losses due to scattering of the radar signal from the target itself. The radar range equation and definition of a radar system performance (Q) are given in Box 12.4 and the components affecting radiated and return power are illustrated schematically in Figure 12.7.

The system performance of modern radar equipment is between 120 and 160 dB, enabling a three-fold improvement in depth penetration under the same ambient conditions over that of a radar system with $Q = 80$ dB. The variation of radar signal range is shown in Figure 12.8 as a function of both attenuation and radar system performance (Q).

Within Box 12.4 are listed three types of target: smooth and rough plane reflectors and a point target. Of particular importance is the gF

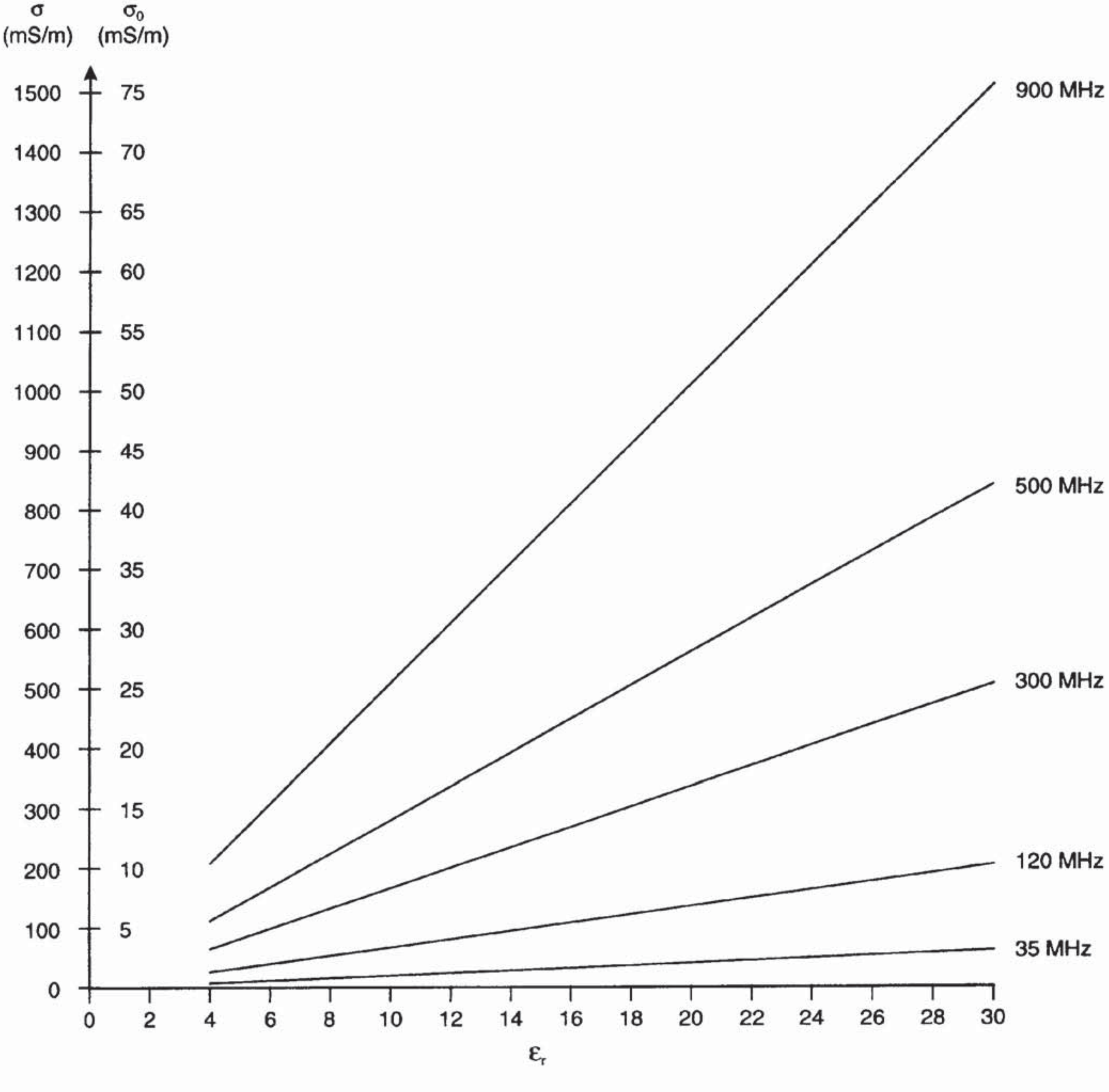

Figure 12.6 Conditions under which the loss factor (tan D) $\ll 1$

term in the first equation in Box 12.4. This product defines the power scattered by the target and also directed back to the receiver. The term g is the backscatter gain of the target and F is the target scattering cross-sectional area.

For a smooth plane reflector, the incident signal returned appears to be an image of the source, albeit reduced in power by the power reflection coefficient R ($=r^2$, where r is the amplitude reflection coefficient) of the interface, radiating upwards from a distance twice as far away as the boundary. The theory behind this is the same as in simple optics for a plane reflector.

Box 12.4 Radar range equation, and definition of Q

(Annan and Davis 1977)

Radar range equation (Ridenour 1947)
Q is the system performance (in decibels):

$$Q = 10\log\left\{\frac{E_{\mathrm{Tx}}E_{\mathrm{Rx}}G_{\mathrm{Tx}}G_{\mathrm{Rx}}V^2(gF)\exp(-4\alpha z)}{64\pi^3 f^2 z^4}\right\}.$$

The various terms are defined in Figure 12.7. Also:

$$Q = 10\log(P_{\mathrm{min}}/P_{\mathrm{s}})$$

where P_{min} is the minimum detectable signal power, and P_{s} is the source power.

In low-loss materials the range of z is approximately $10D_2$. In high-loss materials the range is approximately D_2/D_1, where:

$$D_1 = 2A/(40-10B_2)$$

$$D_2 = \frac{\{-Q+10\log(S)+10\log V^2+10[B_1+(B_3-2)\log f]\}}{40-10B_2}$$

$$S = E_{\mathrm{Tx}}E_{\mathrm{Rx}}G_{\mathrm{Tx}}G_{\mathrm{Rx}}/64\pi^3$$

where B_1, B_2 and B_3 are as listed in the table below.

Type of target	gF	B_1	B_2	B_3
Smooth, plane reflector	$\pi z^2 R$	$\log(\pi R)$	2	0
Rough, plane reflector	$\pi(V^2/16f^2+Vz/2f)R$	$\log(\pi VR/2)$	1	−1
Rayleigh point target	$(64\pi^5 a^6 f^4/V^4)R$	$\log(64\pi^5 a^6 f^4/V^4)$	0	4

For a rough, specular reflector, there is difficulty in defining the cross-sectional area of the target. Cook (1975) suggested that it equates to the area of the first Fresnel zone (see Figure 12.9). Consequently, where the wavelength of the roughness of the surface is greater than the diameter of the first Fresnel zone, the cross-sectional area, and hence the gF product, can be estimated. Where the wavelength of the surface roughness is less than the diameter of the first Fresnel zone, and especially when the amplitude of the roughness is greater than one-quarter wavelength, the actual cross-sectional target area is difficult to calculate. The power reflection coefficient would be reduced as a consequence of the greater scatter arising from such a surface roughness. The significance of the first Fresnel zone in terms of interpretation and resolution is discussed further in Section 12.5.

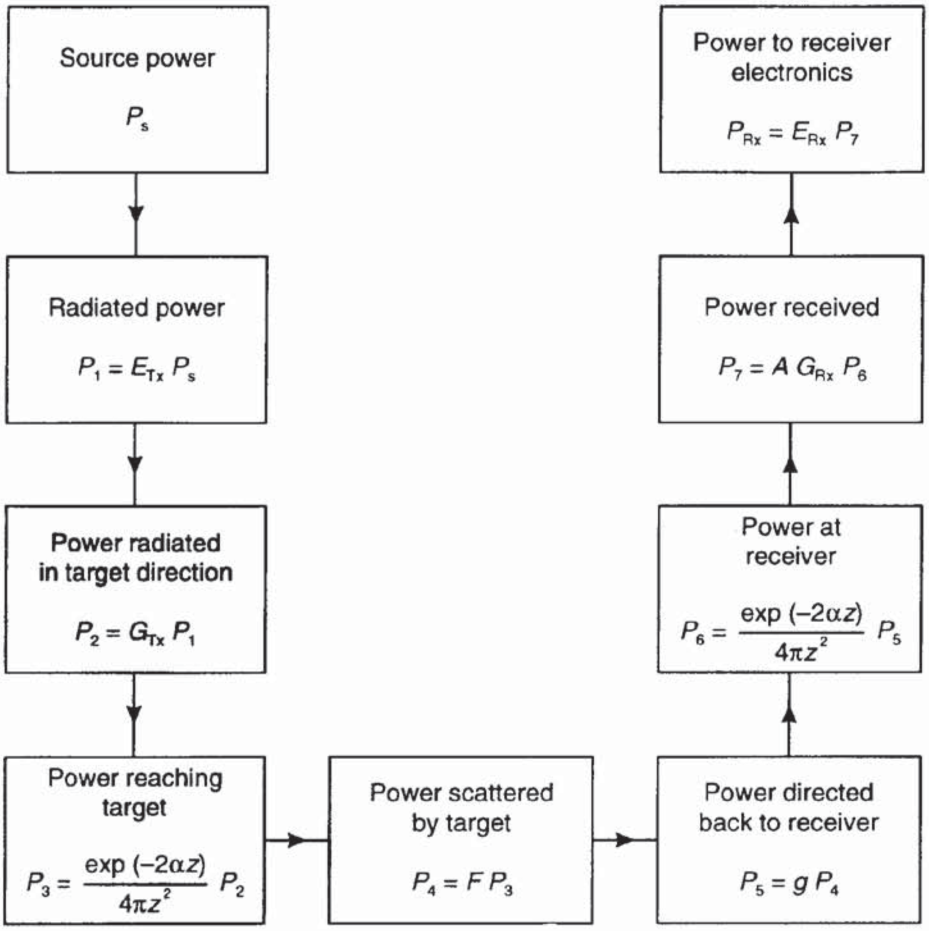

$E_{Tx, Rx}$ = efficiency of transmitter/receiver antenna
$G_{Tx, Rx}$ = transmitter/receiver gain
g = backscatter gain of target
F = target scattering cross-sectional area
z = distance of target from antenna
α = attenuation coefficient of medium
V = radiowave velocity of medium
A = effective area of receiver antenna ($= V^2/4\pi f^2$)
f = frequency of signal
R = power reflection coefficient at a boundary

Figure 12.7 Block diagram illustrating radiated and return power for a radar system. After Annan and Davis (1977), by permission

For a point target, the characteristics of the returned energy is described by the Rayleigh Law of scattering in which the gF product is very strongly dependent upon frequency (to the fourth power). It is assumed for the expression in Box 12.4 for a point source, that the radius of the target (a) is much smaller than the wavelength of the incident radiation. In materials that consist of cobbles and gravel, for example, or where the geological units are severely distorted over distances shorter than the wavelength of the incident energy, then the

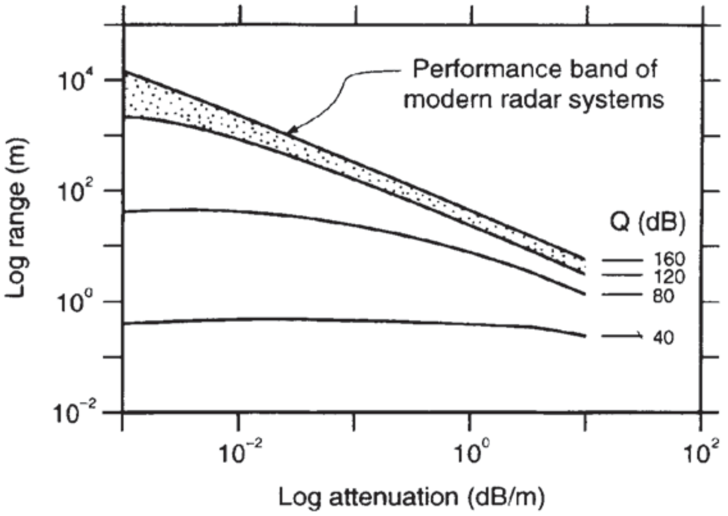

Figure 12.8 Radar range for radars with different system performances (Q) over a range of attenuation. From Davis and Annan (1989), by permission

amount of energy scattered is likely to be large and the resulting radargram is likely to show very few, if any, coherent reflection events associated with such materials. This characteristic can in itself be used indirectly during interpretation as being diagnostic of such material.

It has been shown (see Box 12.3) that attenuation is directly proportional to frequency. The higher the frequency, the greater will be the amount of attenuation. It is also evident that the bulk relative dielectric constant (ε_r) and bulk conductivity at the given frequency (σ) also affect attenuation significantly. Each of these properties is affected by the composition of the material and the electrical behaviour and relative abundance of each constituent. The loss factor ($\tan D$ in Box 12.3) is directly proportional to conductivity and inversely proportional to the relative dielectric constant and frequency. For saturated granular media, the conductivity and the relative dielectric constant of the saturating fluid will dominate over the respective matrix values. The bulk relative dielectric constant (ε_r) is roughly equal to the product of porosity (ϕ) and relative dielectric constant for the fluid (ε_f). The effect of this is that the more conductive the saturating fluid, and the greater the proportion of fluid present with a correspondingly high relative dielectric constant (remember: ε_r for water $= 81$), the greater will be the attenuation. Similarly, the greater the clay content, the greater will be the loss factor and hence attenuation. The importance of clay is that it possesses bound water within its lattice structure. Clay minerals also exhibit particular electrical properties as a result of their physicochemical structure, the details of which are beyond the scope of this section.

For both geological and engineering materials the electrical and dielectric properties, especially as functions of frequency, are still poorly understood. Furthermore, the petrophysical characteristics of such materials are largely unknown. The electrical and dielectric properties of materials are discussed in Section 12.4.

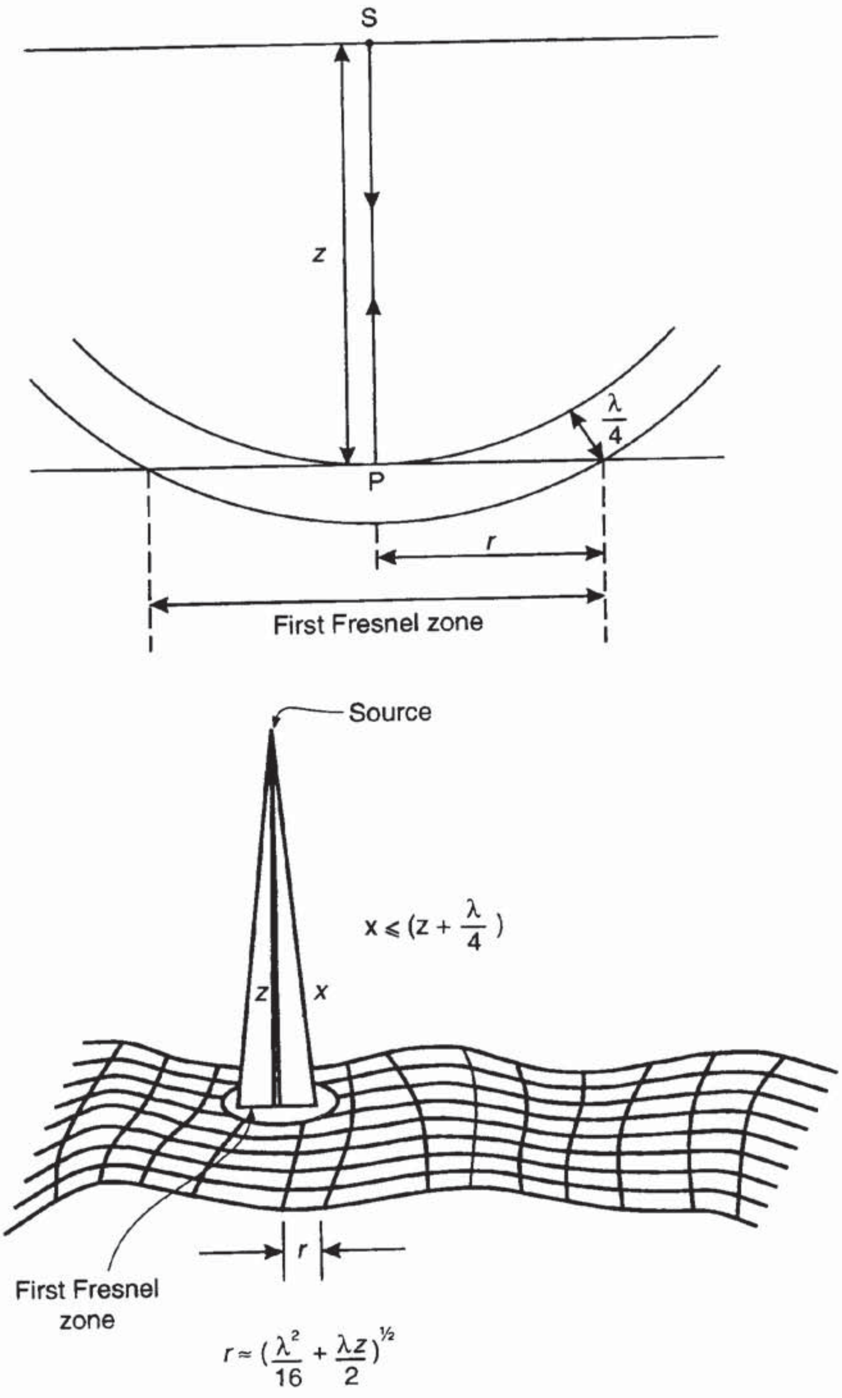

Figure 12.9 Reflection from a rough, specular interface; the target cross-sectional area is equivalent to the area of the first Fresnel Zone. After Annan and Davis (1977), by permission

12.3.3 Horizontal and vertical resolution

Vertical resolution is a measure of the ability to differentiate between two signals adjacent to each other in time. Simplistically, vertical resolution is a function of frequency. Each radar antenna is designed to operate over a range of frequencies (bandwidth) where the peak power occurs at the centre frequency of the antenna. It is the centre frequency that labels individual antenna; hence a 500 MHz antenna has a centre frequency of 500 MHz, for instance. The centre frequency is also inversely proportional to the pulse period (in nanoseconds). The

Table 12.2 Theoretical vertical resolution for two geological materials at three frequencies

	Antenna frequency (MHz)		
	120	500	900
Soil			
Wavelength (cm)	62.5	15	8
Resolution (cm)	15.6	3.75	2
Bedrock			
Wavelength (cm)	92	22	12
Resolution (cm)	23	5.5	3

500 MHz antenna, therefore, has a pulse period of 1/500 MHz = 2 ns, and for 35 MHz the pulse period is $1/35 \times 10^6$ or 28.6 ns. The equivalent length (in metres) of the pulse is the product of the pulse period and the radiowave velocity for the appropriate material. In a wet soil ($V = 0.06$ m/ns) and with a 100 MHz antenna (pulse period = 10 ns), the pulse (wave) length is 0.06×10 m or 0.6 m. Resolution can be taken as one-quarter of the wavelength (h) of incident radiation; $h = V/f$, where V is the radiowave velocity, and f is its frequency. In the last case, if the wavelength is 60 cm, the *theoretical* vertical resolution is 15 cm.

Examples of theoretical minimum resolutions for two different materials at three separate frequencies are listed in Table 12.2. The first example in the table is for a typical soil with $V = 0.075$ m/ns, and the second, a massive rock such as limestone with $V = 0.110$ m/ns. The vertical resolutions given are the very best that could be achieved theoretically. In reality, the resolution is less than these figures owing to the complex nature of the source waveform and the ground responses.

An antenna placed directly on the ground will produce a 'ground coupled' signal. That is, the transmitted waveform in air will not be reproduced when being transmitted into the ground. The material affects the shape, form and amplitude (power) of the downgoing source wavetrain and effectively filters it. The source pulse length decreases with increasing frequency, but describes the main pulse lobe only. With ground coupling, and depending upon the transmitter efficiency, the downgoing wavetrain is usually several times longer than the pulse length described in the manufacturer's literature for a given antenna. This complexity of source waveshape has serious consequences for interpretation.

If the downgoing radar wave has, for instance, three cycles with a total period of 25 ns, this means that a reflection from any interface will have equal if not greater complexity of shape and longer period. The lengthening is due to the loss of higher frequency components within the signal as higher frequencies are attenuated preferentially with respect to lower frequencies.

If two interfaces are separated by only a few tens of centimetres, for example, and the radiowave velocity of the material in between is such that the time interval between a reflection from the first (uppermost) interface and one from the second is shorter than the period of the source wavetrain, the onset of the second reflection will be masked by the tail of the first, and thus may not be resolved.

Another complexity is that the downgoing signal travels from the transmitter in a cone of radiation with a finite-sized footprint. The first Fresnel zone describes the minimum area in which features with smaller dimensions will not be imaged. The radius of the first Fresnel zone is indicated in Figure 12.9. The finite size of this footprint affects both the vertical resolution (when interfaces are steeply dipping or have high-amplitude surface roughness relative to the wavelength of the incident radiowaves), and the horizontal resolution. The larger the first Fresnel zone, the lower will be the horizontal resolution in discriminating between adjacent targets. Furthermore, spatial resolution is also affected by the conical beam width of the downgoing radiowaves (see Figure 12.10); the narrower the beam width, the greater will be the spatial resolution. Horizontal resolution is inversely proportional to $\sqrt{\alpha}$, where α is the attenuation coefficient (Daniels *et al.* 1988). Consequently, the horizontal resolution is actually better over a high-loss material than over a low-loss medium. Where radar systems permit horizontal stacking of adjacent scans to improve the signal-to-noise ratio, horizontal resolution is reduced as the amount of horizontal stacking is increased. There is a practical compromise to

Figure 12.10 Horizontal resolution due to beam width

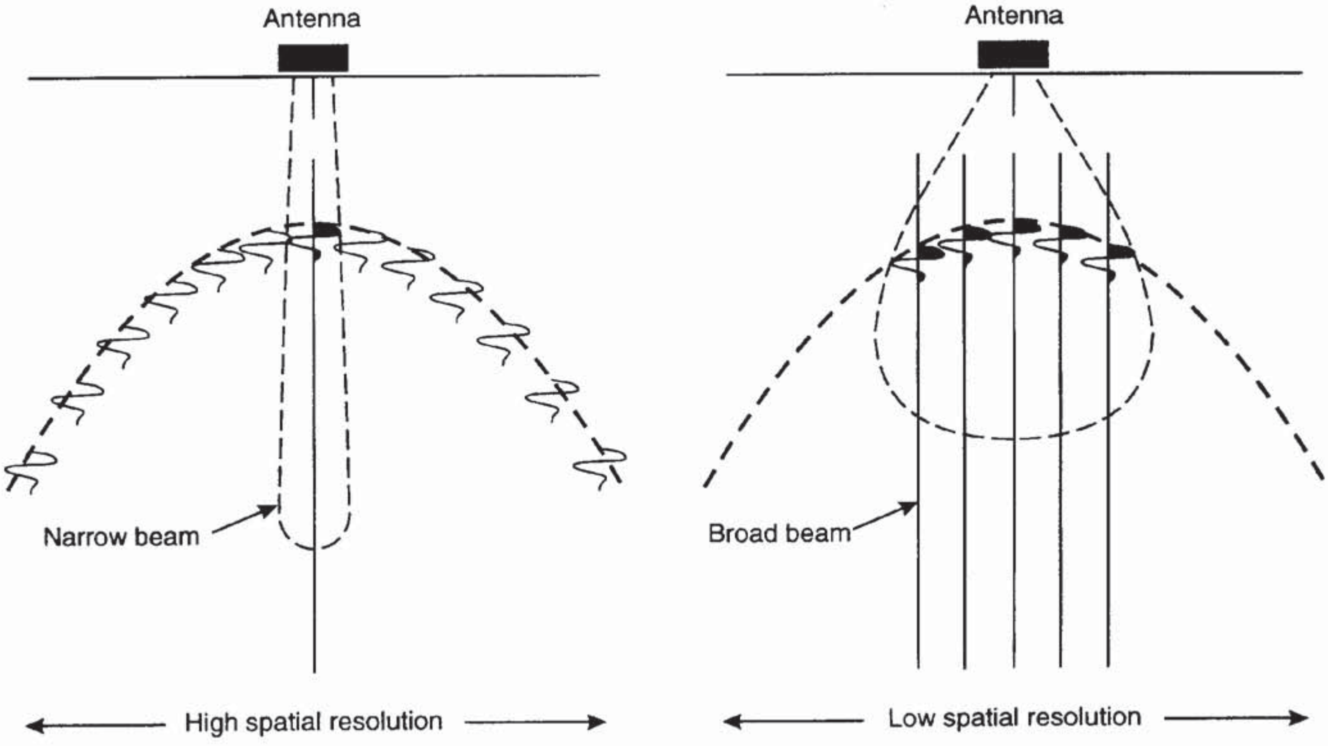

be reached between optimising return signal strengths by horizontal stacking and reducing horizontal resolution.

When *synthetic aperture radar* (SAR) is used, measurements are made by a single antenna at a number of different positions and the results combined to simulate a narrower beam than would have been achieved by using just an isolated antenna at one location. Details of the SAR or holographic radar are beyond the scope of this chapter.

12.4 DIELECTRIC PROPERTIES OF EARTH MATERIALS

The dielectric behaviour of a material is described in terms of its complex permittivity (ε^*) and complex conductivity (σ^*) which are interrelated (see Box 12.5). The high-frequency permittivity (ε_∞) is taken as the lowest real permittivity when the imaginary permittivity (ε'') is zero (see Figure 12.11). The real permittivity (ε') increases as frequency decreases. When the material is a non-conductor, the frequency–permittivity behaviour is described by a semicircle, the centre of which is located on the real permittivity axis half-way between the high-frequency and static permittivities (ε_∞ and ε_s respectively). The imaginary permittivity (ε'') indicates the absorption or energy loss within the dielectric material, and this in turn contributes to the absorption of radiowaves within the ground.

Box 12.5 Complex permittivity and conductivity

Complex permittivity ε^* of a non-conductive material is given by:

$$\varepsilon^* = \varepsilon' + i\varepsilon''.$$

When ε'' is plotted as a function of ε', the resultant graph is a semicircle. The plot is known as a Cole–Cole plot after its originators, Cole and Cole (1947).

If the material has a conductivity σ, then:

$$\varepsilon^* = \varepsilon' + i(\varepsilon'' + \sigma_s/\omega\varepsilon_0)$$

where σ_s is the static or DC conductivity, and ε_0 is the permittivity of free space. At low frequencies, the DC term dominates and produces a characteristic low-frequency tail (see Figure 12.11). The ε'' term is the frequency-dependent loss related to the relaxation response phenomena associated with water molecules (King and Smith 1981).

The complex conductivity σ^* is given by:

$$\sigma^* = \sigma' + i\sigma'' = j\omega\varepsilon_0\varepsilon^*.$$

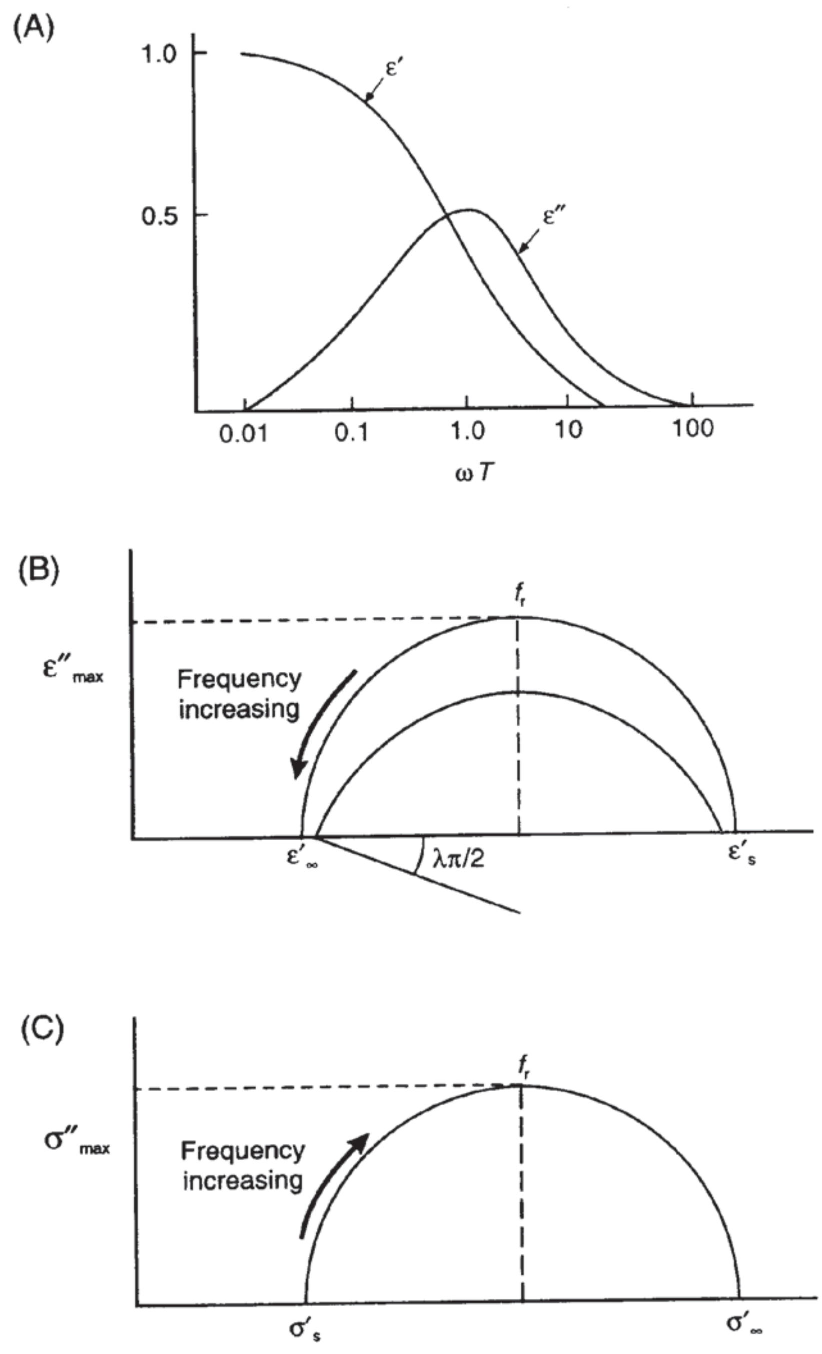

Figure 12.11 Cole–Cole plot of complex permitivity

If the material is conductive, then an appropriate additional term has to be included within the definition of the complex permittivity (Box 12.5). Conductivity also contributes to the loss within the material.

The relative dielectric constant (ε_r) varies from 1 in air through to 81 in water. For most geological materials, ε_r lies in the range 3–30. Consequently, the range of radiowave velocities is large (see Box 12.1), from around 0.06 to 0.175 m/ns (Figure 12.12). The speed of radiowaves in air is 299.8 mm/ns. In trying to estimate depths to any given target it is *essential* to have a detailed knowledge of the

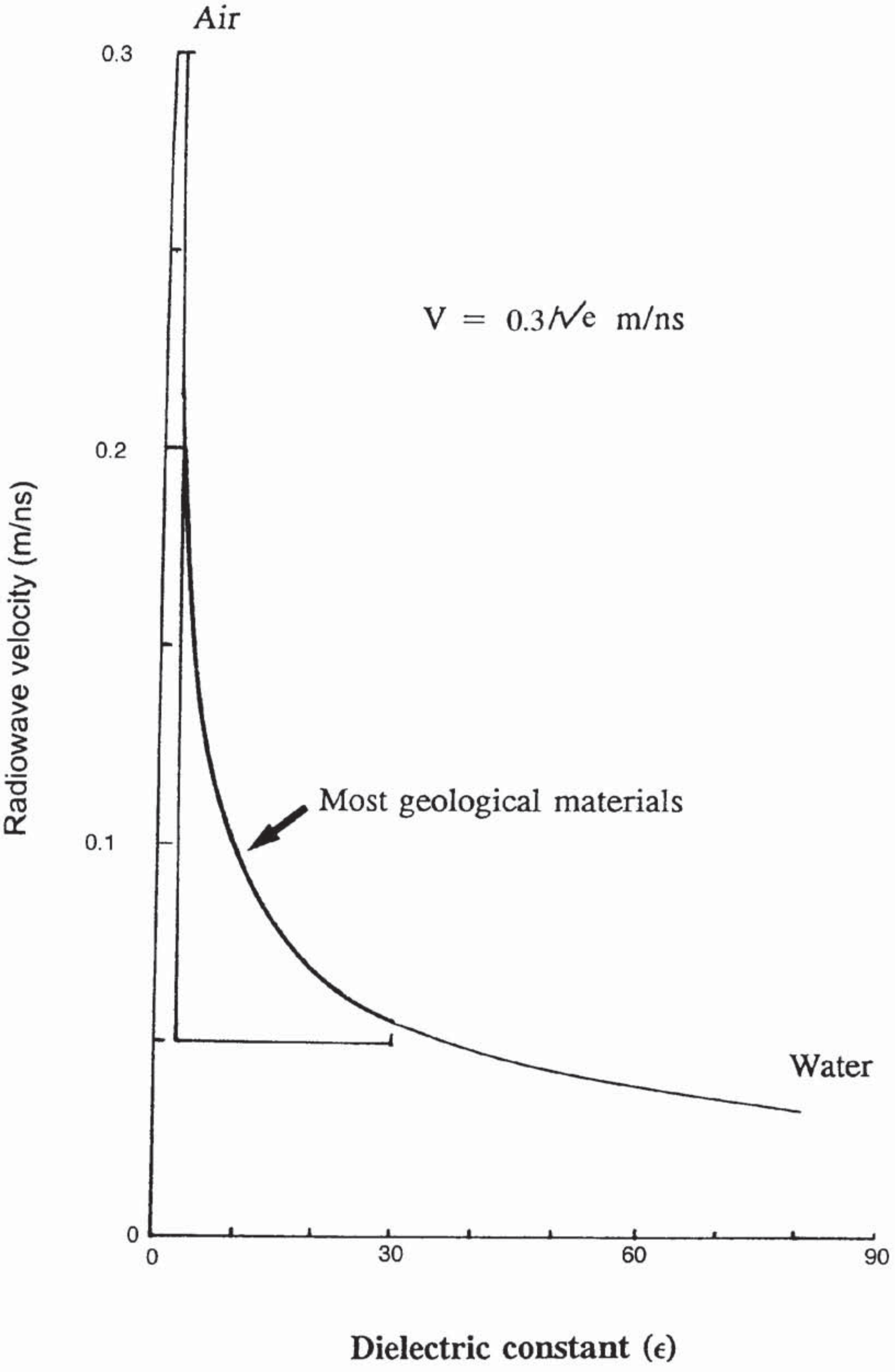

Figure 12.12 Radiowave velocities as a function of relative dielectric constant

radiowave velocities through the sub-surface materials present. This aspect of radar interpretation will be dealt with in Section 12.6.

A list of the relative dielectric constants and associated radiowave velocities for a variety of geological and man-made materials is given

Table 12.3 Table of relative dielectric constants and radiowave velocities for a range of geological and man-made materials

Material	ε_r	V(mm/ns)
Air	1	300
Water (fresh)	81	33
Water (sea)	81	33
Polar snow	1.4–3	194–252
Polar ice	3–3.15	168
Temperate ice	3.2	167
Pure ice	3.2	167
Freshwater lake ice	4	150
Sea ice	2.5–8	78–157
Permafrost	1–8	106–300
Coastal sand (dry)	10	95
Sand (dry)	3–6	120–170
Sand (wet)	25–30	55–60
Silt (wet)	10	95
Clay (wet)	8–15	86–110
Clay soil (dry)	3	173
Marsh	12	86
Agricultural land	15	77
Pastoral land	13	83
Average 'soil'	16	75
Granite	5–8	106–120
Limestone	7–9	100–113
Dolomite	6.8–8	106–115
Basalt (wet)	8	106
Shale (wet)	7	113
Sandstone (wet)	6	112
Coal	4–5	134–150
Quartz	4.3	145
Concrete	6–30	55–112
Asphalt	3–5	134–173
PVC, Epoxy, Polyesters	3	173

Data from Johnson *et al.* (1979), McCann *et al.* (1988), Morey (1974), Reynolds (1990b, 1991b)

in Table 12.3. It should be emphasised that the values of both relative dielectric constants and radiowave velocities should be taken only as guide figures. The lack of ranges for some materials is due to the paucity of measurements made and is not meant to imply that there is no variation within these materials. The ranges given are also not meant to be extremes. As more results are published the ranges listed may need to be extended as the true variability of both parameters becomes more widely realised.

Cook (1975) has produced a schematic illustration (Figure 12.13) to show the likely probing distances achievable for different geological

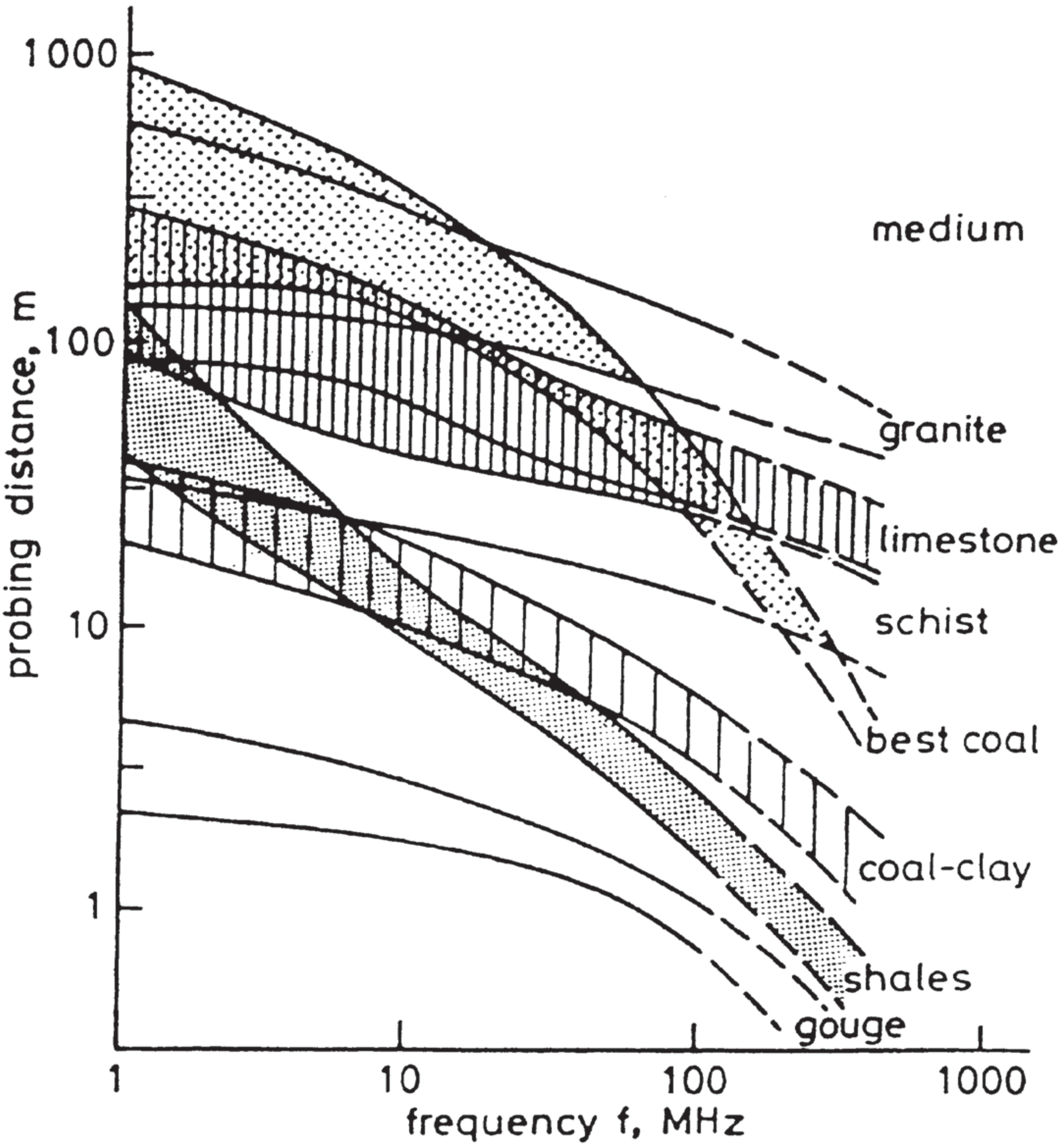

Figure 12.13 Probing distances as a function of frequency for different geological materials. From Cook (1975), by permission

materials over the frequency range from 1 to 500 MHz. Clay-rich materials have much shorter probing distances than more massive rocks such as granite and limestone.

Most materials, whether geological or man-made, are a complex mixture of components each of which is likely to have different electrical and dielectric properties. Grain size and even grain shape can affect bulk electrical and dielectric behaviour. Most rocks contain a degree of moisture, either as 'free' liquid contained within pore spaces, or 'bound' within the mineral lattice as with many types of clay minerals. Since the relative dielectric constant of water is high (81) relative to that of dry rock, even a small amount of water may increase the bulk permittivity of the rock. An example of the effect of soil moisture content of a variety of rocks on the relative dielectric constant is shown in Figure 12.13. Furthermore, the amount of water present within a rock will also affect the speed of propagation of radiowaves. The radar velocity through freshwater is 3.3×10^7 m/s (0.033 m/ns) whereas it is 1.2×10^8 m/s (0.12 m/ns) through a low-porosity sandstone (McCann *et al.* 1988).

The relative dielectric constant of a layered material has been demonstrated to be related to porosity (ϕ) by considering the proportion of constituents present and their respective relative dielectric constants. The relationships between constituent and bulk relative dielectric constants and porosity are given in Box 12.6; the variations of radiowave velocity with porosity for water-saturated and air-saturated porous media are illustrated in Figure 12.14. If the relative dielectric constant for each constituent of the material is known and that of the bulk material is measured or derived from the radiowave velocity, then the total porosity can be calculated.

Box 12.6 Relative dielectric constants and porosity

(Parkomenko 1967)

The relationship between bulk relative dielectric constant (ε_r) and porosity (ϕ) is:

$$\varepsilon_r = (1 - \phi)\,\varepsilon_m + \phi\varepsilon_w \tag{1}$$

where ϕ is the porosity, ε_m and ε_w are the relative dielectric constants for the rock matrix and pore fluid water, respectively. This is valid when the external field is applied parallel to the bedding.

When the external field is applied perpendicular to the bedding, then:

$$\varepsilon_r = \varepsilon_m\varepsilon_w/[(1 - \phi)\varepsilon_m + \phi\varepsilon_w].$$

Using the simplified relationship that $V = c/\sqrt{\varepsilon_r}$, for low-loss materials, where c is the radiowave velocity in air, and substituting in equation (1) for ε_r, then:

$$V = c/[(1 - \phi)\varepsilon_m + \phi\varepsilon_w]^{1/2}.$$

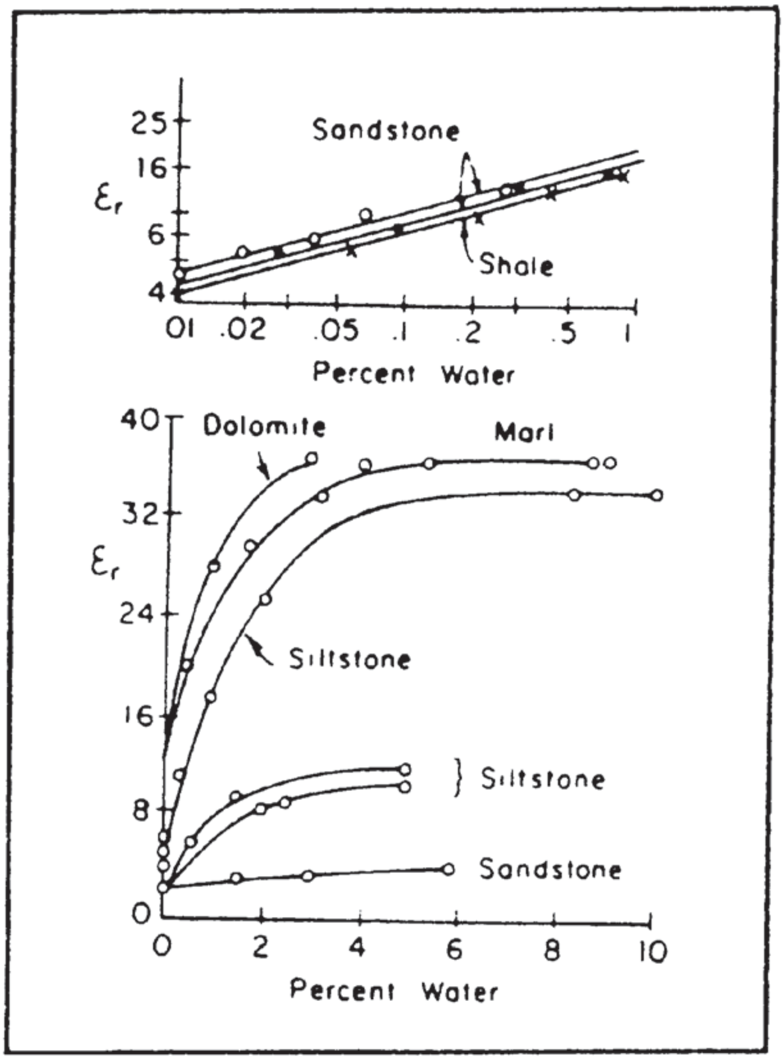

Figure 12.14 Effect of soil moisture content of rock on ε_r. From King and Smith (1981), by permission

From Figure 12.15 it can be seen that the radiowave velocity decreases with increasing soil moisture content. Consequently, wetter materials have a better vertical resolution than dry materials, although the attenuation in wetter materials is greater than for dry so depth penetration is likely to be smaller.

The determination of porosity assumes only a two-component system, i.e. made up of a matrix and pore spaces that are saturated with either air or another fluid of known relative dielectric constant. It also assumes that all the pore spaces are saturated with one fluid. This situation may not be achieved in many cases in nature.

Total porosity is the proportion of volume not filled by the solid constituents within a material and includes isolated pore/fracture space. The *effective porosity* is the porosity available to free fluids and excludes the isolated unconnected pores/fractures and space occupied by bound water in clays (Sheriff 1991). The isolated pore/fracture space (*residual porosity*) is thus the difference between the total and effective porosities. The permeability of a material is a measure of the

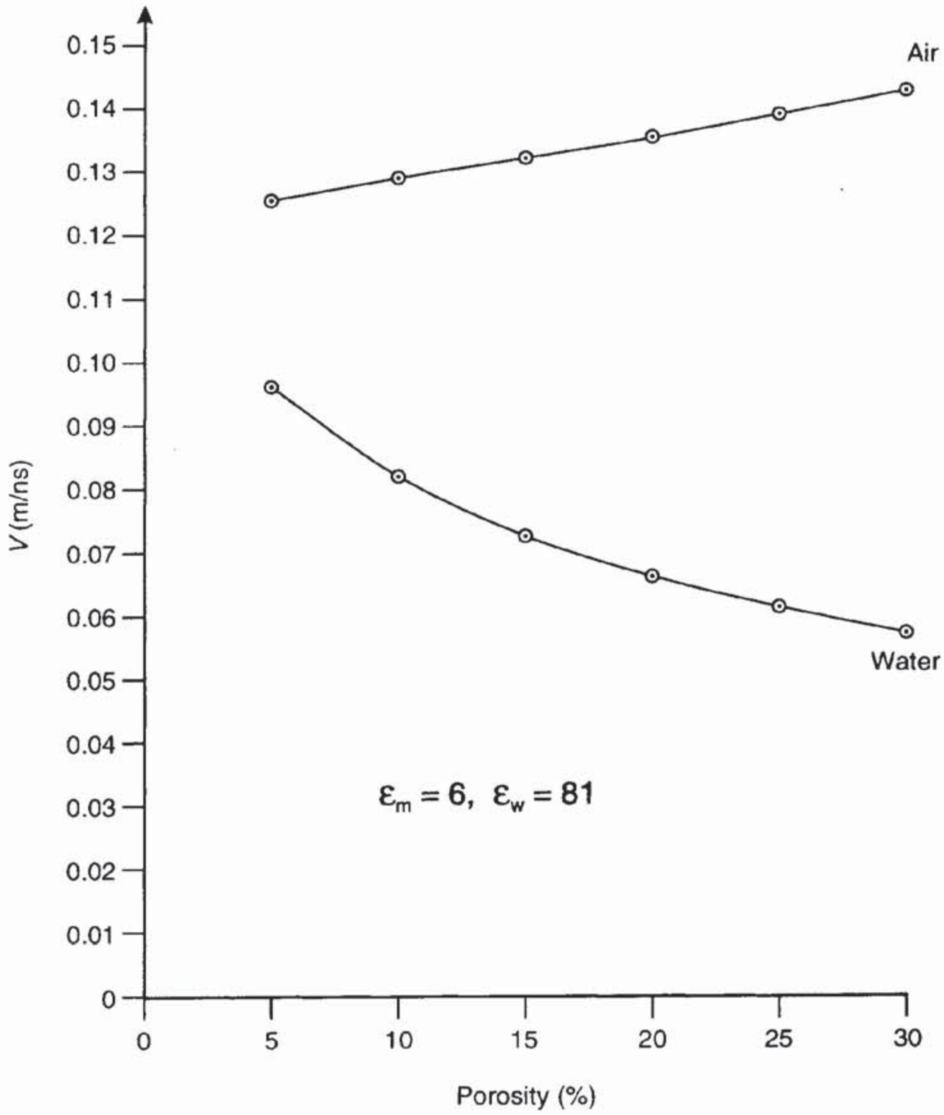

Figure 12.15 Radar velocities as a function of porosity for air- and water-saturated granular materials

ease with which a fluid can flow through the pore spaces within a given medium and thus is a function of the connectivity of the pore space, i.e. the effective porosity. Permeability is also a function of the viscosity of the fluid, the rate of fluid flow and the hydraulic pressure gradient causing the flow.

When electrical resistivity is used to derive porosity of clean granular rocks, such as by using Archie's Formula, it is the effective porosity which is being determined. Electrical continuity is provided by the electrolytes within the connected interstitial spaces. Dielectric measurements, however, are not dependent upon the connectivity and thus can be used to determine the total porosity. Conversely, values of porosity derived from the use of radiowave velocities are always likely to be overestimates of the effective porosity.

Microporosity – i.e. porosity at a scale of the order of microns but still large relative to the sensitivity of the electrical measuring system –

becomes especially significant in dielectric analysis. Electrical conductivity is affected by pore geometry and pore surface area. Clay not only affects the physical communication between pores and pore throats (affecting permeability as well as porosity), but the type of clay provides differing surface areas for double-ionic polarisation (Reynolds and Taylor 1992). For example, authigenic kaolinite occurs as disc-like 'booklets' whereas illite forms ribbons (Klimentos and McCann 1990; Klimentos 1991). The form of the clay, therefore, can affect the surface area within the pore space and it is probable that, at the scale of the order of microns, the microporosity has a measurable effect on the electrical properties. In contrast, ultrasonic acoustic methods appear to be less sensitive to this. This is not to say, however, that the microporosity does not influence the physical properties measured using acoustic methods, but that as yet the acoustic methods are not able to resolve the effects of microporosity. Indeed, electrical properties are being modelled by reference to the fractal nature of porosity (Ruffet *et al.* 1991). As it is the *effective* porosity that is directly related to permeability, the latter will only be determinable once the former can be derived accurately.

The significance of porosity, permeability and the dielectric properties of fluids is of particular importance in dielectric logging of hydrocarbon wells and in contamination mapping, for example.

Dielectric properties of concretes have also been demonstrated to exhibit a surprisingly large degree of variation (Reynolds 1991b; Reynolds and Taylor 1992). The relative dielectric constant can vary by more than 50% over a distance of less than 0.1 m within the same mix of concrete; the resulting change in radiowave velocity is of the order of 35%, with velocity decreasing with depth into the concrete. The effect is thought to be related to the amount of micro-cracking present within the concrete, with a greater amount of cracking present nearer the surface (hence more air present, thus the higher radiowave velocity). While this is but one isolated example, it does serve to demonstrate that even within a relatively controlled material like concrete, there is still a high degree of variability in the electrical properties.

12.5 MODES OF DATA ACQUISITION

There are three modes of deployment of radar systems; reflection profiling (using either monostatic or bistatic antennae); wide-angle reflection and refraction (WARR) or common-midpoint (CMP) sounding; and transillumination or radar tomography.

12.5.1 Radar reflection profiling

Figure 12.1 provides an example of radar being used to obtain a reflection profile. One or more radar antennae are moved over the

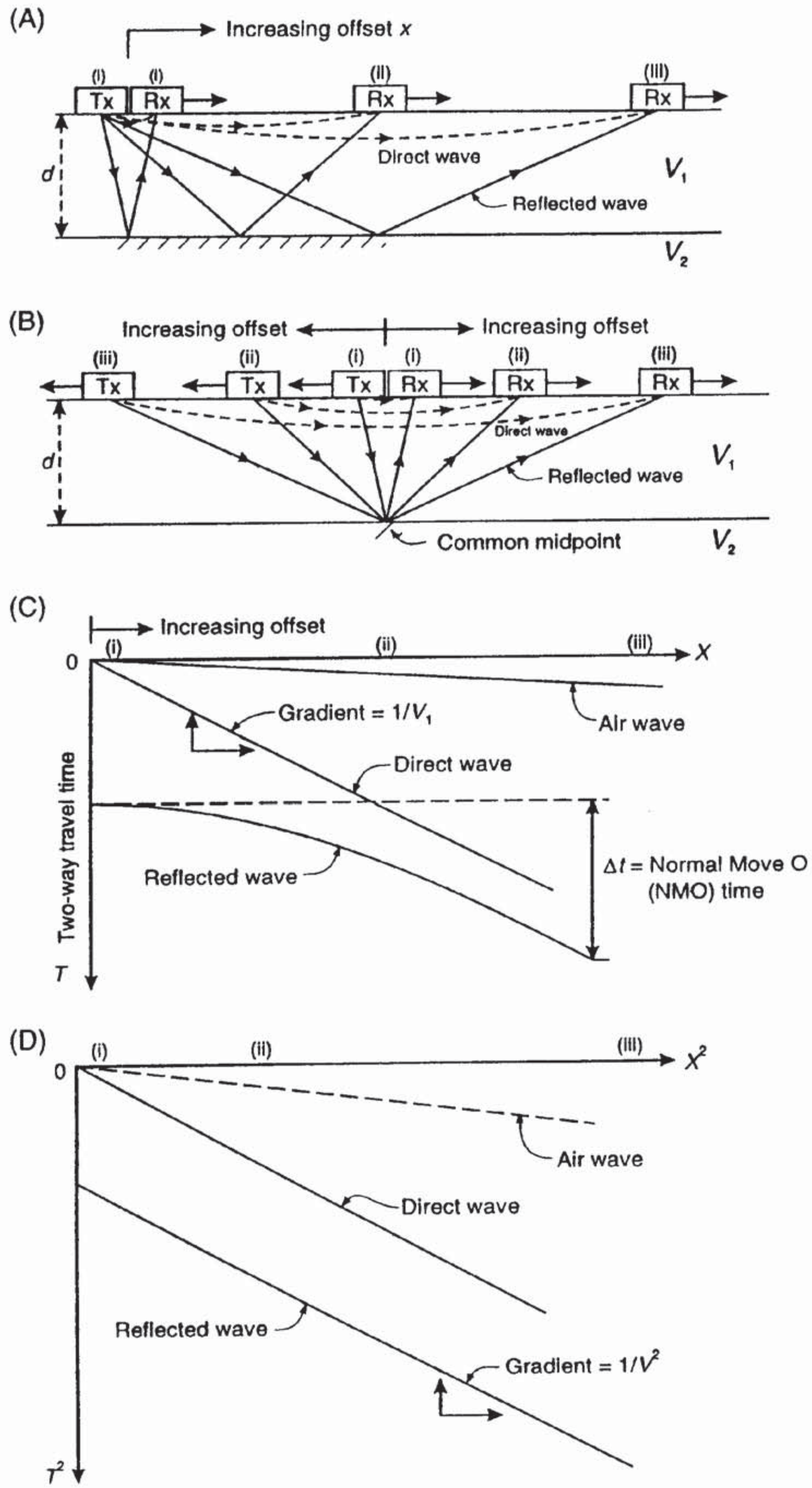

Figure 12.16 (A) WARR sounding and (B) CMP sounding with (C) a time-distance (T–X) graph with normal moveout, and (D) the corresponding T^2–X^2 graph

ground surface simultaneously, with the measured travel times to radar reflectors being displayed on the vertical axis while the distance the antenna has travelled is shown on the horizontal axis. This mode of surveying is analogous to continuous seismic reflection profiling (see Chapter 6).

If the radiowave velocities have been measured independently (see next section) or reflections correlated with changes in ground characteristics observed from borehole data, then depths to the reflectors can be determined. See Section 12.7 for more details of interpretation techniques.

12.5.2 Wide-angle reflection and refraction (WARR) sounding

The WARR antenna configuration is shown in Figure 12.16A. The transmitter is kept at a fixed location and the receiver is towed away at increasing offsets. The location of a WARR sounding should be over an area where the principal reflectors are planar and either horizontal or dipping only at very shallow angles. It is also assumed that the material properties are uniform and that the reflector characteristics are the same over the sub-surface area over which the WARR sounding is undertaken. This assumption may not be true in all cases.

To avoid having to make this last assumption, an alternative and preferable deployment for the same analysis is the common midpoint (CMP) sounding. In this case, both the transmitter and receiver are moved away from each other so that the midpoint between them stays at a fixed location (see Figure 12.16B). In the CMP case, the point of reflection on each sub-surface reflector is used at each offset, and thus areal consistency at depth is not a requirement. The equivalent positions between the WARR and CMP soundings are given as (i), (ii) and (iii) in Figure 12.16.

12.5.3 Transillumination or radar tomography

The transillumination mode of deployment is where the transmitter and receiver are on opposite sides of the medium under investigation (Figure 12.17). The method is used underground within mines, for example, where the transmitter is located in one gallery and the receiver is either in a gallery to one side of the transmitter, or in a gallery above or below. Alternatively, the radar antennae can be located down boreholes and the radar signals are then propagated from one, through the medium in between, to the other.

The transillumination mode is also common in non-destructive testing (NDT) investigations of man-made structures, particularly using very high frequency and hence small antennae (e.g. 900 MHz centre frequency). Examples include testing concrete columns and masonry pillars.

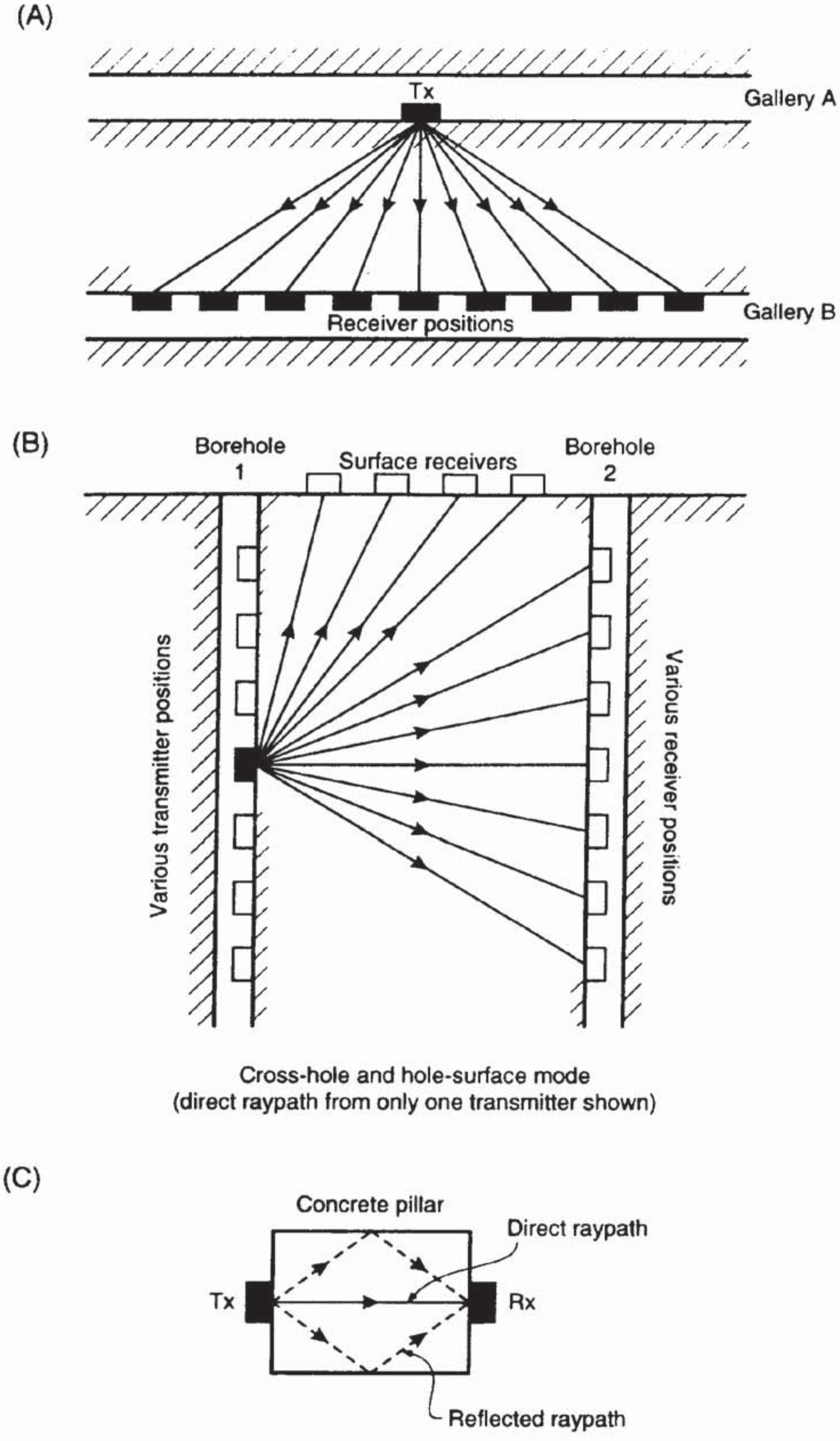

Figure 12.17 Transillumination and cross-hole radar modes of data acquisition: (A) between galleries in a mine, (B) between boreholes or hole-surface, and (C) through a concrete pillar. In all cases the direct distance between transmitter (Tx) and receiver (Rx) antennae is known. Modes shown in (A) and (B) are also known as *radar tomography*

As the relative positions of the antennae are known at all times, and hence the distances between them, it is a simple matter to calculate the mean radiowave velocity of the appropriate raypath. If the signal amplitude is also measured, in addition to travel times, then attenuation can be determined. More details of this method have been given by Annan and Davis (1977). Sophisticated data-processing routines exist in order to produce tomograms that are analogous to seismic equivalents (see Chapter 6).

12.6 DATA PROCESSING

12.6.1 During data acquisition

All ground radar systems provide a means of filtering the data during acquisition. It is usually possible to set both highpass and lowpass filters to sharpen the signal waveform at the time of the survey. As with seismic filtering during acquisition, there is a significant element of qualitative feel to choosing appropriate filter settings. More sophisticated digital systems allow vertical and horizontal filtering as well as more powerful gain-setting options with which to optimise the data quality. As a rule of thumb, it is advisable to keep the filter settings as broadband as possible so that potentially valuable data are not excluded during the acquisition phase. It is far cheaper to filter broadband data after the field work has been completed than to realise that the data quality has been compromised by the use of filter settings which are too harsh, thereby necessitating a repeat of the fieldwork!

Digital systems have the function of stacking a limited number of adjacent traces in order to improve the signal-to-noise ratio. This works well in areas where the structure is largely parallel or subparallel to the ground surface. When steeper structures are present, horizontal stacking over too many adjacent scans can produce lateral smearing and a defocusing of the radar image.

12.6.2 Wide-angle reflection and refraction (WARR) sounding

If two separate antennae are used, one as a transmitter and the other as a receiver, in bistatic mode, it is possible to determine the vertical variation in radiowave velocity (and hence relative dielectric constant). If only one antenna is available in monostatic mode, it is not possible to undertake WARR sounding and hence velocity determination can only be by either direct correlation with adjacent borehole logs, targets at known depths of burial or by guesswork; the latter is the most commonly employed and may give depth estimates accurate to ±20%.

In each of the WARR or CMP configurations three types of waves may be identified:

- the airwave, travelling from the transmitter to the receiver through the air at the speed of radiowaves in air (0.3 m/ns);
- the direct wave, travelling directly from the transmitter through the near-surface ground to the receiver at the speed of radiowaves in the near-surface medium (V_1);
- the reflected wave, travelling from the transmitter to the interface from which it is reflected to the receiver, also at the speed of radiowaves in the first layer (V_1).

The travel times for both the airwave and the direct wave plot as straight-line segments on the T–X graph, but those for the reflected wave plot on a curved (hyperbolic) line. The difference in travel time between zero offset and at finite offset is the *normal moveout* (NMO) time (Figure 12.16C). However, when these travel-time data are plotted on a T^2–X^2 graph, all the segments appear as straight lines (Figure 12.16D). The inverse gradients of each line are equal to the respective radiowave velocity squared. Further details of the velocity sounding techniques have been given by Arcone (1984).

The radiowave velocity determined for layer 1 is a time-averaged value over the interval from zero time to t_0, and is hence a root-mean-squared velocity (V_{RMS}). Where travel-time data are obtained for deeper reflections, the velocities determined from the above analysis for each layer are also RMS values. To determine a geologically more meaningful velocity for a particular layer, it is then necessary to use the Dix Formula to derive the 'interval velocity'. This analysis is exactly the same as for seismic reflection data and more complete details are given in Chapter 6.

12.6.3 Post-recording data processing

Only digital data can be processed post-recording. The degree of processing is often determined by (a) the budget available; (b) the time available; (c) data quality; (d) the available processing capability (software and hardware); (e) the requirement that the final interpretation justifies further analysis; and (f) the structural detail on the raw record meriting detailed quantitative data processing.

The first step is to filter the data in order to focus the image. For many applications this is sufficient in order to locate sub-surface features. For more detailed analysis, a wide range of processes are available, up to and including the same as for multifold seismic reflection data, including attribute analysis, details of which are given in Chapter 6.

The radar system produced by Geophysical Survey Systems Inc. has a suite of data-processing packages available called RADAN™

(Radar Data Analyser). The format of data recorded on to magnetic media, typically 2.5 Gbyte magnetic tape or magneto-optical disk, can be converted from SEG 2 to SEG Y format in order to be compatible with seismic industry-standard workstations. A program to convert from SEG 2 to SEG Y has been published by Bennett (1990). Datafile formats for radar data have been specified by the SEG Engineering and Groundwater Geophysics Committee (Pullan 1990). Similarly, Sensors & Software Ltd have a range of computer software designed for use with their PulseEKKO system, which produces data in a format compatible with seismic data-processing software.

Of particular significance is the ability to restore correct sub-surface geometrical relationships through the process of migration. Diffraction hyperbolae can be migrated back to the apex from which the diffraction originated. Dipping planar surfaces can be corrected to their correct position relative to ground locations. Otherwise, significant errors can be made by believing that the location of a particular sub-surface feature on a raw radargram is exact, whereas it is only a virtual image and may be displaced from its actual position by significant horizontal and vertical distances. The principles of migration are discussed more fully in Chapter 6.

Other methods of quantitative analysis are available through *image analysis*. Rather than operate on the waveforms of the data, the radargram is scanned for analysis of trends. For example, trends such as reflections dipping in a particular direction can be picked out. Statistically significant trends can be identified from the entire radargram and displayed automatically as line interpretations for subsequent manual analysis.

12.7 INTERPRETATION TECHNIQUES

12.7.1 Graphic interpretation

From both analogue and digital radar data, hardcopy radargrams can be analysed in terms of identifying reflections and diffractions and measuring the two-way travel times to such identifiable events. By assuming, or having measured, a value for the appropriate relative dielectric constant – and hence obtained a realistic radiowave velocity – the two-way travel times to specific events can be translated into depths. Where radar data have been acquired over a regular grid, and reflections identified over significant areas, it is then possible to produce posted two-way travel time maps, or *isopachyte maps*, indicating the depth to, or thickness of, a particular layer, given a realistic measure of the radiowave velocity.

This approach is particularly prevalent in road pavement analysis, where the number of discrete layers is usually well constrained with up to four parallel to sub-parallel layers (bound layer of bitumen or concrete, granular layer, upper and lower sub-grades). The travel times to interpreted interfaces can be digitised off paper radargram records and, using an appropriate radiowave velocity for each of the discrete layers, the depths to each interface can be determined. There would need to be careful consideration of the accuracy of picking the onset of the various reflections on the radargrams as well as the likely reliability of the radiowave velocities used to derive depths. Local variability in radiowave velocities can occur within concretes (see Section 12.4; different mixes, even though all within specification), or due to changes in moisture content (see Section 12.4). Individual horizons, such as the sub-base, may have been prepared in layers, and these may be detected. In some cases the boundary between layers may be fuzzy – so where does the radar reflection come from? Is it always from the same relative position between layers? These are questions that need to be answered in road pavement work prior to the production of final drawings. In all cases, a statement as to the errors and limits of measurement should be made. There is no such thing as an absolute measure of depth using remote methods, particularly radar.

The interpreted data can be displayed in a wide range of ways using modern computer-aided design (CAD) systems and 3-D graphics software packages. While the final output may be extremely colourful and fancy, it should be remembered that the basic data analysis may be just that – basic! While the final drawings may indicate millimetre accuracy, is this justified? At present, the uncertainties and local variability in the dielectric properties of materials and the subjective nature of defining the onset position of reflections tend to make claims of such accuracy unjustified. As the electrical and dielectric properties of materials used in road pavements become better known, accuracies and reliabilities will improve.

In addition to interface mapping, it is possible to use the variations in character displayed on the radargram as an indication of sub-surface conditions. For example, areas of high attenuation may reveal zones with elevated conductivities which may be associated with pollution, or clay pockets. Sub-surface cavities may be evident by the resonance within the void space, indicated on the radargram as a series of large-amplitude pulses which are laterally very restricted. Zones of cobbles or severely distorted strata may be evident by the loss of coherency of primary reflection events. Delamination of road pavements may also be indicated by diagnostic character changes on radargrams (delamination is also evident when imaged using infrared thermography under appropriate conditions).

12.7.2 Quantitative analysis

Basic depth determination depends upon an adequate knowledge of the radiowave velocity and its vertical and lateral variation within a given survey area. Where WARR/CMP data have been acquired, then a detailed picture of the velocity field can be obtained. Consequently, geologically diagnostic values of the radiowave velocity, or more particularly of the relative dielectric constant, can be used to aid interpretation.

Where detailed quantitative attribute analysis has been undertaken of the recorded radiowave data – such as amplitude analysis, reflection coefficient determination, as well as variations in ε_r – then a much more comprehensive understanding of a site can be gained. Indeed, given adequate data quality, careful processing may yield more valuable information about the petrophysics of a given geological or engineering regime than would otherwise have been possible. High-level processing and analysis are becoming much more important where detailed discrimination is required, such as in hydrocarbon exploration and reservoir engineering, and in contaminated land investigations. The use of ground radar in both cases is likely to develop considerably over the next few years.

12.7.3 Interpretational pitfalls

The two commonest pitfalls in the interpretation of radar data are (a) not being able to identify the ground surface, and (b) misidentifying each black band on a black and white radargram as being caused by a discrete horizon. The easiest way to identify ground level, especially with antennae with centre frequencies $\geqslant 500$ MHz, is to raise and lower the antenna above the ground surface. A distinctive cusp appears on the radargram and clearly indicates where the ground level is represented.

The over-identification of the number of layers highlights a real difficulty, especially with analogue radar data: how are the primary reflections to be identified from multiples, secondary events, and the tail of other primary reflections? Furthermore, when waveforms intersect each other, they cause interference which may give the appearance of a 'termination' of one dark band with respect to another. Geologically, this may be misinterpreted as one horizon abutting against another. If the geological conditions are such that the radargram is ambiguous in this regard, then there is justification for detailed quantitative analysis if the data have been recorded digitally. If the data have been produced as an analogue record, there is little that can be done to resolve the dilemma. The quantitative analysis can pick out likely multiple events (these are purely time repeats of earlier primary events), and by deconvolution, the shape of the downgoing wavetrain can be determined and hence primary reflection events identified. Subsequent migration can help to reduce diffraction hyperbolae and, by restoring some of the sub-surface geometry of primary reflections, can help to resolve geologically significant detail that otherwise would have been obscured.

The difficulties in distinguishing between geologically significant reflections and extraneous reverberations, multiples, noise, diffractions, off-section ghosts, etc., make the determination of soil and rock stratigraphy difficult in some cases. In others, the stratigraphy can be determined quite readily; one such example (from Best and Spies, 1990) is shown in Figure 12.18. An analogue record obtained in 1976

Figure 12.18 Radargram obtained in 1976 compared with one in 1991. From Best and Spies (1990), by permission

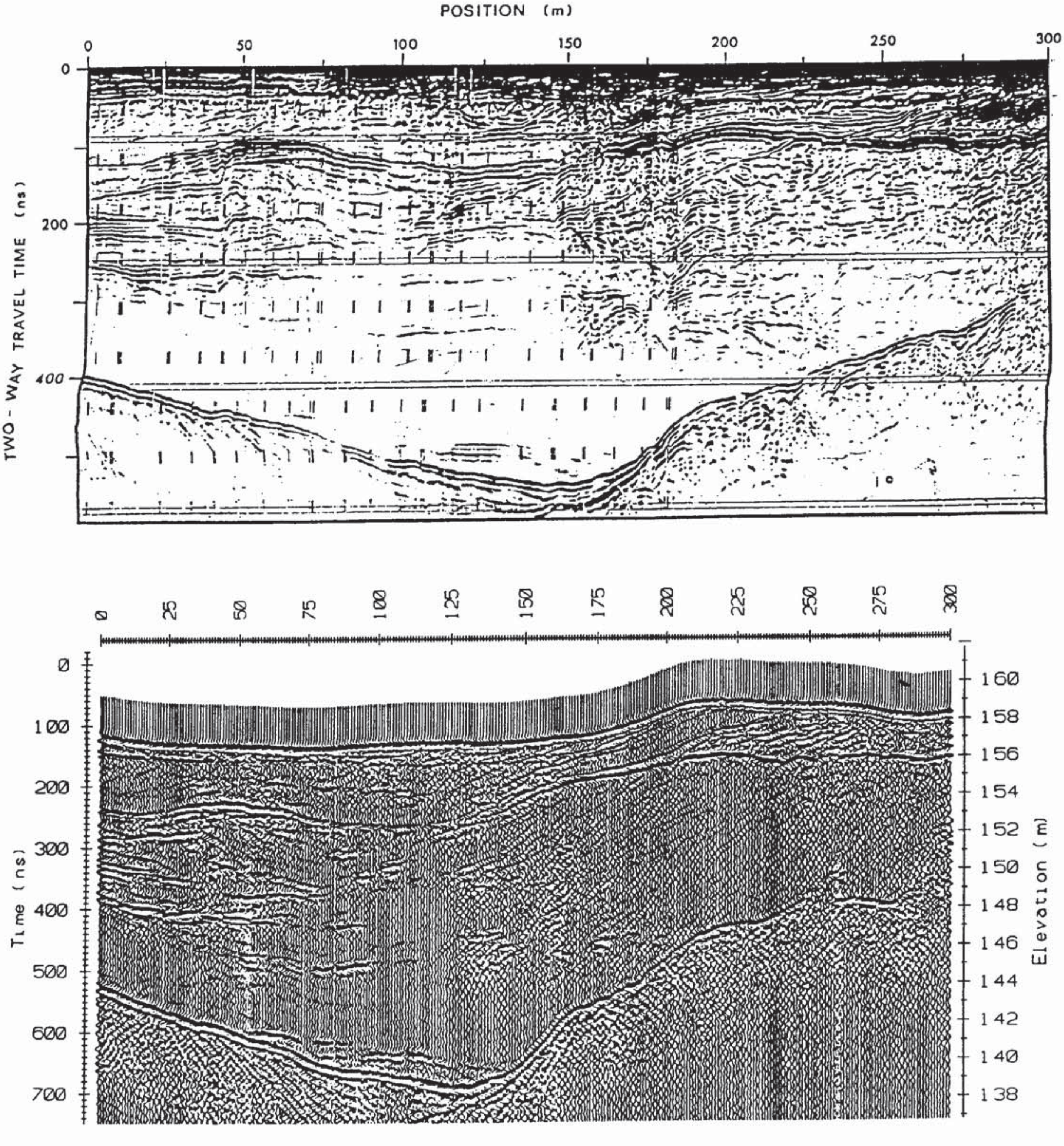

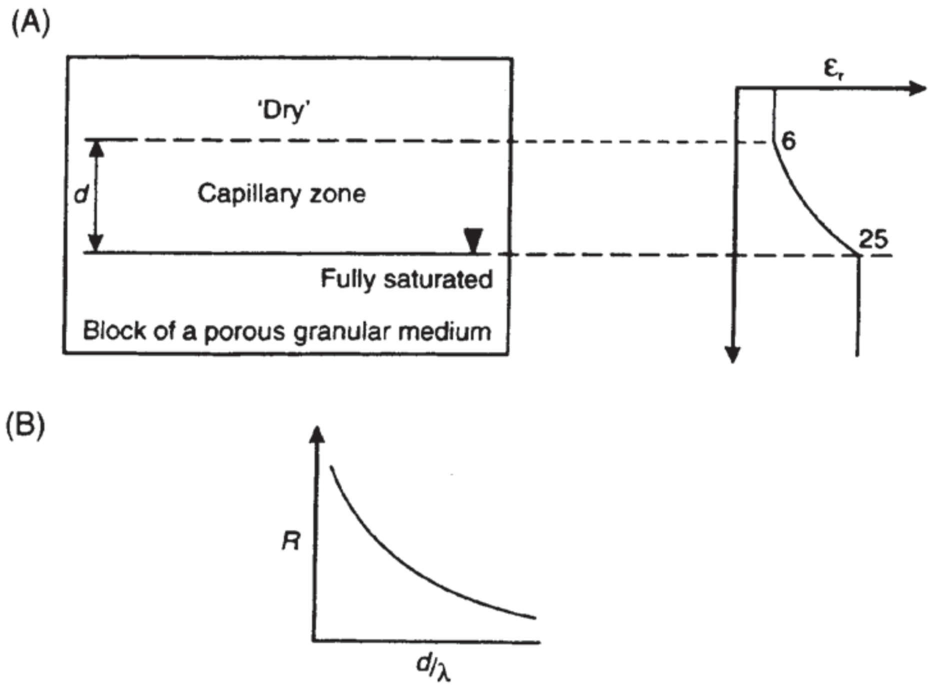

Figure 12.19 Effect of thickness of a capillary zone on the observed reflection strength arising from the water table. (A) A capillary zone of thickness *d* over the water table has a relative dielectric constant (ε_r) which increases to a maximum when fully saturated. (B). The amplitude reflection coefficient (*R*) decreases as the ratio of the thickness of the capillary zone to wavelength of incident radiowaves increases

is compared with a digital radargram produced over the same area more recently. While the gross structure is evident in the 1976 analogue record, the detail is much crisper in the digital record.

There are situations when the water table is detectable on a radargram and others where it is not. The reason for this is that the ratio of the thickness of the capillary zone to the wavelength of the incident radiowaves needs to be small (i.e. $d <$ wavelength) in order to provide sufficient contrast in relative dielectric constant between the unsaturated and saturated material to reflect a significant proportion of the energy (Figure 12.19). If the capillary zone is thick with respect to the wavelength, then the rate of change of relative dielectric constant with depth through this zone is small. The effect of this is that, for each incremental increase in the relative dielectric constant, a proportion of the incident energy is reflected so that the total reflected energy is smeared from the capillary zone, and hence the resulting reflection amplitude is too low to be detected with any clarity. In contrast, if the transition from dry to saturated is virtually instantaneous (e.g. the change in relative dielectric constant is from 6 to 25), then the amplitude reflection coefficient $|R|$ is 0.34 (using the expression in Box 12.2), which is a very strong return.

12.8 APPLICATIONS AND CASE HISTORIES

12.8.1 Sedimentary sequences

Ground penetrating radar has been demonstrated to be a valuable tool in mapping sediment sequences with a high degree of spatial

۲۹

resolution on both land and through freshwater. An example of the improvement in data quality in mapping soil stratigraphy was given in Figure 12.18. Other examples are given in Section 12.8.7. A common failing of the analysis of radargrams acquired in stratigraphic investigations is over-interpretation of the data. Too often apparently coherent events are taken as indicating individual sedimentary interfaces without due regard for the physics of thin-bed interference, vertical and horizontal resolution limits, the finite size of the first Fresnel zone, migration effects, the complex form of the incident wavetrain, etc. It is in these applications that seismic data processing is likely to play an important role; for example, see the paper by Huggenberger *et al.* (1994).

Ground radar can be deployed over frozen lakes and has been used to investigate sub-lake sediments through freshwater up to 27 m deep; an example of a through-ice survey is shown in Figure 12.20. The lake ice provides a stable platform over which the radar was towed. The freshwater within the lake is virtually transparent to radiowaves and the lake sediments are clearly evident through 4.8 m of freshwater. The resolution of the system (100 MHz antenna) is such that individual horizons within the sediment can be picked out. Note that the reflection returns associated with the lake bed comprise at least four bands owing to a ringy source. Furthermore, the period of the initial wavetrain (around 70 ns) might be misinterpreted by some as indicating the presence of up to 6 m of ice (radiowave velocity through ice is

Figure 12.20 Radargram over an icecovered lake obtained using a 100 MHz antenna. Maximum water depth is 4.8 m; width of profile is 25 m; 500 ns two-way travel time range. From Mellett (1993), by permission

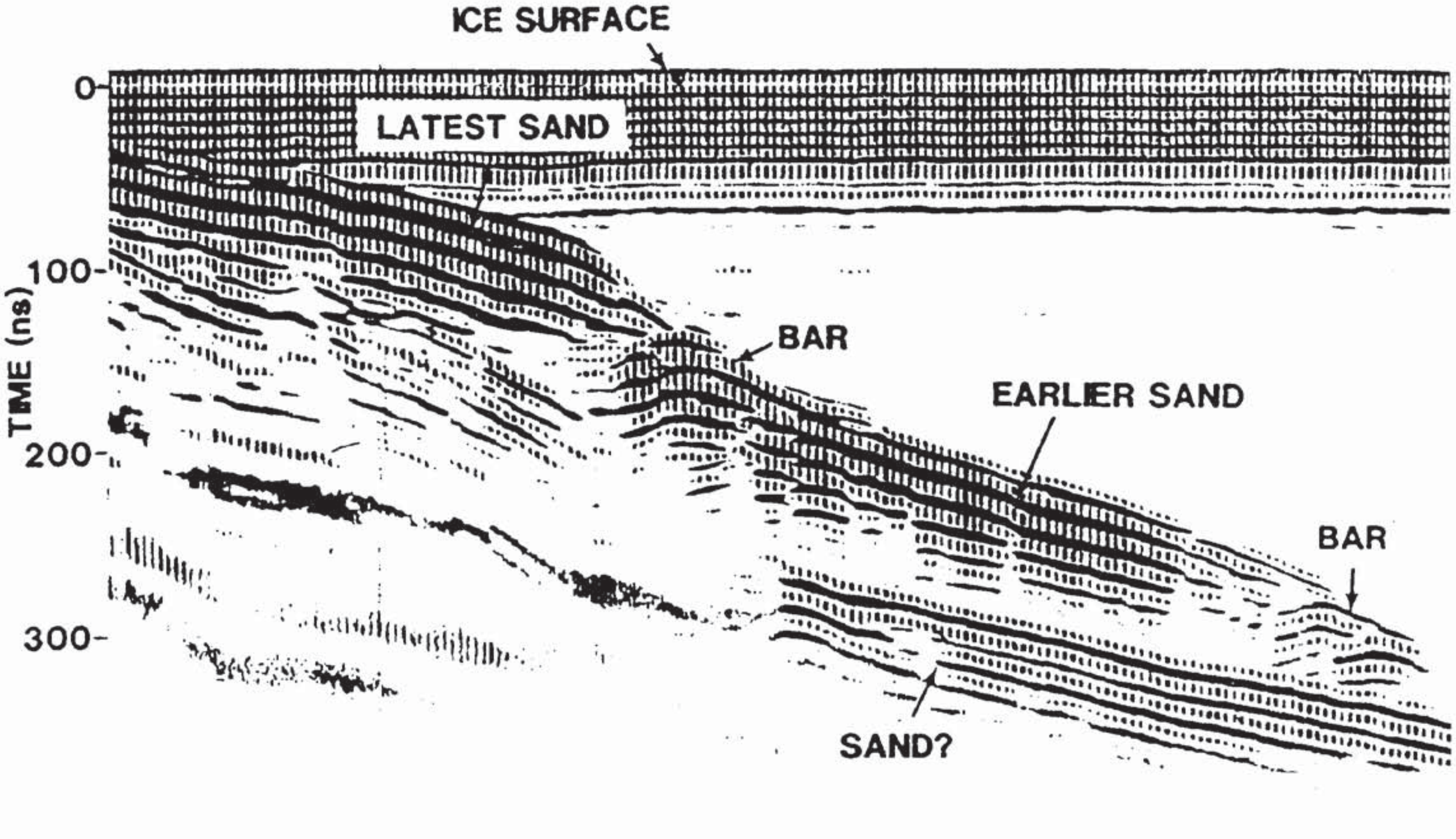

0.167 m/ns). The actual thickness was only 0.15 m. The two-way travel time through the ice layer would only have been around 2 ns. This shows effectively that, using a low-frequency antenna (100 MHz), near-surface features cannot be resolved at all as they are totally masked within the initial ground-coupled wavetrain. The radiowave velocity through the freshwater can be calculated knowing the depth of water (about 4.8 m) and the total travel time (around 300 ns). These values would give a radiowave velocity of 0.032 m/ns (from $2 \times 4.8/300$), ignoring the ice layer and assuming low-loss media. As a double check, the relative dielectric constant of water is 81, which thus gives a radiowave velocity of $0.3/\sqrt{81}$, or 0.033 m/ns (refer to Box 12.1 for the equation).

12.8.2 Hydrogeology and groundwater contamination

As environmental protection measures become more stringent, and the pressure on preserving the quality of groundwater sources increases, so the need to identify groundwater pollution grows. Davis and Annan (1989) have demonstrated how ground radar was used to locate and map out a plume of contaminated water leaking out from a landfill site; a schematic plan of the site area is shown in Figure 12.21A. Along the line of the radar transect shown in this figure, the soil consists of fine sand and overlies bedrock which occurs at a depth of about 20 m. A radar survey was undertaken using a PulseEKKO III radar system and the resulting radargram is shown in Figure 12.21B.

Where penetration of the radiowaves into the superficial sediments occurs, reflections are seen and are thought to be due to horizons with different grain size and density, and hence different soil moisture contents. It is also very clear on this section that there are areas where either only very weak reflections occur, such as at 150 m along the profile at around 400 ns two-way travel time, or the signals are completely attenuated. The presence of contamination, which has an associated high electrical conductivity, attenuates the radar signals severely.

Several boreholes had been constructed along the survey line and the conductivity of the groundwater was measured. The solid line joining a series of black dots on Figure 12.21B indicates the position below which the porewater conductivity is greater than 10 mS/m. As it was known that the superficial deposits were reasonably consistent in their properties over the area of the site, it is evident, therefore, that the pollution plume approaches the surface between 40 and 60 m (as proven by the borehole data) and that it also extends between 110 and 150 m along the profile line at a depth of about 6 m below ground level. The second part of the plume had not been expected, and thus the results from the radar survey were extremely useful in providing this additional information. A ground conductivity survey to

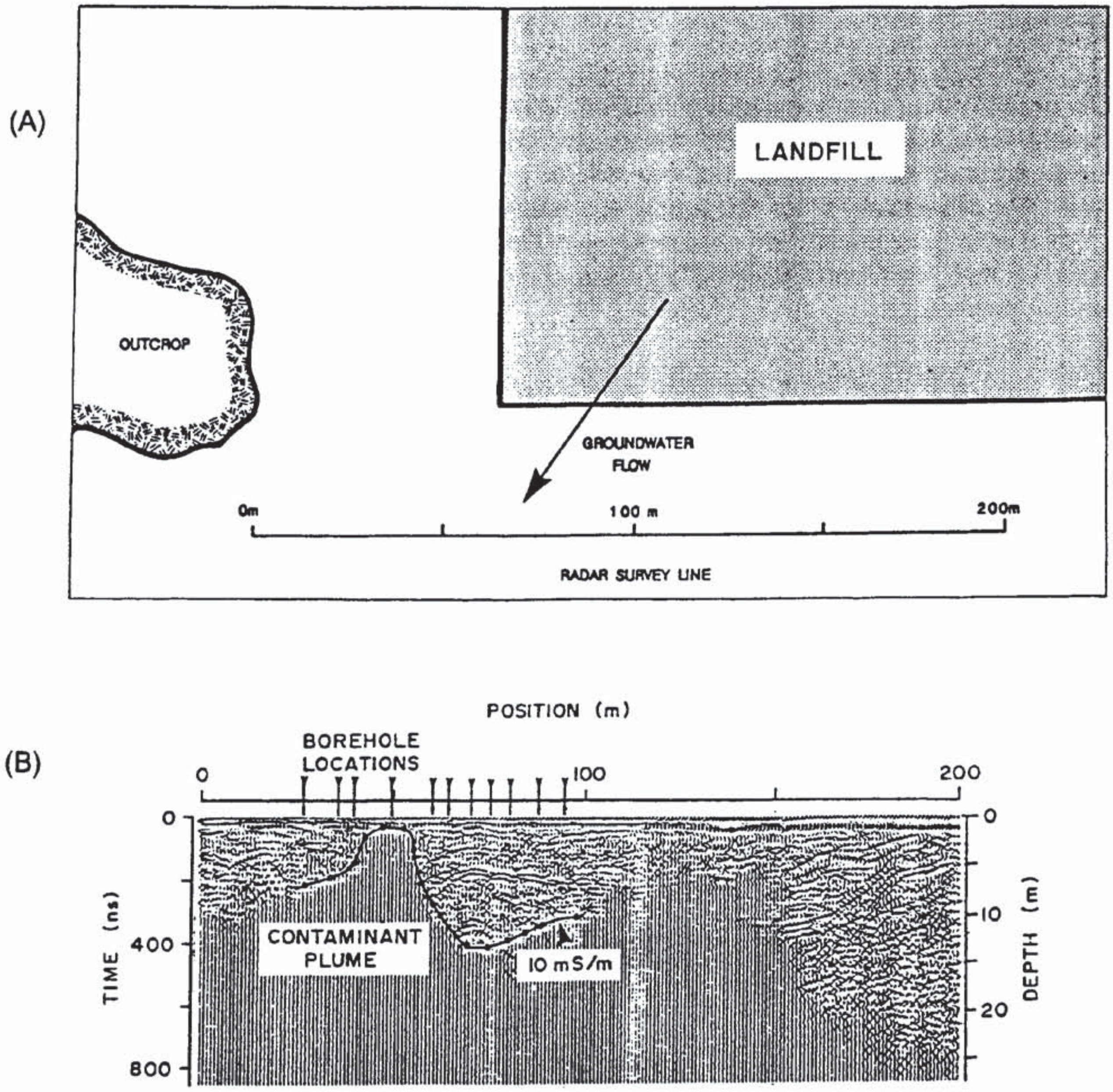

Figure 12.21 Radar section showing the effect of a conductive pollution plume caused by leachate migrating from a landfill. From Davis and Annan (1989), by permission

complement the radar work would have provided a non-invasive method of determining the spatial variation in sub-surface conductivity without having to drill extra boreholes, which in themselves may make the spread of the pollution worse.

Where it can be demonstrated that radar surveys would be useful under the ambient geological and ground conditions, and that the pollution can be detected by radar, then changes in the pollution plume can be mapped. By undertaking repeat surveys along the same ground transects, it is possible to detect changes as a function of time. Furthermore, where remediation measures are undertaken, the success of such treatment can be monitored using radar.

In certain cases, the actual pollution itself may not be detectable using radar, but the containers from which the pollution originated

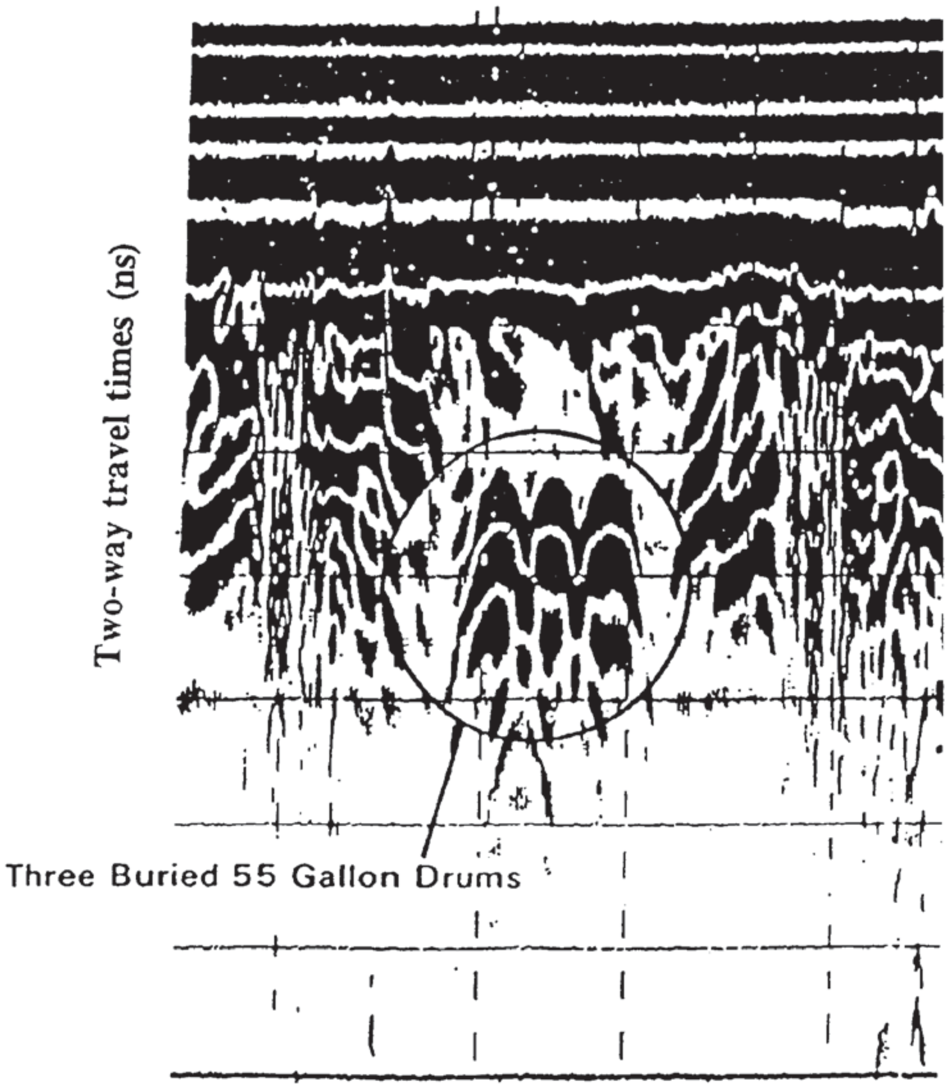

Figure 12.22 Radar record over three buried drums laid side by side

may be. Consider the case of buried 55-gallon steel drums which may have leaked their contents. Figure 12.22 shows a radar record over three buried drums. Note the characteristic diffractions arising from the drums which are located side-by-side. Also note that the incident radar waveform consists of more than one band, and hence the diffractions from the drums give the appearance of lower diffractions; these are the tails of the primary diffractions.

Ground penetrating radar is being used extensively in the Netherlands for hydrogeological assessment in groundwater management. Falling water tables and deteriorating water quality seriously affect agriculture and nature conservation and potable water supplies. Van Overmeeren (1994) has provided examples of types of hydrogeological applications current in the Netherlands where there are four main radar targets: (a) tectonic and sedimentary structures; (b) water tables within sandy deposits in push moraines, river terraces and sand dunes; (c) perched water tables as distinct from regional water tables; and (d) spatial extent and continuity of buried clay and peat layers within the superficial deposits.

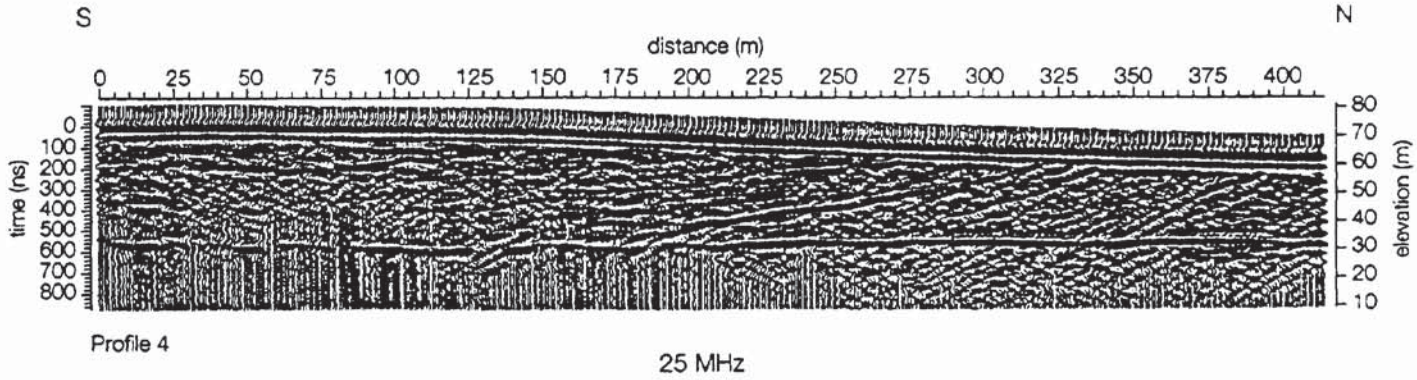

Figure 12.23 Radargram acquired with 25 MHz antennae over a sandy ice-push moraine. The water-table reflection is evident at an elevation of 30 m. Note the slight vertical displacement in this reflection where an inclined reflection due to a clay layer intersects the water table at 185 m. From van Overmeeren (1994), by permission

A radargram acquired using a PulseEKKO IV with 25 MHz antennae and station interval of 1 m is shown in Figure 12.23. The profile was obtained over push moraine comprising mainly sand. The section has been corrected for topography and has identical horizontal and vertical scales. The water table is evident as a horizontal reflection with a large amplitude. In the northern part of the section, the reflection is largely continuous whereas it is less so in the southern, most elevated, part. This suggests that the depth of penetration of the radar is at its limits here and that the greater depth below ground level to the water table in the southern part results in the poorer data quality. Using a radiowave velocity of 0.145 m/ns (derived from CMP measurements), the water table is still evident at 42 m below ground level. The radargram also reveals reflections from interfaces above the water table. The oblique reflections are associated with interfaces between sandy layers of different grain size or between sandy and clayey sediments. In both cases, the interface marks a change in moisture content and hence a contrast in relative dielectric constant.

A conspicuous reflector with a large amplitude and dipping southwards is evident in the middle of the section. There is a small vertical offset (around 2 m) in the water-table reflection where it is intersected by the inclined event. The step in the water table is thought to be caused by an inclined clay layer which gives rise to the strong oblique reflection.

Van Overmeeren (1994) has described another example of the hydrogeological usefulness of GPR, where a radargram (Figure 12.24A) was acquired using a PulseEKKO IV with 50 MHz antennae and a station interval of 0.5 m. The survey transect was over a valley with marine interglacial deposits passing into an uplifted ridge of ice-pushed sediments. A clay layer forms part of the marine formation. The objective of the radar survey was to map the lateral continuity of the clay layer and to locate its western limit (see Figure 12.24B which is a schematic interpretation of part of Figure 12.24A). The clay layer, which occurs at a depth of 15 m below ground level, sustains an artesian aquifer which is recharged by infiltration in the

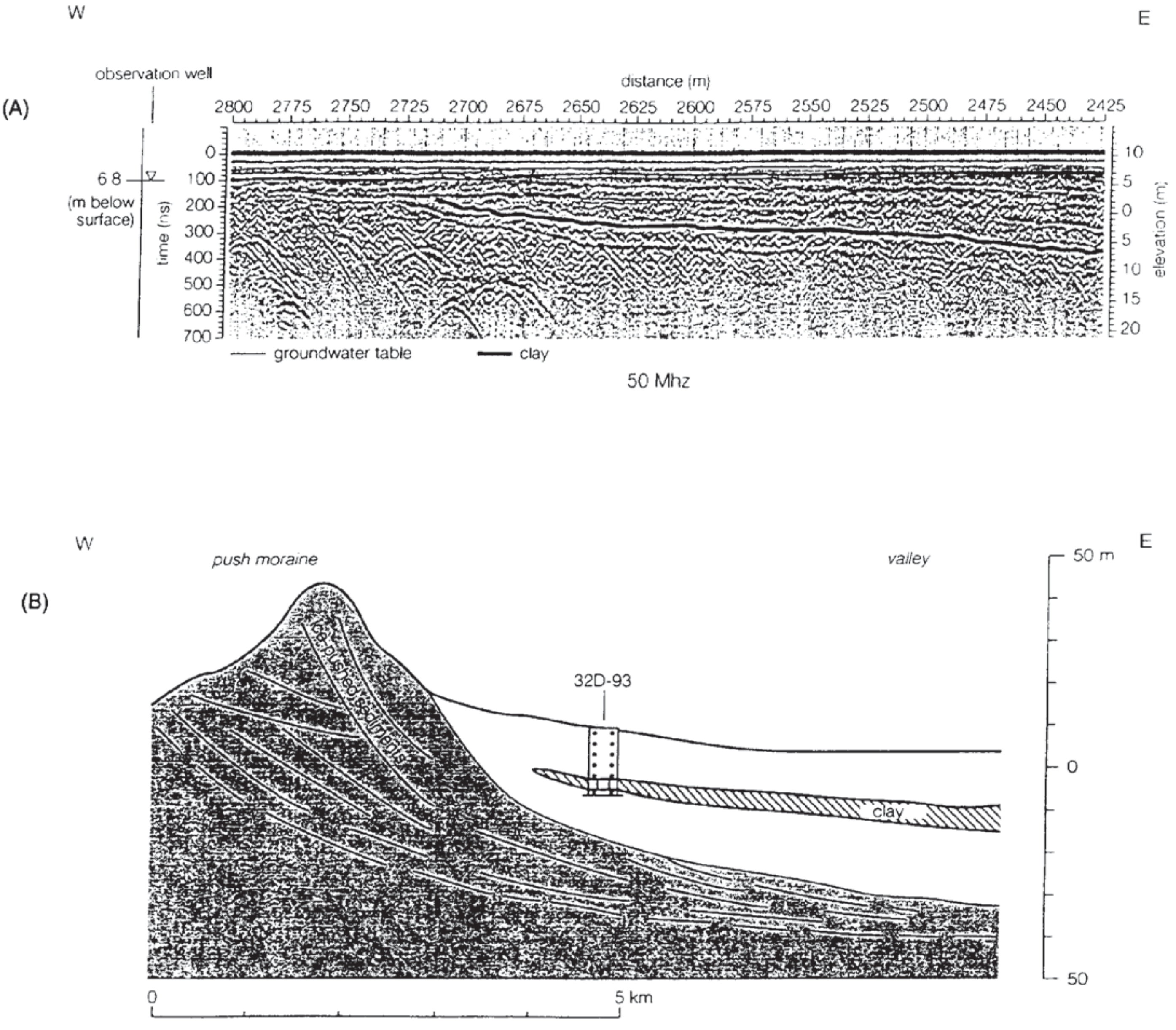

Figure 12.24 (A) Radargram acquired with 50 MHz antennae over a sandy ice-push ridge on to which interglacial marine sediments, including a clay layer, onlap. The clay layer is indicated by a solid black line. The water table occurs at a depth of about 7 m. (B) General interpretation of the part of the radargram shown in (A). The clay layer has been verified by a borehole (32D-93). From van Overmeeren (1994), by permission

higher ice-pushed ridge. The precise boundaries of the clay layer were required for groundwater flow modelling.

In the radargram (Figure 12.24A), the vertical exaggeration is 2.5 times the horizontal scale. The regional groundwater level is at a depth of about 7 m, as determined from a nearby observation well. A radar CMP test near the well produced a value of the radiowave velocity of 0.115 m/ns for the sediments above the water table. In the area of the survey, the average radiowave velocity was found to be 0.075 m/ns for sediments above the clay band, which is in close agreement with a known value of 0.06 m/ns for sand saturated with freshwater. In contrast, dry sand has a radiowave velocity of 0.15 m/ns. The field-derived radiowave velocity is strongly indicative of freshwater-saturated sands above the clay layer, which can be identified on the radargram as a coherent reflection with large amplitude. The reflection from the clay layer persists clearly until station 2715 where it is cross-cut by an onlapping horizon.

The radargram shows that sensible reflection events arising from the sub-surface geology can be identified to an interpreted depth of 12 m, with the exception of several diffraction-like events in the western part of the radargram which occur at interpreted depths of about 16 m. Note in Figure 12.24A that the reflections are largely coherent across the section, but become increasingly incoherent or disturbed west of station 2675 where the ice-pushed ridge is encountered. The more chaotic nature of reflection events here, due to diffraction hyperbolae, is typical of ice-pushed moraine in this area.

Although the water table occurs at shallow depth below ground level (around 3–5 m), reflection events at significant depth are still evident on the radargram. Elsewhere in the Netherlands, the detection of buried clay layers below the water table has proved impossible, yet at this location it is obvious that the radar survey has provided extremely valuable information about the clay layer. This is attributed to the high electrical resistivity of the surface layers resulting in very little attenuation of the radar energy.

The transparency of freshwater saturated sediments to radiowaves has also been demonstrated in North America using a PulseEKKO IV with 100 MHz antennae (Figure 12.25). The reflection arising from the water table is clearly seen as a coherent reflection with a large amplitude between stations 375 and 625 at an elevation of around 500 ft (about 152 m). Diffraction hyperbolae arising from two cables/pipes above the water table are also obvious (arrowed). Note that there are many reflections evident from the sub-surface geology present to depths of around 33 ft (10 m). The data are published

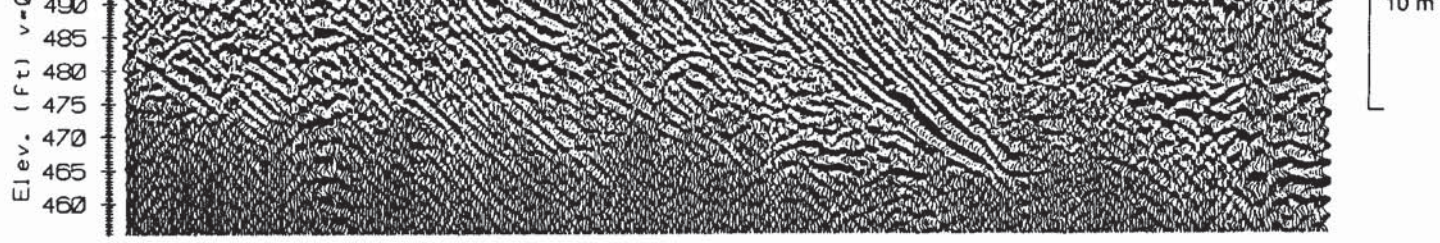

Figure 12.25 Radargram acquired using 100 MHz antennae with a PulseEKKO IV system showing the water table (flat-lying reflection arrowed) and two diffraction hyperbolae from near-surface cables/pipes. Data courtesy of Michigan Department of Natural Resources, Environmental Response Division and Sensors & Software Inc.

courtesy of the Michigan Department of Natural Resources, Environmental Response Division, and of Sensors & Software Inc.

In addition to investigations into natural groundwater resources, there is a growing need to map groundwater contamination (Greenhouse *et al.* 1993). Such pollution can arise from leachate migrating from a landfill, from saline water ingressing inland due to over-exploitation of freshwater sources, natural hydrocarbon contamination (from oil shales, etc.), through to chemical spillages (deliberate or otherwise) over timescales that can range from a few hours to many years. For example, could a chemical spill from an overturned railway tanker be monitored using geophysical methods? Or can petroleum products that have leaked from pipes at a refinery and which have ponded below ground at the water table be mapped?

Some chemicals can migrate from the source of contamination extremely quickly and would be difficult to detect by any means. However, an increasing amount of research is being undertaken to examine the protracted contamination of groundwater. The reason is that there are enormous quantities of carcinogenic organic groundwater contaminants, such as DNAPLs (colloquially pronounced as 'dee-napples') – DNAPLs are dense, non-aqueous phase liquids. The main chemical concerned is perchloroethylene (PCE) which is one of the main constituents of the dry-cleaning and metal-cleaning industries. PCE is but one of a type of liquids known as 'chlorinated organic solvents'. Other well-known chemicals are trichloroethylene (TCE) and dichloromethane (DCM) which are paint-strippers and metal-degreasers. In 1986, it is reported that in the USA alone, 120 million litres of PCE and 200 million litres of TCE were manufactured. Once used, a small but significant proportion of these volumes is disposed of underground, around dry-cleaning establishments, car-service garages, in landfills and waste lagoons, and as residues on old industrial sites.

As their name suggests, DNAPLs are dense (with a density of 1.623 Mg/m^3) and sink rapidly through the local groundwater leaving a residual trail of 5–20% of the pore volume, and eventually ponding for a time on a low-permeability layer such as a clay aquitard. DNAPLs also have low viscosity and low surface tension which allow the chemicals to migrate rapidly through porous media. They can even pass through very fine fractures in clay given adequate time. It is estimated that in the USA, the cost of cleaning up the existing DNAPL contamination to acceptable standards is in excess of one thousand billion dollars.

An excellent overview of a controlled experiment to examine the detectability of DNAPLs has been presented by Greenhouse *et al.* (1993). A schematic of the experimental site is shown in Figure 12.26. A 9 × 9 m cell was constructed by driving corrugated steel sheet piles, sealable at their joints, through the 3.3 m thick surficial aquifer into the underlying clay aquitard. Two concentric walls contained a 0.5 m

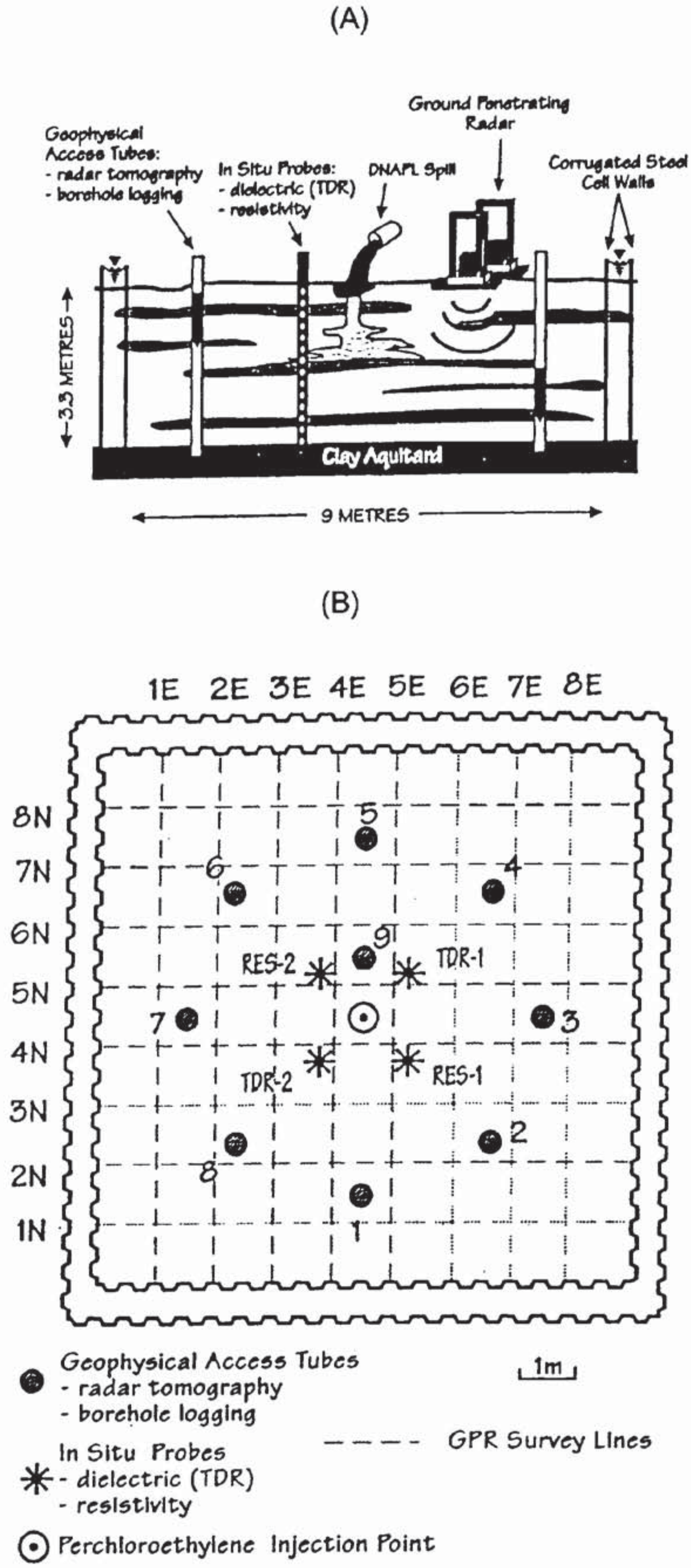

Figure 12.26 (A) Schematic cross-section of the 9 × 9m test cell at Borden. (B) Plan view of the Borden test cell showing access tubes AT1-9, resistivity probe locations RES-1 and RES-2, TDR locations TDR-1 and TDR-2, the 1 m radar grid and the point of PCE injection. From Greenhouse *et al.* (1993), by permission

wide moat which effectively isolated the inner section hydraulically from its surroundings and allowed the interior water table to be maintained at a depth of 0.15 m below the ground surface. A tarpaulin covered the ground to restrict evaporation. The test cell was instrumented via nine vertical access tubes for radar tomography and borehole logging, and had four further vertical *in situ* probes to measure resistivity and relative dielectric constants (using time domain reflectometry; TDR). Surface ground radar traverses were undertaken repeatedly over two sets of orthogonal profiles with a 1 m line interval using a PulseEKKO IV radar system with 200, 300, 500 and 900 MHz antennae. Over a period of 70 hours, 770 litres of PCE were injected under a constant head of 2 m of water at the centre of the test cell at a point 0.6 m below the ground surface. Geophysical imaging of the test cell began several days before the contaminant injection and continued over 912 hours after the injection had been completed. Measurements were made throughout the period of the experiment so as to obtain time-dependent datasets. Geophysical measurements continued for several weeks after the main experiment had been completed in order to monitor the removal of the PCE from the test cell, which was undertaken by flushing the cell with surfactants.

Of the substantial body of data obtained from this experiment, a time series of radargrams obtained along transect 5N (Figure 12.26) using 200 MHz antennae is shown in Figure 12.27. Three radargrams are shown ranging from one obtained before any injection of PCE had occurred, and two acquired at 16 and 920 hours after injection. What is clear from comparing the two radargrams after injection is that PCE appears to pond at a depth of 1 m (iv on Figure 12.27B) and then drains downwards leaving a residual ((v) on Figure 12.27C) at 1 m depth with ponding above the clay aquitard evident at (vi).

These experiments demonstrated that PCEs can be imaged successfully using a variety of geophysical methods, and that GPR can be used to monitor both the migration and the subsequent remediation of the contaminated ground. Further aspects of the radar surveys have been reported by Brewster *et al.* (1992a, b), for example. A GPR survey at a site where DNAPL contamination was known to have occurred has been described by Carpenter *et al.* (1994), although no DNAPLs were imaged directly using radar.

12.8.3 Glaciological applications

Radar mapping of the polar ice sheets has been one of the most widely used geophysical methods in both Greenland and Antarctica. Radio echosounding has been developed substantially since its early use in the 1960s. Determination of ice thicknesses is now accurate to around 1% and has provided excellent agreement with values derived from both seismic and gravity surveys, as well as with borehole control.

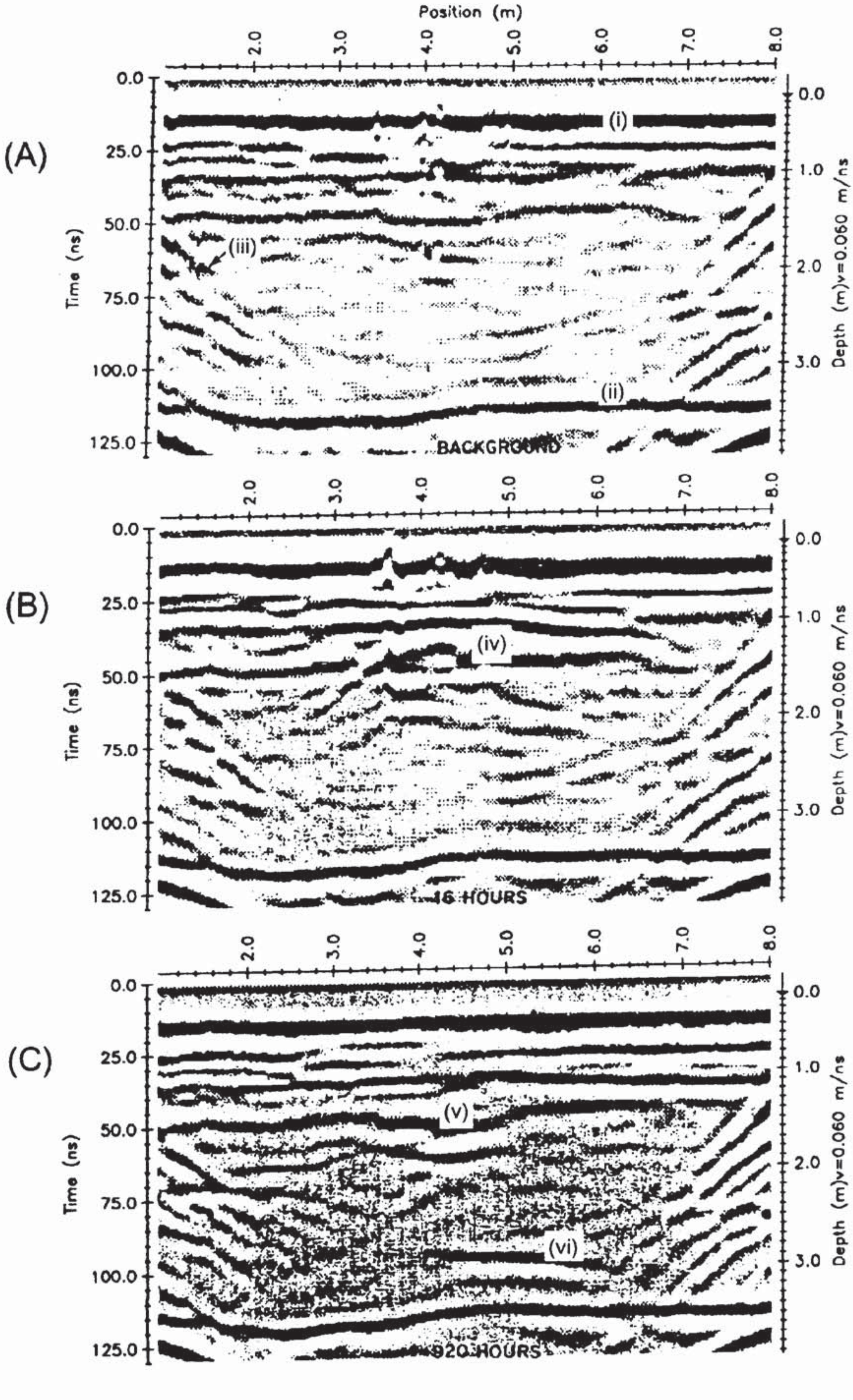
Position (m)
2.0
3.0
4.0
5.0
6.0
7.0
8.0
(A)
(B)
(C)
Time (ns)
0.0
25.0
50.0
75.0
100.0
125.0
Depth (m)v=0.060 m/ns
0.0
1.0
2.0
3.0
(i)
(ii)
(iii)
(iv)
(v)
(vi)
BACKGROUND
16 HOURS
920 HOURS

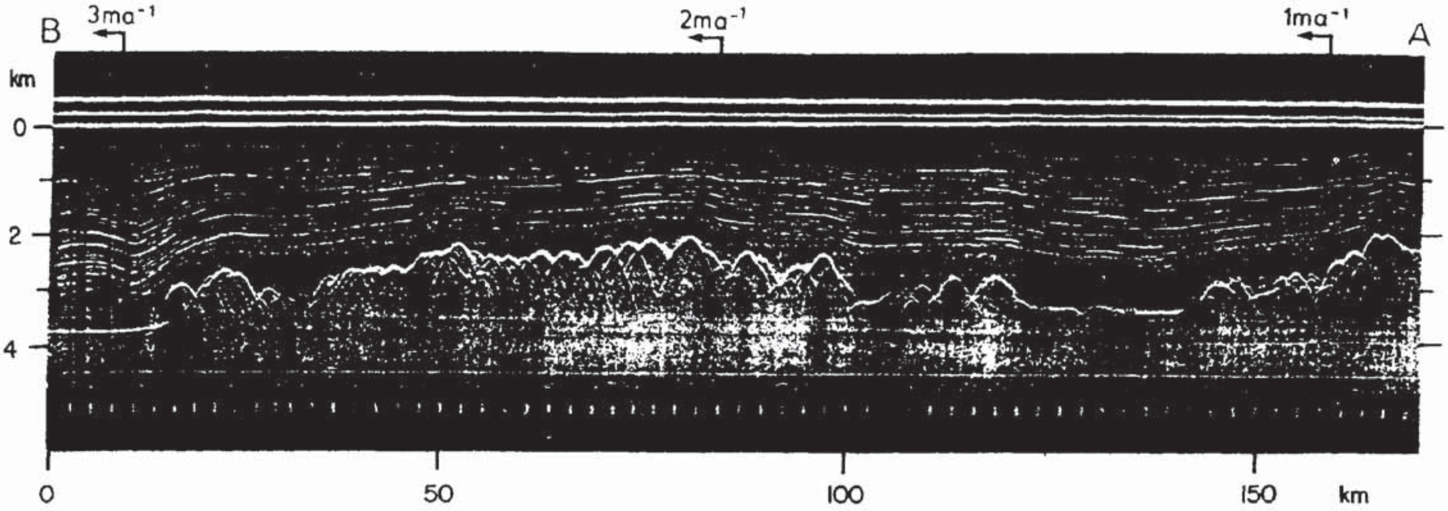

Figure 12.28 Radio echosounding record from along an ice flow line near Vostok, Antarctica. From Robin and Swithinbank (1987), by permission

An example of a radargram obtained using a 60 MHz antenna system over an ice flowline near the Russian research station Vostok, in Central Antarctica, is shown in Figure 12.28 (Robin and Swithinbank 1987). The total depth of penetration is around 3800 m. Three principal features are evident on this profile. The first is that there are a series of sub-parallel reflections within the ice itself. These horizons are thought to be due to elevated concentrations of sulphate (H_2SO_4) arising from large eruptions from volcanoes located outside Antarctica and transported in atmospheric aerosols to become incorporated within the polar snow, or from horizons which have undergone melting during the summer months (when the ice was at the surface) and subsequent refreezing. Ice has a thermal memory and the dielectric properties of the ice can be used to identify layers that have undergone melting and refreezing (Reynolds 1985). Some of the most prominent internal reflections can be traced over thousands of square kilometres and appear to be interfaces formed at the same time, and thus can be used as isochrons. These can then be used in the analysis of the dynamics of the flow of the ice sheet.

The second feature is that the bedrock surface can be seen very clearly and exhibits a range in elevation of about 1500 m. The bedrock topography is thus a hidden range of mountains. The third feature is located at the left-hand end of this profile at the base of the ice sheet. Note the flat, bright reflection at 3800 m depth. This is produced from what has been interpreted to be the surface of a large sub-glacial freshwater lake. The contrast in relative dielectric constants between the basal ice and the freshwater has given rise to this characteristic style of reflection. This type of feature can also be seen in another radio echosounding record shown in Figure 12.29 (Drewry 1986). Also note in both Figures 12.28 and 29 that there is a zone about 500 m wide immediately above the bedrock in which internal reflections are absent. This is possibly due to the basal deformation of the ice being such that the scale of deformation distorts the layering to such an extent that coherency is lost.

Figure 12.27 (*opposite*) Borden test cell imaged along profile line 5 N (see Figure 12.26) using 200 MHz antennae. Radargram (A) was acquired prior to PCE injection, and radargrams in (B) and (C) were obtained 16 and 920 hours after injection. (i) = cell surface; (ii) = top of clay aquitard; (iii) = reflections off the vertical cell walls; (iv) = pooled PCE at 1 m depth; (v) = a zone of residual PCE; and (vi) = PCE pooled on the clay aquitard. After Greenhouse *et al.* (1993), by permission

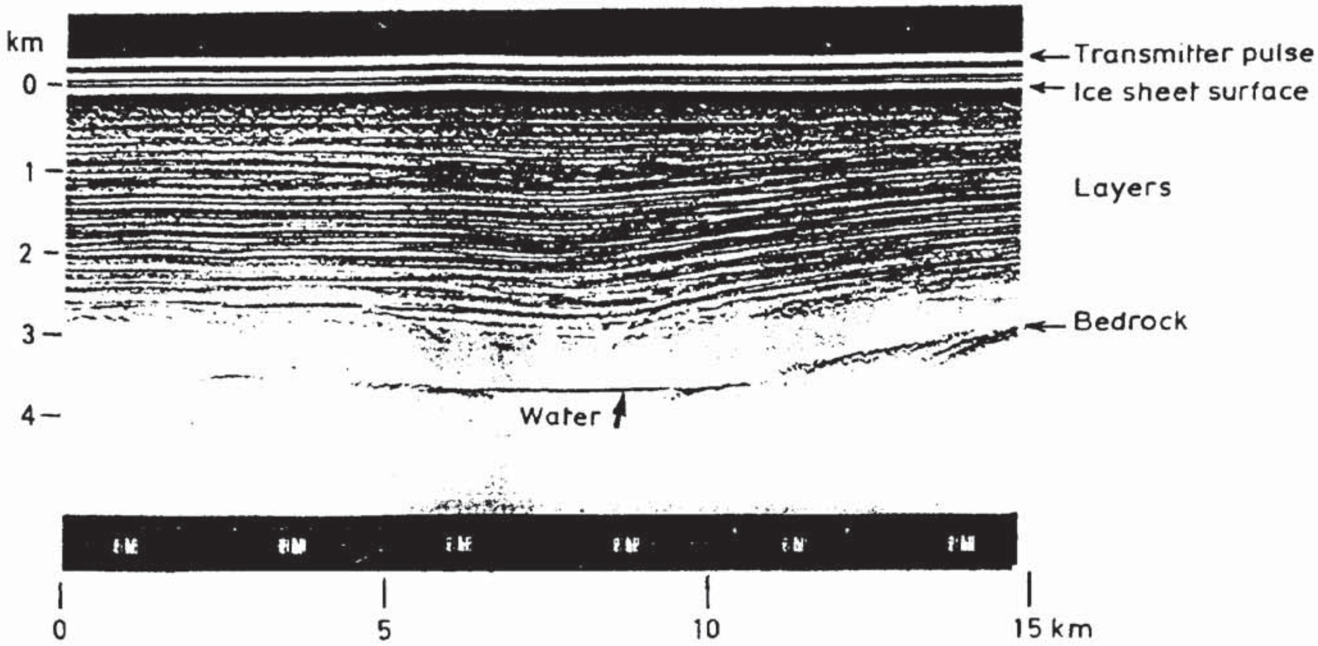

Figure 12.29 Radio echosounding record from a site in East Antarctica. From Drewry (1986), by permission

A radar system developed for radio echosounding (Wright *et al.* 1990) utilises antennae with much lower centre frequencies (1, 2, 4, 8 and 12.5 MHz) than those used previously ($\geqslant 60$ MHz). Records using this new system are shown in Figure 12.30. A 4 MHz centre-frequency antenna was used in this example which was obtained on Ice Stream B, near the Transantarctic Mountains. In Figure 12.30A, diffractions arising from near-surface crevasses and internal reflections are evident. The latter are also evident in Figure 12.30B, which shows the radar record for the lowermost 400 m of ice. In addition, a 'bright spot' is observed within the basal ice and is thought to be due to entrained basal rock debris or trapped water. Strong diffractions also occur at the base of the ice, just below the 400 m mark. These are thought to emanate from either bottom crevasses within the base of the ice or from within a saturated till layer sandwiched between the ice and the bedrock.

At the other extreme of range, Forster *et al.* (1991) have developed a very-high-frequency radar which transmits 200 mW at 11 GHz with a 2 GHz bandwidth to measure detailed snow stratigraphy (Figure 12.31A). This radar has an effective resolution in snow of around 5 cm. The normalised power return is plotted as a function of depth (Figure 12.31B), assuming a uniform radiowave velocity through the snow—which leads to an inaccuracy of about 2% in depth determination over the shallow range of depth penetration (<3 m). The importance of a device like this is that it can be used to determine the effect of shallow sub-surface strata on measurements made by satellite remote sensors, such as synthetic aperture radar imagers, radar altimeters and passive microwave radiometers (Forster *et al.* 1991).

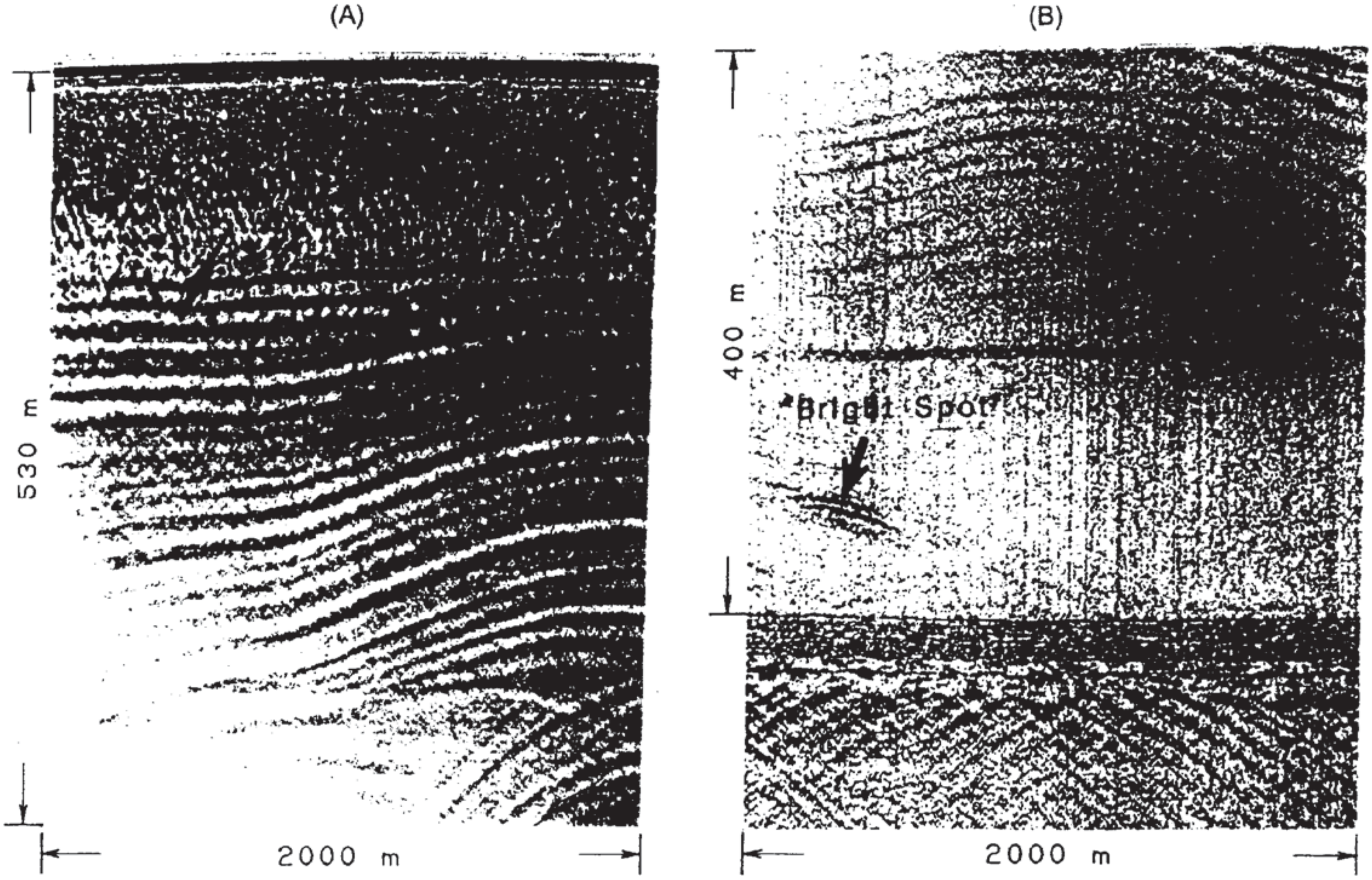

Figure 12.30 Low-frequency (4 MHz) records of sub-ice sheet environs: (A) diffractions from surface crevasses, and internal reflections; and (B) internal reflections and diffractions from basal crevasses and from a deformed sub-glacial sediment zone. From Wright *et al.* (1990), by permission

12.8.4 Engineering applications on man-made structures

Radar has enormous potential for use on engineered constructions. In these cases, the geometry and materials of each structure should be known. However, what can be at odds is whether the structure has been constructed according to the required specifications. Indeed, the construction methods may have left a legacy of subtle differences in physical properties within the structure. Radar can be used to ensure that, for example, reinforcement mesh has been placed at the correct level within concrete slabs. In some cases, the act of pouring the concrete can displace the mesh, so that instead of being located within the middle of a slab it is pushed to the bottom, and therefore cannot perform the function for which it was intended. Similarly, the location of reinforcement bars ('rebars') can be checked using higher-frequency radar (e.g. 500 MHz, 900 MHz or higher centre frequency) as shown in Figure 12.32.

An embankment made of fill material, which consisted largely of crushed dolerite, was thought to be uniform in its properties throughout. A radar survey using a 120 MHz antenna revealed sub-horizontal layering within the fill which were interpreted to be associated with compacted horizons. These layers had been produced by the

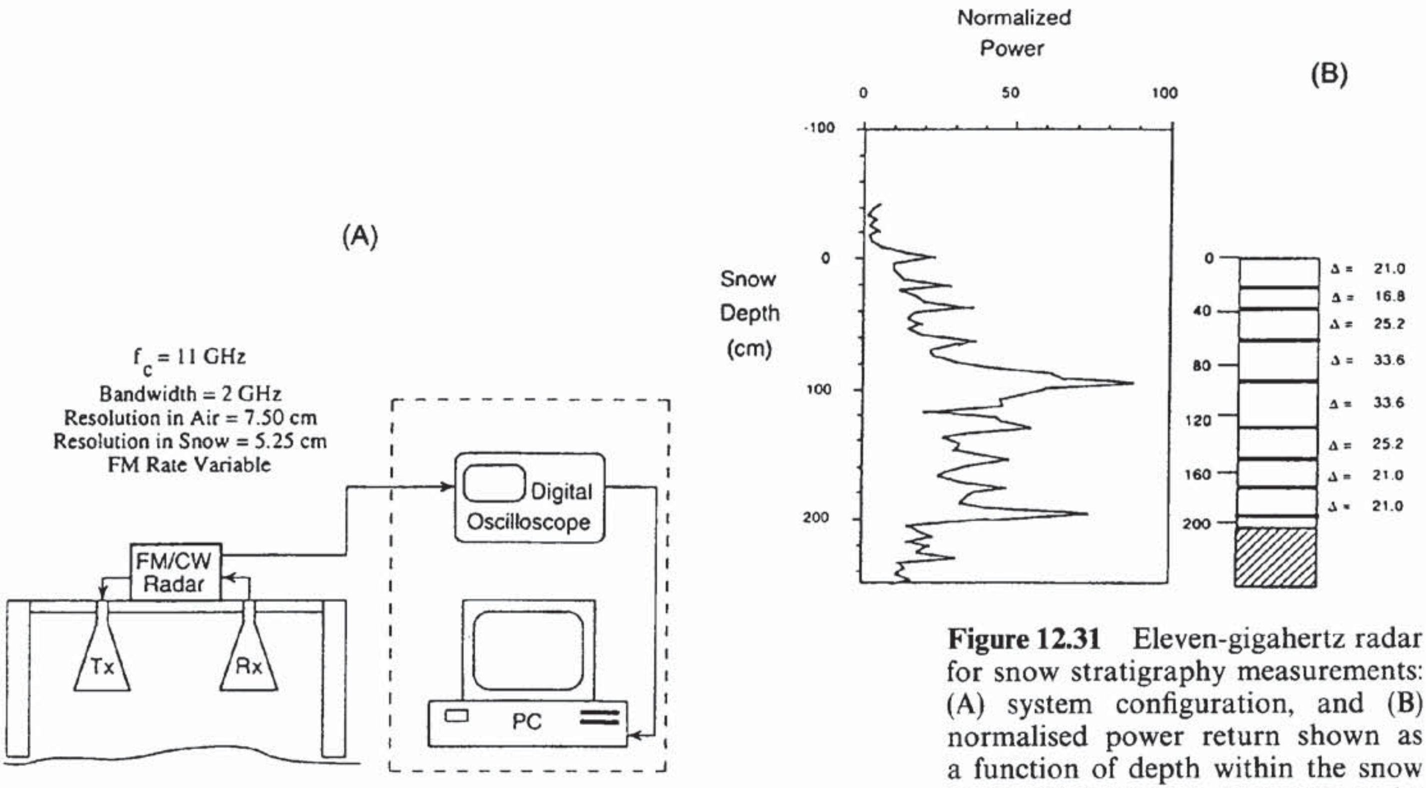

Figure 12.31 Eleven-gigahertz radar for snow stratigraphy measurements: (A) system configuration, and (B) normalised power return shown as a function of depth within the snow pack. After Forster *et al.* (1991), by permission

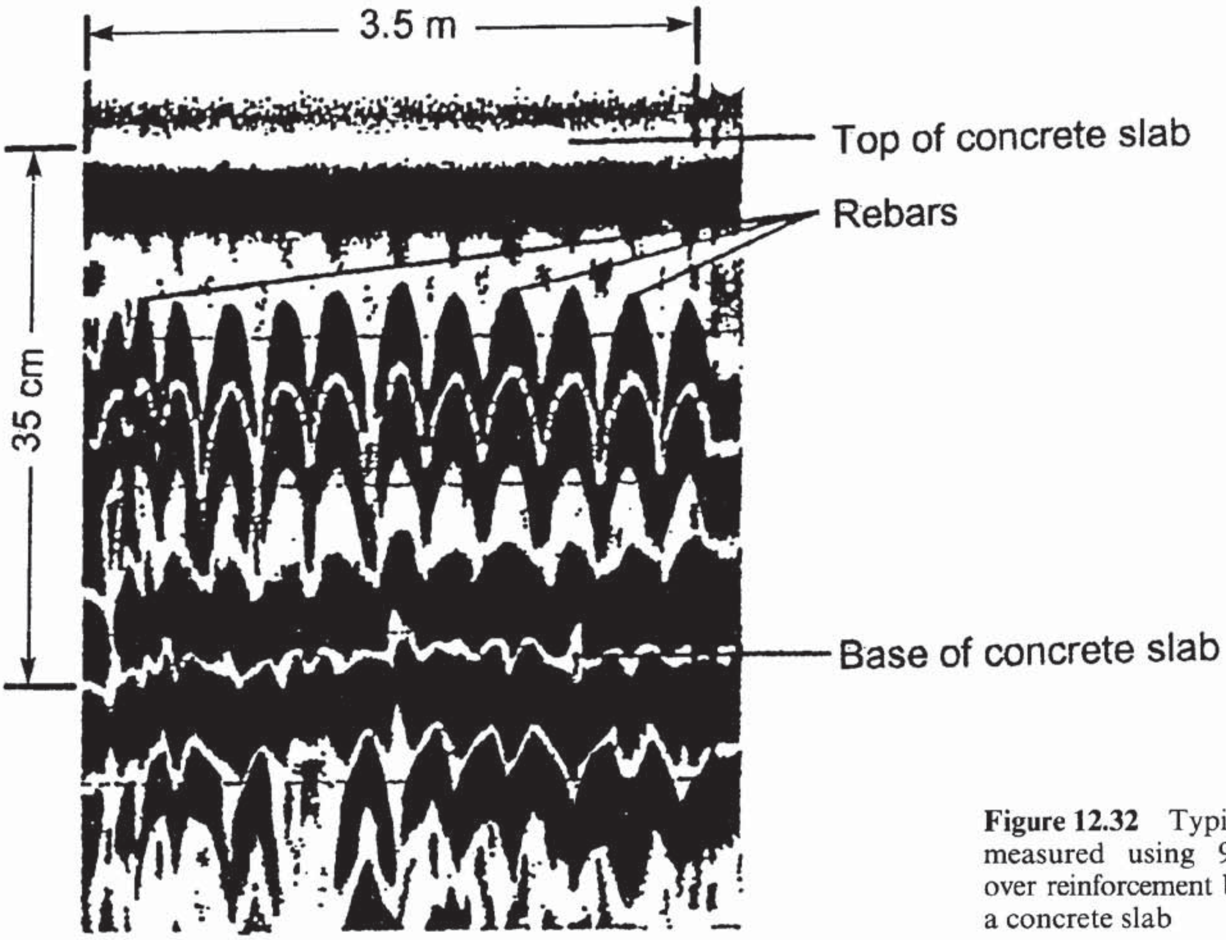

Figure 12.32 Typical radar record measured using 900 MHz antenna over reinforcement bars (rebars) within a concrete slab

contractor's vehicles driving over the fill along roadways. Distinct reflections were evident from these horizons and occurred as a result of the reduction in soil moisture content (and hence altered dielectric constant) of the compacted horizons (Reynolds and Taylor 1992).

Water-retaining dykes along Dutch rivers have been provided at various locations with granular filters. The purpose of these filters is to reduce the groundwater potential inside and below the dyke in order to increase the stability and prevent bursting of a clay layer at the lee side of the dyke (Figure 12.33A). The gravel-filled filter must be in hydraulic contact with the underlying sandy layers. The filters have a working life of several decades but suffer with becoming clogged by finer particles. Consequently, it is necessary to monitor the filters periodically, preferably using non-destructive methods. Ground penetrating radar has been used successfully in such investigations, as reported by de Feijter and van Deen (1990).

Radar surveys were carried out when the groundwater level was at its maximum and also at its minimum, over a time interval of several years. A sample radargram is shown in Figure 12.33B, which was obtained using a 300 MHz antenna with a GSSI radar system. The horizontal reflection arises from the water table (with its multiple). Reflection III is caused evidentally by the filter–dyke interface. Note, however, that none of the horizontal layers within the dyke itself is imaged. Indeed, the zone to the right of the filter–dyke interface shows significant attenuation of the radar energy, most probably because of the presence of water-saturated sandy clay and clay.

The ground radar method lends itself very well to the investigation of road pavements and bridge decks as they are made up of discrete layers. Radar can be used to measure layer thicknesses and to detect areas of delamination, where one horizon separates from another causing weakness in the road. This can lead to rapid deterioration of the road surface. As the depth of investigation is small (usually < 1 m) and as fine vertical resolution is required, high-frequency antennae are used, typically 900 MHz centre frequency. One or more antennae are fixed to a frame on a vehicle so as to maintain a fixed and known geometry. The vehicle drives along the road being surveyed at speeds up to several tens of kilometres per hour. The graphical output is viewed for evidence of anomalous zones which might indicate potential problems within the road base. Radar can also be used to check that the specified thickness of sub-base material has been put down during construction or if there are areas where the sub-base is defective.

The radar method has considerable applications within stone and brick masonry. The method has also been used to investigate the internal composition of statues and of masonry façades of historic buildings.

In most of these applications, the radar method complements other non-destructive testing methods, such as acoustics (e.g. in bridge deck

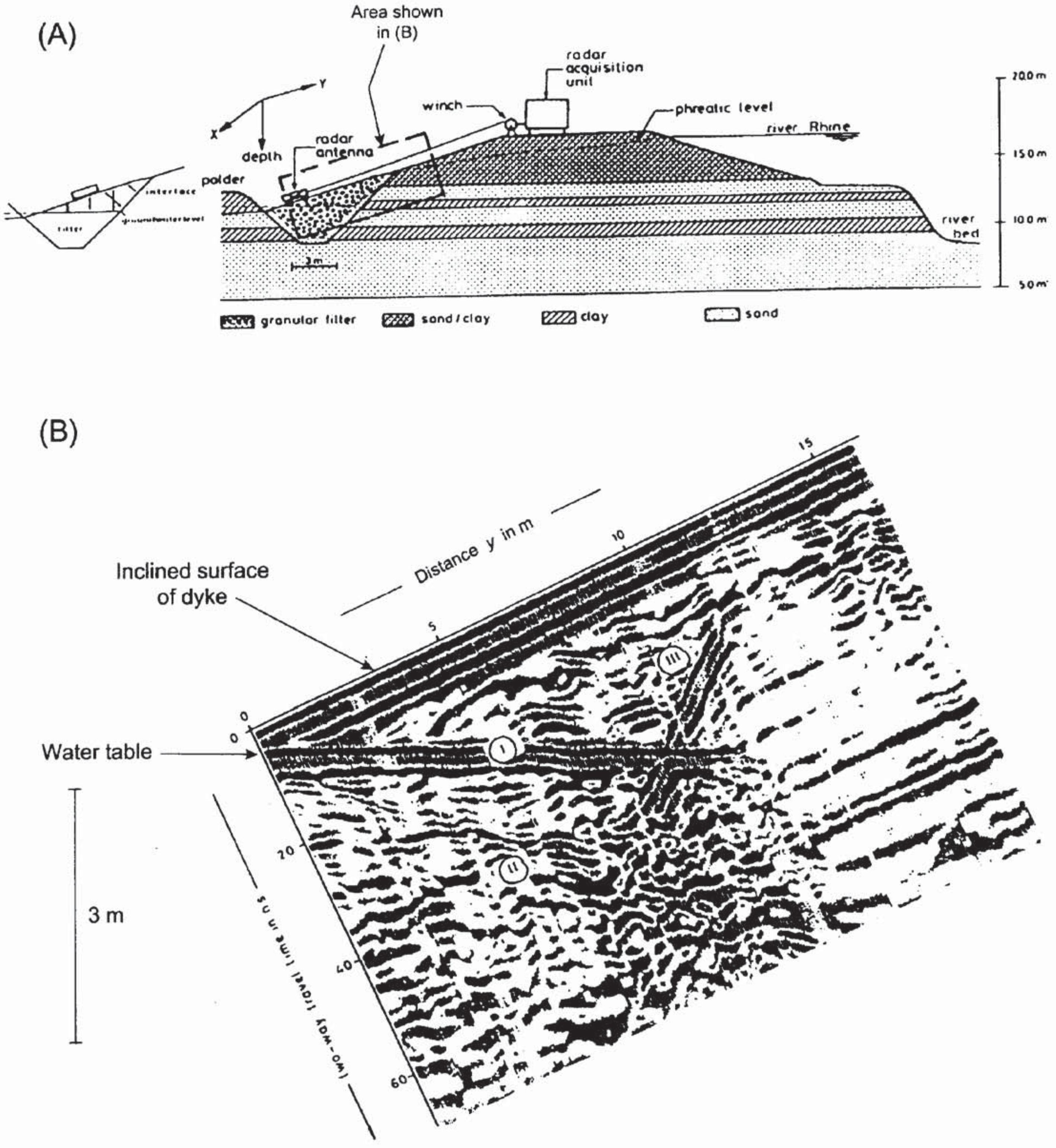

surveys), nuclear density measurements and thermal imaging (e.g. road studies). As with all geophysical methods, some ground-truth data are invaluable for correlation purposes. In road pavement studies, cores are used to provide point-to-point correlation with radargrams. The major advantage of the radar method is that it is entirely non-destructive.

Figure 12.33 (A) Cross-section of a dyke adjacent to the River Rhine, illustrating the engineered sub-structure, and the disposition of a radar transect shown in (B): 300 MHz radargram taken at highwater level. After de Feijter and van Deen (1990), by permission

12.8.5 Voids within man-made structures

One of the commonest applications of ground penetrating radar in the investigation of man-made structures is the detection and location of voids. Radar has been used extensively to inspect the condition of brick-lined tunnels and sewers. In the latter case, radar is often used in conjunction with closed-circuit TV (CCTV).

Two particular aspects of radar make the method particularly suited to such investigations. One is that the speed of radiowaves in air is around three times faster than in solid materials and thus produces a pronounced velocity 'pull-up' effect in association with a significant void. The second is the occurrence of resonance which happens when the wavelength of the incident radiowave energy is the same as, or shorter than, the dimensions of the void.

An example of a radargram acquired in a sewer survey is given in Figure 12.34A. This shows an extract of a radargram obtained where an air void was found above the crown of a sewer. Two features are evident on the radar section: one is the obvious difference in position of the crown of the sewer each side of the void (Figure 12.34B); the second is the obvious lozenge-shaped anomaly associated with the air void (picked out with white dashed lines in Figure 12.34A). The data were acquired using a vertical-looking 500 MHz antenna with a GSSI SIR-3 radar system.

Not all air voids occur as failures in construction. There are examples where radar has been used to locate hidden crypts in churches and in other historic buildings, or old Second World War air-raid shelters whose locations have been lost.

An excellent example of a radargram showing the location of a crypt has been provided by Stratascan from a survey at Worcester Cathedral (Figure 12.35). This particular survey profile was carried out at right-angles to the long axis of the Charnel House which has an arched roof. The stone–air interface of the roof of the Charnel House is obvious by the bright strong amplitude reflections, the apex of which is at 7.5 m along the profile. Note that at about 6 ns above the top of the Charnel House roof reflection, there is a much weaker reflection which has the same shape as the reflection from the crypt. This is interpreted to be from the top surface of a line of stones used to construct the ceiling arch of the Charnel House.

The bright domed reflection at the bottom of the radargram is not due to a heap of rubble on the floor of the Charnel House, but is the reflection arising from the floor itself. That it is domed is purely due to the velocity pull-up effect from the air-filled crypt. Given an air-filled void 2 m deep, the reflection from the floor would occur at a two-way travel time some 26 ns ahead of a reflection from a comparable depth within the adjacent soil. Note also that the reflection from the stone–air interface at the ceiling of the Charnel House has the form of a leading white then positive, etc., whereas the reflection from the

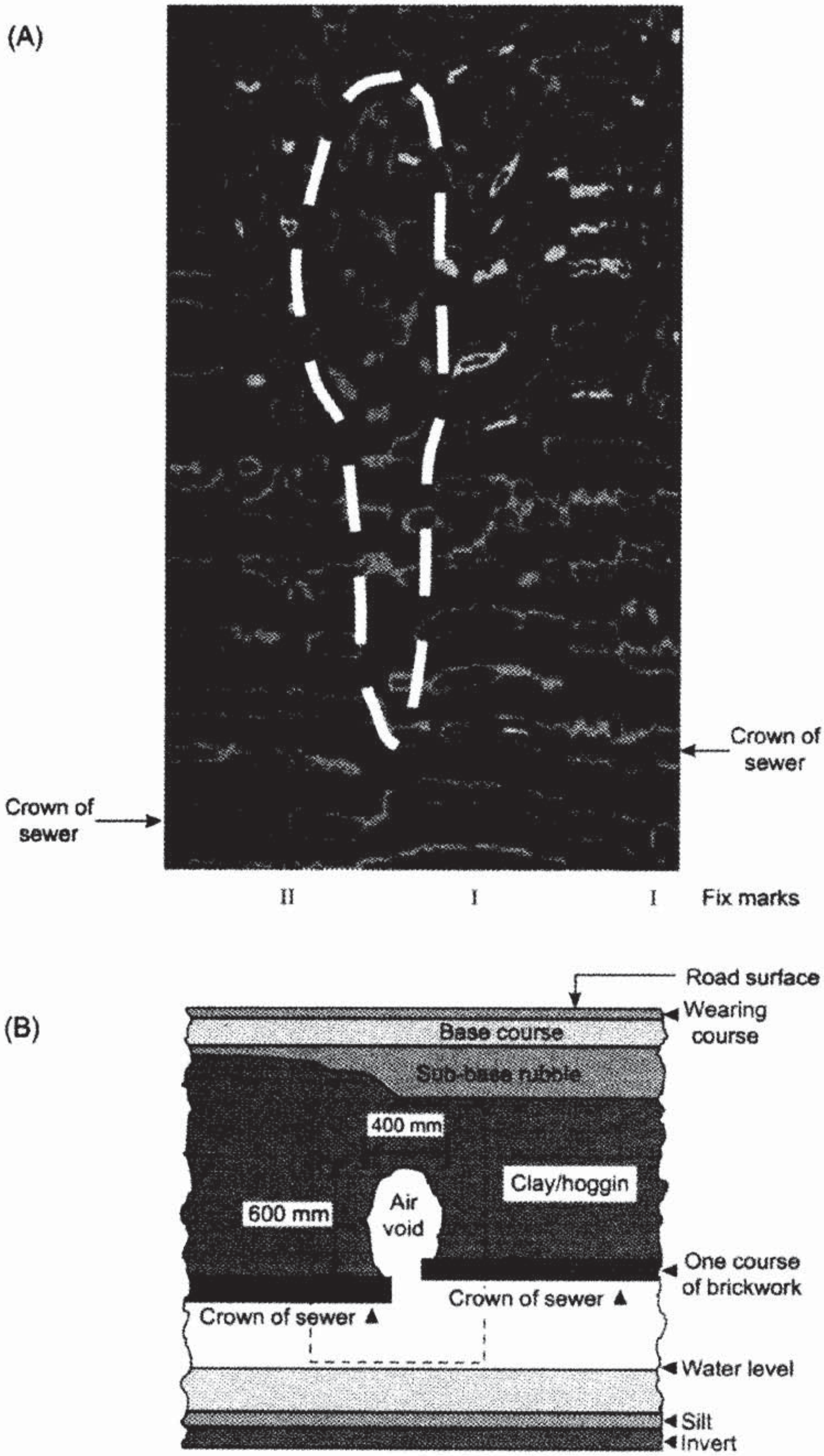

Figure 12.34 (A) Radargram through clay/hoggin material above a damaged sewer; a void is evident on the section and is delineated by dashed lines. The actual situation is shown in (B). Courtesy of Stratascan Ltd

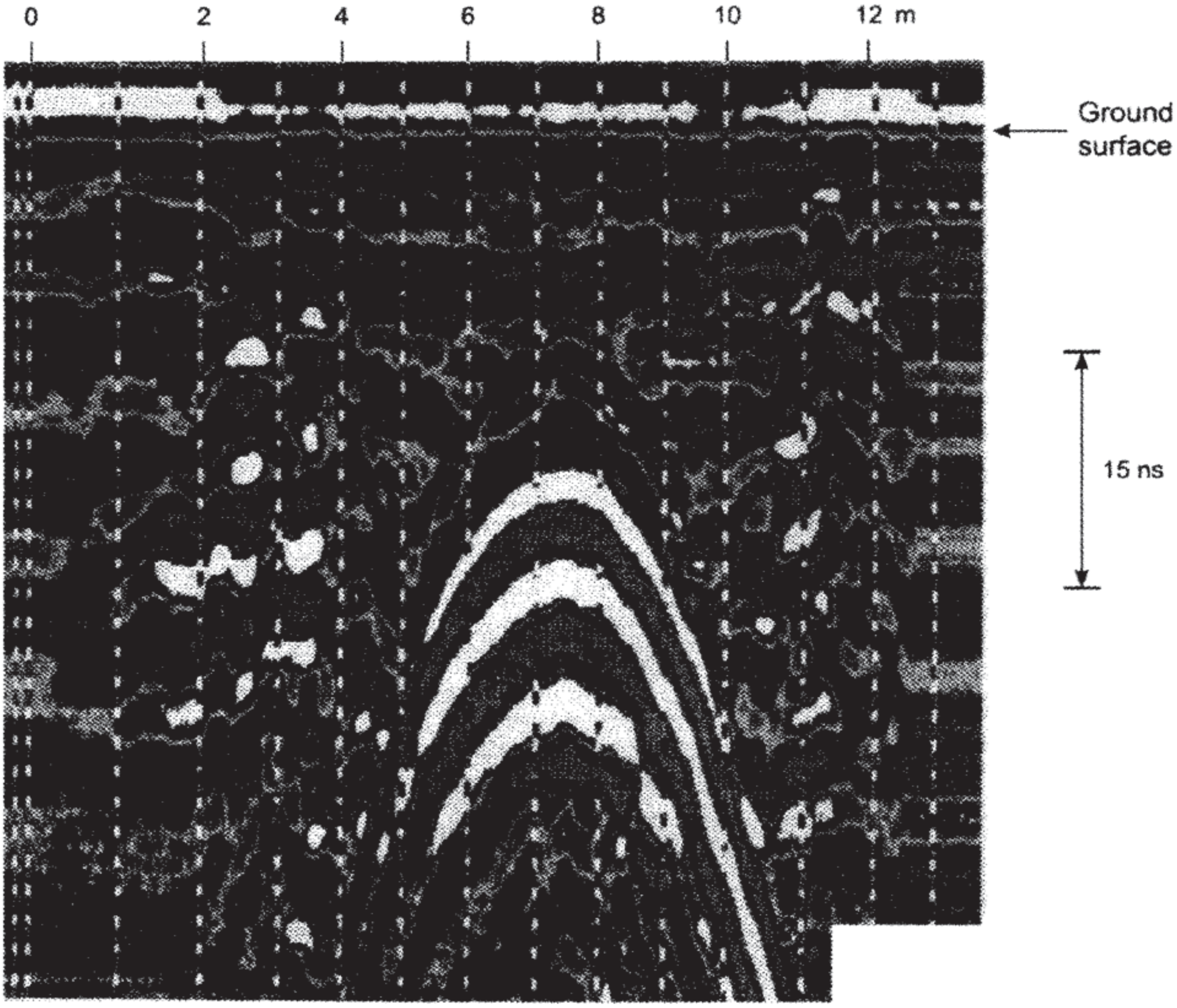

Figure 12.35 Worcester cathedral: radargram over a buried vault. The top of the vault is clearly identified as being at the apex of the strong white anomally which dominates the section. Courtesy of Stratascan Ltd

floor (air–stone interface) has the form positive then negative white. The polarity change is attributable to the passage of radiowaves from (a) a slow to fast medium (stone to air) and then (b) from a fast to slow medium (air to stone). Consequently, the phase of the reflection changes as does the sign of the reflection coefficient (see Section 12.3.1).

In some ancient buildings, additional complications can arise from the dimensions of the stone used in the construction of the building in relation to the wavelength of the incident radiowaves. Using a 500 MHz antenna over stone blocks ($V \approx 0.1$ m/ns), the wavelength is 0.2 m which is comparable to the dimensions of the blocks. Consequently, adverse phase interference can arise from internal reflections from the faces of individual blocks, making the overall radargram much more chaotic than it would otherwise have been. Similarly, building materials used to fill-in behind stone walls can be of a wide variety of materials, ranging from stone rubble to soil which may compact to leave air-filled voids.

12.8.6 Archaeological investigations

Radar has many applications in archaeological no-dig investigations, especially as the depth of penetration required is usually small (commonly less than 3 m). Radar can be used as a first-look technique or as a fill-in method between areas of excavation. One example of the successful use of radar in imaging an archaeological feature is given in Figure 12.36. The radargram was obtained using a 300 MHz antenna (range setting = 40 ns) with a GSSI SIR-3 system over flat ground made up of alluvial silts, gravels and boulder clay at a site at Caersws, Powys, Wales. The radargram shows very clearly the reflections arising from the surface of a Roman road with ditches on each side. The swathe of the carriageway appears as a slightly depressed central zone.

The location of graves can be important for at least two reasons. As consecrated ground, there has to be considerable care exercised if the site is wanted for development. Also, there may be important archaeological information associated with the buried remains. It is doubly important, therefore, that the locations of graves can be determined non-destructively. One such survey of graves using GPR among other techniques has been described by Bevan (1991). Radargrams obtained in two orthogonal directions across a postulated grave are shown in Figure 12.37. To aid the interpretation of the radar results, an electromagnetic ground conductivity meter (an EM31) and a magnetometer were used for corroboration. As can be seen from Figure 12.37C and D, these other tools produced geophysical anomalies which are closed (form concentric contours) around the locations of the graves. It should be emphasised that it is the disturbed ground associated with the graves that tends to show up on radargrams, not the bodies themselves.

Figure 12.36 Example of a radargram over a buried Roman road. Courtesy of Stratascan Ltd

Caersws - Roman road to west of fortress

Radar plots of traverses each 30m long
(markers at 1m centres)
300 MHz antenna with range setting of 40nsec

Subsoil - alluvial silts, gravels and boulder clay

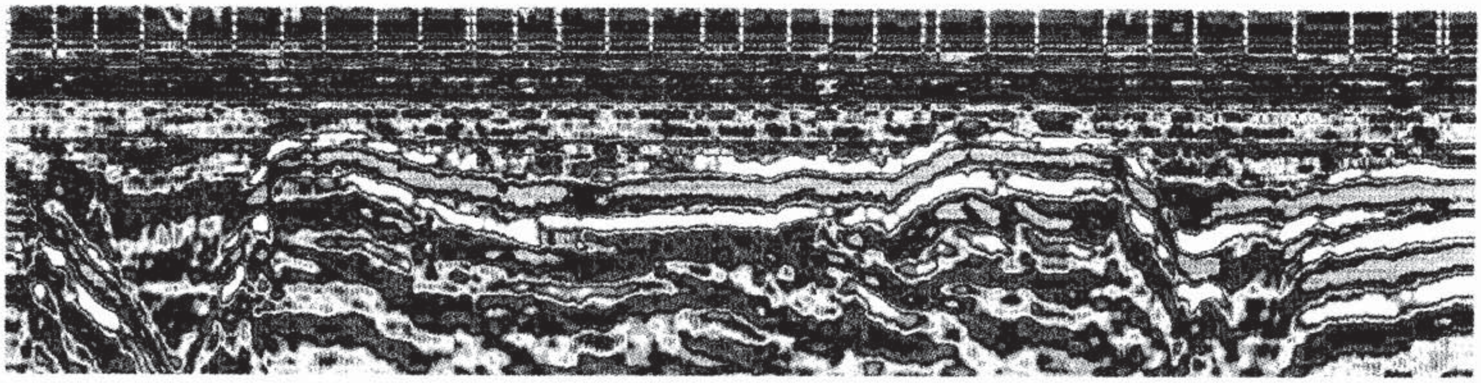

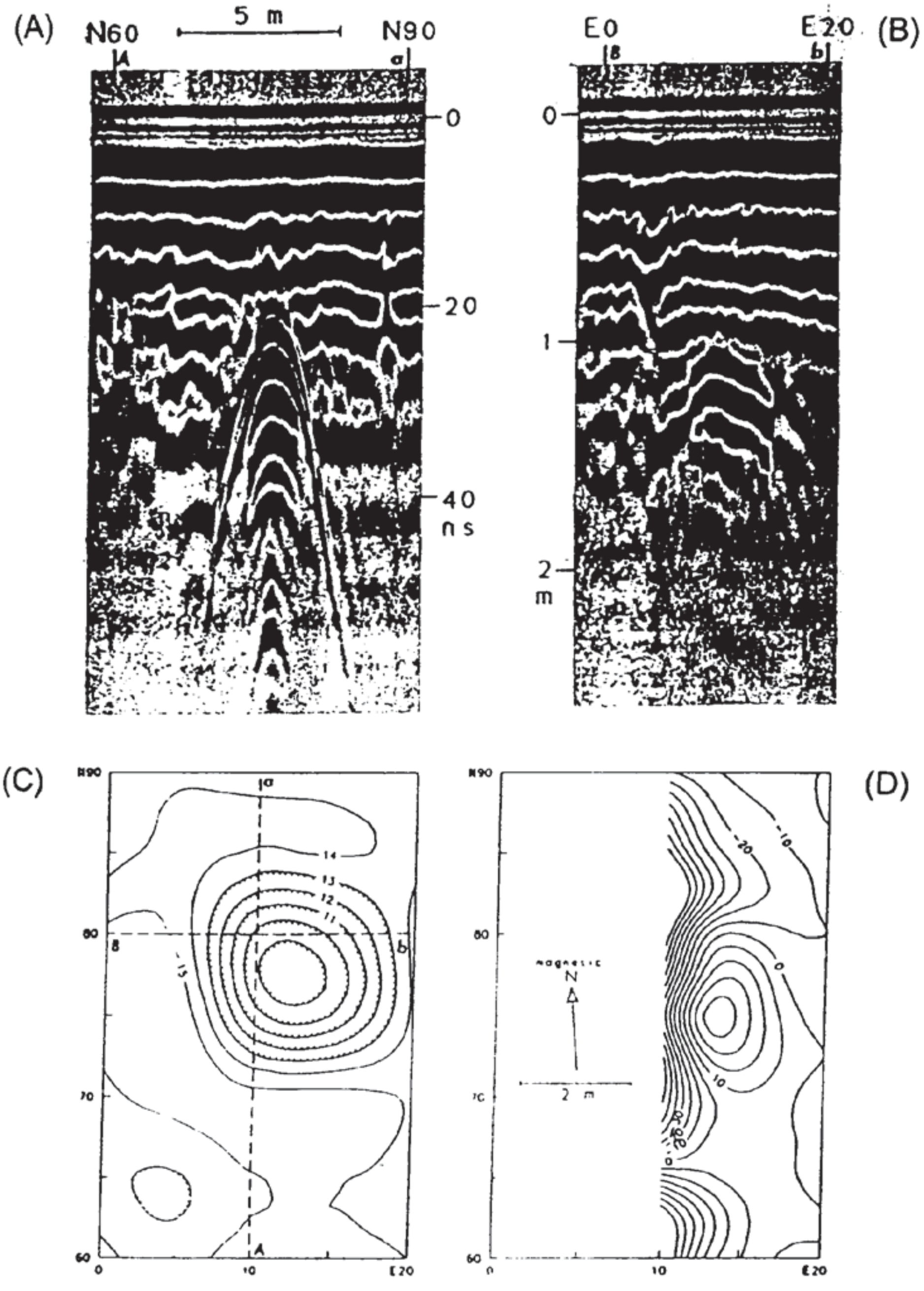

Figure 12.37 (A) North–south radar profile over a possible grave. (B) An east–west profile shows that the object is wider in this direction. (C) Apparent conductivity map with a contour interval of 1 mS/m; dashed lines indicate the orientations of the two radar profiles. (D) There is also buried iron or fired brick; the contour interval of this magnetic anomaly map is 10 nT. From Bevan (1991), by permission

Where human remains are thought to be located in specially protected sites – for example, those which may have been scheduled as 'Ancient Monuments' – radar can be particularly useful. The National Trust of Scotland has used radar in an attempt to locate the remains of the Duke of Northumberland's redcoats who died at the Battle of Culloden in 1746 after the historic routing of Bonnie Prince Charlie and his army. The investigation of the site is important as it is hoped that new information will be forthcoming about one of Scotland's greatest defeats at the hands of the English. It is thought that the remains of some of the English soldiers are buried inside a turf dyke.

12.8.7 Forensic uses of GPR

Radar has been used very successfully in the search not only for ancient graves but also for more recently buried bodies. It has been especially helpful where bodies have been concealed so as to avoid detection. Since the late 1980s, radar has been used increasingly by police in the search for disturbed ground which might indicate where a corpse has been hidden. For example, the States of Jersey, Channel Islands, employed radar to look for the bodies of a married couple which it was thought had been concealed in the back garden of their bungalow. Nothing was found. Radar also played an instrumental role in locating the remains of 12 corpses concealed at three locations in and around Gloucester, UK. A multiple murderer and his accomplice buried the bodies within the concrete foundations and inside newly plastered walls of their own house. The radar was able to identify anomalous targets within the concrete, thereby providing particular locations for excavation. Several more bodies buried in a nearby field were found with the help of radar.

In the USA, at Denton, Maryland, a high-school student Jamie Griffin was murdered, but neither his parents nor local police could locate his body for over seven years. Consequently, the person who had admitted perpetrating the crime could not be tried for murder. The body was thought to have been concealed somewhere within the 20 acres of Gunpowder Falls State Park, north of Baltimore. Previous searches using dogs, scuba divers and earth-moving equipment had been unsuccessful. It was only when a radar system was used that an anomaly was found which turned out to be due to Jamie Griffin's body. Not only was it then possible to convict the suspect of first-degree murder but the victim's family was able to hold a proper funeral for their son.

In addition to aiding the location of concealed corpses, radar has been used in the search for buried bullion following a major robbery in London in the late 1980s. With increasing publicity to such cases, so the forensic applications of radar increase. It is likely that, with the increasing reliability of radar, the applications for forensic investigations will become much more numerous.

12.8.8 Wide-aperture radar mapping and migration processing

Radar surveys are normally executed using one or two antennae in a profiling mode as a single-channel acquisition system. Fisher *et al.* (1992a) carried out a 40-channel GPR survey in a complicated fluvial/aeolian environment in the Ottawa River valley approximately 300 km north-northeast of Toronto, Canada. The receiver antenna was placed at each of 441 survey points at 1 m intervals along the profile line. For each of these receiver locations, data were recorded with the transmitting antenna at each of 40 separate

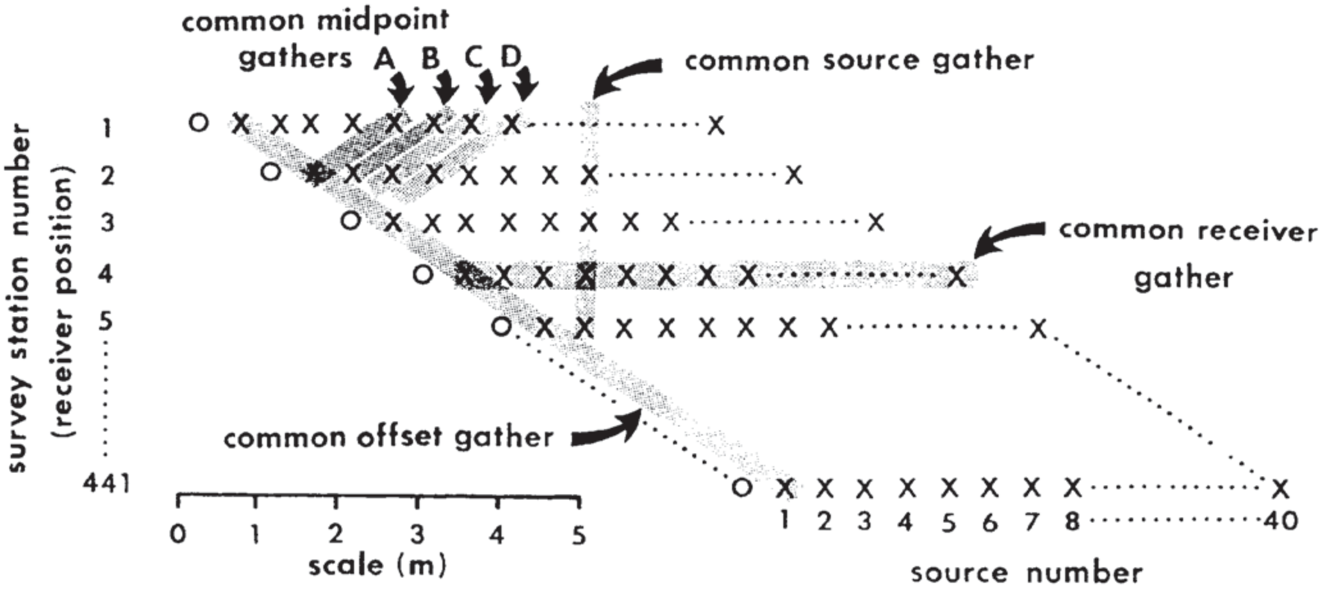

positions along the line, at 0.5 m intervals between 0.5 m and 20 m from the receiver (Figure 12.38). The antennae were orientated parallel to each other with the *E*-plane of the dipoles perpendicular to the survey line. Instead of the usual seismic analogue with a single source recording into a collection of receivers ('common-source gathers'), the common-receiver gathers were acquired. Traces could be sorted into common-source, common-receiver, common-offset or common-midpoint gathers irrespective of the method by which the data were acquired in the field. By obtaining the radar data in this way, traditional seismic processing could be undertaken on the common-midpoint (CMP) gathers.

A PulseEKKO radar system (Sensors & Software Inc.) with 100 MHz antennae was used, producing usable energy within the 50–150 MHz bandwidth. For each recording, 64 source excitations of the 400 V pulser were stacked to improve the signal-to-noise ratio. A total of 1280 samples were recorded with a time sample interval of 800 ps for a total time record of 1024 ns. Given a typical radiowave velocity in soil of 0.065 m/ns, this time range provided a possible depth of penetration of up to 33 m.

The radar data were input into a standard seismic processing sequence (filtering, statics corrections, common-midpoint gathering, velocity analysis, normal- and dip-moveout corrections, stacking and depth migration). More details of the data processing are given in Fisher *et al.* (1992a), and of the migration procedures in Fisher *et al.* (1992b). While the common-receiver and common-midpoint gathers for the radar data look very much like their seismic analogues, the derived RMS velocity estimates from three representative CMP gathers are shown in Figure 12.39. Whereas seismic velocities tend to increase with depth, these velocity panels show that the reverse is true for radar waves.

Figure 12.38 Survey geometry and data-gather definitions. A common-receiver gather contains all the traces recorded at one receiver position. A common-source gather contains all the traces generated at one source position. A common-offset gather contains all the traces with a fixed source-receiver separation. A common-midpoint gather contains all the traces with the same centre point between source and receiver. For the geometry used, there are four common-midpoint positions (cf. A, B, C, D) per receiver position. There are 40 traces in each common-receiver gather and 40 in each common-source gather. Except at the end of the survey, there are 10 traces in each common-midpoint gather. From Fisher *et al.* (1992a), by permission

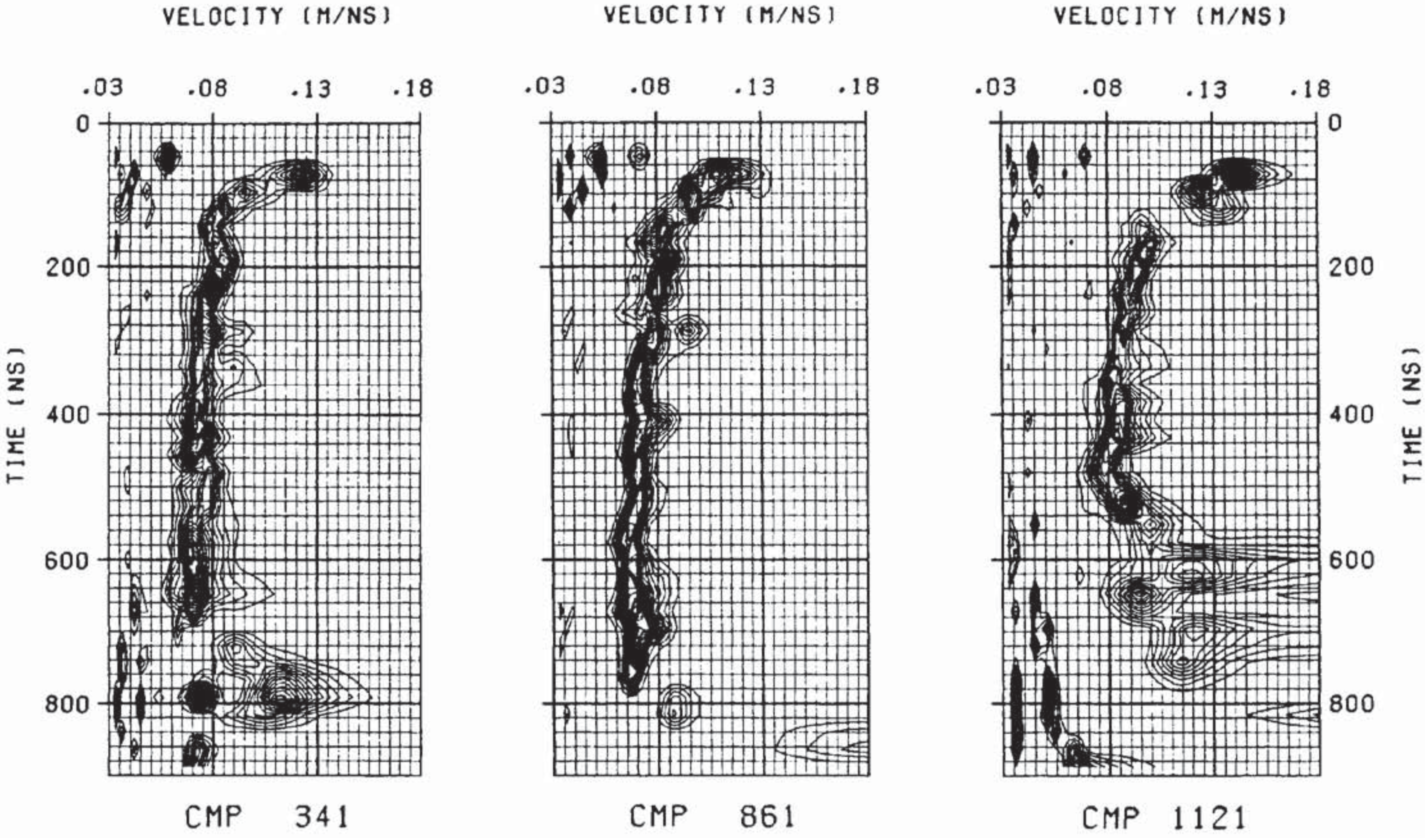

Figure 12.39 RMS velocity estimates from three representative CMP gathers. Velocity generally decreases with increasing depth (i.e. with increasing travel time). Velocity estimates are not reliable at times greater than that at which the last coherent reflection occures. From Fisher *et al.* (1992a), by permission

The results of the data processing are shown in Figures 12.40 and 12.41. Figure 12.40A shows a near-offset section; at each location the trace plotted is that recorded with the smallest (0.5 m) source–receiver separation. Figure 12.40B shows every fourth trace in the stacked time section; at each location, the trace plotted is the stack over the traces at the midpoint.

Note that the two panels in Figure 12.40 are shown as time sections. Compare those with the upper panel in Figure 12.41 which is a migrated depth image; the corresponding interpretation is provided in the lower panel. It is evident that significant detail has been obtained to a depth of over 25 m, as correlated with adjacent boreholes. The final migrated data are quite spectacular and show sub-metre vertical resolution even with a 100 MHz antenna to depths in excess of 20 m. Such success has to be tempered by the fact that, in the UK for example, sites where similar records could be obtained are rare, and comparable depths of penetration and similar resolution would be very difficult to achieve owing to the conductive nature of the soils. However, this example does demonstrate that, given the appropriate field conditions, equipment and processing facilities, exceptionally good results are possible with the method. Comparable results would not be possible using even high-resolution seismic reflection surveying.

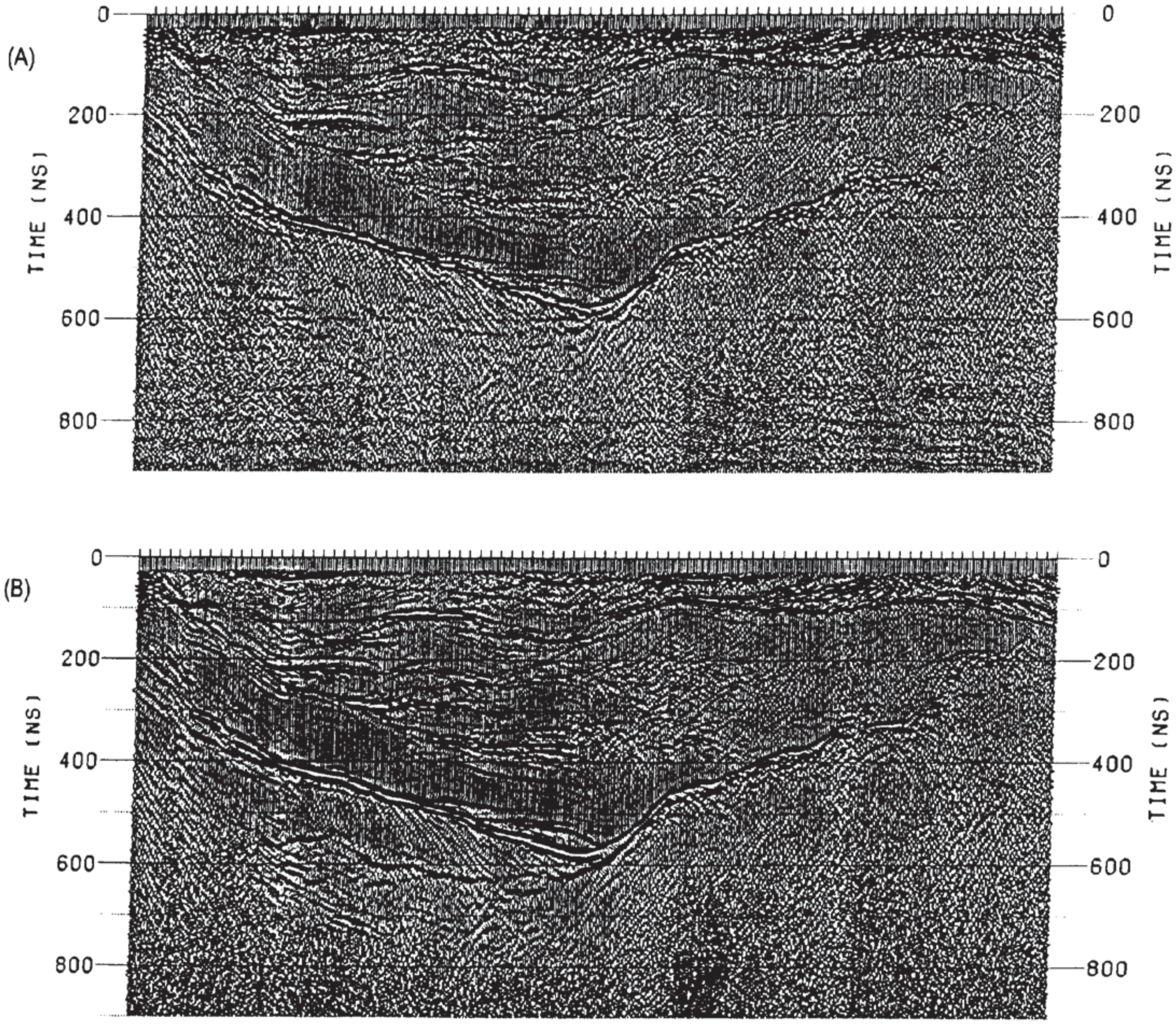

Figure 12.40 Radar sections from a 40-channel radar survey in the Ottawa River valley, Canada. (A) Near-offset section; at each location, the trace plotted is that recorded with the smallest (0.5m) source–receiver separation. (B) Section displayed with every fourth trace of the stacked time section; at each location the trace plotted is the stack over the traces at that midpoint. Both (A) and (B) are plotted with AGC with a 200ns window. From Fisher *et al.* (1992a), by permission

12.8.9 Borehole radar

In parallel with developments in surface ground penetrating radar, borehole systems have been in use since the early 1980s. One system called RAMAC was developed as part of the International Stripa Project in Sweden and is manufactured by Malå Geoscience AB and marketed by ABEM. The Stripa Project was undertaken in order to develop techniques suitable for use in underground nuclear fuel waste repositories. The short-pulse borehole radar was used primarily to obtain information about the structure and integrity of crystalline rock masses at a distance from tunnels and boreholes without affecting the rock in any way. In 1987, a RAMAC survey in Switzerland revealed fractures in granite 160 m away from the surveyed borehole.

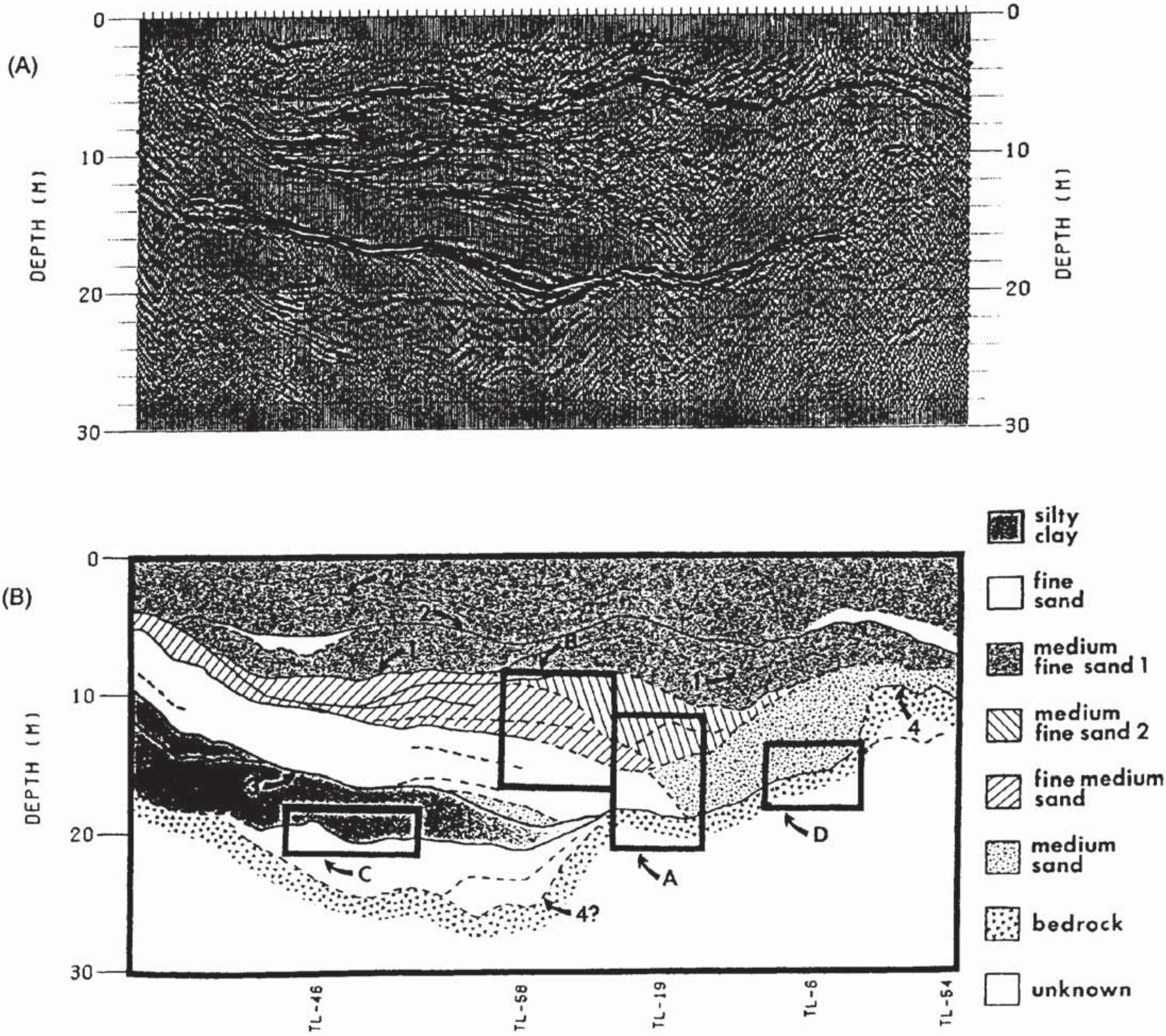

Figure 12.41 (A) Migrated depth image and (B) its interpretation. The image is plotted with AGC and only every fourth trace is shown. Approximate locations of available drill cores are labelled at the bottom of (B). Reflector 1 is a garnet sand; 2 = silt layers; 3 = fine sand gravel; 4 = bedrock. From Fisher *et al.* (1992a), by permission

Since then, RAMAC has been used to record reflections arising from structures at distances greater than 300 m within rocksalt. The system is now well proven and has been used internationally in mining, hydrogeological and rock mechanical investigations. It is also being used to investigate sites for tunnels, dams and other construction type projects.

The basic system is illustrated schematically in Figure 12.42 with a simple radargram. A transmitter is used to generate the radiowaves with a pulse frequency of 43 kHz. A separate receiver is located a short distance further down the hole: typically 2–6 m when surveying in sedimentary rocks, and 5–15 m when in crystalline rocks. The receiver operates with a bandwidth of 10–200 MHz. Different frequency

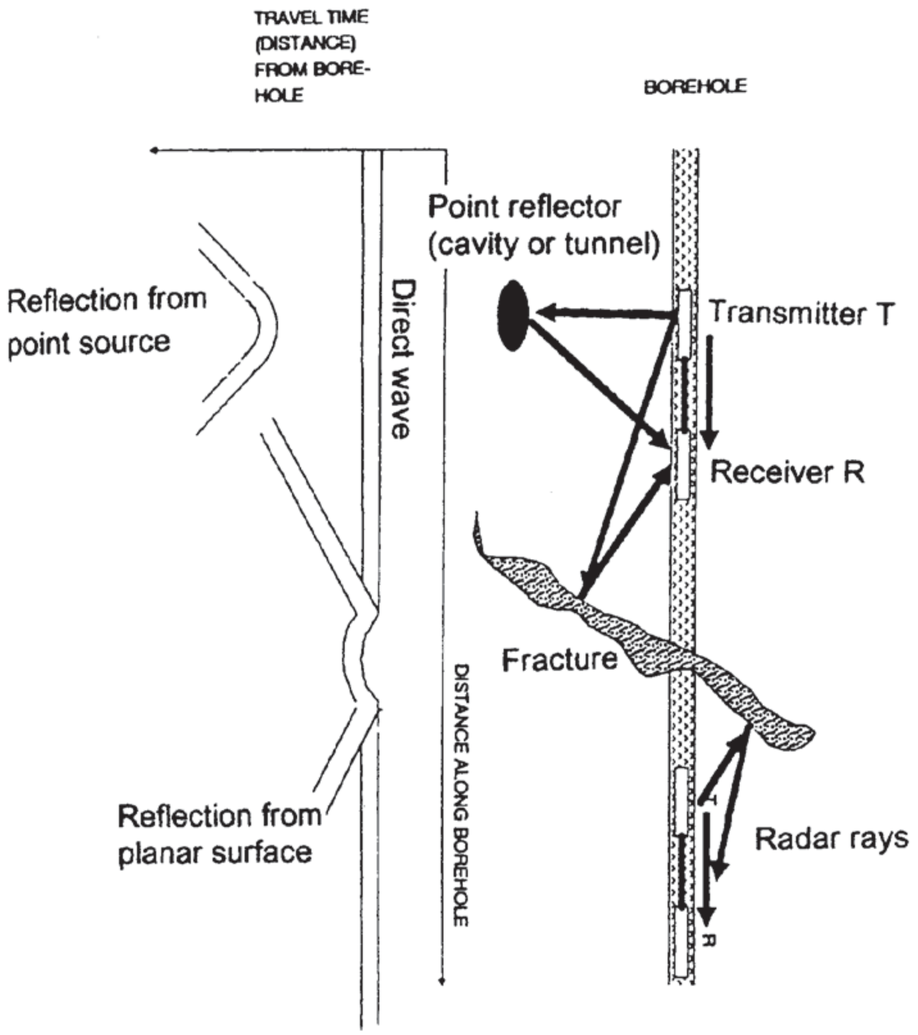

Figure 12.42 Basic arrangement for a borehole radar system with typical radar section images of plane and point reflectors. The cylindrical symmetry of dipole antennae creates V-shaped responses from planar reflectors. Hyperbolae arise from point sources. Courtesy of ABEM

antennae can be used, either 20 MHz or 60 MHz using the standard RAMAC system, or 50, 100, 200 or 400 MHz with a newer version released in 1994. Measurements are made at fixed intervals of 0.5 m or 1 m. It takes at most about 30 seconds at each location to make the required measurements.

Two modes of operation are possible. One uses an omnidirectional dipole antenna, and the other uses directional antennae so that reflections from discretely identified quadrants surrounding the borehole can be identified. The RAMAC system can also be used in cross-hole tomographic configurations with the transmitter antenna in one borehole and the receiver down another. Additionally a receiver can be placed down a borehole while the transmitter is located either in a mine tunnel or on the ground surface, as illustrated in Figure 12.43. Processing of radargrams can be accomplished using on-screen interpretational software.

A simple example of the types of radargrams generated using the RAMAC system is shown in Figure 12.44. The radargram was

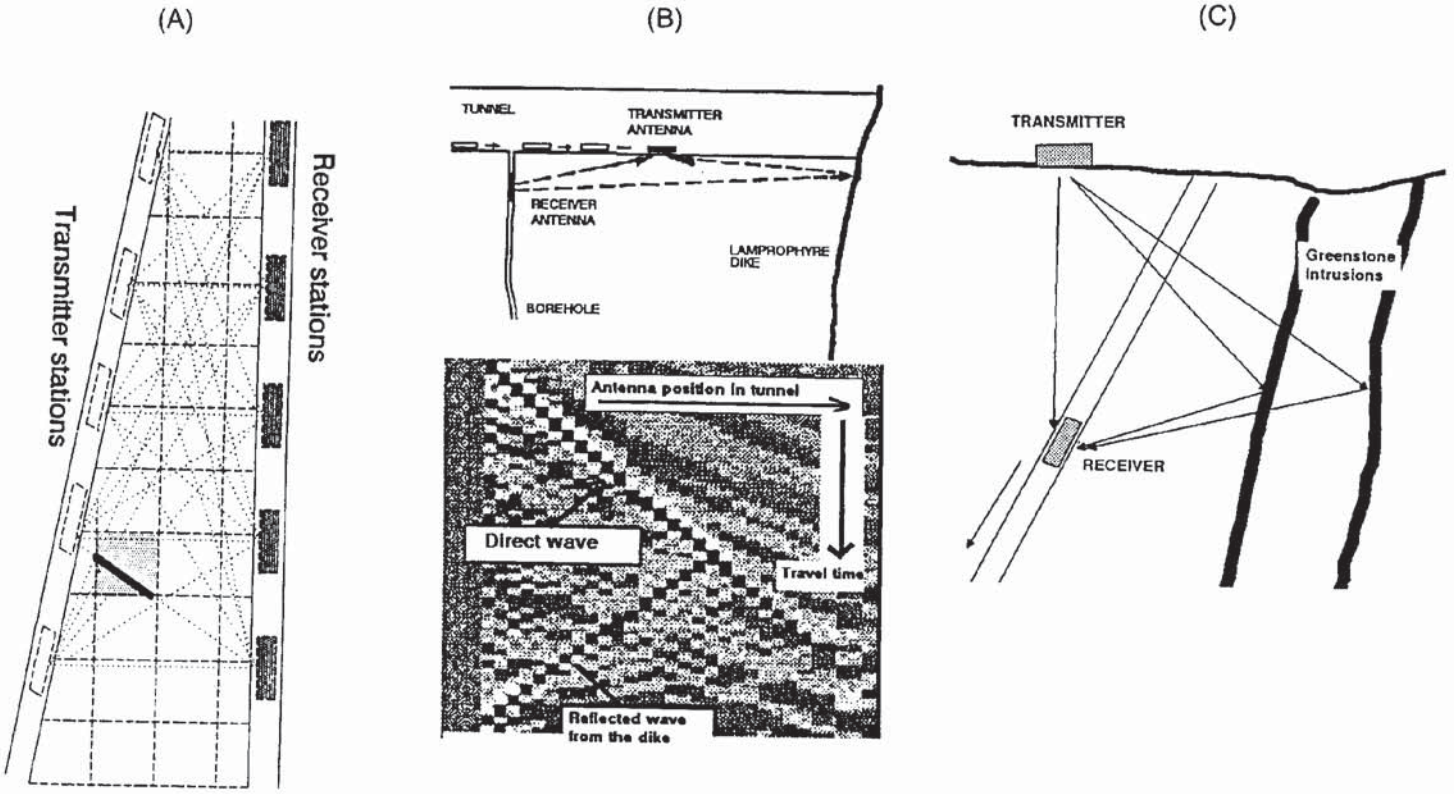

Figure 12.43 (*top*) Three configurations for borehole radar systems: (A) cross-hole tomography; (B) tunnel-to-borehole imaging, and (C) vertical radar profiling where the transmitter is on the ground surface and the receiver is down the borehole. Courtesy of ABEM

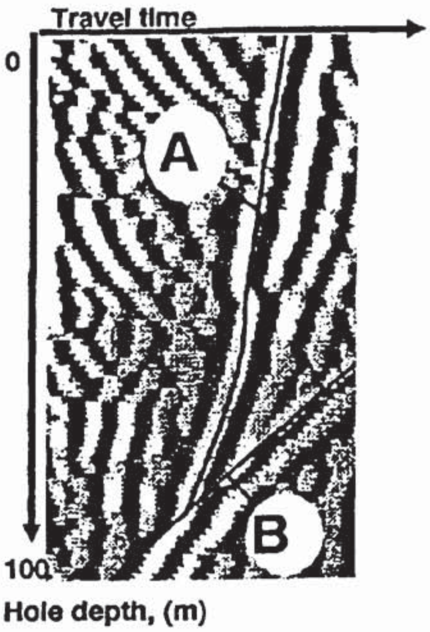

Figure 12.44 (*left*) Borehole radargram showing the location of an abandoned drill string (A) and a major fault zone (B) in which the drillbit was stuck. Courtesy of ABEM

obtained from one of three radar surveys made in three different boreholes to locate an abandoned drill string. Strong reflections from the drill string were observed on radargrams from all three boreholes. The radargrams also revealed the reason why the drill string became stuck – it had intersected an oblique major fault zone.

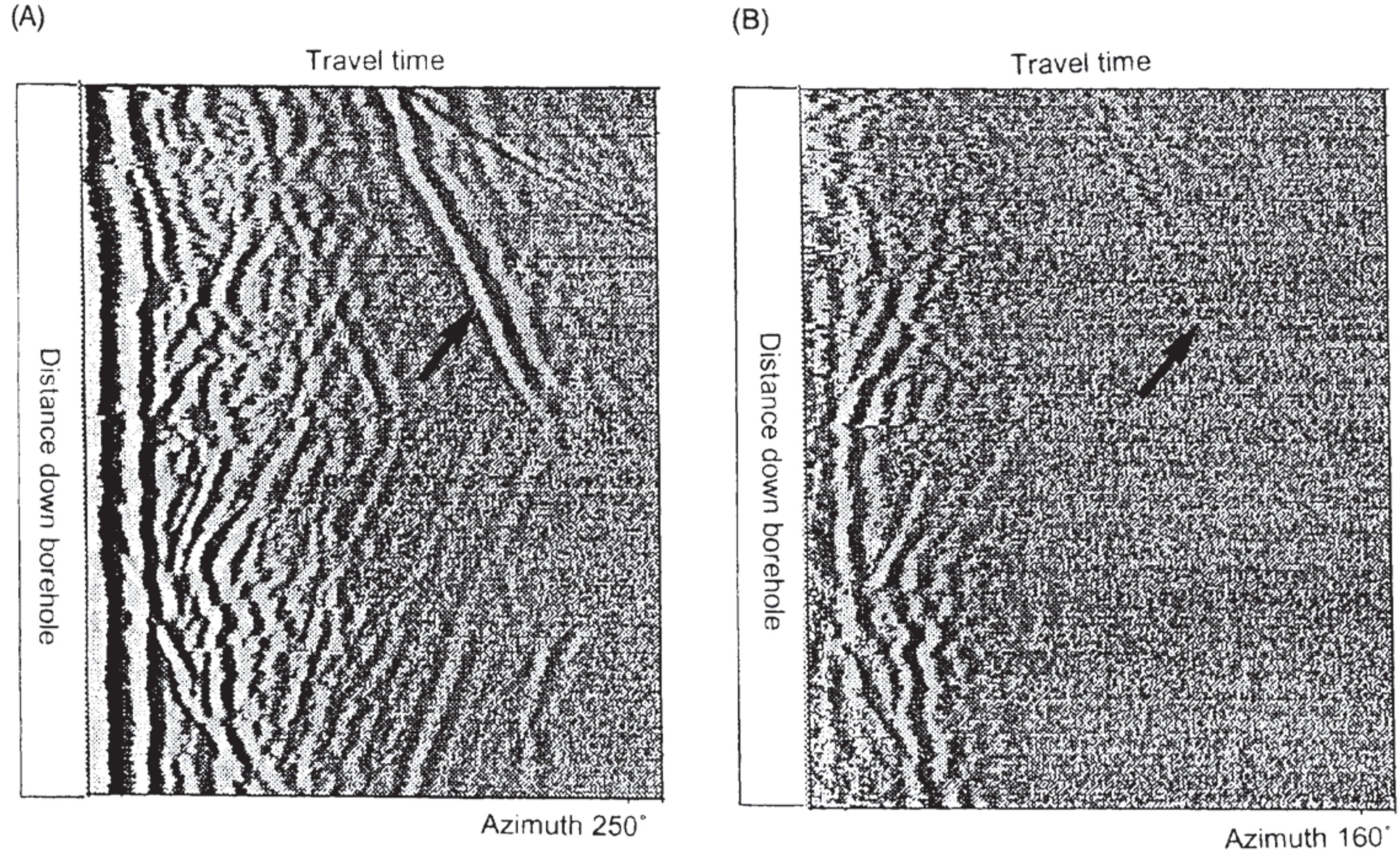

Figure 12.45 Borehole radargrams from the same location showing the effect of azimuth using directional antennae. (A) Azimuth is 250° magnetic with a major strong planar reflection (arrowed). (B) Azimuth is 160° magnetic and the planar reflection strength has decreased to its minimum value. Courtesy of ABEM

A second example presented in Figure 12.45 shows the effect of azimuth. In Figure 12.45A, the antennae are directed at 250° magnetic bearing and a plane reflection is evident (arrowed). The azimuth is rotated by 90° to 160° magnetic and the reflection is at a minimum (Figure 12.45B). Using such information, the dip and strike of planar features can be determined.